NASA-CR-200597

ANALYSIS OF LAC OBSERVATIONS OF CLUSTERS OF GALAXIES AND SUPERNOVA REMNANTS

NASA Grant NAG8-181

Final Report

For the Period 5 March 1991 through 30 September 1994

Principal Investigator
Dr. J. Hughes

February 1996

Prepared for:

National Aeronautics and Space Administration
Goddard Space Flight Center
Greenbelt, Maryland 20771

Smithsonian Institution
Astrophysical Observatory
Cambridge, Massachusetts 02138

The Smithsonian Astrophysical Observatory
is a member of the
Harvard-Smithsonian Center for Astrophysics

The NASA Technical Officer for this grant is Jeannette Vargas, Mail Code EM25, George C. Marshall Space Flight Center, Marshall Space Flight Center, Alabama 35812.

Final Report – Grant NAG8-181
January 30, 1996
John P. Hughes

The following listed publications (also attached) serve as the final report for NASA Grant No. NAG8-181.

1.) "The X-Ray Spectrum of Abell 665," J. P. Hughes, and Y. Tanaka, *Astrophysical Journal*, **398**, 62, (1992).
2.) "Clusters of Galaxies," J. P. Hughes, invited review talk in *Ginga Memorial Symposium – From Ginga to ASTRO-D and Further to DUET*, ISAS Symposium on Astrophysics 1992, (ISAS, Tokyo, Japan), eds. F. Makino and F. Nagase, 104, (1992).
3.) "*Ginga* Observation of an Oxygen-Rich Supernova Remnant," I. Asaoka, J. P. Hughes, and K. Koyama, abstract in *Frontiers of X-Ray Astronomy*, Proceedings of the 28th Yamada Conference, (Universal Academy Press: Tokyo), eds. Y. Tanaka and K. Koyama, p. 385, (1992).
4.) "*Ginga* Observations of the Coma Cluster and Studies of the Spatial Distribution of Iron," J. P. Hughes, J. A. Butcher, G. C. Stewart, and Y. Tanaka, *Astrophysical Journal*, **404**, 611, (1993).
5.) "A Measurement of the Hubble Constant from the X-Ray Properties and the Sunyaev-Zel'dovich Effect of Abell 2218," M. Birkinshaw, and J. P. Hughes, *Astrophysical Journal*, **420**, 33, (1994).
6.) "Non-Polytropic Model for the Coma Cluster," R. Fusco-Femiano, and J. P. Hughes, *Astrophysical Journal*, **429**, 545, (1994).
7.) "Abundance Gradients in Cooling Flow Clusters: *Ginga* LAC & *Einstein* SSS Spectra of A496, A1795, A2142 & A2199," R. E. White, III, C. S. R. Day, I. Hatsukade, and J. P. Hughes, *Astrophysical Journal*, **433**, 583, (1994).

SMITHSONIAN ASTROPHYSICAL OBSERVATORY
60 Garden Street, Cambridge, MA 02138
(617) 495-7000

23 February 1996

NASA Center for Aerospace Information (CASI)
Attention: Accessioning Department
800 Elkridge Landing Road
Linthicum Heights, Maryland 21090-2934

Subject: Final Report

Reference: Grant NAG8-181

Transmitted herewith is one (1) copy of the subject report for the period 5 March 1991 through 30 September 1994, in accordance with the provisions of the above referenced grant.

Very truly yours,

Harvard-Smithsonian
Center for Astrophysics

Preprint Series

No. 3409
(Received April 15, 1992)

THE X-RAY SPECTRUM OF ABELL 665

John P. Hughes
Harvard-Smithsonian Center for Astrophysics

and

Yasuo Tanaka
Institute of Space and Astronautical Science, Kanagawa, Japan

To appear in
The Astrophysical Journal
October 10, 1992

HARVARD COLLEGE OBSERVATORY SMITHSONIAN ASTROPHYSICAL OBSERVATORY
60 Garden Street, Cambridge, Massachusetts 02138

cc: Ms. Joyce Mallory, Code GP29, NASA/MSFC, AL 35812, w/encl.

Center for Astrophysics
Preprint Series No. 3409

THE X-RAY SPECTRUM OF ABELL 665

John P. Hughes
Harvard-Smithsonian Center for Astrophysics

and

Yasuo Tanaka
Institute of Space and Astronautical Science, Kanagawa, Japan

THE X-RAY SPECTRUM OF ABELL 665

John P. Hughes
Harvard-Smithsonian Center for Astrophysics
60 Garden Street, Cambridge, MA 02138
Yasuo Tanaka
Institute of Space and Astronautical Science
1-1, Yoshinodai, 3-chome, Sagamihara-shi, Kanagawa 229 Japan

Received 1991 January 7; accepted 1992 April 14

ABSTRACT

The X-ray spectrum of the Abell 665 cluster of galaxies has been determined by the *Ginga* satellite. The spectrum can be well fitted by an isothermal model with $kT = 8.26^{+0.95}_{-0.81}$ keV and metal abundance 0.49 ± 0.16. Joint analysis with lower energy spectral data from the ***Einstein Observatory*** is used to constrain the temperature distribution in the cluster. For a particular form of the polytropic temperature model we find the best fit to be the isothermal case and we set an upper limit on the polytropic index of 1.35 (99% confidence). The virial mass of the cluster has been determined from both the X-ray data and the galaxy velocity dispersion. The mass estimates from the optical and X-ray analyses are fully consistent with each other. Abell 665 is found to be $0.82^{+0.41}_{-0.26}$ times as massive as Coma if the two clusters are assumed to have the same spatial distribution of virial mass.

Subject headings: galaxies: clustering – intergalactic medium – X-rays: galaxies

1. INTRODUCTION

Abell 665 is a rich distant ($z \sim 0.18$) cluster in the constellation Ursa Major. For some years now it has been the target of extensive radio observations and a strong decrement in the temperature of the cosmic background radiation, the signature of the Sunyaev-Zel'dovich (SZ) effect in the Rayleigh-Jeans portion of the background spectrum, has been observed from the cluster (Birkinshaw 1989). In this article we report primarily on an X-ray spectral study of A665. The intent of the investigation is to determine the average gas temperature of the cluster atmosphere, to set limits on the allowed temperature distributions, and to determine the cluster binding mass. We do this using data from the ***Einstein Observatory*** imaging proportional counter (IPC) and the large area counters (LAC) on the Japanese satellite ***Ginga*** (Makino ***et al.*** 1987). Birkinshaw, Hughes, & Arnaud (1991, hereafter BHA) employ these spectral results to determine the Hubble constant from an analysis of the SZ effect for this single cluster.

The decrement in the cosmic microwave background radiation due to the Sunyaev-Zel'dovich effect is proportional to the line-of-sight pressure ($n_e T$) integral through the cluster. Thus any study of the SZ effect and use of it for distance determination requires an accurate representation of the gas density and temperature structure of the cluster atmosphere. The imaging instruments onboard the ***Einstein Observatory*** have provided excellent information on the gas density distribution for a large number of galaxy clusters (***e.g.***, Abramopoulos & Ku 1983, Jones & Forman 1984) and for A665 in particular. These data, however, were unable to define the temperature distribution or even to determine the mean gas temperature of most galaxy clusters.

Some previous studies of the SZ effect have attempted to compensate for the lack of temperature information by using measured galaxy velocity dispersions to estimate mean gas temperatures (***e.g.***, Birkinshaw 1979, Boynton ***et al.*** 1982). This technique is rather unreliable given the large scatter in the observed correlation between temperature and velocity dispersion (Edge & Stewart 1991) and due to the possible presence of projection effects and/or subclustering which can strongly bias the velocity dispersion for any individual cluster. Other studies have employed both velocity dispersion data and X-ray spectra to infer the temperature distribution (White & Silk 1980) using the assumption of hydrostatic equilibrium and the underlying cluster virial mass distribution to connect the two observables.

Information on the binding mass of galaxy clusters is itself of astrophysical interest because of the presence of significant amounts of dark matter in these systems. We use our X-ray spectral data and the recently measured velocity dispersion from Oegerle ***et al.*** (1991) to estimate the cluster's virial mass. Our work finds that A665 is indeed massive, requiring large amounts of nonluminous matter to gravitationally bind the cluster. We compute the total cluster mass and compare it to the optical luminosity in the galaxies and the mass of X-ray emitting hot gas. The values we obtain for these quantities for A665 are all very similar to the values found for the rich nearby Coma cluster. The binding mass we derive is within a factor of two of the value used by Davidsen *et al.* (1991) to test the hypothesis that the dark matter associated with clusters of galaxies consists of decaying massive neutrinos as suggested by Sciama (1991, and references within).

We also consider polytropic models of the type introduced by Henriksen & Mushotzky (1986), *i.e.*, where $T \propto n^{\gamma-1}$ while the density distribution is given by the isothermal-β form. This polytropic formulation is very convenient for the SZ study, since the functional form of the pressure integral remains the same as in the case of an isothermal distribution. We find that the X-ray data favor an isothermal distribution and that the maximum allowed polytropic index is 1.35.

As mentioned above the IPC was able to produce images of cosmic sources in the 0.2-4 keV X-ray band. In BHA we present the results of a detailed analysis of the A665 image. The IPC was also able to obtain low energy X-ray spectra at moderate resolution ($\Delta E/E \sim 1$ at 1 keV), which has been most useful for determining the absorbing column density to A665 and for constraining the amount of 1 keV temperature gas in the cluster. The *Ginga* LAC is a mechanically collimated (approximately $1^\circ \times 2^\circ$ field of view) large area array (4000 cm^{-2}) of proportional counters with good sensitivity from 1.5 keV to 30 keV (Turner *et al.* 1989). It is the first instrument with the ability to determine the X-ray spectra of faint (10^{-11} erg cm^{-2} s^{-1}) X-ray sources. LAC data are quite good at determining the mean temperatures of clusters from the shape of the bremsstrahlung continuum emission and the mean elemental abundance from the strength of the Kα iron line near 6.7 keV. Joint analysis of the low (IPC) and high (LAC) energy X-ray spectra, such as we carry out here, allows us to constrain strongly the model spectral temperature model for the cluster and thereby allows us to set limits on the virial mass of the cluster.

In the next section we discuss the data reduction of the *Ginga* and IPC data. Isothermal and polytropic model fits follow in §3. Section 4 discusses the virial mass estimates and §5 concludes.

2. DATA REDUCTION

2.1. *Ginga LAC Data*

The A665 cluster of galaxies was observed by the large area counters on the Japanese satellite *Ginga* on 10 November, 1988. During the higher background period of the *Ginga* orbit, we carried out scanning observations. The source was clearly detected at the expected position of the cluster and it was consistent with an unresolved source viewed by the *Ginga* collimator. No other sources were seen in the vicinity. The fitted peak counting rate in the LAC was 4.8 s^{-1} (1.7 - 9.3 keV).

Pointed observations of A665 were done during the lower background remote orbits. During this period over 20000 s of data satisfied the following stringent data selection criteria and were included in the spectrum. The earth elevation angle was required to be larger than 12°. Data from regions in the satellite orbit corresponding to higher background (such as the SAA passage and orbital regions with low cut-off rigidity) were rejected. We rejected data from segments in which the LAC high voltage was turned on or off. The angle from the LAC field of view and the sun was greater than 90°, so contamination from solar X-rays was not a problem. After background subtraction the source yielded a counting rate in the LAC of 3.8 s^{-1} (1.7 – 9.3 keV). This is consistent with the scanning data since the pointing position of the LAC was offset from the cluster position by about 0.3° to avoid a possible contaminating source ($\pi(1)$ UMa). The calculated collimator response at the X-ray position of the cluster was 0.785. There was no significant flux in the mid-layer of the LAC and we only consider the spectrum from the top layer. In each pulse height (PH) channel a systematic error of 1% of the source signal was added in quadrature with the statistical error to account for uncertainties in the energy bin boundaries.

The gain of the LAC is monitored in flight using the Ag Kα line at 22.1 keV, which arises from fluorescence of cosmic X-ray background photons and cosmic ray particles in the silver coating on the LAC collimator. For this observation, we fitted the Ag Kα line energy for each of the eight individual detectors in the top layer and from these computed an average response function which was used subsequently in the model fitting. Note that the overall average gain was such that the Ag Kα line fell in PH channel 35.07, which lies within the nominal range of gain values (between 35.0 and 35.2, S. Tanako, private communication). The one-sigma uncertainty in the statistical determination of the line centroid was ±0.06 keV. We use this value below to represent the systematic uncertainty in the LAC gain. The linearity of the LAC counters was determined pre-launch and it was assumed that this remained stable during the mission.

The background of the LAC has been studied in great detail (Hayashida *et al.* 1989) and for sources at the flux level of A665, proper background subtraction is the single most important consideration. For background subtraction during the A665 observation, we employed two techniques: (1) a direct method, which uses background data from a blank-field pointing on an adjacent day and (2) the background model developed by Hayashida *et al.*. We found that the two techniques yielded slightly different results for best fit values, although the error intervals on those parameters overlapped. Given that the derived spectra were reasonable and that there was no reason to prefer one method over the other (each has its advantages as well as disadvantages), we determined to average the spectra obtained by the separate techniques. We note that the differences between the fitted results in the two cases are at the level of the background-subtraction uncertainty (which we explicitly examine below).

Hayashida *et al.* determined that the one-sigma uncertainty in their background subtraction technique corresponded to a 2 - 10 keV count rate of 0.86 s^{-1}, which they claim arises partly from spatial fluctuations in the diffuse X-ray background (about two-thirds of the total) and partly from other systematic effects in estimating the induced-particle background (the remaining one-third). We have used our scanning data to establish an uncertainty in background subtraction appropriate to this observation of A665. The data from regions of the scan which did not include the cluster were analyzed using the same background-subtraction model as used for generating the source spectrum. We found that there was a residual net positive counting rate of about 0.4 s^{-1} from this region. This is the value which we use below to represent the systematic uncertainty in the background subtraction since it corresponds more closely to the local spatial vicinity of the cluster and is more nearly contemporaneous with the actual source observation.

We have summed the data from the top layer for the eight individual detectors to form the *Ginga* spectrum, which we show in Figure 1. We only consider the spectrum up to about 13 keV; above this energy the signal is dominated by residual systematic errors in background subtraction at a level of about 0.01 cts s^{-1} keV^{-1}. All quoted results are based on the summed spectrum in Figure 1.

2.2. *Einstein IPC Data*

The *Einstein* imaging proportional counter (IPC) observed A665 for 6430.8 s (dead-time corrected exposure time) on 9 October 1979. An extended source with a background-subtracted counting rate of 0.293 ± 0.007 s^{-1} (over the energy band 0.23 – 4.1 keV and within a radius of 8′) was clearly detected at a position of 8h 26m 25s, 66° 1′ 21″ (1950). This is about 3′ south of the Abell (1958) position. In this paper we concentrate on the spectral analysis of the IPC data; further details of the imaging data and a complete spatial analysis are given in the accompanying article (BHA). However we wish to highlight the following points: the cluster X-ray surface brightness distribution is well described by the isothermal-β model with $R_{core} = 1.6'$ and $\beta = 0.66$. Furthermore the cluster can be considered to follow this profile out to radii of 6.0′, 5.0′, and 4.2′ at confidence levels of 68%, 90% and 99% respectively. The *Einstein* high resolution image of the cluster is entirely consistent with this model and in particular, shows no emission from a point-like source near the core of the cluster. The lack of evidence for a central surface brightness spike strongly limits the presence of any cooling flow component in this cluster. Detailed analysis of this dataset is limited by the low signal-to-noise of the observation; the cluster was detected at only the 7 σ confidence level. See BHA for more details on the X-ray imaging analysis.

Three unresolved sources beyond about 15′ from the cluster center were detected by the IPC at the following positions: 8h 24m 12s, 66° 12′ 6″; 8h 28m 42s, 66° 14′ 4″; and 8h 28m 43s, 66° 1′ 21″ (1950 positions) (Harris *et al.* 1990). The first source had a very soft IPC spectrum (hardness ratio of $-0.43^{+0.14}_{-0.13}$), corresponding to a temperature of about 0.2 – 0.3 keV, which does not contribute to the *Ginga* spectral band. The latter two sources were identified with AGN (Gioia *et al.* 1990) and had 0.3 – 3.5 keV X-ray fluxes of 2.48

$\times\ 10^{-13}$ erg cm^{-2} s^{-1} and 4.90 $\times\ 10^{-13}$ erg cm^{-2} s^{-1}, respectively. Because of the large field of view of the *Ginga* collimator (1° by 2° FWHM), it was not possible to avoid these sources in the *Ginga* observation. However, in the *Einstein* IPC band the combined flux of these sources was nearly an order of magnitude smaller than the flux from the cluster. One the other hand, the X-ray spectrum of the average AGN is different enough from that of the average cluster of galaxies that some effect of these confusion sources might be evident, especially in the higher energy X-ray band of *Ginga*. We investigate the effect of these sources on the interpretation of the *Ginga* spectrum in our analysis below.

Since the cluster is significantly extended, background subtraction of the A665 IPC spectrum required use of a separate gain-matched source-free field. For this purpose we used a deep survey field (I31) with a gain of 18.77 versus 17.43 for the A665 pointing. The background spectrum was scaled to the source spectrum by the ratio of live times. This scaling value was sufficient to approximately zero out the background in the source field near the edge of the detector, far from any possible emission from the cluster. We also employed a different deep survey background field (I3670, gain: 16.48); all derived results were consistent at the 68% confidence level with those using field I31 for background. The background rate in the IPC was known to vary from field to field by of order 20%. To incorporate this uncertainty, we included an additional 20% of the background rate in quadrature with the statistical error in each pulse height (PH) channel. An additional systematic error of 3% of the source rate in each PH channel was added in quadrature to the combined statistical and background systematic error. Due to the significant background systematic error, the maximum signal to noise was obtained when the spectrum was extracted from within a radius of 8′ from the cluster center. The IPC X-ray spectrum of A665 is shown in Figure 1.

3. ISOTHERMAL AND POLYTROPIC MODEL FITS

Our aim here is to convert the observed X-ray spectra shown in Figure 1 into information about the temperature structure of the cluster. The density structure can most accurately be determined through analysis of the X-ray images of A665; as we mentioned above, this is done in BHA. In subsection 3.1 immediately following we focus on constraining the spectral parameters, *i.e.*, the hydrogen column density to the source, the average iron abundance, the average gas temperature, and the emission measure, under the assumption that the cluster is isothermal. We give best fit values and error ranges for each parameter. Each parameter is essential, since the conversion from IPC counts to equivalent hydrogen number density used in BHA depends implicitly on the column density, temperature, and iron abundance. Even the relative normalization between the IPC and *Ginga* datasets is useful, since it allows us to assess the systematic uncertainty in the overall flux calibration of the two instruments. The temperature value itself is particularly important since it enters linearly into the SZ effect. In subsection 3.2 we consider polytropic temperature distributions of the form introduced by Henriksen & Mushotzky (1986), *i.e.*, where $T \propto n^{\gamma-1}$ while the density distribution is given by the isothermal-β form. This polytropic formulation is very convenient for the SZ study, since the functional form of the pressure integral remains the same as in the case of an isothermal distribution. In addition at this point we show how important the combination of IPC and *Ginga* data sets is for constraining nonisothermal temperature distributions in distant clusters.

3.1. *Isothermal temperature distributions*

The IPC and *Ginga* datasets were simultaneously fit to redshifted optically-thin collisional ionization equilibrium thermal bremsstrahlung models (Raymond & Smith 1978; J. C. Raymond, private communication; hereafter RS). We introduce a relative normalization parameter to account for numerous possible differences between the IPC and *Ginga* in the area of overall flux determination. Some effects which might influence this quantity include the absolute flux calibration of both instruments, background subtraction, the *Ginga* collimator transmission function, the spatial integration region for the IPC data, and the hydrogen column density to the source. Both this parameter and the hydrogen column density were allowed to be variable. For the metal abundance, the elements C, N, O, Ne, Mg, Si, S, Ar, Ca, Fe, and Ni were varied in unison, while the [He]/[H] ratio was fixed at 0.085. The best fit values for the parameters of this model are shown in the Table and the best fit spectrum is plotted in Figure 1. These results are for a fixed redshift value of 0.18144 (Oegerle *et al.* 1991). We also determined the redshift from our data by fitting (of course it is the strong iron line which gives us our sensitivity to this parameter) to be 0.154 ± 0.039 (90% confidence), consistent with the optical value. The fitted hydrogen column density is consistent with the Stark *et al.* (1984) value of 4.3×10^{20} atoms cm^{-2}.

The best-fit relative normalization between the datasets (IPC/*Ginga*) is some 5% smaller than the value expected based on calculating the *Ginga* collimator transmission alone. This is largely due to the region of integration for the IPC spectrum. When we integrate the best fit isothermal-β model for the IPC surface brightness profile within a radius of $8'$ and compare it to the same calculation within $16'$, we find that there should be about 12% less flux from the smaller region. For this calculation to be relevant, of course, one must assume that the cluster follows the modeled surface brightness law out to $16'$, about 10 core radii. If anything the surface brightness should fall off more rapidly at large radii, since the exact King (1966) model does differ from the isothermal-β model approximation in just this fashion. However recent results from the ROSAT all sky survey show that the Coma cluster follows the isothermal-β surface brightness model out to a radius of about 10 core radii (Briel, Henry, & Böhringer 1991). We consider the 12% value to be a lower limit to the decrease in flux we might expect to see in the IPC spectrum compared to the *Ginga* one. In light of these points, we consider the agreement between the IPC and *Ginga* datasets to be excellent and we suggest that it validates our background subtraction and the absolute flux calibration of the two instruments. Furthermore it establishes a systematic uncertainty of about 5% in the overall flux calibration of each instrument.

The 2 – 10 keV flux of A665 (corrected for pointing position) is 1.0×10^{-11} erg cm^{-2} s^{-1} which implies a luminosity of 1.6×10^{45} erg s^{-1} (for $H_0 = 50$ km s^{-1} Mpc^{-1}, $q_0 = 0.5$). Correlations of X-ray luminosity and gas temperature for samples of galaxy clusters have been given by a number of authors now (Mushotzky 1988, Edge 1989, Hatsukade 1989). Our measured gas temperature and X-ray luminosity for A665 are consistent with the correlations given by these authors. We estimate the cluster velocity dispersion to be 1050 km s^{-1}, based on the measured X-ray temperature and employing the correlations in Edge (1989). This is in excellent agreement with the Oegerle *et al.* (1991) measurement of 1201^{+183}_{-126} km s^{-1}.

Before investigating nonisothermal temperature distributions, we would like to examine the dependence of some of our present results on the uncertainty in gain and background subtraction for the *Ginga* data. We generated results for plus and minus one-sigma variation in gain and background subtraction, using the values determined in Section 2. The best fit temperature changed by ± 0.15 keV when the gain was varied and by $^{+1.32}_{-1.19}$ keV when the background was varied (upper value comes from subtracting less background, lower value from more background). The iron abundance was much less sensitive to these variations, changing by only ± 0.006 (gain) and $^{-0.007}_{+0.019}$ (background). The relative normalization changed by $^{-0.069}_{+0.082}$, and the flux by $\pm 1.4 \times 10^{-12}$ erg cm^{-2} s^{-1} when background was varied. It is clear that some of these systematic errors are comparable in importance to the statistical errors on the measured parameters. Varying the background for the IPC data was significantly less important than for the *Ginga* data since the background in this case represents a considerably smaller fraction of the overall count rate.

We have investigated the contribution to the *Ginga* spectrum of the two AGN observed in the IPC image. When a power-law model with photon index -1.7 is included with the RS thermal model, the best fit for the normalization of the power-law component turns out to be zero. If the flux of this power-law component is fixed at the value inferred from the IPC observation (summing the contributions of the two sources), then the best fit temperature of A665 decreases by 0.39 keV and the elemental abundance increases by 0.047. These errors are dominated by the other systematic and statistical errors discussed above and shown in the Table.

3.2. *Polytropic temperature distributions*

In this section of the paper we relax the assumption that the cluster temperature distribution is isothermal. We assume that the distribution is polytropic and that the underlying density distribution is given by the isothermal-β model with $R_{\mathrm{core}} = 1.6'$ and

$\beta = 0.66$. We have fixed the hydrogen column density and the relative normalization to the best-fit values from the isothermal model. Note that our results concerning the degree of nonisothermality in A665 do not change significantly if we fix the column density to the Stark *et al.* (1984) value and the relative normalization to the calculated *Ginga* collimator transmission value.

Figure 2 shows results from fitting the combined IPC and *Ginga* data sets to the polytropic model. Contours of constant χ^2 for central temperature versus polytropic index (γ) are shown at the 68%, 90%, and 99% confidence level. The best fit is an isothermal model and we can exclude an adiabatic temperature distribution at very high confidence. A meaningful constraint on the polytropic index is not possible when either the IPC or *Ginga* data set is analyzed separately. It is possible only because of the broad energy coverage of the combined data sets.

4. VIRIAL MASS MODELS

Here we use the X-ray spectral data and the velocity dispersion of the galaxies to determine a likely value for the virial mass of A665. We follow closely the technique developed by Hughes (1989) (see also The & White 1986 and Merritt 1986) in a detailed study of the mass distribution of the Coma cluster. This technique assumes a parameterized functional form for the virial mass distribution from which the gas temperature distribution and the velocity dispersion can be calculated (see below). For the Coma cluster, it was possible to explore the effect of using different functional forms for the spatial distribution of the binding mass; however, the optical and X-ray data for A665 are considerably less extensive than that from Coma and thus we have decided to fix the shape of the A665 mass distribution and only determine its overall normalization. For ease of comparison between Coma and A665, we have chosen the mass-follows-light model for Coma, which is the preferred binding mass distribution from Hughes (1989). Specially we assume $\rho_b = \rho_0 \left[1 + (r/298 \text{ kpc})^2\right]^{-1.36}$ (The & White 1986) and determine limits on the central concentration of the binding mass distribution, ρ_0. Note that this distribution is somewhat different from both the A665 gas distribution (core radius 380 kpc) and the galaxy distribution (core radius 530 kpc; Dressler 1978), although the latter quantity is not known so precisely.

Even for a well-studied cluster like Coma, Hughes (1989) showed that uncertainties of ± 50% in the total mass are possible when this method is applied. This is in addition to uncertainties arising from the model assumptions: *e.g.*, that the gas is in hydrostatic equilibrium, the system is spherically symmetric, there is no substructure in the galaxy distribution, and the galaxy velocity distribution is isotropic. There is evidence for substructure in both the galaxy (Geller & Beers 1982) and gas (BHA) distributions of A665, which suggests that our results on the cluster binding mass could be subject to considerable uncertainty. However the mass values we derive from the galaxy dynamics and the gas temperature are fully consistent with each other at the 68% confidence level, perhaps indicating that the observed substructure does not play too strong a role in biasing the mass measurement for this cluster.

4.1. *X-ray derived virial mass*

The X-ray analysis begins with the equation of hydrostatic equilibrium $\nabla P = -\rho_g \nabla \Phi$, which can be expressed as a first order differential equation in gas temperature T

$$\frac{dT}{dR} = -\frac{1}{\rho_g}\frac{d\rho_g}{dR}T - \frac{4\pi\mu m_{\rm H} G}{k}\frac{M(R)}{R^2}. \tag{1}$$

$M(R)$, of course, is the total virial mass contained within radius R, obtained by integrating ρ_b and ρ_g is the gas density distribution; we use the isothermal-β model with parameter values determined from the ***Einstein*** X-ray imaging observations and given above (§2.2). We do not impose an explicit boundary condition on the temperature distribution (*e.g.*, requiring the temperature to approach zero at infinity), but instead allow the X-ray spectral data to constrain it. We have chosen to represent this boundary condition on temperature as the emission-measure-weighted average temperature, $kT_{\rm AVE}$. This gives us a two-parameter family of solutions for the temperature distribution: ρ_0 and $kT_{\rm AVE}$, which are to be constrained by the X-ray spectral data.

We constructed a large grid of spectral models with varying ρ_0 and $kT_{\rm AVE}$. For each set of parameters, a model temperature distribution was first calculated by solving equation 1. Next the model X-ray spectrum was built up by summing the spectra from single temperature RS thermal models, weighted by the appropriate relative emission measure at each temperature. Four more parameters were required to obtain acceptable fits to the joint IPC/***Ginga*** spectral data: the overall emission measure, the metal abundance, the interstellar column density, and the relative normalization between the IPC and ***Ginga*** spectra. As was done for for the polytropic temperature models mentioned above, we fixed the hydrogen interstellar column density and the relative normalization to the best-fit values from the isothermal fit. For this model there are as many free parameters (6) as for the polytropic temperature model, which itself includes only one more free parameter than the isothermal model.

The results are shown in Figure 3 as χ^2 contours at 68%, 90% and 99% confidence for two interesting parameters. The central concentration of the binding mass distribution ρ_0 is plotted as the ordinate and the emission-measure-weighted average temperature is plotted as the abscissa. For A665, the constraints from the X-ray spectra have been augmented by the additional consideration that the external pressure not exceed a given value, which we have taken to be 0.001 $\rm cm^{-3}$ keV at the outer boundary of our model (about 10 Mpc). This constraint limits models with large positive radial temperature gradients, occurring for small values of central concentration. These are strictly speaking pressure-bounded models, in which the temperature rises to match the fall-off of gas density and the pressure reaches a constant non-zero finite value at large radii. We have chosen a very conservative limit in this case corresponding to an external pressure no less than about 2% of the central value. Since this value is somewhat "soft", we have extended our contours (as dashed lines) beyond the limit. In the figure we also mark the line corresponding to the boundary between gravitationally-bounded models and pressure-bounded models (the small-dashed straight line extending through the contours). Below the line the temperature rises to large values at large radii. These models could potentially correspond to situations where there is still infall into the cluster at large radii. Above this line the temperature drops to zero at large, but finite, radii, effectively defining the boundary of the cluster gas distribution. This boundary occurs at progressively smaller radii as ρ_0 increases. The fact that we see emission in the X-ray image out to a certain radius potentially allows for an additional constraint on the models. In the current situation this turns out not to be effective, since the boundary lies beyond 4.2′ for all accepted models.

The numerical value of the binding mass as derived from the X-ray spectrum is $\rho_0 = (0.80^{+0.13}_{-0.18}) \times 10^{-25}$ g cm^{-3}, where the error is at the 68% confidence level for a single interesting parameter.

The two small contours near the left-hand side of the figure show the results for the binding mass of Coma at 90% and 99% confidence (Hughes 1989). The average temperature of A665 is about 1 keV higher than that of Coma. Although the best fit value for the mass of A665 is 0.82 times that of Coma, the 90% confidence range on mass allows for A665 to be from 0.56 to as much as 1.23 times the mass of Coma. Yet if we require that the temperature distributions be approximately the same for the two clusters, then the virial mass of A665 is very nearly the same as Coma.

4.2. *Optically derived virial mass*

The determination of the cluster virial mass from galaxy dynamics rests on the Jeans equation which we write as

$$\frac{d\rho_G\sigma^2}{dR} = -\frac{G\rho_G M(R)}{R^2}. \tag{2}$$

The galaxy distribution is ρ_G and the velocity dispersion, σ, is assumed to be equal in the radial and tangential directions, *i.e.*, isotropic orbits. We set σ to zero at the boundary of the cluster, chosen to lie at a large radius ($\sim$ 50 Mpc). We have assessed the effect of reducing this boundary radius to 10 Mpc and find that our derived masses increase slightly (about 7%) in this situation. The galaxy spatial distribution is taken from Dressler (1978): $\rho_G \sim \left[1 + (R/530\ \mathrm{kpc})^2\right]^{-1}$. Integration of equation 2 for each value of ρ_0 yields the radial run of σ, which is projected to the line-of-sight and averaged over an appropriate region of the cluster to yield the total cluster velocity dispersion. As we have formulated the problem, there is only one unknown parameter, ρ_0, to be determined by the measured velocity dispersion.

Current data on the galaxy dynamics of A665 consist of radial velocities for 33 cluster member galaxies from Oegerle *et al.* (1991), which were used to determine the total projected velocity dispersion: 1201^{+183}_{-126} km s^{-1}. We compared the radial distribution of these galaxies with that expected from Dressler's profile and found a pronounced deficit of galaxies in the Oegerle *et al.* sample beyond about 7.5′. Thus the total dataset (out to a radius of $\sim$ 20′) is demonstrably not a representative sample of the galaxy distribution of A665. However the 23 galaxies within 7.5′ of the X-ray determined cluster center did accurately follow the expected profile and the velocity dispersion for this limited sample was not significantly different: 1130^{+218}_{-139} km s^{-1}. Although we feel that this subset is more representative of the cluster as a whole, our main reason for selecting it was to be able to more carefully define the region of the cluster over which to average the model velocity dispersion. In our models the velocity dispersion decreases with radius from the cluster center and the total velocity dispersion is rather sensitive to the choice of integration region. For example, increasing the integration region from 7.5′ to 20′ reduced the calculated model velocity dispersion by 15% and consequently increased the mass estimate by some 30%.

The results are shown in Figure 3 as the band stretching along the $kT_{\rm AVE}$ axis. The numerical value derived from the galaxy dynamics is $\rho_0 = (1.19^{+0.51}_{-0.27}) \times 10^{-25}$ g cm^{-3}. This value is consistent with the X-ray determined one at the 68% confidence level. When the X-ray and optically determined values are combined we derive a value of $\rho_0 = (0.94^{+0.27}_{-0.15}) \times 10^{-25}$ g cm^{-3} (68% confidence).

5. DISCUSSION & CONCLUSIONS

We have presented a detailed analysis of the X-ray spectrum of the Abell 665 cluster of galaxies. We find consistency between the ***Einstein Observatory*** data and data obtained by the ***Ginga*** satellite. Joint fitting of these data sets allows us to set strong limits on the polytropic index ($\gamma < 1.35$ at 99% confidence), under the assumption that the temperature distribution is polytropic. The best fit is the isothermal case. We have also determined the average temperature, the hydrogen column density to the source, the iron abundance, the emission measure, and the relative normalization between the datasets. We have examined the effect of systematic errors due to gain and background subtraction.

A665 is very similar to the Coma cluster in many of the properties of its gaseous atmosphere. The average temperatures of the two clusters are similar (7.5 keV for Coma versus 8.3 keV for A665). The luminosities are comparable: 8.8×10^{44} ergs s^{-1} for Coma and 1.3×10^{45} ergs s^{-1} for A665. The core radii (305 kpc versus 380 kpc) and β values (0.63 versus 0.66) from the X-ray surface brightness distributions are also nearly the same.

And in addition, when a detailed model for the distribution of mass in these clusters is constructed we find that A665 is very likely as massive as the Coma cluster.

The values of the total cluster mass for A665 inferred from the X-ray spectrum and the galaxy dynamics are consistent at the 68% confidence level. Oegerle *et al.* (1991) discuss a slight inconsistency for A665 between β_{spec}, the ratio of gas to galaxy scale-heights, and β_{fit}, the slope of the X-ray surface brightness distribution at large radii. For the velocity dispersion value we used to estimate the cluster mass, $\beta_{spec} = 0.97^{+0.50}_{-0.27}$. This is only different at the 1.1 sigma level from the β_{fit} value of 0.66 and so no strong conclusion is possible. Only when a considerably large number of galaxy redshifts are available will it be possible to make an accurate comparison between β_{spec} and β_{fit}.

Within a radius of 2 Mpc (about 8.5′) the virial mass of A665 is $1.01^{+0.29}_{-0.16} \times 10^{15}$ $M_{\odot}$, the gas mass is $2.76^{+0.07}_{-0.12} \times 10^{14}$ $M_{\odot}$, and the visual luminosity of the galaxies is approximately 1.2×10^{13} $L_{\odot}$ (Dressler 1978). This implies a ratio of gas mass to virial mass of $0.27^{+0.06}_{-0.07}$ and a mass-to-light ratio of 97^{+28}_{-15} in solar units, values which are consistent with those found in other massive rich clusters of galaxies. When we convert our optical luminosity to stellar mass using a mass-to-light ratio of 5 (M/L_V, Pickles 1985), we find that the gas mass to stellar mass ratio is 4.6, again consistent with what one expects for a massive cluster.

The Hopkins Ultraviolet Telescope (HUT) observed A665 to search for ultraviolet photons from the decay of massive neutrinos, which have been suggested as a candidate for the dark matter in clusters of galaxies (Sciama 1991). No clear spectral line feature which could be associated with the purported decay photons was observed. We have integrated our virial mass profile over the HUT aperture (17 × 116 arcsec) to obtain a total mass from A665 within this region of $2.23^{+0.64}_{-0.36} \times 10^{13}$ $M_{\odot}$. A significant fraction of this mass is baryonic: the X-ray emitting gas is 0.34×10^{13} $M_{\odot}$ and the mass in galaxies is 0.07×10^{13} $M_{\odot}$, leaving $1.82^{+0.64}_{-0.36} \times 10^{13}$ $M_{\odot}$ which could potentially be composed of massive neutrinos. Davidsen *et al.* (1991) conclude that Sciama's theory of decaying massive neutrinos could only survive if A665 were several times less massive than they estimated or if there were substantial UV absorption along the line of sight. Our analysis here indicates that the cluster's mass is about 60% of the value used by Davidsen *et al.* (1991). This, by itself, is not a sufficient enough reduction in the cluster's mass to bring the HUT observations into agreement with Sciama's theory.

We find a rather high elemental abundance 0.49 ± 0.16 (fraction relative to cosmic) for this cluster. Recent work with *Ginga* and EXOSAT (Hatsukade 1989, Arnaud *et al.* 1991) has found a correlation of iron abundance and gas temperature: hotter clusters show lower iron abundance than cooler ones. Their correlation would suggest an elemental abundance of 0.28 for a temperature of 8.3 keV, a value which is somewhat inconsistent (at about the 95% confidence level) with the A665 data presented here. The abundance-temperature correlation has been interpreted in the following manner: since there is known to be more gas per stellar mass in richer (or hotter) clusters, the iron (which is assumed to be produced by the cluster stellar population) is more diluted in the hotter clusters. However Arnaud *et al.* (1991) showed that the iron mass in clusters is correlated with the stellar mass in elliptical and S0 galaxies; no correlation was observed for spirals. Research into the current galaxy population of A665 may help us to investigate further this apparent discrepancy.

The results from this spectral study have been used to determine the Hubble constant (and associated observational uncertainties) from the SZ effect (BHA). In that work we find the best fit value to be $H_0 = (40 \text{ to } 50) \pm 12$ km s^{-1} Mpc^{-1} where the range expresses the maximum range of systematic errors associated with the zero level uncertainty in the Sunyaev-Zel'dovich data and the other systematic errors have been added in quadrature to the random error. However the systematic errors dominate the statistical error and the worst case (most conservative) estimate gives a range of 26 ± 8 to 65 ± 10 km s^{-1} Mpc^{-1} for the Hubble constant. A significant component of that error arises from the measurement of X-ray temperature. The next Japanese X-ray astronomy satellite (Astro-D), scheduled for launch in early 1993, will be able to determine the X-ray spectra of distant ($z \sim 0.2$) clusters with high precision. Until then improvement in the uncertainty on the Hubble constant determination awaits reduction in the systematic errors associated with the radio measurements. Deep images with ROSAT, in addition to the structural information, will allow improved determination of the low energy (0.2 - 2 keV) X-ray spectrum of the cluster. As we have shown in this article, this is an essential feature for characterizing the X-ray spectrum and constraining the temperature distributions in distant galaxy clusters.

JPH acknowledges support from NASA grants NAG8-699 and NAG8-181.

TABLE

Best fit parameters: RS model

Parameter	Best fit value [a]
Emission integral ($n_{\rm H}^2 V$) [b] (10^{68} cm^{-3})	1.12 ± 0.05
kT (keV) [c]	$8.26^{+0.95}_{-0.81}$
Abundance [d]	0.49 ± 0.16
$n_{\rm H}$ (10^{20} atoms cm^{-2})	$4.1^{+2.8}_{-1.7}$
Relative norm (IPC/*Ginga*)	0.95 ± 0.08
χ^2 (d.o.f)	13.4 (25)

[a] Statistical errors at 90% confidence.

[b] Assumes $z = 0.18144$, $H_0 = 50$ km s^{-1} Mpc^{-1}, and $q_0 = 0.5$

[c] Source temperature

[d] Relative to cosmic: [Fe]/[H] = 4×10^{-5}.

REFERENCES

Abramopoulos, F., & Ku, W., H.-M. 1983, ApJ, 271, 446

Arnaud, M., Rothenflug, R., Boulade, O., Vigroux, L., & Vangioni-Flam, E. 1991, A&A, submitted

Birkinshaw, M. 1979, MNRAS, 187, 847

Birkinshaw, M. 1989, in *The Cosmic Microwave Background: 25 Years Later*, ed. N. Mandolesi & N. Vittorio, (Dordrecht: Kluwer), in press

Birkinshaw, M., Hughes, J. P., & Arnaud, K. A. 1991, ApJ, 379, 466

Briel, U. G., Henry, J. P., and Böhringer, H. 1991, *Proceedings of the NATO ASI on Clusters and Superclusters of Galaxies (Contributed Talks and Poster Papers)*, ed. M. M. Colless, A. Babul, A. C. Edge, R. M. Johnstone, and S. Raychaudhury, p. 91.

Boynton, P. E., Radford, S. J. E., Schommer, R. A., & Murray, S. S. 1982, ApJ, 257, 473

Davidsen, A. F., Kriss, G. A., Ferguson, H. C., Blair, W. P., Bowers, C. W., Dixon, W. V., Durrance, S. T., Feldman, P. D., Henry, R. C., Kimble, R. A., Kruk, J. W., Long, K. S., Moos, H. W., & Vancura, O. 1991, Nature, 351, 128

Dressler, A. 1978, ApJ, 226, 55

Edge, A. C. 1989, Ph. D. Thesis, University of Leicester

Edge, A. C., & Stewart, G.C. 1991, preprint

Geller, M. J., and Beers, T. C. 1982, ApJ, 94, 421.

Gioia, I. M., Maccacaro, T., Schild, R. E., Wolter, A., Stocke, J. T., Morris, S. L., & Henry, J. P. 1990, ApJS, 72, 567

Harris, D. E., Forman, W., Gioia, I. M., Hale, J. A., Harnden, F. R., Jr., Jones, C, Karakashian, T., Maccacaro, T., McSweeney, J. D., Primini, F. A., Schwarz, J., Tananbaum, H. D., & Thurman, J. 1990, *The Einstein Observatory Catalog of IPC X-Ray Sources*, NASA RP - 1247

Hatsukade, I. 1989, Ph. D. Thesis, Osaka University

Hayashida, K., Inoue, H., Koyama, K., Awaki, H., Takano, S., Tawara, Y., Williams, O. R., Denby, M., Stewart, G. C., Turner, M. J. L., Makishima, K., & Ohashi, T. 1989, PASJ, 41, 373

Henriksen, M. J., & Mushotzky, R. F. 1986, ApJ, 302, 287

Hughes, J. P. 1989, ApJ, 337, 21

Jones, C., & Forman, W. 1984, ApJ, 276, 38

King, I. R. 1966, AJ, 71, 64

Makino, F., & the Astro-C team 1987, ***Astrophys. Lett. and Communications***, 25, 223

Mushotzky, R. F. 1988, in ***Proceedings of NATO ASI: Hot Thin Plasmas in Astrophysics***, ed. R. Pallavacini, (Reidel), p. 273

Oegerle, W. R., Fitchett. M. J., Hill, J. M., & Hintzen, P. 1991, ApJ, 376, 46

Raymond J. C., & Smith, B. W. 1977, ApJS, 35, 419

Sciama, D. W. 1991, ApJ, 367, L39

Turner, M. J. L., ***et al.*** 1989, PASJ, 41, 345

White, S. D. M., & Silk, J. 1980, ApJ, 241, 864

FIGURE CAPTIONS

Fig. 1 – The X-ray spectrum of A665 as observed by the ***Einstein Observatory*** IPC and the ***Ginga*** LAC. The best fitting isothermal model is also shown.

Fig. 2 – Contours of constant χ^2 for the polytropic model at the 68%, 90%, and 99% confidence level. The central temperature is plotted versus the polytropic index γ.

Fig. 3 – The virial mass of A665. The central concentration of the binding mass distribution (ρ_0) is plotted versus the mean gas temperature of the cluster. The closed contours represent the region allowed by the X-ray data at 68%, 90%, and 99% confidence. The sloping dashed line within these contours separate the two classes of temperature solutions (see text). The binding mass of A665 derived from the galaxy velocity dispersion is shown as the band stretching along the temperature axis. For reference, the region of parameter space for the binding mass of the Coma cluster is shown as the small contours to the left (90% and 99%).

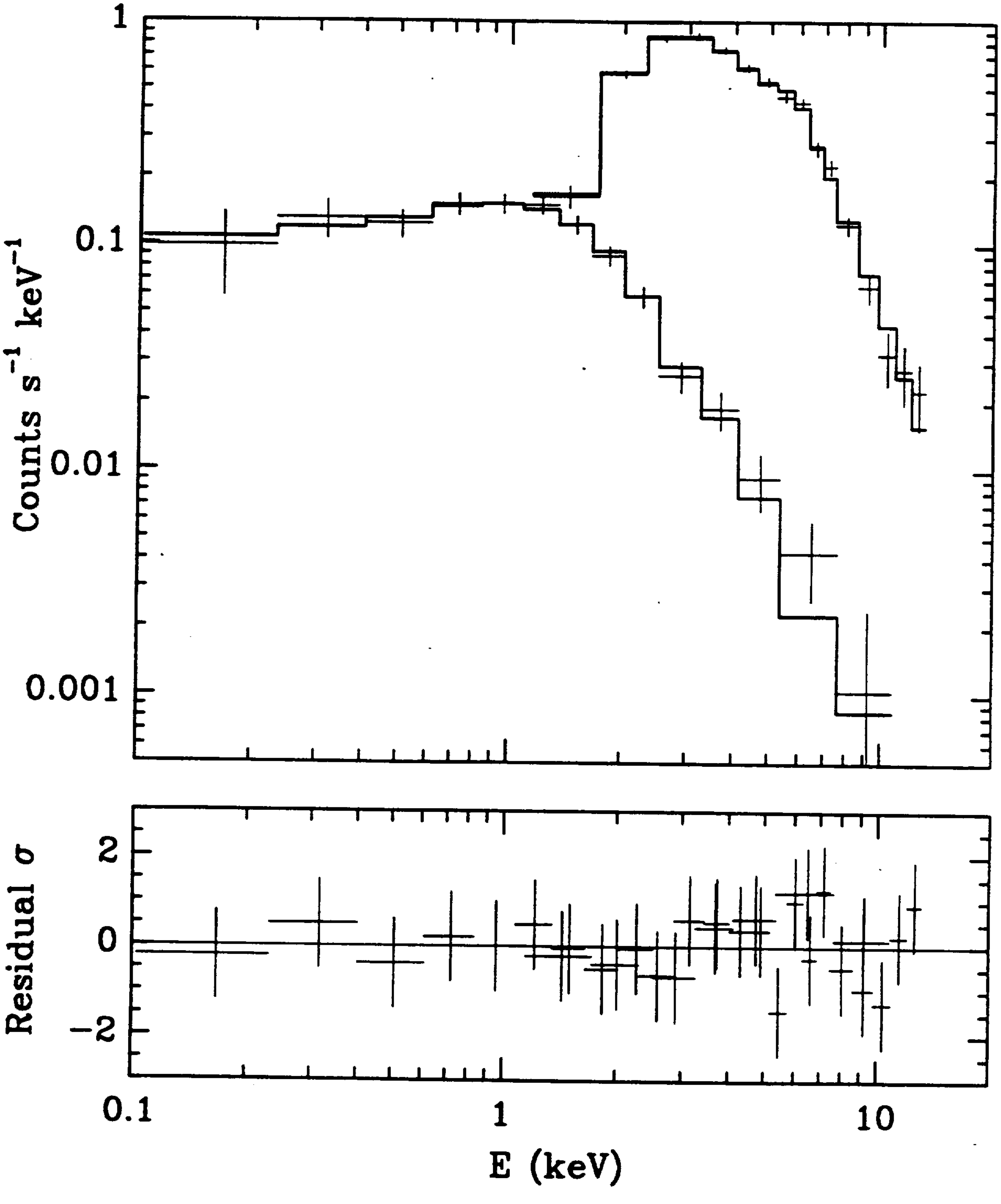

FIGURE 1

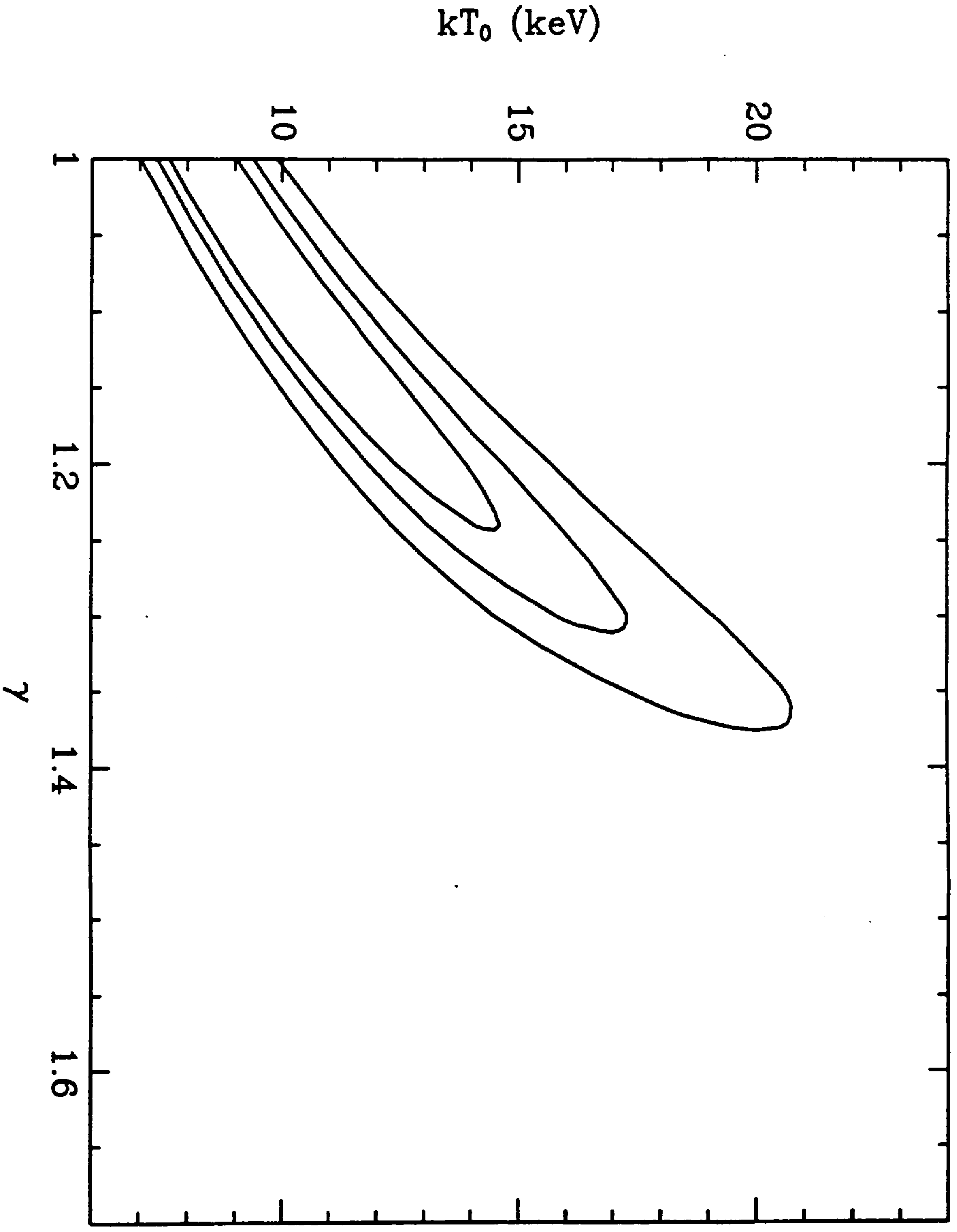

FIGURE 2

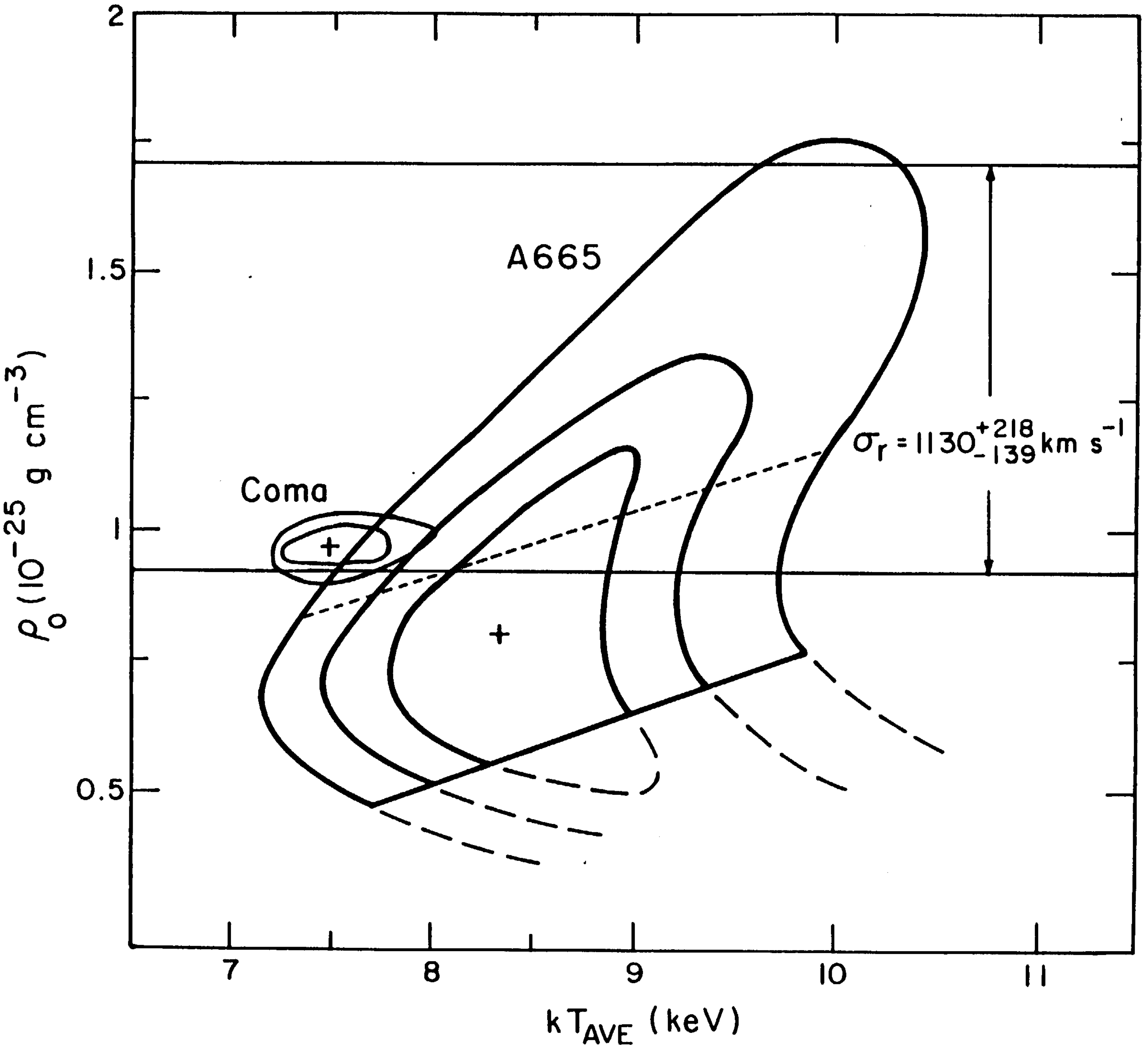
A665
Coma
$\sigma_r = 1130^{+218}_{-139}$ km s^{-1}
$\rho_o\ (10^{-25}$ g cm$^{-3})$
0.5
1
1.5
2
kT_{AVE} (keV)
7
8
9
10
11

FIGURE 3

Harvard-Smithsonian
Center for Astrophysics

Preprint Series

No. 3462
(Received August 20, 1992)

CLUSTERS OF GALAXIES

John P. Hughes
Harvard-Smithsonian Center for Astrophysics

Invited review paper
To appear in
From Ginga to ASTRO-D and Further to DUET
Proceedings of the Annual ISAS Symposium on Space Astrophysics
February 4–5, 1992
F. Nagase and F. Makino, editors

HARVARD COLLEGE OBSERVATORY SMITHSONIAN ASTROPHYSICAL OBSERVATORY
60 Garden Street, Cambridge, Massachusetts 02138

Center for Astrophysics
Preprint Series No. 3462

CLUSTERS OF GALAXIES

John P. Hughes
Harvard-Smithsonian Center for Astrophysics

Clusters of Galaxies

John P. Hughes

Harvard-Smithsonian Center for Astrophysics
60 Garden Street, Cambridge, MA 02138

ABSTRACT

Studies with *Ginga* of the hot plasma comprising the intracluster medium in clusters of galaxies have brought a number of new insights into the nature and evolution of these objects. In this brief review I touch upon a selection of these studies.

1. Introduction

Clusters of galaxies are the largest gravitationally-bound systems in the universe. Of particular relevance to X-ray astronomers is the presence in these systems of a hot diffuse plasma filling the medium between the visible galaxies. The temperature of the gas ($kT \sim 1 - 10$ keV) corresponds roughly to the system virial temperature. Galaxy clusters are luminous X-ray sources ($L_X \sim 10^{42} - 10^{45}$ ergs s^{-1}) because they contain large amounts of hot gas - masses comparable to and, in some cases exceeding, the mass in optically visible galaxies. This gas has interesting dynamical consequences in rich systems, where it can constitute as much as 50% of the mass required to bind the cluster. The detection of iron Kα lines (and a few other features) from a number of clusters has shown that the intracluster gas is not of primordial composition, but is enriched in metals to an abundance of about 0.25 to 0.5 solar.

The large area counter (LAC) was the principal instrument aboard *Ginga*, the third Japanese satellite devoted to X-ray astronomy. This instrument was useful for cluster research because of its high sensitivity in the 2–10 keV band and low internal background, which allowed the spectral study of clusters over a large range of luminosities and redshifts. In addition, the mechanically-collimated field of view (roughly 1° × 2°, FWHM) was adequate for studies of the spatial variation of temperature and metal abundance in a few nearby clusters.

In this review I focus on three aspects of cluster research in which *Ginga* LAC data have made fundamental contributions: the correlation between iron abundance and temperature, the X-ray spectra of distant clusters, and the Sunyaev-Zel'dovich (SZ) effect. This choice is motivated as much by my own interests as anything else. *Ginga* data also facilitated other interesting cluster studies including cooling flow clusters such as A478 (Johnstone *et al.* 1991) and Perseus (Allen *et al.* 1991); poor clusters and groups, such as AWM 7 and Hydra A (Tsuru 1991) and the Fornax cluster (Ikebe *et al.* 1992); the remarkable collection of rich clusters in the Shapley Supercluster region (Day *et al.* 1991); and the spatial distributions of temperature and abundance for at least two clusters, Coma (Hughes *et al.* 1992) and Virgo (Koyama, Takano, & Tawara 1991).

2. Iron Abundance – Temperature Correlation

Hatsukade (1989) used a sample of 11 clusters observed by the *Ginga* LAC in 1987 and 1988 to suggest that there was a correlation between the observed mean gas temperature and metal abundance in the sense that hotter clusters tend to have lower metallicities than cooler clusters. This result was confirmed, and put on firmer statistical grounds, by Butcher & Stewart (1991) and Arnaud *et al.* (1992b). The hypothesis that the iron abundance is the same for all clusters can be rejected with high confidence ($> 99.99\%$), while a simple power-law function where $[Fe/H] \propto kT^{-0.37}$ is an acceptable description of the correlation.

There have been a number of interpretations of this correlation. Hatsukade (1989) proposed that clusters were composed of two components: (1) a central core with low temperature and high abundance, and (2) an outer region of high temperature and low abundance. The variation of the proportions of these two components from cluster to cluster could then produce the observed correlation. Some support for this scenario was provided by the *Ginga* LAC data for A1060, which required a two-temperature thermal model for an acceptable fit. In this interpretation the cool component would be naturally explained as arising from the presence of a cooling flow in the cluster core. Observations of two clusters containing cooling flows, Perseus (Ponman *et al.* 1990; Kowalski *et al.* 1992) and Virgo (Koyama, Takano, & Tawara 1991), did show strong gradients in the iron abundance with the distribution clearly peaking in the center. However, the results for Perseus have not been confirmed by BBXRT (Mushotzky 1991).

An alternative explanation attributes the correlation to the metal enrichment of the intracluster gas by early-type galaxies (David, Forman, & Jones 1991; Arnaud *et al.* 1992b). David *et al.* (1990) observed that the ratio of gas mass to stellar mass in clusters is a function of richness (or temperature), increasing from values near unity for poor groups to values of 7 or so for the richest systems. Since the iron seen in clusters can only be produced by stellar nucleosynthesis and hence should be proportional to the stellar mass, this would suggest that the ratio of the mass in iron to gas mass should decrease with richness. In other words, rich clusters have lower iron abundances because they contain more primordial, unprocessed, gas which effectively dilutes the iron-enriched stellar ejecta to a greater extent than in poor clusters. This argument requires that the iron in clusters be uniformly distributed (or nearly so) in order that estimates of the total iron mass based on the emission-weighted spectrum are accurate. Some support for this comes from an analysis of the *Ginga* LAC data for the Coma Cluster (Hughes *et al.* 1992), which indicates that the mass of iron in Coma is not less than about 75% of the value one would obtain assuming a perfectly uniform spatial distribution.

These studies relate to the important issues of the origin of the intracluster gas, the fraction of gas that is primordial, where and when the iron was produced and how it was distributed throughout the cluster, the efficiency of galaxy formation in clusters, the role of cooling flows, and so on. One major unknown is the role that evolution plays. Edge *et al.* (1990) and Gioia *et al.* (1991) have presented evidence for the recent ($z \sim 0.1$)

evolution of the X-ray luminosity of clusters. Both studies find that the number of high luminosity clusters decreases with increasing redshift, which has been interpreted to mean that rich clusters grow through the merger of smaller units. Early results from ROSAT indicate that we actually may be witnessing such merging events in a number of nearby rich systems (*e.g.*, the Coma Cluster: Briel, Henry, & Böhringer 1991; and A2256: Briel *et al.* 1991).

3. Distant Clusters

During its lifetime, the *Ginga* satellite obtained LAC spectra (over the 2-10 keV X-ray band) of some 40 clusters of galaxies. These included, for the first time, a significant number (9) of high redshift objects ($z > 0.1$). Two other distant clusters, A33 (Arnaud *et al.* 1991) and CL0016+16 (Yamashita 1991), were observed by *Ginga*, but were not detected. In this section I discuss the results of studying this sample in order to find evidence for temperature evolution of clusters.

Arnaud *et al.* (1991) was the first to use *Ginga* data to explore the question of temperature evolution in clusters. These authors compiled a sample of 11 clusters with redshifts well distributed over the range 0.028 to 0.280. No evidence for evolution was observed, contrary to predictions based on a high ($\sim$ unity) value of Ω, the density parameter for the universe.

Figure 1 shows plots of kT and L_X against redshift for 14 clusters with 1.2×10^{45} ergs $\text{s}^{-1} < L_X < 3.2 \times 10^{45}$ ergs s^{-1}. These data are the same as those in Arnaud *et al.* (1991) with the inclusion of the distant clusters A665, A1689, and A2009 (increasing the number of high redshift objects to 7) and with the temperature of A401 updated to reflect the *Ginga* LAC data. There is no obvious trend of either luminosity or temperature with redshift. The solid horizontal line in the kT vs redshift plot corresponds to the mean temperature for the sample: 8.46 keV. The dashed curve is one particular model for the evolution of cluster temperatures (Perrenod 1980) with $\Omega = 1$ and the index of the primordial mass fluctuation spectrum, n, set to 0 (this is the most extreme evolution model presented in Arnaud *et al.* 1991). A χ^2 comparison between the data and these two simplified models gives values of 29.6 for the constant temperature scenario and 42.9 for the evolving temperature model (for 12 degrees of freedom in both cases). Although neither χ^2 value is acceptable from a statistical point of view (which is not surprising since it is not expected that all clusters, even those with the same luminosities, should have the same temperature), it is clear that the particular scenario for temperature evolution shown ($\Omega = 1$, $n = 0$) is a poor description of the data.

I summarize some results for the cluster sample in Table 1. Since it is well-known that the luminosity and temperature of clusters is correlated (Mushotzky 1988, Edge 1989, Hatsukade 1989, Edge & Stewart 1991), I first examined the sample in terms of luminosity. The mean redshift of the high and low luminosity sub-samples are comparable, and although the X-ray luminosities differ by about 60%, the mean temperatures

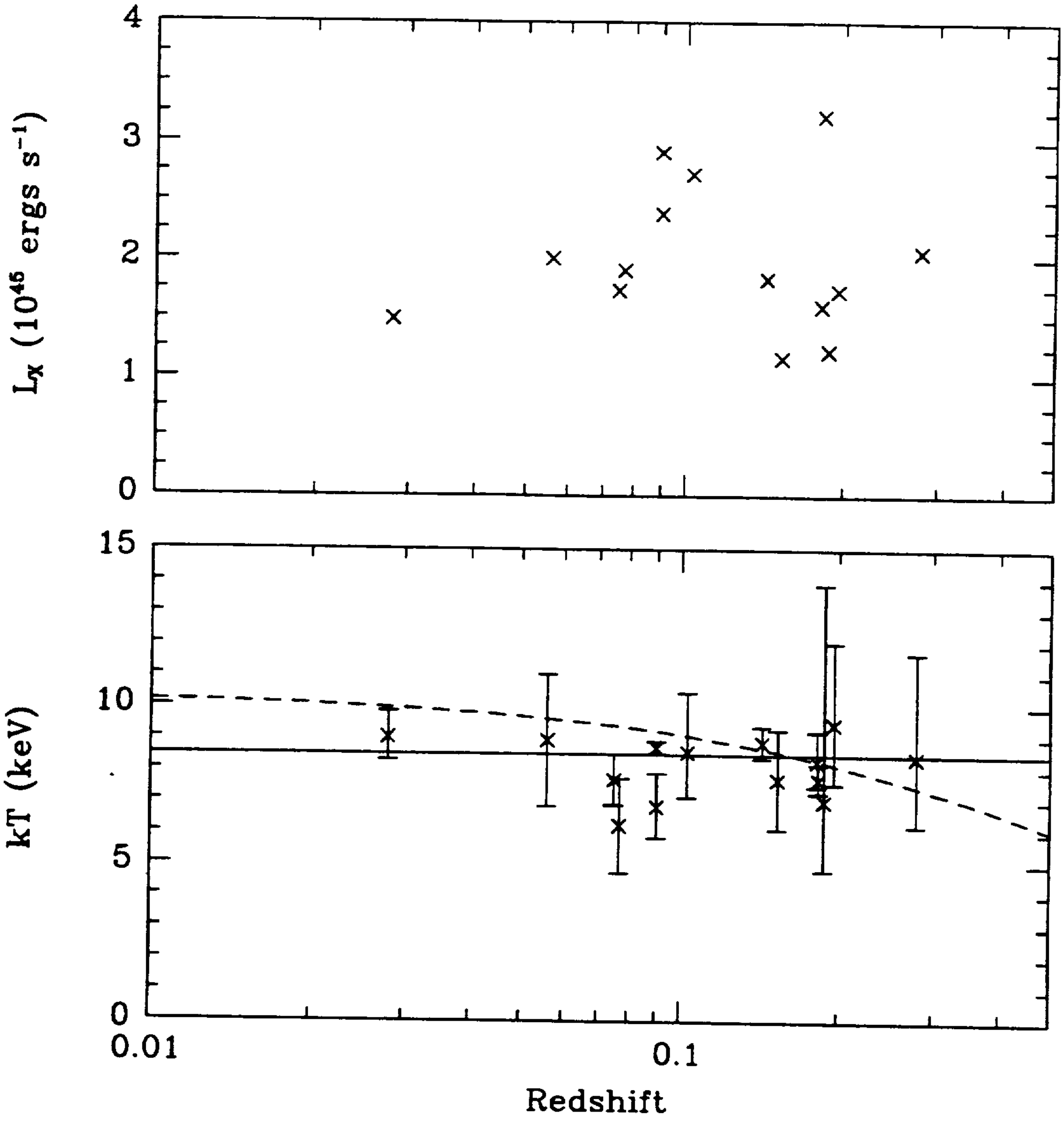

Figure 1 – X-ray luminosity vs. redshift (top panel) and measured temperature vs. redshift (bottom panel) for a sample of 14 clusters.

Table 1 Cluster Sample

	Subdivided by L_X		Subdivided by z	
Parameter	Low ($L_X < \bar{L}$)	High($L_X > \bar{L}$)	Low ($z < \bar{z}$)	High ($z > \bar{z}$)
$< z >$	0.138	0.126	0.074	0.189
$< L_x >$ (ergs s^{-1})[a]	1.5×10^{45}	2.5×10^{45}	2.2×10^{45}	1.8×10^{45}
$< kT >$ (keV)[b]	8.54 ± 0.20	8.44 ± 0.20	8.55 ± 0.19	8.23 ± 0.21
χ^2 (6 d.o.f)	6.7	22.8	18.8	8.7

[a] $H_0 = 50$ km s^{-1} Mpc $^{-1}$, $q_0 = 0.5$.

[b] Errors are 1 σ on the mean value.

derived from the sub-samples are in agreement with each other. This suggests that the sample is free of any strong bias from the luminosity-temperature correlation.

When the sample is examined in terms of redshift, it is apparent that any evolution of cluster temperature is weak: as the mean redshift changes by a factor of 2.6 (from $z = 0.189$ to $z = 0.074$) the mean temperature of these clusters increases by only 1.039 ± 0.035 (1 σ error). This value allows me to assign quantitative confidence levels to the two simplified evolution models mentioned above. The constant temperature case is acceptable, while the evolving temperature scenario can be rejected at greater than 5 σ, since it implies a temperature ratio of 1.23. My conclusions are similar to Arnaud *et al.* (1991): a high Ω universe seems to require considerably more temperature evolution than is observed.

It is perhaps unwise to place too much emphasis on the ability of this small, heterogeneous sample and simple model to limit the values of cosmological parameters, but the implications for future studies are important. The next Japanese satellite, Astro-D (scheduled for launch in February 1993), will be able to obtain high quality X-ray spectra of clusters at flux levels about an order of magnitude less than was possible with the *Ginga* LAC. This will allow accurate determination of luminosities, redshifts, temperatures, and elemental abundances for a large number of clusters over a range of luminosity and redshift, greatly increasing sensitivity to evolutionary effects. A key element of this program will be minimizing selection effects in the sample by the proper choice of clusters.

Before closing this section, I wish to comment on the *Ginga* LAC study of a remarkable cluster of galaxies, A2163 (Arnaud *et al.* 1992a). This source was among the ten most luminous clusters detected in the *HEAO-1* (A-1) all-sky X-ray survey (Johnson *et al.* 1983). Follow-up X-ray imaging observations (Ulmer, Kowalski, & Cruddace 1986) with the *Einstein Observatory* revealed a $3'$ displacement between the centroid of the X-ray emission and the Abell center and called into question the earlier redshift measurement of $z = 0.1689$, which had been based on observation of only 3 galaxies (Kowalski, Ulmer, & Cruddace 1983). In addition, through some error, the soft X-ray flux and luminosity quoted for A2163 in this paper were too low by a factor of 20.

Based on its high luminosity in the *HEAO-1* survey A2163 was chosen for study by *Ginga*. The LAC observations were found to imply a temperature $kT = 13.9 \pm 1.0$ keV and an X-ray luminosity of 6.4×10^{45} ergs s^{-1} for a redshift of 0.201, now well-determined from some 80 galaxies (M. Arnaud, private communication). This makes A2163 by far the hottest cluster known. For comparison the mean temperature of other rich clusters (*e.g.*, those shown in Figure 1) is closer to 8 keV. The existence of a gravitationally-bound object as hot as A2163 has interesting cosmological implications. Such a high temperature implies a massive cluster and in fact A2163 is estimated to be about twice as massive as the Coma Cluster. In the framework of a particular model for the formation of structure in the universe (*e.g.*, cold dark matter), one can estimate the number of such massive clusters expected in the volume out to a redshift of $z \sim 0.4$ (a conservative estimate of the volume sampled by the *HEAO-1* survey). The result depends on the assumed level of biasing between the dark matter and galaxy distributions: for no biasing one expects 1.5 such massive clusters, while for a bias factor of 1.5 (within the range of values favored by most cosmologists) one expects 10^{-6} clusters. Once again strong conclusions regarding these cosmological models are hampered by the small number of objects (in this case, only one!). As before, it is expected that Astro-D will provide a good sample of clusters for these sorts of studies.

4. Sunyaev-Zel'dovich Effect Clusters

The signature of the Sunyaev-Zel'dovich (SZ) effect is a distortion in the spectrum of the cosmic microwave background radiation when viewed along the line-of-sight to a cluster of galaxies. The hot electrons in the intracluster medium which emit the observed X-ray thermal bremsstrahlung emission also inverse-Compton scatter the background photons, shifting the spectrum to higher energies. In the Rayleigh-Jeans portion of the spectrum, the effect appears as a decrement in the brightness temperature of the background radiation.

It has been known for some time now that a comparison of the X-ray properties and the SZ effect may be used to measure the distance to a cluster of galaxies and, when combined with the cluster's redshift, determine the Hubble constant (Gunn 1978, Silk & White 1978, Cavaliere, Danese, & DeZotti 1979, Birkinshaw 1979). Distance determinations to clusters of galaxies using this effect rest on three separate and equally important sets of observable quantities. These are (1) the change in brightness of the cosmic microwave background when viewed along the line-of-sight to a cluster (SZ data), (2) the electron density space distribution, and (3) the electron temperature space distribution.

There are three galaxy clusters for which a highly significant detection of the SZ effect has been made: A2218, A665, and CL0016+16 (Birkinshaw *et al.* 1992). These observations were carried out over the last several years at the Owens Valley Radio Observatory using the 40-m telescope, observing at a frequency of 20.3 GHz. Reasonably accurate estimates of the electron density space distribution for these three clusters have been possible using *Einstein* X-ray images. However because of the limited high energy response of the *Einstein* high resolution mirror (which cutoff at X-ray energies above about 4 keV), it was not possible to determine even the mean temperatures of these rich clusters of galaxies. Various attempts were made in the past (White & Silk 1980; Boynton *et al.* 1982) to compensate for the lack of good X-ray spectral data, but the results were inconclusive.

The situation changed, at least for the two clusters A665 and A2218, with the advent of *Ginga* LAC X-ray spectra. This meant that the minimum complement of data necessary for the complete analysis of the SZ effect had at last been assembled. From these spectra McHardy *et al.* (1990) determined the temperature of A2218 to be $kT = 6.7(-0.6, +0.8)$ keV, while Hughes & Tanaka (1992) found the temperature of A665 to be $kT = 8.3(-0.8, +1.0)$ keV. In both instances the clusters were found to be described best by isothermal plasma models, although the limits on nonisothermal temperature distributions were weak.

Birkinshaw, Hughes, & Arnaud (1991) analyzed the full complement of X-ray data for A665 in conjunction with the most up-to-date SZ data and derived a Hubble constant of $H_0 = 45 \pm 13$ km s^{-1} Mpc $^{-1}$ from this one cluster alone. More recently Hughes & Birkinshaw (1991, also Birkinshaw & Hughes 1992) analyzed the data for A2218 and derived a similar value: $H_0 = 60 \pm 15$ km s^{-1} Mpc $^{-1}$. Note that an earlier study of this cluster (McHardy *et al.* 1990) utilized an inconsistent description of the cluster's atmosphere between the X-ray and SZ analyses, which lead them to infer a smaller (and presumably incorrect) value for the Hubble constant. It would appear, at least on the basis of agreement in results between A665 and A2218, that the technique for determining distances to clusters using the SZ effect has finally been demonstrated convincingly.

With the steadily accumulating database of superb ROSAT X-ray images for clusters, the anticipated launch of Astro-D, and the improvement in sensitivity of microwave instruments, this field of research has great potential to grow over the next few years. There are several obvious studies which should be done. First the sample of clusters with the necessary complement of data needs to be increased. In the very near future, for example, we look forward to measuring the gas temperature of CL0016+16, which is already well-studied in the SZ effect (and which is now scheduled for a long pointing with the ROSAT PSPC), and detecting the SZ decrement from the hot cluster A2163, which should show a decrement approximately twice that of A665. As we move beyond the stage of merely demonstrating the technique to actually utilizing it for studies of large scale structure in the universe, the proper selection of candidate clusters in order to avoid biases due to the three dimensional structure of clusters (see Birkinshaw, Hughes, & Arnaud 1991) will be critical. The ROSAT all sky X-ray survey will be an excellent source of such candidates.

Better models for the space distributions of gas density and temperature in cluster atmospheres, including the effects of subclustering and small scale clumping, should result from detailed studies of ROSAT and Astro-D data for nearby clusters. The early results from ROSAT on the Coma Cluster and A2256 (see above) already show how common subclustering is in nearby clusters. This clearly will complicate the analysis of cluster atmospheres. However, there are indications from BBXRT (Mushotzky 1991) and elsewhere (see David, Hughes, & Tucker 1992), that isothermal temperature distributions might be a reasonable description in the cores of clusters at least for those clusters without cooling flows. Whether or not further progress in this field finally determines the cosmic distance scale of the universe, we surely will learn many new and interesting things about the hot atmospheres of galaxy clusters.

5. Astro-D and Further to DUET

In my final comments, I present some thoughts about the upcoming Astro-D mission and look further ahead to DUET (the Deep Universe Exploring Telescope). This involves some looking backward to the *Einstein Observatory* and sideways, to the current ROSAT mission.

Recall that the observational goals of cluster research in the X-ray band are to determine the density, temperature, elemental composition, and bulk motion of the intracluster gas as a function of position for a well-selected large sample (with well-understood completeness properties). Until the launch of the *Einstein Observatory* with its pioneering X-ray imaging capabilities, researchers were mostly limited to studying the average X-ray properties such as emission measure, temperature, metal abundance, etc. of any cluster. X-ray maps of clusters with *Einstein* (and now ROSAT) reveal complex morphologies and allowed the distribution of gas density to be traced as a function of position in many clusters. However, astrophysicists were (and remain) limited to studying emission-measure weighted quantities of the other interesting observables, temperature and abundance in particular, for most clusters.

Astro-D, with its ability to provide high-sensitivity X-ray spectra over a broad energy band at a spatial resolution of 2–3 arcmin, is exceptionally suitable as a tool to change this picture. Astro-D will trace out the spatial distributions of temperature and abundance for many clusters, and for small or distant clusters it will make accurate measurements of their average properties. As an example, a 40 ks observation of the distant cluster CL0016+16, which has a 2–10 keV flux of $\sim 2 \times 10^{-12}$ ergs cm^{-2} s^{-1}, should result in the determination of the mean temperature to ±7%, the fractional metal abundance to ±6%, and the redshift to ±0.002. This latter capability is new for X-ray astronomy and might make it possible to find and identify clusters from X-ray data alone.

Planning for the next Japanese X-ray satellite (DUET) has already begun. It is clear that results from Astro-D would be the best guide to the detailed goals and design of this next mission. Given the absence of such results, I will hazard a guess based on the analogy of the ROSAT and *Einstein* facilities. In two important respects ROSAT has been an improvement upon *Einstein*: a field of view twice as large and a factor of three better spatial resolution. This has allowed ROSAT to make important new discoveries about the structure of clusters both at the subcluster level and at much larger scales. Similar modest improvements from Astro-D to DUET, by improving the spatial resolution to $1'$ or better and increasing the field of view to a degree or more, would make the DUET mission a powerful follow-on to Astro-D for the study of galaxy clusters. The larger field of view would make it easier for DUET to image the largest, closest clusters, such as Coma. A spatial resolution of $1'$ or so marks an important watershed, since it corresponds to the X-ray core radius of a typical cluster at redshift of 0.2. Thus instead of obtaining average spectral properties for clusters in this redshift range, DUET would be able to study the spatial distributions of temperature and abundance, opening up a whole new field in the study of cluster evolution. The field of X-ray studies of clusters changed dramatically with the first generation of imaging satellites. The capabilities that Astro-D and DUET will provide will allow further qualitative improvement in our understanding of clusters.

6. References

Allen, S. W, Fabian, A. C., Johnstone, R. M., Nulsen, P. E. J, & Edge, A. C. 1991, in *Proc. of the NATO ASI on Clusters and Superclusters of Galaxies (Contributed Talks and Poster Papers)*, ed. M. M. Colless *et al.*, p. 81.

Arnaud, M., Lachieze-Rey, M., Rothenflug, R., Yamashita, K., & Hatsukade, I. 1991, *Astr. & Ap.*, **243**, 56.

Arnaud, M., Hughes, J. P., Forman, W., Jones, C., Lachieze-Rey, M., Yamashita, K., & Hatsukade, I. 1992a, *Astrophys. J.*, **390**, 345.

Arnaud, M., Rothenflug, R., Boulade, O., Vigroux, L., & Vangioni-Flam, E. 1992b, *Astr. & Ap.*, **254**, 49.

Birkinshaw, M. 1979, *M.N.R.A.S.*, **187**, 847.

Birkinshaw, M., Gull, S. F., Hardebeck, H. E., Moffett, A. T. 1992, *Astrophys. J.*, submitted.

Birkinshaw, M., & Hughes, J. P. 1992, *Astrophys. J.*, in preparation.

Birkinshaw, M., Hughes, J. P., & Arnaud, K. A. 1991, *Astrophys. J.*, **379**, 466.

Boynton, P. E., Radford, S. J. E., Schommer, R. A., & Murray, S. S. 1982, *Astrophys. J.*, **257**, 473.

Briel, U. G., Henry, J. P., & Böhringer, H. 1991, in *Proc. of the NATO ASI on Clusters and Superclusters of Galaxies (Contributed Talks and Poster Papers)*, ed. M. M. Colless *et al.*, p. 91.

Briel, U. G., Henry, J. P., Schwarz, R. A., Böhringer, H., Ebeling, H., Edge, A. C., Hartner, G. D., Schindler, S., Trümper, J., & Voges, W. 1991, *Astr. & Ap.*, **246**, L10.

Butcher, J. A., & Stewart, G. C. 1991, in *Proc. of the NATO ASI on Clusters and Superclusters of Galaxies (Contributed Talks and Poster Papers)*, ed. M. M. Colless *et al.*, p. 25.

Cavaliere, A., Danese, L., & DeZotti, G. 1979, *Astr. & Ap.*, **75**, 322.

David, L. P., Arnaud, K. A., Forman, W., & Jones, C. 1990, *Astrophys. J.*, **356**, 32.

David, L. P., Forman, W., & Jones, C. 1991, *Astrophys. J.*, **380**, 39.

David, L. P., Hughes, J. P., & Tucker, W. H. 1992, *Astrophys. J.*, in press (to appear 1 August 1992).

Day, C. S. R., Fabian, A. C., Edge, A. C., & Raychaudhury, S. 1991, *M.N.R.A.S.*, **252**, 394.

Edge, A. C. 1989, Ph. D. thesis, University of Leicester.

Edge, A. C., & Stewart, G. C. 1991, *M.N.R.A.S.*, **252**, 414.

Edge, A. C., Stewart, G. C., Fabian, A. C., & Arnaud, K. A. 1990, *M.N.R.A.S.*, **245**, 559.

Gunn, J. E. 1978, in *Observational Cosmology*, eds. A. Maeder, L. Martinet, & G. Tammann (Geneva: Geneva Observatory).

Hatsukade, I. 1989, Ph. D. thesis, Osaka University (ISAS Research Note, 435).

Gioia, I. M., Henry, J. P., Maccacaro, T., Morris, S. L., Stocke, J. T., & Wolter, A. 1991, *Astrophys. J. (Letters)*, **356**, L35.

Hughes, J. P., & Birkinshaw, M. 1991, in *Proc. of the NATO ASI on Clusters and Superclusters of Galaxies (Contributed Talks and Poster Papers)*, ed. M. M. Colless *et al.*, p. 73.

Hughes, J. P., Butcher, J. A., Stewart, G. C., & Tanaka, Y. 1992, *Astrophys. J.*, submitted.

Hughes, J. P., & Tanaka, Y. 1992, *Astrophys. J.*, in press (to appear 10 October 1992).

Ikebe, Y., Ohashi, T., Makishima, K., Tsuru, T., Fabbiano, G., Kim, D.-W., Trinchieri, G., Hatsukade, I., Yamashita, K., & Kondo, H. 1992, *Astrophys. J. (Letters)*, **384**, L5.

Johnson, M. W., Cruddace, R. G., Ulmer, M. P., Kowalski, M. P., & Wood, K. S. 1983, *Astrophys. J.*, **266**, 425.

Johnstone, R. M., Fabian, A. C., Edge, A. C., & Thomas, P. A. 1991, in *Proc. of the NATO ASI on Clusters and Superclusters of Galaxies (Contributed Talks and Poster Papers)*, ed. M. M. Colless *et al.*, p. 29.

Kowalski, M. P., Cruddace, R. G., Snyder, W. A., Fritz, G. C., Ulmer, M. P., & Fenimore, E. E. 1992, *Astrophys. J.*, submitted.

Kowalski, M. P., Ulmer, M. P., & Cruddace, R. G. 1983, *Astrophys. J.*, **268**, 540.

Koyama, K., Takano, S., & Tawara, Y. 1991, *Nature*, **350**, 135.

McHardy, I. M., Stewart, G. C., Edge, A. C., Cooke, B. A., Yamashita, K., & Hatsukade, I. 1990, *M.N.R.A.S.*, **242**, 215.

Mushotzky, R. F. 1988, in *Proc. of NATO ASI on Hot Thin Plasmas in Astrophysics*, ed. R. Pallavacini, (Dordrecht: Reidel), p. 273.

Mushotzky, R. F. 1991, in *Proc. of the NATO ASI on Clusters and Superclusters of Galaxies*, in press.

Perrenod, S. C. 1980, *Astrophys. J.*, **236**, 373.

Ponman, T. J., Bertram, D., Church, M. J., Eyles, C. J., Watt, M. P., Skinner, G. K., & Willmore, A. P. 1990, *Nature*, **347**, 450

Silk, J., & White, S. D. M. 1978, *Astrophys. J. (Letters)*, **226**, L103.

Tsuru, T. 1991, Ph. D. thesis, University of Tokyo.

Ulmer, M. P., Kowalski, M. P., & Cruddace, R. G. 1986, *Astrophys. J.*, **303**, 162.

White, S. D. M., & Silk, J. 1980, *Astrophys. J.*, **241**, 864.

Yamashita, K. 1991, in *Proc. of the 28th Yamada Conference on Frontiers of X-Ray Astronomy*, in press.

Harvard-Smithsonian
Center for Astrophysics

Preprint Series

No. 3477
(Received September 8, 1992)

GINGA OBSERVATIONS OF THE COMA CLUSTER AND STUDIES OF THE SPATIAL DISTRIBUTION OF IRON

John P. Hughes
Harvard-Smithsonian Center for Astrophysics

Jackie A. Butcher and Gordon C. Stewart
Department of Physics, University of Leicester

and

Yasuo Tanaka
Institute of Space and Astronautical Science, Sagamihara-shi, Japan

To appear in
The Astrophysical Journal
February 20, 1993

HARVARD COLLEGE OBSERVATORY SMITHSONIAN ASTROPHYSICAL OBSERVATORY
60 Garden Street, Cambridge, Massachusetts 02138

Center for Astrophysics
Preprint Series No. 3477

GINGA OBSERVATIONS OF THE COMA CLUSTER AND STUDIES OF THE SPATIAL DISTRIBUTION OF IRON

John P. Hughes
Harvard-Smithsonian Center for Astrophysics

Jackie A. Butcher and Gordon C. Stewart
Department of Physics, University of Leicester

and

Yasuo Tanaka
Institute of Space and Astronautical Science, Sagamihara-shi, Japan

GINGA OBSERVATIONS OF THE COMA CLUSTER AND STUDIES OF THE SPATIAL DISTRIBUTION OF IRON

John P. Hughes
Harvard-Smithsonian Center for Astrophysics
60 Garden Street, Cambridge, MA 02138

Jackie A. Butcher, Gordon C. Stewart
X-Ray Astronomy Group, Department of Physics
University of Leicester
University Road, Leicester, LE1 7RH, U.K.

Yasuo Tanaka
Institute of Space and Astronautical Science
1-1, Yoshinodai, 3-chome, Sagamihara-shi, Kanagawa 229 Japan

Received 1991, February 25; Accepted 1992, August 28

ABSTRACT

The large area counters on the Japanese satellite *Ginga* have been used to determine the X-ray spectrum from the central region of the Coma cluster of galaxies over the energy range from 1.5 keV to 20 keV. The spectrum is well represented by an isothermal model of temperature 8.21 ± 0.16 keV and a heavy element (iron) abundance of 0.212 ± 0.027, relative to the cosmic value. The *Ginga* spectrum was found to be consistent with the X-ray spectra from the *Tenma* and EXOSAT satellites for a large class of nonisothermal temperature distributions. The measured iron elemental abundances were used to set a lower limit on the total mass of iron in Coma under the assumption that the iron is not distributed uniformly throughout the cluster. The mass ratio of iron relative to hydrogen (within 2 Mpc) is not less than 18% of the cosmic iron to hydrogen mass ratio. This compares to an average abundance of 24% if the iron is distributed uniformly. We discuss these results in terms of models for the production of iron in galaxy clusters.

Subject headings: galaxies: clustering – galaxies: intergalactic – X-rays: sources

1. INTRODUCTION

The Coma cluster of galaxies has been observed by nearly all space-borne X-ray observatories. It is relatively nearby (z=0.0232), extended (core radius $\sim 8'$), and luminous in X-rays (about 10^{45} ergs s^{-1}) with a high gas temperature (about 8 keV). As part of its performance verification program, the third Japanese X-ray astronomy satellite *Ginga* ("Galaxy") (Makino *et al.* 1987) observed the Coma cluster. In this article we report on the analysis and modeling of the *Ginga* X-ray spectral data.

The principal experiment on *Ginga* is the large area counter (LAC) (Turner *et al.* 1989), an array of eight sealed proportional counters with a total geometric collecting area of 4000 cm^2. The efficiency for absorbing X-rays is high (greater than 10%) from 1.5 keV to nearly 30 keV. These detectors have energy resolution of 18% (FWHM) at about 6 keV. The LAC has a very low internal background rate which makes it a very sensitive instrument for X-ray spectral studies. The field of view is mechanically collimated to 1° by 2° (FWHM).

One of the aims of this research was to demonstrate consistency between the *Ginga* X-ray spectrum of the Coma cluster and the spectra obtained by the earlier *Tenma* (Hughes *et al.* 1988) and EXOSAT (Hughes, Gorenstein, and Fabricant 1988) satellites. These earlier studies showed that the Coma cluster almost certainly deviates from isothermality, and that a model with an isothermal core surrounded by a region with temperature decreasing radially outward could describe the spectral and imaging data. In addition, a large class of rather general models for the binding mass distribution of the Coma cluster was found to be consistent with the X-ray (as well as the optical galaxy and velocity dispersion) data (Hughes 1989). The present study confirms that these models describe the *Ginga* data, and rule out pure polytropic models of the form used to describe the *HEAO 1* A-2 observations of this cluster by Henriksen and Mushotzky (1986). For completeness, we have investigated the effects of background subtraction and detector gain uncertainties. We find that the uncertainty in most derived results (the metal abundance determination is an exception) is dominated by the inclusion of these systematic effects.

The spatial distribution of the metals in clusters of galaxies has been of interest for some time. At the most basic level, knowing the space distribution allows one to determine the total mass of iron in the cluster. Knowledge of the distribution also should yield clues to the source of the metal enrichment in clusters and perhaps to the origin and evolution of the hot gas itself. In this article we introduce a simple parameterization for the radial distribution of iron atoms in the cluster, and use the observed metal abundances from four different spatial regions in the Coma cluster corresponding to the *Tenma*, EXOSAT (two separate data sets) and *Ginga* data sets to constrain the allowed iron distribution parameters. We find a strong lower limit to the mass of iron in the

Coma cluster: the iron mass cannot be less than about 75% of the uniformly distributed value. We consider a simplified model for ram-pressure stripping of the enriched gas in Coma member galaxies by the intracluster medium. Our observations are not sensitive enough to be able to reject this scenario based solely on the predicted spatial distribution of iron.

This article is organized in the following manner. The next section (§2) discusses the *Ginga* data reduction, *i.e.*, data selection criteria, background subtraction and gain determination. Next we describe our model fits in §3 including nonisothermal temperature distributions and models for the spatial distribution of iron. Discussion and conclusions are in §§4 and 5.

2. DATA REDUCTION

Coma was observed by the large area counters (LAC) on the Japanese satellite *Ginga* on 1 July, 1987, during the performance verification phase of the mission. There were 4352 s of data which satisfied several stringent data selection criteria to be discussed below. The source yielded a total counting rate (top plus middle layers) of 162 s^{-1} (1.5-20 keV) and the spectrum was statistically well-determined over this energy range. In each pulse height (PH) channel a systematic error of 1% of the source signal was added in quadrature with the statistical error to account for uncertainties in the energy bin boundaries. This value also was necessary to obtain an acceptable fit to the standard celestial X-ray calibration source (the Crab Nebula). In this work we explore separately systematic effects due to uncertainties in the gain of the LAC as well as the background subtraction. Further constraints on the systematic errors in the data and their analysis were obtained by comparison between results obtained using the independent analysis procedures available at Leicester and ISAS.

The gain of the LAC is monitored in flight using the Ag Kα line at 22.1 keV, which arises from fluorescence of cosmic X-ray background photons (plus cosmic ray particles) in the silver coating on the LAC collimator. For this observation, we determined the Ag Kα line energy for each of the eight individual detectors in the top and middle layers. The raw count rate data in the energy range 16 - 30 keV was fitted with two power law components to approximate the continuum and a doublet line (energy separation of 2.91 keV) was used to approximate the Ag Kα and Kβ line blends. The intensity of the Kβ line was fixed at a value equal to 0.1 of the Kα line intensity. This includes the difference in LAC detection efficiency at the energies corresponding to the two lines, as well as the intrinsic line ratio (Salem, Panossian, and Krause 1974). The LAC energy resolution function was included as $\Delta E/E = 0.18\,(E/5.9\,\mathrm{keV})^{-0.5}$.

The 16 individual gain values for the top and middle layers were combined (using an average based on weighting by the count rates in the two layers) to form 8 gain values for the summed spectrum. An average response function computed from these gain values was used in the model fitting. Note that the overall average gain was such that the Ag Kα fluorescent line from the collimator fell in PH channel 35.25 ± 0.08 close to the nominal gain which lies between 35.0 and 35.2 (S. Takano, private communication). We use this value below to represent the systematic uncertainty in the LAC gain. Finally, the linearity of the LAC counters was determined pre-launch and it was assumed that this remained stable during the mission.

The background of the LAC has been studied in great detail (Hayashida *et al.* 1989, Butcher *et al.* 1991). For background subtraction during the Coma observation, we used one of the techniques (so-called Method II) developed by these authors. We used four parameters: the SUD rate (counts above the upper discriminator level), the PIM rate (counts from LAC sense wires screened from the field of view), the charged particle cut-off rigidity (COR), and the argument of perigee of the satellite, to determine the intrinsic particle-induced background spectrum. (The large flux of this bright X-ray source gives a significant count-rate in the MID rate often used as an additional background monitor.) For the diffuse extragalactic X-ray background, an average of a large number of source-free fields at high galactic latitude was used.

This technique yielded excellent results. The 2 - 10 keV count rate of the cluster after background subtraction showed no time variability and there were no residual correlations between this source count rate and the SUD rate, the PIM rate, or the COR. We also checked for correlations between the SUD rate and both the background subtracted source count rate above PH channel 31 and the MID rate, which would be most sensitive to improper background subtraction. No significant correlations were found. Between about 20 keV and 25 keV imperfect subtraction of the Ag Kα line introduced an "S" shaped artifact in the spectrum, but this can be attributed to the slightly higher fluorescence caused by the presence of Coma in the field of view. Hence we will only consider the spectrum out to 20 keV.

The principle uncertainty in the background subtraction arises from spatial fluctuations in the diffuse X-ray background (*e.g.*, Warwick and Stewart 1989). From a large number of *Ginga* pointings toward apparently source-free regions of the sky these authors have determined the average spectrum of the diffuse background as viewed by *Ginga*Furthermore they find that the root-mean-square deviation from pointing to pointing is about 5% of the average spectrum. We use this RMS spectrum to represent the systematic uncertainty in the background subtraction for this study of the Coma cluster.

Only data from the remote pass, which tends to have the lowest background on average, were used in this analysis. The earth elevation angle was required to be larger than 20°. Data from regions in the satellite orbit corresponding to higher background (such as the SAA passage and orbital regions with COR < 10) were rejected. We rejected data from segments in which the LAC high voltage was turned on or off. Since the angle from the LAC field of view and the sun was about 83°, contamination from solar X-rays was possible. We restricted ourselves to data taken only in the earth shadow and thereby discarded about 9000 s of data. Since we intended to search for evidence of nonisothermality in the cluster X-ray spectrum, we required accurate knowledge of that spectrum even in the lowest energy channels (where solar scattered X-rays would have the largest effect). In addition, even for only 4352 s of data, the errors on the spectrum are dominated by the inclusion of a 1% systematic error (as discussed above), and the fitted parameters (temperature, iron abundance, etc.) are dominated by the systematic uncertainty in gain and background subtraction. We have summed the data from the top and middle layers as well as the eight individual detectors to form the spectrum, which we show in Figure 1. We carried out fits to each layer separately for the redshifted optically-thin plasma emission model (see §3.1.2 below) and the fitted results were consistent with each other at about 1-sigma. All quoted results are based on the summed spectrum in Figure 1. It should be noted, however, that the excluded data are entirely consistent with the restricted dataset utilized here.

3. MODEL FITS

3.1 *Isothermal temperature distributions*

Isothermal models yield acceptable χ^2 values. We have considered two types of model fits: (1) bremsstrahlung continuum models with Kα and Kβ lines introduced as gaussian profiles, and (2) redshifted optically-thin collisional ionization equilibrium (CIE) thermal bremsstrahlung models (Raymond and Smith 1978; J. C. Raymond, private communication; hereafter RS). In both cases we fix the hydrogen column density to a value of $10^{20.3}$ cm^{-2}, which is well below the level to which the LAC is sensitive, is the average value determined from 21 cm measurements, and is consistent with the value obtained from lower energy X-ray spectra (Gorenstein *et al.* 1979).

3.1.1 *Continuum plus gaussian lines*

The thermal bremsstrahlung model used for the continuum is based on the gaunt factor for a pure hydrogen plasma (Karzas and Latter 1961) as calculated by Kellogg, Baldwin, and Koch (1975). In order to simulate a narrow line, the energy width of the gaussian lines was fixed at 0.1 keV, significantly less than the energy resolution of the LAC at about 7 keV. The introduction of both Kα and Kβ lines was highly significant: the minimum χ^2 values were 229.2, 32.6, and 20.8 for fits with no, one and two lines. The results of this fit are summarized in Table 1. We have also used another calculation of the gaunt factor (Gould 1980, 1981) and the best-fit temperature in this case was 7.96 ± 0.09 with a χ^2 value of 19.5. The energies and equivalent widths of the emission lines were virtually unchanged from the ones shown in Table 1.

The redshifted Fe lines lie at energies of 6.79 ± 0.09 keV and 8.50 ± 0.40 keV and the redshifted temperature is 8.26 keV. We have determined the expected values for the line energies and ratio of Kα to Kβ line emission to be 6.772, 8.163, and 5.97 (at the redshifted temperature) from the calculations of RS. The agreement is excellent. The calculated equivalent width assuming cosmic abundances (Fe/H ratio of 4×10^{-5} by number) is 972 (252) eV for Kα (Kβ), requiring an abundance of 0.225 (0.250) for the Coma cluster.

For comparison to the *Tenma* results (Okumura *et al.* 1989) we have fit our data with the gaunt factor based on the calculations of Matteson (1971) and Maxon and Corman (1967) which these authors used. While this model yielded a χ^2 value of 70.4 for the *Ginga* data, which allows us to reject it at greater than 99.95% confidence, there was good agreement for the fitted Fe line energies and equivalent widths, although the emission integral and best-fit temperatures were different. This difference between datasets is also apparent when the RS model is used (see below) and is a result of the differing fields of view of the two instruments and represents strong evidence for a nonisothermal temperature distribution in the Coma cluster.

3.1.2 *RS thermal models*

The best fit values for the parameters of this model are shown in Table 2 and the best fit spectrum is plotted in Figure 1. The photon spectrum, based on the best fit parameters for this model, is shown in Figure 2. The iron abundance is consistent with the value derived above from the fits to a continuum model with gaussian lines. For the RS model the abundances of C, N, O, Ne, Mg, Si, S, Ar, Ca, Fe, and Ni were varied both in unison and with the Fe abundance separate, while the He/H ratio was fixed at 0.085. Previous analyses of data from *Tenma* and EXOSAT have used the same model (Hughes *et al.* 1988 and Hughes, Gorenstein, and Fabricant 1988) and thus a comparison of the results on temperature can be made easily and reliably (see Table 3). Each of the four sets of data in Table 3 yielded acceptable fits for isothermal models, yet each of the temperatures measured was different! However, the pattern is clear: the larger the field of view, the lower the measured temperature. In column 4 of the Table we give the average effective radius (the radius weighted by the cluster surface brightness and collimator response) of each observation.

Before investigating nonisothermal temperature distributions, we would like to examine the dependence of some of our present *Ginga* results on the uncertainty in gain and background subtraction. We generated results for plus and minus one-sigma variation in gain and background subtraction, using the values determined in §II. The best fit temperature changed by ± 0.13 keV when the gain was varied and by ± 0.04 keV when the background was varied. These in fact dominate the statistical error on the temperature determination. If we add the systematic and statistical errors in quadrature, we derive a total error on the temperature of ± 0.16 keV. The iron abundance was much less sensitive to these variations, changing by only ± 0.005 (gain) and ± 0.002 (background).

If we again add systematic and statistical errors in quadrature, the total uncertainty in abundance becomes ± 0.027. We show this graphically in Figure 3. We plot contours of constant χ^2 at the 90% confidence level for temperature (kT) versus iron abundance (χ^2_{min} + 4.61; Avni 1976; Lampton, Margon, and Bowyer 1976) for five datasets: (1) nominal gain, nominal background subtraction; (2) higher gain, more background; (3) lower gain, more background; (4) higher gain, less background; and (5) lower gain, less background. It is clear that the dominant uncertainty arises from systematic errors in the gain and background subtraction.

Before leaving this section, we wish to describe our limits on nonthermal (*i.e.*, power-law) emission from the Coma cluster. We find no significant evidence for a high energy tail in the X-ray spectrum out to almost 40 keV. Our data allows us to set limits to the on-axis power-law emission (flux at 1 keV) of 1.6×10^{-3} photons $\mathrm{cm}^{-2}\ \mathrm{s}^{-1}\ \mathrm{keV}^{-1}$ for a photon index of 1.33, 7.7×10^{-3} photons $\mathrm{cm}^{-2}\ \mathrm{s}^{-1}\ \mathrm{keV}^{-1}$ for an index of 1.77, and 1.8×10^{-2} photons $\mathrm{cm}^{-2}\ \mathrm{s}^{-1}\ \mathrm{keV}^{-1}$ for an index of 2.21. These values are about an order of magnitude less than values quoted by balloon-borne hard X-ray experiments: Bazzano *et al.* (1984) and more recently by Fusco-Femiano *et al.* (1990) and are insensitive to the assumed absorption for the power-law component.

3.2 *Nonisothermal temperature distributions*

3.2.1 *Ginga collimator response*

Accurate knowledge of the collimator response is essential for the study of nonisothermal temperature distributions in large diffuse clusters such as Coma. Fortunately, the Ginga collimator has been well-studied thanks to the analysis of observations of SN 1987a in the Large Magellanic Cloud (Dotani *et al.* 1987). From scans of the Crab Nebula the energy dependence of the collimator has been calibrated in flight. Lower energy X-ray photons have a broader response than higher energy ones, due to scattering from the collimator. We constructed a collimator response including this scattered component using the observed spectrum of Coma. The top panel of Figure 4 shows the average *Ginga* transmission as a function of radial distance from the center of the Coma cluster ($\alpha_{1950} = 12^{\mathrm{h}}\ 57^{\mathrm{m}}\ 19^{\mathrm{s}}$, $\delta_{1950} = 28^\circ\ 13'\ 7''$; Abramopoulos, Chanan, and Ku 1981). The full width half maximum of this response curve is about 80′. The lower panel shows the average transmission times the area at each radius (the curve which is higher beyond about 20′) and the product of that curve with the X-ray surface brightness of Coma from Hughes *et al.* (1988). The latter curve peaks at about 10′ in the figure. The vertical dashed line at $14\rlap{.}'2$ is the average effective radius of this observation.

We compared this response to a purely geometric model of the collimator (*i.e.*, one with no scattered component). Differences between the two only became apparent beyond about 70′, where the average response is less than 10% and the surface-brightness-weighted response is more than two orders of magnitude less than near the center. We also constructed collimator responses for slightly different pointing positions relative to the center of the Coma cluster. From among the sub-frames of accepted data, we chose the two pointing positions with the highest and lowest transmission at the cluster center. The response functions constructed from these were different by less than 1% over the whole radial range sampled. Finally, we used each of these collimator response functions for our analysis of nonisothermal temperature distributions (see immediately below) and the fitted parameters were indistinguishable.

3.2.2 *Isothermal/Polytropic Hybrid Models*

In previous work (Hughes *et al.* 1988, Hughes, Gorenstein, and Fabricant 1988) a model for the nonisothermal temperature distribution of the Coma cluster was introduced, which successfully described the *Tenma* and EXOSAT X-ray spectra of the cluster. We use this same model for the *Ginga* data. Briefly, we assume that the temperature of the cluster is isothermal (at value T_{ISO}) out to a certain radius (R_{ISO}), beyond which the temperature decreases as a polytrope (density and temperature related through the equation $T \propto \rho^{\gamma-1}$). The radius and temperature of the isothermal region are variables to be determined by fitting to the data, while the polytropic index of the outer region ($\gamma = 1.555$) and the parameters describing the X-ray surface brightness ($R_{core} = 6\rlap{.}'9$ and $\beta = 0.60$) are fixed at the values used in the previous analyses. For each trial value of T_{ISO} and R_{ISO} a model spectrum based on the RS plasma emission model (appropriately redshifted) is generated in the following manner. We divide the cluster into a large number of constant temperature radial shells. Each shell is projected onto the plane of the sky, weighted by the square of its hydrogen number density, and convolved with the *Ginga* collimator response. This gives the weighting factor for this temperature value. An isothermal RS model is calculated at each temperature and multiplied by the weighting factor. The final spectrum is the sum of these individual spectra from the various radial shells.

For the data set with nominal gain and background subtraction, we find that this model yields a slightly better χ^2 value than the isothermal model (25.1 versus 27.5 for 27 and 28 degrees of freedom, respectively), although the reduction in χ^2 is not significant. The best fit values, $T_{ISO} = 8.8$ keV and $R_{ISO} = 4.2$ (in units of R_{core}), are consistent with the EXOSAT results at 68% confidence and with the *Tenma* results at better than 90% confidence. In addition, the 68% confidence contours for all three data sets have a significant region of overlap in parameter space around $T_{ISO} = 9$ keV and $R_{ISO} = 3.5$.

The systematic uncertainty in gain and background subtraction have a large effect in this study. We show this in Figure 5 for the five *Ginga* data sets representing these systematic uncertainties. We show contours of constant χ^2 at 90% confidence in the T_{ISO}, R_{ISO} parameter space. The cross shows the best fit result with 90% errors from the combined *Tenma* and EXOSAT analysis. Even when the systematics are included, the *Ginga* data are slightly more constraining for this model than the EXOSAT data alone. This is due to the higher statistical signal of the *Ginga* data, as well as the lower background and higher energy response of *Ginga*. However because of the large angular size of the *Ginga* collimator, it is not likely that one will be able to obtain high quality spectra from a set of spatially disjoint regions of the cluster as was done with EXOSAT by Hughes, Gorenstein, and Fabricant (1988).

We have reproduced the outer envelope of the contours shown in Figure 5 by fitting to the nominal *Ginga* dataset with the inclusion of additional systematic error. After some trial and error, we found that a total systematic error of 4 to 5% roughly reproduces the envelope of contours.

For completeness we have also fit the *Ginga* data with the polytropic models used by Henriksen and Mushotzky (1986). For $\beta = 0.6$, we find a best fit value of the central temperature $T_c = 9.0^{+2.8}_{-0.9}$ keV and polytropic index $\gamma = 1.05^{+0.11}_{-0.05}$ but this model is not a significant improvement on the isothermal model. Fixing β at a value of 0.76 as used by Henriksen and Mushotzky results in values of $T_c = 8.45^{+2.4}_{-0.4}$ keV and $\gamma = 1.015^{+0.12}_{-0.015}$, significantly different from the revised allowed range of γ determined by Cowie, Henriksen, and Mushotzky (1987) of $1.33 < \gamma < 1.43$.

Figure 5 demonstrates rather clearly the problem with interpreting global integrated X-ray spectral data for clusters of galaxies in terms of nonisothermal models. It is obvious that variations in gain and background subtraction can mimic the effects under investigation. Only truly spatially distinct spectral observations (as done crudely in the EXOSAT study and which will become routine with the X-ray facilities planned for later this decade) can give reliable results about the distribution of temperatures in clusters of galaxies. However, at this juncture, based on data from three different experiments the evidence is compelling that the gas in the Coma cluster consists of material emitting over a large range of temperatures.

3.3 *Spatial Distribution of Iron*

The results of isothermal fits to the *Ginga*, *Tenma*, and EXOSAT spectra all yield rather similar values for the fractional iron abundance ($\sim 20\%$). In this section we discuss the constraints that can be applied to the spatial distribution of iron in the Coma cluster from these observations. Immediately below we describe the re-analysis of the *Tenma* and EXOSAT data using nonisothermal models to obtain a self-consistent set of iron abundance values. Then we describe our parameterization for the spatial distribution of iron in the cluster and how we use the measured abundances as constraints.

3.3.1 *Analysis*

The present iron abundance values from the different instruments are based on fits to (different) isothermal temperature models, *i.e.*, the temperatures presented in Table

3. In general, fitted values for the iron abundance are sensitive to the continuum temperature due to both the intrinsic variation of iron line flux with temperature and the change in continuum shape near the line. In the case of Coma, we have already argued that the global X-ray spectra is best described by a nonisothermal model with a radial temperature gradient. For these reasons, we have refitted the *Tenma* and EXOSAT spectra using the best-fit nonisothermal temperature model discussed above to derive self-consistent iron abundance values from the different instruments. As in the *Ginga* analysis discussed above, the model was projected onto the plane of the sky and convolved with the collimator response appropriate to the instrument under study.

X-ray fluxes and fractional iron abundances derived from fits to the best-fitting nonisothermal model (with parameters $T_{ISO} = 9.1$ keV and $R_{ISO} = 3.33\ R_{core}$) are shown in Table 4. The measured flux values clearly depend on the field-of-view of the instrument (increasing from EXOSAT to *Ginga* to *Tenma*), while the iron abundance is consistent with a uniform value of 0.239 ± 0.013. This set of measured iron abundances can be used to derive a strong lower limit on the amount of iron present in the cluster.

3.3.2 *Models for the Iron Distribution*

We have chosen a convenient well-known three-parameter form for the distribution of iron atoms as a function of radius in the cluster

$$n_{Fe} = n_{Fe,0}[1 + (R/R_{Fe})^2]^{-3\beta_{Fe}/2},$$

and our program entails determining what values of $n_{Fe,0}$, R_{Fe}, and β are allowed by the abundance values in Table 4. The distribution of hydrogen atoms is given by the same functional form but with values for R_H and β_H set by the X-ray surface brightness distribution (from the *Einstein* IPC image). This simplification requires that the 0.5-4 keV X-ray surface brightness be dominated by emission from hydrogen and helium atoms, *i.e.*, that the iron enrichment be nowhere very extreme. We have confirmed *post facto* that this requirement is satisfied for the range of models we accept.

First we determined the projected surface brightness emission from iron

$$\Sigma_{Fe}(R) = 2 \int_R^\infty \frac{dr\, r}{\sqrt{r^2 - R^2}} n_{Fe}(r)\, n_H(r)\, \Lambda_{Fe}[T(r)].$$

Here we show the implicit dependence of the iron Kα line emissivity function Λ_{Fe} (calculated using the RS model) on the temperature distribution. Next we convolved both the iron surface brightness distribution and the overall X-ray surface brightness with the various collimator response functions and took the ratio of these values. Comparison with the iron abundance data results yielded the overall normalization of the model iron distribution and a χ^2 value for the given set of R_{Fe} and β_{Fe} values. For a given value of R_{Fe}, β_{Fe} was reasonably well constrained by the data: for example with $R_{Fe} = 10'$, we found $\beta_{Fe} = 0.52^{+0.32}_{-0.19}$ (90% confidence level). However we were considerably less sensitive to variations in R_{Fe}; values from $0.01'$ to $100'$ all yielded essentially similar quality fits (for different β_{Fe} values of course).

Nevertheless, when the allowed range of R_{Fe} and β_{Fe} values are used to determine the total mass of iron contained within a given radius of the cluster center, the data are quite constraining. In Figure 6 we show the total mass of iron relative to hydrogen (relative to the cosmic mass ratio) contained within a 2 Mpc radius (at 90% confidence). The minimum mass of iron (19% of the cosmic value) is obtained for R_{Fe} values of $0.1'$ or less. Note that within a radius of 3 Mpc (nearly 10 optical or X-ray core radii) the minimum iron mass decreases to only 17%. Recall that the mass of iron is 24% under the uniform abundance distribution, which corresponds to an iron mass of $1 \times 10^{11}\ M_{\odot}$ (within 2 Mpc). In the next section we discuss the implications of these constraints on scenarios for the elemental enrichment of the intracluster medium.

4. DISCUSSION

4.1 *Cluster Binding Mass Determination*

It is well known that one of the important uses of X-ray spectral data is the determination of cluster binding masses. In an earlier study of the Coma cluster (Hughes 1989), *Tenma* and EXOSAT spectral data were used with *Einstein Observatory* imaging data to determine the allowed binding mass distributions. We have chosen the preferred mass distribution model from that article, *i.e.*, where the binding mass follows the distribution of optical light, calculated the X-ray spectrum from the model temperature distribution and fitted to the *Ginga* Coma spectrum. The inferred mass of the cluster as determined by the best fit to the *Ginga* spectrum is entirely consistent with the value obtained in the previous study. The value obtained by *Ginga* for the central binding mass density ρ_{b0} is $1.02^{+0.05}_{-0.04} \times 10^{-25}$ g cm^{-3} (68% confidence level for one interesting parameter). However, including effects of background subtraction and gain uncertainty on the *Ginga* spectral data greatly increases the range of allowed central ρ_{b0} values. In fact, since it is not possible to determine the radial gradient of the temperature distribution from only the integrated X-ray spectrum, it is not possible even to determine the minimum allowed binding mass of the cluster from the *Ginga* data alone. Improvement in determining the binding mass of the Coma cluster may be possible with existing *Ginga* scanning data (H. Kondo, private communication) and significant improvements will be possible with Astro-D and Spectrum X-γ. Watt *et al.* (1991) recently used data on the center of the Coma cluster from Spacelab-2 to constrain the temperature distribution and thereby the virial mass distribution. Their results are consistent with those presented here.

4.2 *Iron Spatial Distribution*

If the iron in galaxy clusters is primordial, from a very early generation of stars, or if all of the gas in the cluster was lost by the member galaxies, then the present distribution of iron should be nearly the same as the gas, if the settling timescale is as large as believed (Rephaeli 1978). This is certainly allowed by the observational constraints, and in fact it corresponds very nearly to the best fit case with $\chi^2 = 1.3$ for 3 degrees of freedom (confidence level for rejection is 26.7%). If the iron in galaxy clusters is a result of gas processed by stars in the member galaxies which was lost to the intracluster medium *irrespective* of the galaxy's position or velocity, then the spatial distribution of iron should be roughly proportional to the galaxy space density. This too is allowed, although it is a poorer fit to the data yielding $\chi^2 = 5.5$ again for 3 degrees of freedom (confidence level for rejection is 86.3%).

Let us consider next a stripping scenario, wherein most of the hydrogen is primordial, but the iron is a result of ram-pressure stripping of the gas in the member galaxies by the intracluster medium. In this case the iron distribution should be proportional to $n_{\rm gal}\, S_E$, where $n_{\rm gal}$ is the source term for the iron and S_E is the stripping efficiency. The latter quantity varies from 0 to 1 and represents the fraction of total available gas in the galaxy which is removed by ablation. That is to say, when the efficiency for stripping is high, as it is near the core of the cluster, then this quantity would be near unity, while in the outskirts of the cluster where stripping is less efficient, the value would be closer to zero.

In order to pursue a more quantitative discussion we have employed the results of Gaetz, Salpeter, and Shaviv (1987, hereafter GSS), who studied the effects of steady-state ram pressure ablation from spherical galaxies using a hydrodynamical simulation. GSS introduce a quantity called Φ, which is the total mass fraction retained by the galaxy; we clearly want $S_E = 1 - \Phi$. With the relations in GSS we obtain

$$S_E = 1 - [1 + (\xi/0.6)^{1.23}]^{-1}$$

where

$$\xi = 91\, f_{\rm GSS} \left(\frac{v}{1750\,{\rm km\,s^{-1}}}\right)^{2.4} \left(\frac{n_{\rm gas}}{10^{-3}\,{\rm cm^{-3}}}\right).$$

We have set model parameter values to those corresponding to GSS's standard galaxy, which has a luminosity of 2×10^{10} $L_\odot$ and a mass-to-light ratio of 20 (in solar units). These are reasonable values for bright galaxies in Coma. The other relevant model parameters are the internal galaxian gas replenishment rate, assumed to be 0.6 $M_\odot\ {\rm yr}^{-1}$, and the radial extent of the gas replenishment distribution. As formulated by GSS, the latter quantity can be expressed equivalently in terms of the effective half-mass radius for the gravitational mass distribution; GSS assume a value of 17.4 kpc. This value, in particular, is rather uncertain and so we include a fudge factor $f_{\rm GSS}$ to account for this, plus other, uncertainties in the galaxy model. We assume a constant value (independent of radial position) for the galaxy speed, and use the measured velocity dispersion of Coma (1010 km s^{-1}: Zabludoff, Huchra, and Geller 1990), converted to a three-dimensional value of 1750 km s^{-1}.

For $f_{\rm GSS} = 1$, we find almost no difference in the expected iron distribution compared to the case where the iron is distributed like the galaxies. Quantitatively we obtain $\chi^2 = 5.7$ for 3 degrees of freedom (confidence level for rejection is 87.2%). This can be understood by realizing that stripping is extremely efficient in this situation and that S_E is close to unity over most of the cluster. In fact S_E drops to a value of 0.5 only at the considerable distance of 7.3 Mpc from the cluster center. For a case with $f_{\rm GSS}$ lowered to 0.1 (corresponding roughly to decreasing the galaxy half-mass radius by a factor of three), the iron distribution deviates somewhat more from the galaxy distribution. A fit to the data yields a χ^2 of 7.0 for 3 degrees of freedom corresponding to a confidence level for rejection of 92.7%. Here the half-value radius for S_E is 2.1 Mpc, where the gas density is 6.6×10^{-5} $\rm cm^{-3}$.

There is some observational evidence that ram-pressure stripping has been efficient in the core of the Coma cluster. Observations of Coma cluster member galaxies in H I (Bothun, Schommer, and Sullivan 1984) and Hα (Kennicutt, Bothun, and Schommer 1984) reveal a significant deficit of both types of emission for the galaxies located within about 1° (~2.4 Mpc) of the center. This suggests that it would not be realistic to lower $f_{\rm GSS}$ to values much below 0.1. Unfortunately, then, given the results in the preceding paragraph, we are not able to constrain strongly the amount of iron in the Coma cluster which could have been stripped out of the galaxies, based solely on the current data for the spatial distribution of iron. Other authors (Arnaud *et al.* 1992), however, have considered the origin of the total *amount* of iron seen in galaxy clusters and have concluded that it is probably impossible to produce using a standard iron yield from the current galaxy population. With new sensitive data on the spatial distribution of iron in clusters of galaxies expected from upcoming X-ray astronomy missions, we will to be able to confirm these conclusions.

Our result on the iron distribution for Coma seems to be at odds with the results from the Spacelab 2 coded mask observations of Perseus (Ponman *et al.* 1990), who find a strong gradient in the iron abundance of the intracluster medium and thus derive a total iron mass which is about a factor of 4 less than the homogeneous value. First we note that a simple re-analysis of the outermost four abundance data points shown in Figure 2a of Ponman *et al.* suggests a uniform abundance component in Perseus of $0.15^{+0.23}_{-0.15}$ (relative to the cosmic value used here), which is not so different from the uniform value for Coma. The difference between the clusters lies in the presence of an abundance gradient in the core of the Perseus cluster, which contains an active galaxy and a strong cooling flow and therefore is a considerably more complicated system to model than Coma. Furthermore, preliminary analysis of BBXRT data for Perseus (Mushotzky 1991) does not support the claims of Ponman *et al.* regarding the iron distribution. Lastly, the analysis we present here for the gas stripping model shows that it is extremely difficult to produce strong gradients in the iron distribution in the cores of rich clusters. Clearly it will be interesting to follow up both results on Coma and Perseus with new observations, and to study the spatial distribution of iron in a large sample of additional clusters.

5. CONCLUSIONS

The X-ray spectrum of the Coma cluster of galaxies has been measured by the LAC onboard the *Ginga* satellite. The spectrum was statistically well determined from 1.5 keV to 20 keV. From this data, we have measured the gas temperature of the Coma cluster and find that it can be well represented by an isothermal model of temperature 8.21 ± 0.16 keV with an iron abundance relative to the cosmic value ($\mathrm{Fe/H} = 4.0 \times 10^{-5}$) of 0.212 ± 0.027. The dominant source of uncertainty in the fitted results arises from systematic uncertainties in the gain and background subtraction.

We have shown that the *Ginga* X-ray spectrum of the Coma cluster is entirely consistent with results from *Tenma* and EXOSAT. Although each data set yielded a different isothermal temperature, the several observed temperatures are quantitatively consistent with each other and arise from the different regions of the cluster observed by the different instruments. The temperature must decrease with radius from the center of the cluster, since the instruments with larger fields of view (*Tenma*) show lower temperatures than those with smaller ones (EXOSAT and *Ginga*). Detailed fits to a particular nonisothermal model yield consistent results at better than 68% confidence among the data sets.

The *Ginga* spectrum was also used to determine the binding mass of the cluster under the assumption that the binding mass is distributed as the galaxies, using the techniques developed by Hughes (1989). Again, the *Ginga* results were found to be consistent with those from *Tenma* and EXOSAT. Because of the uncertainty in gain and background subtraction, the *Ginga* data alone were not able to constrain significantly the allowed binding mass values.

We have set limits on the spatial variation of iron in the Coma cluster. The observed iron abundance values from the various data sets were used to set a strong lower limit on the total mass of iron contained in the cluster: within 2 Mpc the mass of iron relative to hydrogen is not less than 18% of the cosmic value. Under the assumption that the iron is distributed uniformly in space, then the average abundance is about 24%. We examined various scenarios for the origin of the iron in the Coma cluster and found that abundance distributions which are proportional to either the gas space density or the galaxy space density are fully consistent with the observational data. A simplified model for ram-pressure stripping of the gas in member galaxies was considered and the resulting abundance distributions were also found to be reasonably consistent with the current observations. One interesting result of this modeling attempt was the fact that a strong gradient in the abundance distribution did not arise from the ram-pressure stripping model. Data from future X-ray astronomy satellites will allow us to discriminate between these various scenarios for the origin of the heavy elements in galaxy clusters.

Thanks are extended to the large number of scientists, engineers, and technicians who conceived, designed, built, launched and operated *Ginga*. We also would like to thank the team that designed and built the LAC. We appreciate K. Hayashida's and O R. Williams significant contribution to modeling of the LAC background. We acknowledge useful discussions with M. Arnaud, W. Forman, P. Gorenstein, and C. Jones. We also appreciate the referee's helpful comments concerning our ram-pressure stripping model for the iron distribution. JPH was supported under NASA grants NAG8-699 and NAG8-181. GCS acknowledges receipt of an SERC advanced fellowship and JAB an SERC research studentship.

TABLE 1

Best fit parameters: Continuum Plus Gaussian Lines

Parameter	Best fit value [a]
Emission integral (n^2V) [b] (10^{67} cm^{-3})	9.81 ± 0.11
Continuum temperature (kev)	8.07 ± 0.09
Kα line equivalent width (eV)	219 ± 30
Kα line energy (kev)	6.64 ± 0.09
Kβ line equivalent width (eV)	63 ± 31
Kβ line energy (kev)	8.31 ± 0.42
Kα to Kβ ratio	5.81 ± 2.91
n_{H} (atoms cm^{-2})	2×10^{20}
χ^2 (d.o.f)	20.8 (25)

[a] Statistical errors at 90% confidence for 1 interesting parameter.

[b] Uses geometric collecting area of 4000 cm^2, average transmission of 0.70, and H = 50 km s^{-1} Mpc^{-1}.

TABLE 2

Best fit parameters: RS model

Parameter	Best fit value [a]
Emission integral ($n_{\mathrm{H}}^2 V$) [b] (10^{67} cm^{-3})	9.37 ± 0.09
Continuum temperature (kev) [c]	8.21 ± 0.09 [d]
Abundance [e,f]	0.212 ± 0.026 [g]
n_{H} (atoms cm^{-2})	20.3
χ^2 (d.o.f)	27.5 (28)

[a] Statistical errors at 90% confidence for 1 interesting parameter.

[b] Uses geometric collecting area of 4000 cm^2, average transmission of 0.70, and H = 50 km s^{-1} Mpc^{-1}.

[c] Source temperature ($z = 0.0232$).

[d] Statistical error only. Error including systematics is ±0.16 keV.

[e] Relative to cosmic: [Fe]/[H] = 4×10^{-5}.

[f] With iron tied to other heavy elements; with iron free $A_{Fe} = 0.19$

[g] Statistical error only. Error including systematics is ±0.027.

TABLE 3

Temperature Measurements of the Coma Cluster

Instrument	kT (keV)	FOV (°)	R_{eff} (′)	Reference [a]
Tenma	7.5 ± 0.2	3	20	1
EXOSAT	8.50 ± 0.3	0.75	11	2
EXOSAT	7.39 ± 0.7	0.75	22	2
Ginga	8.21 ± 0.2	1×2	14	3

[a] References:

1) Hughes *et al.* 1988.

2) Hughes, Gorenstein, and Fabricant 1988

3) This work

TABLE 4

X-Ray Fluxes and Iron-Abundance Measurements of the Coma Cluster for Best-Fit Hybrid Model ($T_{ISO} = 9.1$ keV, $R_{ISO} = 3.33$)

Instrument	2-10 keV Flux (erg cm^{-2} s^{-1})	Iron abundance
Tenma	3.66×10^{-10}	0.237 ± 0.017
EXOSAT (center)	2.84×10^{-10}	0.231 ± 0.032
EXOSAT (off-center)	0.39×10^{-10} [a]	$0.344^{+0.081}_{-0.146}$
Ginga	3.39×10^{-10}	0.247 ± 0.024

[a] Average of three pointings: east, west, and south of cluster center

REFERENCES

Arnaud, M., Rothenflug, R., Boulade, O., Vigroux, L., and Vangioni-Flam, E. 1992, A&A, 254, 49

Abramopoulos, F., Chanan, G. A., and Ku, W. H.-M. 1981, ApJ, 248, 429

Avni, Y. 1976, ApJ, 210, 642

Bazzano, A., Fusco-Femiano, R., La Padula, C., Polcaro, V. F., Ubertini, P., and Manchanda, R. K. 1984, ApJ, 279, 515

Bothun, G. D., Schommer, R. A., and Sullivan, W. T., III 1984, AJ, 89, 466

Butcher, J. A., *et al.* 1991, in preparation

Dotani, T., *et al.* 1987, Nature, 330, 230

Cowie, L. L., Henriksen, M., and Mushotzky, R. 1987, ApJ, 317, 593

Fusco-Femiano, R., Bazzano, A., Ubertini, P., Perotti, F., Quadrini, E., and Dean, A. J. 1990, in Workshop on Supercluster and Clusters of Galaxies and Environmental Effects, in press

Gaetz, T. J., Salpeter, E. E., and Shaviv, G. 1987, ApJ, 316, 530 (GSS)

Gorenstein, P., Fabricant, D., Topka, K, and Harnden, F. R., Jr. 1979, ApJ, 230, 26

Gould, R. J. 1980, ApJ, 238, 1026; Gould, R. J. 1981, ApJ, 243, 677 (errata)

Hayashida, K., Inoue, H., Koyama, K., Awaki, H., Takano, S., Tawara, Y., Williams, O. R., Denby, M., Stewart, G. C., Turner, M. J. L., Makishima, K., and Ohashi, T. 1989, PASJ, 41, 373

Henriksen, M. J., and Mushotzky, R. F. 1986, ApJ, 302, 287

Hughes, J. P. 1989, ApJ, 337, 21

Hughes, J. P., Gorenstein, P., and Fabricant, D. 1988, ApJ, 329, 82

Hughes, J. P., Yamashita, K., Okumura, Y., Tsunemi, H., and Matsuoka, M. 1988, ApJ, 327, 615

Karzas, W., and Latter, R. 1961, ApJS, 6, 167

Kellogg, E., Baldwin, J. R., and Koch, D. 1975, ApJ, 199, 299

Kennicutt, R. C., Bothun, G. D., and Schommer, R. A. 1984, AJ, 89, 1279

Kondo, H., *et al.*, in preparation

Lampton, M., Margon, B., and Bowyer, S. 1976, ApJ, 208, 177

Makino, F., and the Astro-C team 1987, Astrophys. Lett. and Communications, 25, 223

Matteson, J.L. 1971, Ph. D. Thesis, University of California, San Diego

Maxon, M. S., and Corman, E. G. 1967, Phys. Rev., 163, 156

Mushotzky, R. 1991, in Proceedings of the NATO ASI on Clusters and Superclusters of Galaxies, p. 91

Okumura, Y., Tsunemi, H., Yamashita, K., Matsuoka, M., Hayakawa, S., Masai, K., and Hughes, J. P. 1988, PASJ, 40, 639

Ponman, T. J., Bertram, D., Church, M. J., Eyles, C. J., Watt, M. P., Skinner, G. K., Willmore, A. P. 1990, Nature, 347, 450

Rephaeli, Y. 1978, ApJ, 225, 335

Raymond J. C., and Smith, B. W. 1977, ApJS, 35, 419

Salem, S. I., Panossian, S. L., and Krause, R. A. 1974, Atomic Data and Nuclear Data Tables, 14, 91

Turner, M. J. L., *et al.* 1989, PASJ, 41, 345

Warwick, R. S., and Stewart, G. C. 1989, in Proceedings of the 23rd ESLAB Symposium on Two Topics in X-Ray Astronomy, ESA SP-296, Vol. 2, p. 727

Watt, M. P., Ponman, T. J., Bertram, D., Eyles, C. J., Skinner, G. K., Willmore, A. P. 1992, MNRAS, in press

Zabludoff, A. I., Huchra, J. P., Geller, M. J. 1990, ApJS, 74, 1

FIGURE CAPTIONS

Fig. 1 – *Top panel:* *Ginga* X-ray spectrum of the Coma cluster with best fit isothermal RS model. *Bottom panel:* Residual spectrum (observed data minus best fit model).

Fig. 2 – Incident photon spectrum of the Coma cluster from the best fit isothermal RS model.

Fig. 3 – Results of fits to the *Ginga* X-ray spectrum of Coma. Two dimensional χ^2 contours at the 90% confidence level for fractional iron abundance versus temperature using the isothermal RS model. The five curves correspond to the five datasets with systematic variations in the background subtraction and detector gain. The bold curve corresponds to nominal gain and background subtraction.

Fig. 4 – *Top panel:* Average *Ginga* collimator transmission as a function of radial distance from the center of the Coma cluster. *Bottom panel:* Average transmission times the area at each radius (dotted curve) and the product of that curve with the X-ray surface brightness of Coma (solid curve). The vertical dashed line at $14\overset{\prime}{.}2$ is the average effective radius of this observation.

Fig. 5 – Results of fits to a nonisothermal temperature model, consisting of an isothermal core surrounded by a polytropic distribution. We display two dimensional χ^2 contours at the 90% confidence level for the temperature of the isothermal region (T_{iso}) versus its radius (R_{iso}) in units of the core radius. The five curves correspond to the five datasets with systematic variations in the background subtraction and detector gain. The bold curve corresponds to nominal gain and background subtraction. The cross designates the allowed region of parameter space from the combined analysis of *Tenma* and EXOSAT X-ray spectra.

Fig. 6 – Ratio of total mass (within 2 Mpc) of iron relative to hydrogen (relative to the cosmic value of 4.0×10^{-5}) versus the core radius for the spatial distribution of iron atoms. For each iron core radius plotted, the range in mass ratios comes from the allowed range in β_{Fe} at 90% confidence. The mass ratio corresponding to the best-fit β_{Fe} at each iron core radius is plotted as an $\times$. The uniform iron abundance value of 0.238 is shown as the dotted line.

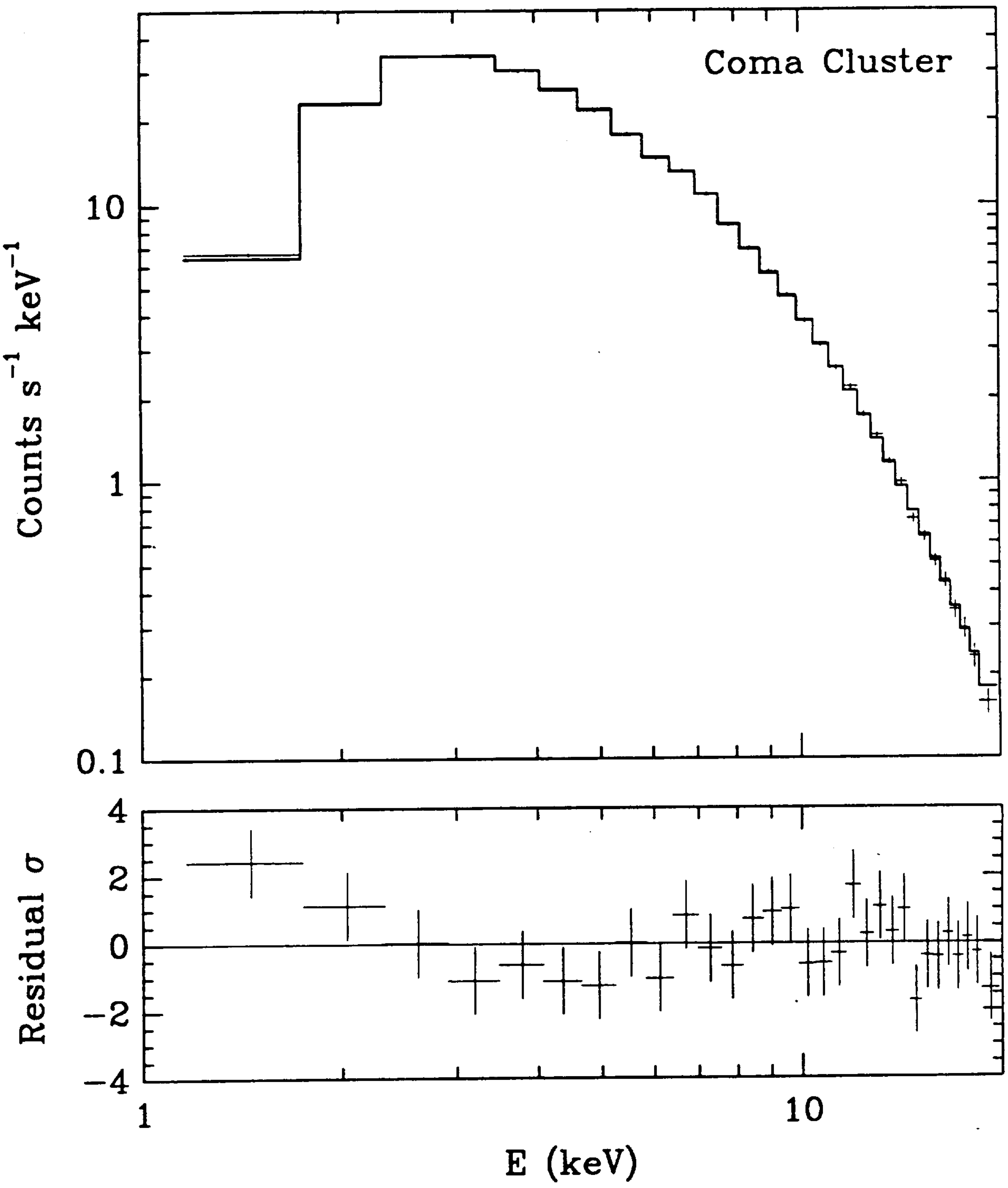

Figure 1

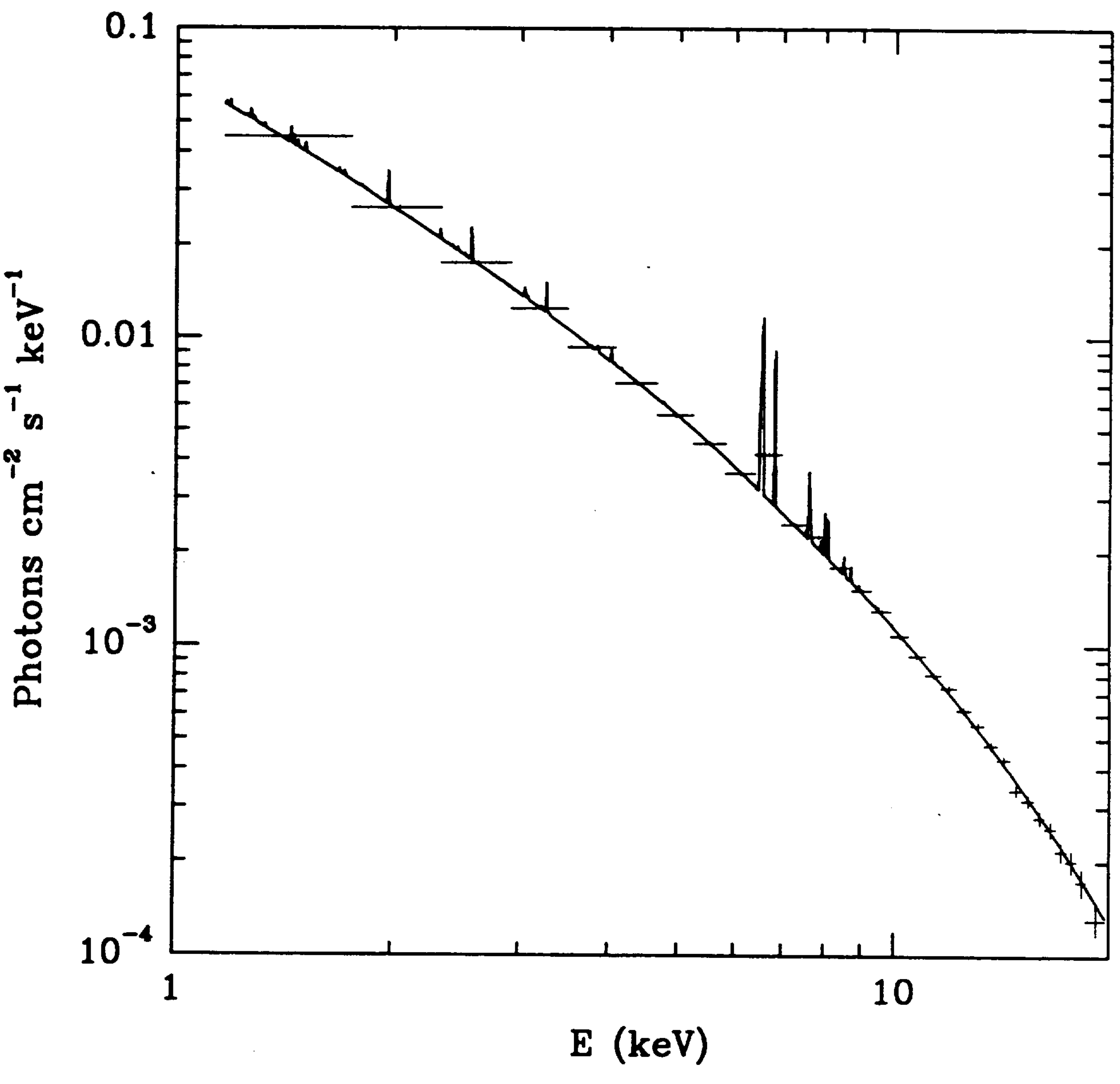

Figure 2

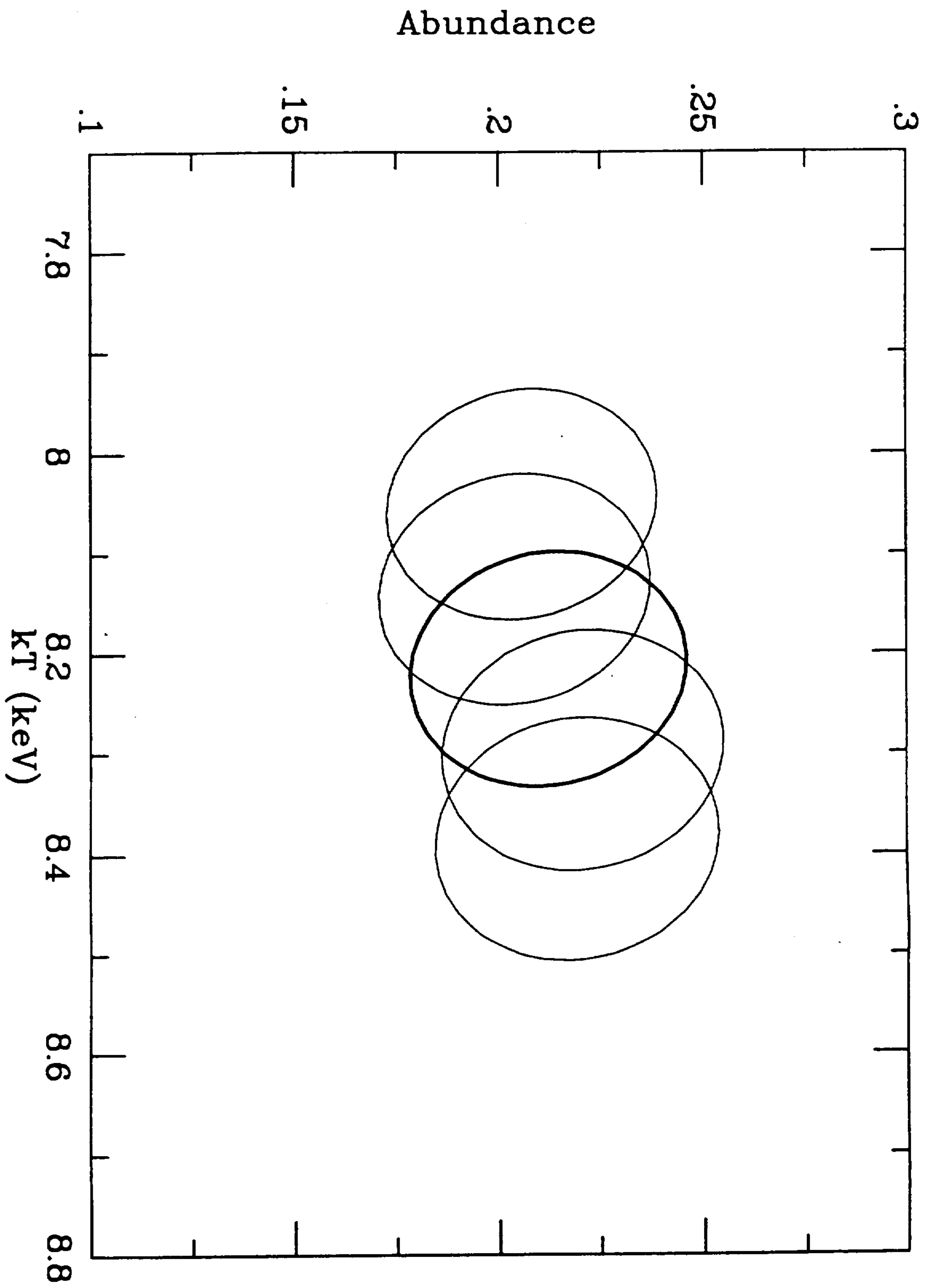

Figure 3

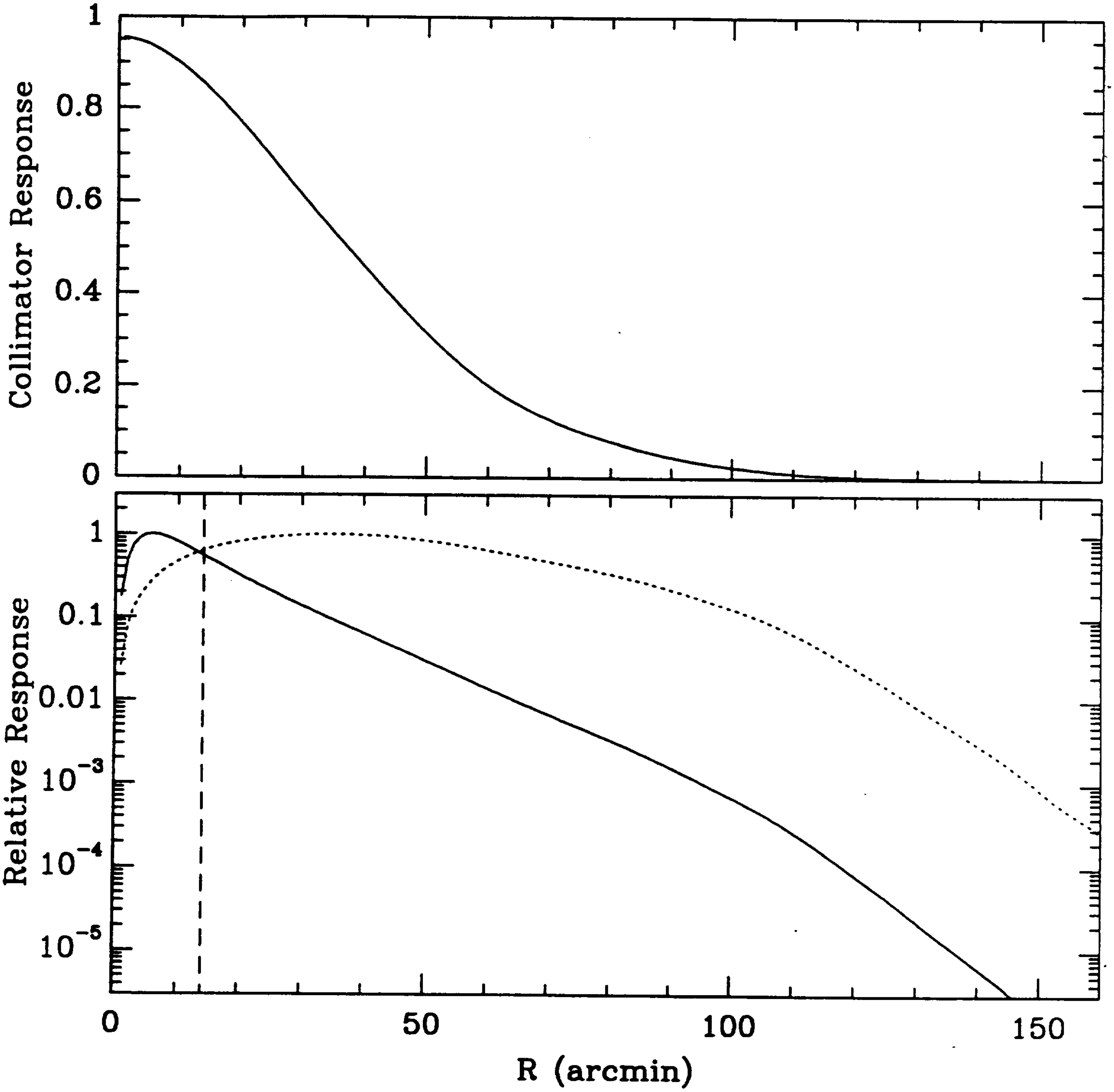

Collimator Response
1
0.8
0.6
0.4
0.2
0
Relative Response
1
0.1
0.01
10^{-3}
10^{-4}
10^{-5}
0
50
100
150
R (arcmin)

Figure 4

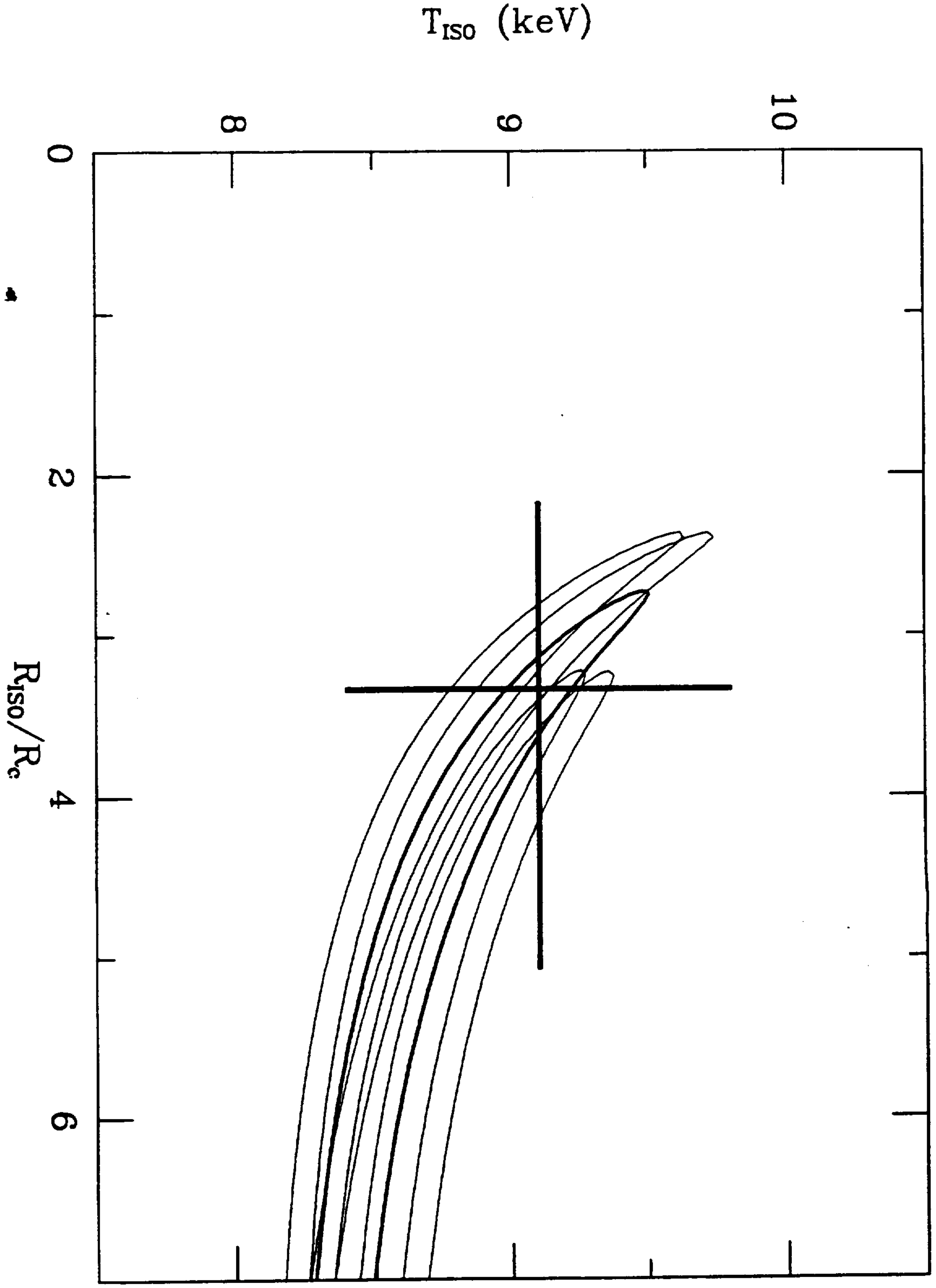

Figure 5

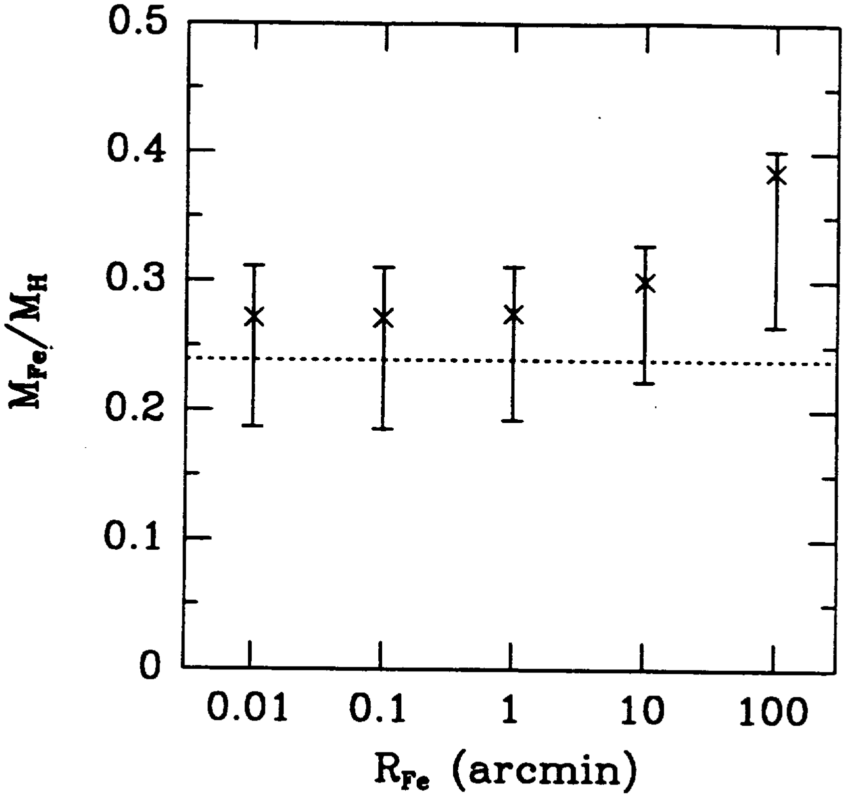

Figure 6

Harvard-Smithsonian
Center for Astrophysics

Preprint Series

No. 3676
(Received July 21, 1993)

A MEASUREMENT OF THE HUBBLE CONSTANT FROM THE X-RAY PROPERTIES AND THE SUNYAEV-ZEL'DOVICH EFFECT OF ABELL 2218

M. Birkinshaw and J.P. Hughes
Harvard-Smithsonian Center for Astrophysics

To appear in
The Astrophysical Journal

HARVARD COLLEGE OBSERVATORY SMITHSONIAN ASTROPHYSICAL OBSERVATORY
60 Garden Street, Cambridge, Massachusetts 02138

Center for Astrophysics
Preprint Series No. 3676

A MEASUREMENT OF THE HUBBLE CONSTANT FROM THE X-RAY PROPERTIES AND THE SUNYAEV-ZEL'DOVICH EFFECT OF ABELL 2218

M. Birkinshaw and J.P. Hughes
Harvard-Smithsonian Center for Astrophysics

A MEASUREMENT OF THE HUBBLE CONSTANT FROM THE X-RAY PROPERTIES AND THE SUNYAEV-ZEL'DOVICH EFFECT OF ABELL 2218

M. Birkinshaw and J.P. Hughes

Harvard-Smithsonian Center for Astrophysics
60 Garden Street, Cambridge, MA 02138, U.S.A.

To appear in *The Astrophysical Journal*

Keywords: Cosmic Background Radiation; cosmology; X-rays: sources; Galaxies: intergalactic medium; Galaxies: clustering.

ABSTRACT

The distance of the cluster of galaxies Abell 2218, and hence the value of the Hubble constant, has been measured by comparing the X-ray properties and the Sunyaev-Zel'dovich effect of the cluster. The result for the Hubble constant is $H_0 = 65 \pm 25\ \mathrm{km\,s^{-1}\,Mpc^{-1}}$, where the error includes the random and systematic errors, combined in quadrature, and the largest contributions to the overall error come from systematic errors in the Sunyaev-Zel'dovich effect data and in the X-ray spectrum of the cluster. The X-ray and Sunyaev-Zel'dovich effect data are consistent with the same model for the intergalactic medium in Abell 2218 (an isothermal β model with $\beta \approx 0.65$ and cluster core radius ≈ 1.0 arcmin). A previous report of a smaller Hubble constant, found by applying the same method on the same cluster, is shown to be based on a model for the cluster gas that is inconsistent with the *Einstein* IPC data. The present result for the Hubble constant is consistent with the value found earlier for the cluster Abell 665: by combining the results of the method for both clusters we conclude that the value of the Hubble constant is $H_0 = 55 \pm 17\ \mathrm{km\,s^{-1}\,Mpc^{-1}}$.

1. INTRODUCTION

The uncertainty in the value of the Hubble constant ($H_0 = 50 - 100\ \mathrm{km\,s^{-1}\,Mpc^{-1}}$) reflects not the quoted errors on the values estimated by different workers, but rather the spread of those independent estimates. Since the spread of values is much wider than the typical errors quoted, there remain large, unrecognized, systematic errors in some or all of the published values. Under these circumstances, a variety of non-standard ('astrophysical') approaches have been used in the attempt to measure H_0. These methods derive distances for distant objects directly, from an understanding of the physics responsible for the observed properties of those objects. Among these methods is one that measures the distance of a cluster of galaxies by comparing its X-ray emission, which is the thermal radiation from hot gas in the cluster, with its Sunyaev-Zel'dovich effect, the reduction in the brightness of the microwave background radiation caused by inverse-Compton scattering by electrons in the hot gas, (Gunn 1978; Silk and White 1978; Birkinshaw 1979; Cavaliere *et al.* 1979).

Recent improvements in the Sunyaev-Zel'dovich effect data (Birkinshaw, Gull & Hardebeck 1984; Uson 1986; Birkinshaw *et al.* 1993), and in the X-ray spectroscopy of the distant ($z > 0.1$) clusters of galaxies for which good Sunyaev-Zel'dovich effect scans have been measured (McHardy *et al.* 1990; Hughes & Tanaka 1992), have allowed this method of estimating the value of the Hubble constant to be used for two clusters of galaxies. For the first, Abell 665, Birkinshaw, Hughes & Arnaud (1991) found $H_0 = (40\text{ to }50) \pm 12\ \mathrm{km\,s^{-1}\,Mpc^{-1}}$ (including an assessment for possible systematic errors), which tends to support the long ($H_0 \approx 50\ \mathrm{km\,s^{-1}\,Mpc^{-1}}$) distance scale of the Universe. For the second cluster, Abell 2218, McHardy *et al.* (1990) found $H_0 = 24^{+23}_{-10}\ \mathrm{km\,s^{-1}\,Mpc^{-1}}$. However, this estimate did not use the best recent Sunyaev-Zel'dovich effect data, and appears to have used an inconsistent modelling of the intracluster medium in deriving this value of H_0 (Birkinshaw *et al.* 1991). The purpose of the present paper is to re-estimate the value of H_0 based on the data for Abell 2218, making use of the best recent Sunyaev-Zel'dovich effect data, and with a fully-consistent treatment of the intracluster medium in Abell 2218.

Although the errors on measurements of the Hubble constant using this method are large ($\gtrsim 25$ per cent), the method is valuable since it can be applied directly at redshifts > 0.1. The more standard methods of measuring H_0, which are applied at redshifts < 0.03, are subject to large sampling errors from the small volume of the Universe lying in this range of redshift. The importance of a global estimator of the Hubble constant is evident in the result of Turner, Cen & Ostriker (1992) that even if all the galaxies with $z \lesssim 0.025$ were surveyed and used in an H_0 measurement, the 95 per cent confidence range on the resulting value of H_0 would be $50 - 128\ \mathrm{km\,s^{-1}\,Mpc^{-1}}$ (if the true value of $H_0 = 80\ \mathrm{km\,s^{-1}\,Mpc^{-1}}$) because this volume represents too small a sample of the Universe to average effectively over the gravitationally-induced motions of the galaxies that it contains.

Abell 2218 lies at a redshift of 0.171 (Dressler & Spinrad private communication), and because of its richness (Abell richness class 4: Abell 1958) it has been well-studied in the X-ray (by *Einstein* imaging, and *Ginga* spectroscopy; McHardy *et al.* 1990), in the optical (Dressler 1978a, 1978b; Dressler & Spinrad private communication), and in the Sunyaev-Zel'dovich effect (Birkinshaw 1990 and references therein, Birkinshaw *et al.* 1993). The center of the galaxy distribution in the cluster was found (Birkinshaw 1979) to be $16^{\mathrm{h}}35^{\mathrm{m}}37^{\mathrm{s}}$, $+66^\circ 18' 30''$ (B1950), with an error of about 30 arcsec in each coordinate, and the galaxy distribution does not appear to show strong subcondensations in position (Birkinshaw 1979) or velocity (Dressler & Spinrad, private communication). The velocity dispersion of the cluster, $\sigma_z \approx 1350\ \mathrm{km\,s^{-1}\,Mpc^{-1}}$ (Dressler & Spinrad) is comparable with that of other rich clusters and is consistent with the large gravitating mass required to confine a hot, X-ray-emitting, atmosphere.

In Section 2 the data on Abell 2218 are reviewed, with particular emphasis on the critical systematic errors that may remain in the data. The X-ray images and Sunyaev-Zel'dovich effect data are fitted to models for the intracluster atmosphere in Section 3, where a value for the Hubble constant is derived. Section 4 discusses the differences between the present treatment and that of McHardy *et al.* (1990), identifying the cause of the discrepancy in the H_0 estimates, and combines the new result for H_0 with that derived earlier for Abell 665 (Birkinshaw *et al.* 1991) to produce a best overall result.

2. THE DATA

2.1 Sunyaev-Zel'dovich effect data

Abell 2218 has been observed more frequently in the Sunyaev-Zel'dovich effect than has any other cluster, and in consequence the published results for Abell 2218 have often been used to illustrate the level of inconsistency in the independent measurements. However, the most recent measurements of the Sunyaev-Zel'dovich effect are in better agreement (see Birkinshaw 1990; Birkinshaw *et al.* 1993), which suggests that the current observational results are sufficiently reliable for strong astrophysical and cosmological conclusions to be based on the data.

The most extensive Sunyaev-Zel'dovich effect data for Abell 2218 are those of Birkinshaw *et al.* (1993). These data were obtained through several years of observation over the period 1983–1990 using the OVRO 40-m telescope at 20.3 GHz. In the 'microwave background' configuration that was used, the 40-m telescope provides two 1.78-arcmin FWHM beams separated by 7.15 arcmin in azimuth. Data were taken using both beam-switching and position-switching in a 7-point scan down the declination axis and through the center of the cluster (taken from the galaxy-count result of Birkinshaw 1979). The details of the experimental method, and a discussion of the sources of both random and systematic error in the data, have been given by Birkinshaw *et al.* (1993), which should be consulted for a detailed discussion of the observations.

The data collected from the 40-m telescope during the best weather conditions were selected and averaged to produce the results given in Table 1 and plotted in Figure 1. Brightness temperature ($\Delta T_{\rm RJ}$) values are reported both with and without corrections for contaminating radio sources near Abell 2218: it can be seen that the magnitudes of these corrections are small (less than the errors on the measurements) at all points except point e, which lies 2 arcmin north of the cluster center. The $\Delta T_{\rm RJ}$ values represent the brightness temperature differences between points in the scan and reference arc regions (7.15-arcmin distant from these points) which are sampled by the "off" positions in the beam and position-switching scheme. The varying weights at which different parallactic angles within these arcs are sampled cause the $\Delta T_{\rm RJ}$ values in Table 1 to be complicated functions of the underlying Sunyaev-Zel'dovich effect of Abell 2218.

The major contributions towards the systematic errors given in Table 1 are listed below. More complete descriptions of the sources of these errors and of the methods used to estimate their sizes are given in Birkinshaw *et al.* (1993), but some description of these errors is necessary here to elucidate later descriptions of the uncertainties underlying the value of the central Sunyaev-Zel'dovich effect in the cluster and the value of the Hubble constant. The most important sources of error are those that are coherent across the scan, and hence have large effects on fits of models to the data.

(1) The most serious of these errors is the uncertainty in the zero level of the scan, estimated to be -43 ± 25 μK (see Birkinshaw *et al.* 1993). This offset is represented by the dotted lines in Figure 1, and might be caused by differential spillover effects.

(2) A second coherent error is caused by the uncertainty in the efficiency of the 40-m telescope, which causes the brightness temperature scale in Table 1 and Fig. 1 to be uncertain by a factor 1.00 ± 0.06.

Systematic errors which are not coherent across the scan will in general have smaller effects on the parameters estimated by fitting models to the data, unless they appear at points with large 'leverage' on those parameters. Into this class fall the following errors.

(3) Errors caused by the uncertainty in the flux-density to brightness temperature conversion used in the correction for contaminating radio sources. The only significant error from this cause arises for point e (2 arcmin north of the nominal cluster center) for which the measurement is contaminated by radio emission from Moffet & Birkinshaw (1989)'s source 16. A contribution of ± 22 μK to the error in Table 1 has been assessed from this cause.

(4) A significant contribution to the systematic error, of about ± 16 μK, arises at each point because of the possibility that radio sources which were not detected in the Moffet & Birkinshaw (1989) survey might be affecting the apparent brightnesses in Table 1.

(5) Where the Sunyaev-Zel'dovich effect of the cluster has a large gradient, or where the scan point lies near a radio source, small pointing errors in the telescope can cause significant variations in the detected signal. The size of this systematic error is estimated to vary from ± 1 μK for source-free points far from the central Sunyaev-Zel'dovich effect peak in the cluster to ± 20 μK for point e, where both the proximity of the radio source and the gradient in the Sunyaev-Zel'dovich effect contribute appreciably to the error.

(6) The apparent random error for each point has also been increased by a factor to take account of the discordance in the data from year-to-year. This factor, which varies between 1.00 and 1.51, is intended to take some account of the variations in the data due to instrumental effects or other, unknown, effects, which varied from season to season of the observations.

Even when all these systematic errors are taken into account, the Sunyaev-Zel'dovich effect in Abell 2218 is clearly highly significant (Fig. 1), and strongly peaked near the center of the optical cluster. The apparent angular size of the Sunyaev-Zel'dovich effect in Fig. 1 is about 2 arcmin, which is close to the FWHM of the 40-m telescope (1.78 arcmin) — the Sunyaev-Zel'dovich effect is not well resolved in these data. This does *not* imply that the FWHM of the Sunyaev-Zel'dovich effect from the atmosphere of Abell 2218 is about $(2^2 - 1.78^2)^{1/2} = 0.9$ arcmin, since the beam-switching method of observing with the 40-m telescope causes components of the Sunyaev-Zel'dovich effect on angular scales greater than the beam-switching scale (7.15 arcmin) to be subtracted out. The structure of the atmosphere can be determined from these data only after careful fits that take the observational sampling explicitly into account: in general, the subtraction caused by the beam-switching causes the Sunyaev-Zel'dovich effect data to be less sensitive than the X-ray images to the overall structure of the atmosphere of Abell 2218.

2.2 X-ray images

Abell 2218 was observed by both imaging instruments on board the *Einstein* Observatory. The imaging proportional counter (IPC) imaged the cluster for 3398.6 s (live-time corrected exposure) on 1979 February 25. The high resolution imager (HRI) was pointed toward Abell 2218 for 39283.3 s (live-time corrected exposure) on 1979 April 19. We utilize both of these datasets in our analysis. Although the IPC observation is relatively short, the cluster is clearly detected and its surface brightness remains above the background level out to a radius of about 4.5$'$ from the cluster center. The HRI data are of higher angular resolution, but their usefulness in constraining the structural parameters of the diffuse cluster emission is limited by that instrument's higher intrinsic background and smaller effective area. In the HRI data, the X-ray surface brightness from A2218 exceeds the instrumental background only within a radius of about 40$''$ from the center of the cluster.

The IPC was a low-background gas-filled device capable of producing images (with spatial resolution of 36$''$) and spectra (with energy resolution $\Delta E/E \sim 1$ at 1 keV) in the 0.15 – 4.5 keV X-ray band. For the imaging analysis of Abell 2218 the range of observed photon energies was restricted to 0.8 – 3.5 keV (PI bins 5 – 10). This reduced the average level of the background (which contains a strong soft component) and decreased the sensitivity of the fitted electron number density in the cluster to the value of the line-of-sight hydrogen column density. Background was subtracted using the two standard background template maps: DSMAP, the sum of a large number of deep survey observations with bright sources removed, and BEMAP, an image of the bright Earth. The DSMAP was scaled to the Abell 2218 image using the ratios of the live times on the cluster and the deep surveys, and the remaining background was subtracted by scaling the BEMAP to the number of counts in the entire field of the image that lies more than 16 arcmin from the cluster center (as described in detail in Birkinshaw, Hughes, and Arnaud 1991). The resulting image (using this nominal background subtraction) is shown in Figure 2a, where gaussian smoothing ($\sigma = 36''$) has been applied to the data to reduce statistical fluctuations. The effect of systematic errors in background subtraction was studied by varying the amount of the DSMAP subtracted by ±20% and redetermining the BEMAP scaling. Including an uncertainty caused by the errors in the background subtraction, the counting rate of the cluster in 0.8 – 3.5 keV within a radius of 8 arcmin of the center is $0.161 \pm 0.009\ \mathrm{s}^{-1}$ (1σ error).

The HRI was a micro-channel plate detector for broad-band imaging at high spatial resolution (roughly 4$''$) but with no intrinsic energy resolution, and with much lower sensitivity to diffuse X-ray emission than the IPC. In the central region of the detector the background was fairly spatially uniform. Two techniques were employed for estimating background in the Abell 2218 observation. In the first, the annular region 4$'$ to 6$'$ from the cluster center was fitted with a uniform background model assuming no cluster emission.

Then the region within 4′ was modeled with both this background level (held fixed) and emission from an isothermal-β cluster model. The parameters of the cluster model were adjusted to obtain the best fit. The emission from this cluster model was extrapolated to the 4′ to 6′ annular region and a new background estimate was made. This procedure was iterated until the change in background rate was less than the statistical uncertainty; in fact only a single iteration was necessary. The second technique estimated the background by examining the annular region from 8′ to 10′ and assuming it to be source free. Both techniques yielded consistent values for the background of $(5.20 \pm 0.05) \times 10^{-3}$ counts s^{-1} $arcmin^{-2}$. The resulting background-subtracted HRI image, smoothed by a gaussian with $\sigma = 16''$ is shown in Figure 2b. Within a radius of 4′, the HRI counting rate of the cluster is 0.0509 ± 0.0037 s^{-1} (1σ error, including the background subtraction uncertainty).

These images of A2218 show a smooth, symmetric distribution of X-ray emission, with no evidence for a strong central point source or surface brightness spike, as might arise from the presence of a cooling flow. Our detailed fits, discussed below, confirm these qualitative impressions and allow us to demonstrate consistency between the two data sets.

2.3 X-ray spectrum

A *Ginga* X-ray spectrum of Abell 2218 has been observed and analyzed by McHardy *et al.* (1990). Since the large area counters (LAC) on board *Ginga* which produced this spectrum were insensitive to levels of interstellar absorption less than about several times 10^{21}, McHardy *et al.* fixed the absorption at the galactic value of 3×10^{20} cm^{-2} (Stark *et al.* 1984). Their analysis showed that the spectrum was consistent with an isothermal plasma model with

$$T_e = 6.7 \pm 0.45 \text{ keV} \tag{1}$$

$$\text{metallicity} = 0.2 \pm 0.2 \text{ solar} \tag{2}$$

for the intergalactic gas in Abell 2218, where we have replaced the errors on the estimate of the electron temperature, T_e given by McHardy *et al.* (1990) by a symmetrical error bound. Results (1) and (2) are fully consistent with the independent analysis of the same *Ginga* data performed by Hatsukade (1989).

The result (1) for the temperature of the intracluster gas in Abell 2218 is sensitive to the uncertain background count rate in the *Ginga* LAC. McHardy *et al.* suggest that the largest plausible error in the background might cause the estimate of the electron temperature to be in error by about 2 keV. We will assume, therefore, that a systematic error at the level ±1 keV (at $\pm 1\sigma$) might be present in (1). This is similar to the error caused by the uncertain background subtraction estimated from the analysis of *Ginga* spectral data for Abell 665 (Hughes and Tanaka 1992), a cluster with a similar *Ginga* count rate to Abell 2218.

The *Einstein* IPC also produced an X-ray spectrum of the cluster, albeit over a lower energy band (0.2-4.0 keV) and with limited statistical precision. Because of the upper energy cutoff of the IPC band, this spectrum cannot provide a useful determination of the cluster temperature, but the lower energy band makes it useful for determining the line-of-sight absorbing column density, which is found to be

$$N_{\rm H} = 6.6^{+12.5}_{-4.7} \times 10^{20}\ {\rm cm}^{-2} \tag{3}$$

(with 90% errors) when we make use of the *Ginga* results for the temperature to specify the intrinsic spectrum of the cluster. The observed fluxes from the IPC and LAC for the spectral model given by (1), (2), and (3) are consistent to within the uncertainties of the background subtraction.

It was also possible to place a constraint on the absorbing column density from the ratio of IPC to HRI fluxes. Because the source is extended we could not simply take the ratio of observed count rates in the two instruments, but rather we compared the normalizations (N_X) from our fits to the X-ray images for the same isothermal β-model (see § 3.2), taking account of the differing background subtraction and spatial resolution functions. The ratio of the IPC and HRI normalizations is 3.05 ± 0.26 where the error includes uncertainty due to background subtraction and a 5% error in the relative normalization of the instruments both added in quadrature to the statistical error, and is not sensitive to the particular values choosen for the structural parameters.

We calculated the expected IPC/HRI ratios for a range of column density values assuming the spectral parameters (1) and (2). When the predicted values are compared to the observed ratio we constrain the column density to a value

$$N_{\rm H} = 6.5^{+5.0}_{-3.0} \times 10^{20}\ {\rm cm}^{-2} \tag{4}$$

where the (90%) errors have been increased to account for the uncertainty caused by the errors on T_e and metallicity, although for such high gas temperatures the ratio depends only weakly on these quantities.

Estimates (3) and (4) for the column density are not independent, so we are not justified in combining the results to reduce the errors. The best fit values are consistent so we will utilize the more precise result (4) in further analysis. This result indicates at about the 90% confidence level that the column density toward Abell 2218 is larger than the galactic value. Although we will not pursue further discussion of the astrophysical implications of this result (since it is not statistically significant), in § 4.1 we demonstrate its importance in determining the proper value and error range for the Hubble constant.

3. ANALYSIS

3.1 Models for the cluster gas

The analysis of these results to produce an estimate of the Hubble constant follows the analysis used for Abell 665 (Birkinshaw *et al.* 1991). That is, the X-ray image and the Sunyaev-Zel'dovich effect scan are fitted with the same isothermal β-model for the intracluster medium, and the results of these fits are used to calculate the normalizations of the models.

The isothermal β model for the cluster gas is described by an electron density distributed with radius in the cluster as

$$n_{\rm e} = n_{\rm e0} \left(1 + \frac{r^2}{r_{\rm cx}^2}\right)^{-\frac{3}{2}\beta} \tag{5}$$

and a constant electron temperature $T_{\rm e} = T_{\rm e0}$. Note particularly the assumption here that the cluster gas is distributed spherically, and that the intracluster medium is not clumpy. It can be shown (e.g., Sarazin 1984) that this model for the intracluster medium leads to an X-ray surface brightness distribution of the form

$$b_X(\theta) = N_X \sqrt{\pi} \frac{\Gamma(3\beta - \frac{1}{2})}{\Gamma(3\beta)} \theta_{\rm cx} \left(1 + \frac{\theta^2}{\theta_{\rm cx}^2}\right)^{\frac{1}{2}-3\beta} \tag{6}$$

and a Sunyaev-Zel'dovich effect of the form

$$\Delta T_{\rm RJ}(\theta) = N_{\rm RJ} \sqrt{\pi} \frac{\Gamma(\frac{3}{2}\beta - \frac{1}{2})}{\Gamma(3\beta)} \theta_{\rm cx} \left(1 + \frac{\theta^2}{\theta_{\rm cx}^2}\right)^{\frac{1}{2}-\frac{3}{2}\beta} \tag{7}$$

where θ is the angle from the center of the cluster, $\theta_{\rm cx}$ is the angular equivalent of the core radius $r_{\rm cx}$, and $N_{\rm X}$ and $N_{\rm RJ}$ are normalization constants.

Fits to the X-ray surface brightness and the Sunyaev-Zel'dovich effect of a cluster can use (6) and (7) to estimate several structural parameters: the location of the center of the cluster in RA and declination (although it is clear that the one-dimensional scan in the Sunyaev-Zel'dovich effect will not produce any useful constraint on the RA position the cluster center), the angular core radius of the cluster, $\theta_{\rm cx}$, and the β parameter that describes the concentration of the density profile. The two normalizations $N_{\rm X}$ and $N_{\rm RJ}$ can also be fitted from the data.

Birkinshaw *et al.* (1991) showed that the angular diameter distance of the cluster can be obtained from the normalizations $N_{\rm RJ}$ and $N_{\rm X}$ using

$$D_{\rm A} = \left(\frac{N_{\rm RJ}^2}{N_{\rm X}}\right) \left(\frac{m_{\rm e}c^2}{k_{\rm B}T_{\rm e0}}\right)^2 \frac{\Lambda_{\rm e0}}{16\pi\, T_{\rm r}^2\, \sigma_{\rm T}^2 (1+z)^3} \tag{8}$$

where Λ_{e0} is the X-ray spectral emissivity of the cluster gas (calculated over the emitted energy range appropriate to the energy range of the X-ray detector), σ_T is the Thomson scattering cross-section, k_B is the Boltzmann constant, c is the speed of light, m_e is the electron mass, $z = 0.171$ is the redshift of the cluster gas, and $T_r = 2.74$ K (Mather *et al.* 1990) is the thermodynamic temperature of the microwave background radiation. In deducing (8) it has been assumed that the cluster is at rest in the Hubble flow, since any motion of the cluster can cause an additional contribution (with the same angular dependence as equation 7) to the Sunyaev-Zel'dovich effect (e.g., Rephaeli & Lahav 1991).

Fits to the data will be made based on (6) and (7), with the X-ray fit taken to be of primary importance since the two-dimensional X-ray image will provide far better structural information than will the one-dimensional (and noisier) Sunyaev-Zel'dovich effect scan. The results for the location of the center of the cluster, β, and θ_{cx} from the X-ray fit are then used to demonstrate consistency with the Sunyaev-Zel'dovich effect scan, and the normalizations from the two sets of fits are used to calculate D_A and hence the value of the Hubble constant.

3.2 Fits to the X-ray images

The *Einstein* IPC and HRI images for Abell 2218 were fitted in the same way as was the IPC image of Abell 665 in Birkinshaw *et al.* (1991). That is, a maximum-likelihood estimator was used to find the best-fitting cluster center, β, θ_{cx}, and N_X and to generate confidence intervals for these parameters. Since maximum-likelihood estimators do not produce goodness of fit statistics, the quality of the fit that was obtained was estimated by applying the Kolmogoroff-Smirnov test to the cumulative distribution of counts in the image, and by making a χ^2 test of the best-fit radial distribution.

Good fits were found to both the IPC and the HRI X-ray images of Abell 2218, with consistent centers for the atmosphere: $16^h35^m42.8^s$, $+66°18'44.5''$ from the IPC fit, and $16^h35^m41.3^s$, $+66°18'28.0''$ from the HRI with statistical errors of about $10''$ for each. Within the errors, these are consistent with the center of the galaxy distribution in the cluster, $16^h35^m37^s \pm 12^s$, $+66°18'30'' \pm 30''$, but are strongly inconsistent with the location of the cluster center in right ascension determined by Klein *et al.* (1991) from their Sunyaev-Zel'dovich effect data, $16^h35^m26^s$. (A fit to the X-ray data using the Klein *et al.* center for the cluster also produces values of β and r_{cx} which would be unusual for a cluster atmosphere, and which would cause a bad fit to the Sunyaev-Zel'dovich effect data of Fig. 1.)

Confidence-level contours for fits to the IPC data are shown in Figure 3: it can be seen that the best-fit model has $\beta = 0.65$ and $\theta_{cx} = 1.0$ arcmin. These results are not sensitive to variations in the background subtraction or to the region of the detector over which the fit was performed. Varying the background by ±20% (as outlined in § 2.2) changed the best fit core radius by at most ±0.05 arcmin while the value of β changed by ±0.02. Decreasing the radius of the fitted region in the detector from the nominal value (of 16′) to 8′ reduced θ_{cx} by 0.06 arcmin and β by 0.015. These values are much smaller than the statistical errors associated with the fits, of (-0.25 to +0.33) arcmin in θ_{cx} and of (-0.05 to +0.09) in β (90% confidence ranges).

We note that the derived core radius of the cluster is similar in value to the spatial resolution of the IPC, which has been modeled as a gaussian with $\sigma = 36''$. In practice the spatial resolution of the IPC is energy dependent and the value used corresponds to the on-axis spatial resolution of the IPC for pulse height channel 7 (Harnden *et al.* 1984), which is at the middle of the range of pulse height channels we accept. Over this range of pulse heights the variation in sigma is roughly 10%, which when used to fit the IPC data introduces an uncertainty of ± 0.10 arcmin in θ_{cx} and ± 0.015 in β. Again this systematic error is much smaller than the statistical error.

The fractional error on the X-ray normalization, N_X, including systematics due to background subtraction and the uncertain spatial resolution, is 7.6% (at 90% confidence), where the error is also dominated by the statistical uncertainty.

The left panel in Figure 4 shows a comparison between the best fit model and the azimuthally-averaged radial profile of the IPC data about the best fit cluster center. The value of χ^2 from this comparison is 61.5 for 25 degrees of freedom. Most of the deviation comes from the last six data points where the background dominates the signal; excluding them reduces the χ^2 to 24.2 for 19 degrees of freedom. As mentioned above, our fits are not sensitive to reducing the radius of the fitting region by even as much as a factor of two. The data and model extracted from separate quadrants of the image were also compared. There was no evidence for a deviation from azimuthal symmetry.

Although the HRI image of Abell 2218 contains far more counts than the IPC image, the determination of β and θ_{cx} based on the HRI data is much less precise than with the IPC. For nominal background subtraction (determined as discussed in §2.2), fitting over the central 4 arcmin radius of the cluster, we derive values of $\beta = 0.59(-0.10, +0.16)$ and $\theta_{cx} = 1.00(-0.30, +0.42)$ arcmin. These parameters are consistent with the results of the IPC fit at about the 90% confidence level. The right panel in Figure 4 shows the radially summed HRI data compared to the data: the corresponding value of χ^2 is 48.9 for 50 degrees of freedom. A comparison of the data and model in quadrants again shows no significant deviation from azimuthal symmetry. Note from Figure 4 the dominant effect of background on the HRI data: the structural parameters of the cluster derived from the HRI image are less certain than those based on the IPC image because the cluster emission is an appreciable fraction of the background to fewer core radii in the HRI data.

Fits based on the HRI data were somewhat sensitive to variations in the background subtraction and the region of the detector over which the fit was performed. Varying the background by $\pm 1.8\%$, which is the statistical error on the uniform background level, changed the best fit core radius by $(-0.11, +0.07)$ arcmin while the value of β changed by ± 0.06. Increasing the radius of the fitted region in the detector from the nominal value of 4′ to 8′ increased θ_{cx} by 0.09 arcmin and β by 0.04. The spatial response of the HRI was modeled as a double exponential with scale lengths of 2 arcsec and 12 arcsec (Henry and Henriksen 1986). Errors in this response model introduce only insignificant variations in the fitted structural parameters of the cluster since the width of the point response function is much less than the angular size of the cluster.

The value of 0.65 derived for β is close to that found earlier for Abell 665 ($\beta = 0.66$; Birkinshaw *et al.* 1991), and is in the range that is normal for a rich X-ray cluster. Formally, however, $\beta = 0.65$ is not a permissible value, since it corresponds to $n_e \propto r^{-1.95}$ at large radius, and hence an infinite gas mass. This implies that some outer cutoff, $r_{\max}$ should be used for the model density distribution (5), but since the divergence is slow at large r, a large $r_{\max}$ cut-off ($r_{\max} \gtrsim 10 r_{\rm cx}$) will not have a significant effect on the shape of the X-ray or Sunyaev-Zel'dovich effect structures (equations 6 and 7). However there is some effect on the fitted normalizations, and hence the value of the Hubble constant, as discussed in § 4.2.

We fitted the IPC data with two independent isothermal-β models to search for evidence of substructure in the cluster. We tried a number of cases: (1) fixing the center of both components to the same position, (2) fixing $\theta_{\rm cx}$ and β to the same values, and (3) letting free the positions and structural parameters of both models. In no case was a significant reduction in the likelihood parameter obtained.

We examined the HRI image for evidence of a point source near the cluster center which might indicate the presence of a strong cooling flow in the cluster core. An improved fit to these data was obtained when we included a point source in addition to the cluster model. The point source was located 5.4″ west and 23.9″ south of the cluster center with an intensity of $6.4 \times 10^{-4}\ {\rm s}^{-1}$, about one per cent of the count rate of the cluster. The 3σ upper limit to the intensity of a point source near the cluster center is $1.3 \times 10^{-3}\ {\rm s}^{-1}$. The inclusion of the point source resulted in a reduction in the likelihood parameter of 10, a value which indicates that the introduction of the three additional free parameters is statistically significant at about the 98% confidence level, but the influence of this source on the normalization of the β-model atmosphere, and hence on the derived Hubble constant, is negligible.

The X-ray normalization enters linearly into the value of the Hubble constant, so that its overall error (of ±8 per cent at 90 per cent confidence) is not the limiting factor in the accuracy of our final result. If the value of the Hubble constant is taken to be $50\ {\rm km\,s^{-1}\,Mpc^{-1}}$, then the corresponding proton density at the cluster center is $n_{\rm p0} = 5.4 \times 10^{-3}\ {\rm cm}^{-3}$: other assumptions for H_0 cause this value to vary as $H_0^{1/2}$.

3.3 Fits to the Sunyaev-Zel'dovich effect scan

Since the Sunyaev-Zel'dovich effect data exist at only seven points on a north-south line through the optical center of the cluster, they cannot be used to obtain good estimates of the structural parameters of the β model atmosphere. In particular, no useful result on the RA of the cluster center is to be expected. After fixing the RA of the center of the atmosphere at $16^{\rm h}35^{\rm m}43^{\rm s}$, as suggested by the IPC image, the scan can be used to fit β, $\theta_{\rm cx}$, $N_{\rm RJ}$, and the declination of the cluster center. However, the small apparent angular size of the cluster (Fig. 1) indicates that only limits to the values of β and $\theta_{\rm cx}$ can be obtained from such fits: effectively only the FWHM of the cluster atmosphere, as sampled by the beam and position-switching system of the 40-m telescope can be estimated. However, the X-ray structural parameters $\beta = 0.65$, $\theta_{\rm cx} = 1.0$ arcmin, are found to be consistent with the Sunyaev-Zel'dovich effect data, and lead to good fits. We therefore adopt these values of β and $\theta_{\rm cx}$ in fitting the Sunyaev-Zel'dovich effect data for the declination of the cluster center and $N_{\rm RJ}$.

The best-fit center of the atmosphere found under these assumptions lies at $+66^\circ18'40''\pm20''$, consistent with both the X-ray and optical centers of the cluster, and this center produces a good fit to the data. Thus the simple isothermal β model for the cluster atmosphere (5) appears to provide an adequate description of the gas in Abell 2218. The corresponding value of $N_{\rm RJ}$ implies that the central Sunyaev-Zel'dovich effect in Abell 2218 is -0.62 ± 0.08 mK. The observed central decrement of -0.43 mK (Table 1) thus reflects the $\sim$ 60 per cent efficiency of the 40-m telescope in observing the Sunyaev-Zel'dovich effect in a cluster at this redshift.

In performing this fit, account has been taken of all the individual point errors, $\Delta T_{\rm syst}$, in the Sunyaev-Zel'dovich effect data, of the apparent offset, $\Delta T_{\rm zero}$, in the overall zero level of the scan data, and of the factor 1.00 ± 0.06 scale error. The individual point systematic errors, $\Delta T_{\rm syst}$, were combined with the random error in quadrature before the fits were performed. The zero level offset was taken into account by finding the variation in the results of the fits as $\Delta T_{\rm zero}$ changes, and the overall scale factor produces a final multiplicative error on the results of the fits. The overall result for $N_{\rm RJ}$ found in the Sunyaev-Zel'dovich effect fits carries an error of 13 per cent: from equation (8) we see that this will produce an error $\approx$ 25 per cent in the resulting estimate for the Hubble constant. Thus the uncertainties in the Sunyaev-Zel'dovich effect (which are dominated by those in the zero level and the scale error) are a major source of error in the estimate for the Hubble constant.

3.4 The value of the Hubble constant

Since the X-ray and Sunyaev-Zel'dovich effect data are consistent with the same, simple, spherical, isothermal, model for the gas in Abell 2218, the normalizations found in Secs 3.2 and 3.3 can be used to calculate the Hubble constant, with the assistance of equation (8). The results of this calculation are shown in Fig. 3, where contours of constant H_0 appear superimposed on the confidence level contours for β and $\theta_{\rm cx}$ found from the X-ray fit.

The best-fitting model on Fig. 3 has $H_0 = 65 \pm 19\ {\rm km\,s^{-1}\,Mpc^{-1}}$, where the error has been calculated from the error in $N_{\rm RJ}$, including both random and systematic components, and the error in $N_{\rm X}$, including random and systematic errors, but using only the result

(1) from McHardy *et al.* (1990) for the temperature of the gas. If account is taken of the possible ±1 keV systematic error in T_{e0} (Sec. 2.3), and of the dependence of the result for the Hubble constant on the values of the structural parameters β and θ_{cx} (Fig. 3), the overall result from this calculation is

$$H_0 = 65 \pm 25 \ \mathrm{km\,s^{-1}\,Mpc^{-1}}. \tag{9}$$

In this result, approximately ±15 $\mathrm{km\,s^{-1}\,Mpc^{-1}}$ of the error can be attributed directly to the systematic errors in N_{RJ} (principally from the zero level and gain errors), ±3 $\mathrm{km\,s^{-1}\,Mpc^{-1}}$ can be attributed to the systematic errors in N_X, and ±15 $\mathrm{km\,s^{-1}\,Mpc^{-1}}$ can be attributed to the ±1 keV systematic error in T_{e0}. Clearly improvements in the estimate (9) require further work on the Sunyaev-Zel'dovich effect data, and on the X-ray spectrum of the cluster.

4. DISCUSSION

4.1 Comparison with the results of McHardy *et al.*

The result (9) for the Hubble constant should be compared with McHardy *et al.* (1990)'s estimate

$$H_0 = 24^{+23}_{-10}\ \mathrm{km\,s^{-1}\,Mpc^{-1}} \tag{10}$$

based on the same method for the same cluster. The discrepancy between our result (9) and McHardy *et al.*'s result (10) is serious, and requires explanation if this method of deriving the value of the Hubble constant is to prove useful. A close examination of the two distinct calculations indicates that the difference between (9) and (10) consists of several parts

(1) the differences in the model used for the electron density, n_e, as derived from the HRI data by McHardy *et al.*, or from the IPC and HRI data in the present paper,

(2) McHardy *et al.*'s use of the Stark *et al.* (1984) value for the neutral hydrogen column density towards the cluster, which we find (Sec. 3.2) to be somewhat too low; and

(3) McHardy *et al.*'s use of a inconsistent description of the gas in comparing the X-ray surface brightness profile and the Sunyaev-Zel'dovich effect.

McHardy *et al.* derived the electron density in Abell 2218 based only on the HRI image. Figure 4 has demonstrated that these data are dominated by the background, so that small variations in the background subtraction will lead to large changes in the apparent structure of the X-ray emission from the cluster. No details of the background subtraction techniques are contained in McHardy *et al.*'s paper, so that our comparison of their results with ours are based solely on the derived density distributions.

The electron density model derived by McHardy *et al.* from the *Einstein* HRI data corresponds roughly to an isothermal-β model with $\beta = 0.5$ and $\theta_{cx} = 0.6$ arcmin, which is formally unacceptable from our fits to the IPC data. However, because of the low sensitivity of the HRI to extended X-ray emission (Fig. 4), McHardy *et al.* were unable to trace this X-ray emission beyond about 3 arcmin from the cluster center, so that they have no direct information on the outer part of the cluster atmosphere. This is important because about 25% of the total electron pressure integral (which appears in the expression for the Sunyaev-Zel'dovich effect from the cluster) originates in gas lying between 3 and 10 arcmin from the cluster center, where McHardy *et al.*'s extrapolation of the electron density distribution is unsupported by their X-ray data. Since the derived value of the Hubble constant depends on the square of the pressure integral (equation 8), this part of the cluster atmosphere contributes almost 60% of the value of the Hubble constant (10). By contrast, the approach of using the IPC data, followed in the present paper, allows the gas density profile to be traced out to a radius $\gtrsim 7$ arcmin. About 90% of the line-of-sight electron pressure integral arises from gas within this radius (if the electron distribution is assumed to extend to infinity), while 97% of the pressure integral within 10 arcmin is produced by gas whose distribution is directly sampled in the X-ray surface brightness profile (Fig. 4). The different structural models for the cluster used in the present paper and by McHardy *et al.* produces the largest single contribution to the discrepancy between results (9) and (10) for H_0: we find that McHardy *et al.*'s estimate of the line-of-sight integral of the electron pressure is about 31% less than our value.

An additional component of the discrepancy in the values of H_0 originates in McHardy *et al.*'s assumption that the column density to the cluster is given by the Stark *et al.* (1984) value. We have shown (Sec. 3.2) that this value is at the lower limit of acceptable values, as determined by fits to the low-energy X-ray spectrum. Since the HRI has no intrinsic energy resolution, and includes counts from X-ray photons with energies as low as 0.1 keV, the count rate measured using the HRI is more sensitive to the absorbing column density than is the count rate measured using the IPC. Furthermore, in our present analysis we have been able to use the intrinsic energy resolution of the IPC to perform our analysis using only counts corresponding to photon energies above 0.8 keV, where variations in the absorbing column have little effect on our results. The effect of McHardy *et al.*'s choice of the Stark *et al.* (1984) column towards Abell 2218 causes their integrated electron pressure to be underestimated by about 12%.

Combining these two effects, we can show that McHardy *et al.*'s estimate of the electron pressure integral (or, equivalently, any fiducial electron density in the cluster) will be about 48% smaller than our value. Since the value of the Hubble constant is proportional to the square of this pressure integral, we would expect McHardy *et al.*'s estimate of the Hubble constant to be too low by a factor of 2.1. This difference explains most of the discrepancy between the results (9) and (10).

The remaining part of the discrepancy comes from the normalization of the Sunyaev-Zel'dovich effect. Our present normalization is equivalent to a central Sunyaev-Zel'dovich effect of $\Delta T_0 = -0.62 \pm 0.08$ mK in Abell 2218, where this value was determined by fitting the same model atmosphere (with $\beta = 0.65$ and $\theta_{\rm cx} = 1.0$ arcmin; Sec. 3.1) that produces a good fit to the X-ray surface brightness. However, the normalization used by McHardy *et al.*, $\Delta T_0 = -0.69 \pm 0.10$ mK, was based on a fit by Birkinshaw (1986) to earlier Sunyaev-Zel'dovich effect data using models with $\beta = 0.5$ and $\theta_{\rm cx} < 1$ arcmin. This earlier value for the normalization is therefore based on a density model that is consistent with neither the model atmosphere derived from our present analysis of the X-ray structure of the cluster, nor with the model atmosphere of McHardy *et al.*, and we would not expect the use of this earlier normalization to produce a useful estimate of the Hubble constant. Thus McHardy *et al.*'s use of the normalization $\Delta T_0 = -0.69 \pm 0.10$ mK produces a further error in their estimate for H_0: we find that the McHardy *et al.* result would be an underestimate by a further 23%.

Combining all three factors, we calculate that the McHardy *et al.* result (10) is too low by a factor of about 2.6, because it was derived using an incorrect electron number density distribution and inconsistent models for the X-ray and Sunyaev-Zel'dovich effect data. If the result (10) is corrected by this factor, the result is consistent with our result (9).

4.2 The model-dependence of the value for the Hubble constant

In calculating the result (9) for the value of the Hubble constant, we have already included a systematic error (of $\pm 7\ \mathrm{km\,s^{-1}\,Mpc^{-1}}$ in quadrature) based on the the dependence of our estimate for H_0 on the parameters of the isothermal β models that we use to fit the X-ray emission. However, the choice of isothermal β models to describe the atmosphere of the cluster does not exhaust the list of plausible structures that the atmosphere might adopt — in particular, it restricts the thermal structure of the atmosphere to a simple form that is not consistent with the more complicated structures seen in some nearby clusters (e.g., the Coma cluster; Hughes *et al.* 1993). Thus it is of interest to examine the effect that qualitative variations of the model atmosphere have on the estimate for H_0.

In order to assess these effects, we have chosen to modify the isothermal β model (5) by incorporating an outer density cut-off (so that $n_e = 0$ at $r > r_{\max}$), and by allowing the temperature to assume a polytropic dependence on density (with the polytropic index chosen to be the maximum value consistent with a physical cluster potential holding a β-model atmosphere in hydrostatic equilibrium, $\gamma = 1 + \frac{1}{3\beta} = 1.51$; Hughes *et al.* 1988) outside an isothermal region of radius r_{iso}. We chose several values of $r_{\mathrm{iso}}/r_{\mathrm{cx}}$ and $r_{\max}/r_{\mathrm{cx}}$, and fitted the X-ray surface brightness and the X-ray spectrum of Abell 2218 self-consistently using these models to produce estimates of the temperature of the gas in the isothermal core of the cluster and the X-ray surface brightness normalization. Values of the Sunyaev-Zel'dovich normalization fitted using these same models were also calculated from the scan data (Table 1), and these normalizations and temperatures were then combined to produce further estimates for the Hubble constant.

If the isothermal radius is much larger than the core radius, then the results of Sec. 3 are little altered: values of the Hubble constant which differ by less than 10 per cent from (9) are obtained for $r_{\mathrm{iso}} \gtrsim 10 r_{\mathrm{cx}}$. If the isothermal radius is only a few r_{cx}, however, substantially larger values of the Hubble constant are obtained — for $r_{\mathrm{iso}} \approx 4 r_{\mathrm{cx}}$, the best-fitting models have values of $H_0 \approx 80\ \mathrm{km\,s^{-1}\,Mpc^{-1}}$. The increase in the apparent Hubble constant arises mostly from the different central electron temperatures required in the cluster for a good fit to both the spectrum and the surface brightness profile: the result for the Hubble constant scales approximately as T_{e0}^2, and the central electron temperature is about 10% higher for these models than for wholly isothermal models.

We conclude, therefore, that it is possible that the result (9) for the Hubble constant is an underestimate if Abell 2218 displays an outer polytropic temperature profile. However, the changes in the Hubble constant that are produced are comparable with the systematic error caused by the ±1 keV systematic error in the temperature deduced from the *Ginga* spectrum: a more precise determination of the X-ray spectrum of Abell 2218 would provide stronger constraints on thermal structure in the cluster and produce a substantial reduction in the T_e-based systematic error on the estimate of the Hubble constant (9).

The position offset of ~ 1.5 arcmin between the center of the cluster as determined from the X-ray image and from the Klein *et al.* (1991) Sunyaev-Zel'dovich effect data (see

§ 3.2) was interpreted by Klein *et al.* as a possible indication of a complicated density and thermal structure in Abell 2218. If real, a major feature in the cluster atmosphere, with the unusual property of producing a large Sunyaev-Zel'dovich effect but little X-ray emission, is implied by the Klein *et al.* position shift: on the basis of the model atmosphere that best fits the *Einstein* IPC and HRI data, Klein *et al.* should have detected only about 10 per cent of the peak Sunyaev-Zel'dovich effect at their center, and no indication of a corresponding X-ray feature can be found in the HRI image (Fig. 2b). If the complicated structure implied by the Klein *et al.* result is present in Abell 2218, then far more detailed X-ray and Sunyaev-Zel'dovich effect mapping of the cluster is needed if the present method is to be used to derive the Hubble constant. However, the Klein *et al.* data have low significance (they measured an effect of -0.6 ± 0.2 mK), so that the evidence for a major structural feature in the cluster atmosphere that would invalidate the derived value of the Hubble constant (eq. 9) is weak.

4.3 The overall value for the Hubble constant

The present result for the Hubble constant can be compared with the result obtained from Abell 665 (Birkinshaw *et al.* 1991), to discover whether this method of determining H_0 produces consistent results, and hence whether there are substantial unknown variations in the properties of the cluster atmospheres (for example, in strongly varying clumping in the gas, or dramatic thermal structures) that cause large scatter in the Hubble constant values.

Birkinshaw *et al.* used data for Abell 665 to find $H_0 = 45 \pm 13 \ \mathrm{km\,s^{-1}\,Mpc^{-1}}$, where we have taken the error range quoted in that paper and converted it into a $\pm 1\sigma$ error. This result has been updated by Birkinshaw *et al.* (1993), who used the full available Sunyaev-Zel'dovich effect data set, and a more conservative set of systematic error estimates, to obtain $H_0 = 51 \pm 18 \ \mathrm{km\,s^{-1}\,Mpc^{-1}}$, For Abell 2218, we have shown in Sec. 3 that $H_0 = 65 \pm 25 \ \mathrm{km\,s^{-1}\,Mpc^{-1}}$, from which we deduce an average value for the Hubble constant, based on the two clusters taken together, of

$$H_0 = 55 \pm 17 \ \mathrm{km\,s^{-1}\,Mpc^{-1}} \tag{11}$$

where the error sum has taken account of the fully-correlated errors in the two estimates produced by the uncertainty in the sensitivity of the 40-m telescope.

The consistency of the results for the Hubble constant based upon two different clusters suggests that this method is fairly robust, although the errors in the Hubble constant values are still large. In gaining the estimates based on clusters Abell 665 and 2218 we ignored the effects of clumping in the intracluster medium (which could cause these values of the Hubble constant to be overestimates, if the clumping is isobaric), we assumed that the clusters were at rest in the Hubble flow, we ignored any thermal structure in the clusters (the gas is assumed to be isothermal), any large-scale substructure in the clusters was also ignored, it was assumed that the clusters were spherical, and it was implicitly assumed that the somewhat different gas that contributes to the X-ray surface brightness (dominated by gas in the cluster cores) and the Sunyaev-Zel'dovich effect (dominated by gas further out in the clusters) can be related by a smooth density law of the form (5). Since the two clusters Abell 665 and Abell 2218 now produce similar estimates for the Hubble constant, it appears that these assumptions are either valid, or invalid in similar ways, in the two clusters: thus, for example, if both clusters contain isothermal cores and polytropic halos of the type considered in Sec. 4.2, the value of the Hubble constant (11) may be underestimated by 20 to 30%.

Since these data are subject to a selection effect, that elongated clusters are more readily detected if they are elongated along the line of sight, it could still be true that similar biases in the derived value of H_0 are present in the two clusters, causing perhaps a factor 1.5 or 2 decrease in the reported value of the Hubble constant (11) from its true value (see the discussion in Birkinshaw *et al.* 1991). In order to eliminate this selection effect, it will be necessary to repeat this process of deducing the Hubble constant using a number of clusters selected in a way that is not biased by their surface brightnesses — for example by selecting clusters on the basis of their total X-ray flux densities.

For most of the other assumptions that are necessary to derive the value of the Hubble constant there is little reason to suspect similar effects in different clusters. Thus, for example, the clumping of the intracluster medium is either weak (and hence has little effect on the estimate of the Hubble constant), or is strong, and should vary substantially according to the detailed structure of the clusters, producing large variations in the apparent Hubble constant. No such effect is seen at the $\sim$ 30 per cent level implied by the consistency of the results for Abell 665 and 2218. Similarly, large-scale thermal structure in clusters, or substructure in the gas caused by substructure in the clusters, might not be expected to be the same, and could have an effect at the 50 per cent level on the value of the Hubble constant, but such large variations are not present.

Thus the agreement of the estimates for the Hubble constant based on clusters Abell 665 and 2218, which leads to the overall estimate (11), argues that if these results are strongly affected by selection effects or other biases, then those biases are similar in these two clusters. The best test of the presence or otherwise of these biases would be to repeat this procedure, measuring the Sunyaev-Zel'dovich effects and X-ray properties of more clusters, and then calculating a larger set of estimates of the Hubble constant.

5. CONCLUSIONS

The conclusions of this paper can be summarized as follows

(1) the structure of the intracluster medium in Abell 2218 is well described by a spherical, isothermal β model with $\beta \approx 0.65$ and $\theta_{\rm cx} \approx 1.0$ arcmin, centered at the optical center of the cluster;

(2) the value of the Hubble constant implied from these data for Abell 2218 is

$$H_0 = 65 \pm 25 \ {\rm km\,s^{-1}\,Mpc^{-1}}; \tag{12}$$

(3) McHardy *et al.* (1990)'s estimate of $H_0 = 24^{+23}_{-10}\ {\rm km\,s^{-1}\,Mpc^{-1}}$, based on the X-ray and Sunyaev-Zel'dovich effect data for Abell 2218 appears to be in error principally because of their use of the HRI data to obtain the electron density profile, and their use of an inconsistent description of the cluster gas in fitting the X-ray and Sunyaev-Zel'dovich effect data; and

(3) combining the present result for the Hubble constant with that obtained earlier for Abell 665, we find an overall result

$$H_0 = 55 \pm 17 \ {\rm km\,s^{-1}\,Mpc^{-1}}. \tag{13}$$

Further work on the estimation of the value of the Hubble constant by this method should attempt to produce better-quality X-ray spectra of the clusters that might constrain their thermal structure, and must work to reduce the systematic errors in the Sunyaev-Zel'dovich effect measurements: both factors make an appreciable contribution to the large errors in (12) and (13) above. Better structural data for clusters could reduce the qualitative uncertainty in the choice of models and would also be valuable: thus ROSAT PSPC data on Abell 2218 (which are not yet available to us) will restrict the set of permissible models of the gas distribution through its improved angular and spectral resolution compared to the *Einstein* IPC data.

ACKNOWLEDGEMENTS

This research was supported by NSF grant AST-9005038, NASA grants NAG8-699, and NAG8-181, and NASA contract NAS5-30934.

REFERENCES

Abell, G.O., 1958. ApJS, 3, 211.

Birkinshaw, M., 1979. MNRAS, 187, 847.

Birkinshaw, M., 1987. NRAO GreenBank Workshop 16, 261; eds O'Dea, C. & Uson, J.; NRAO GreenBank, WV.

Birkinshaw, M., 1990. The Cosmic Microwave Background: 25 Years Later, 77; eds Mandolesi, N. & Vittorio, N.; Kluwer, Dordrecht.

Birkinshaw, M., Gull, S.F. & Hardebeck, H., 1984. Nature, 309, 34.

Birkinshaw, M., Gull, S.F., Hardebeck, H.E. & Moffet, A.T., 1993. ApJ, submitted.

Birkinshaw, M., Hughes, J.P & Arnaud, K.A., 1991. ApJ, 379, 466.

Cavaliere, A., Danese, L. & De Zotti, G., 1979. A&A, 75, 322.

Dressler, A., 1978a. ApJ, 223, 765.

Dressler, A., 1978b. ApJ, 226, 55.

Gunn, J.E., 1978. In Observational Cosmology, 1; eds Maeder, A., Martinet, L. & Tammann, G.; Geneva Obs., Sauverny, Switzerland.

Harnden, F.R., Jr., Fabricant, D.G., Harris, D.E., & Schwarz, J., 1984, Scientific Specification of the Data Analysis System for the Einstein Observatory Imaging Proportional Counter, SAO Special Report 393, p. 22.

Hatsukade, I. 1989, Ph.D. thesis, Osaka University.

Hughes, J.P., Butcher, J.A., Stewart, G.C., & Tanaka, Y., 1993 ApJ, in press (Feb. 20).

Hughes, J.P., & Tanaka, Y., 1992, ApJ, 398, 62.

Hughes, J.P., Yamashita, K., Okumura, Y., Tsunemi, H., & Matsuoka, M., 1988, ApJ, 327, 615.

Klein, U., Rephaeli, Y., Schlickeiser, R. & Wielebinski, R., 1991. A&A, 244, 43.

Mather, J.C., Cheng, E.S., Eplee, R.E.Jr., Isaacman, R.B., Meyer, S.S., Shafer, R.A., Weiss, R., Wright, E.L., Bennett, C.L., Boggess, N.W., Dwek, E., Gulkis, S., Hauser, M.G., Janssen, M., Kelsall, T., Lubin, P.M., Moseley, S.H.Jr., Murdock, T.L., Silverberg, R.F., Smoot, G.F. & Wilkinson, D.T., 1990. ApJ, 354, L37.

McHardy, I.M., Stewart, G.C., Edge, A.C., Cooke, B.A., Yamashita, K. & Hatsukade, I., 1990. MNRAS, 242, 215.

Moffet, A.T. & Birkinshaw, M., 1989. AJ, 98, 1148.

Rephaeli, Y. & Lahav, O., 1990. ApJ, 372, 21.

Sarazin, C.L., 1986. Rev. Mod. Phys., 58, 1.

Silk, J.I. & White, S.D.M., 1978. ApJ, 226, L103.

Stark, A.A., Heiles, C., Bally, J., & Linke, R. 1984, privately distributed magnetic tape.

Turner, E.L., Cen, R. & Ostriker, J.P., 1992. AJ, 103, 1427.

Uson, J., 1987. Radio Continuum Processes in Clusters of Galaxies, NRAO GreenBank Workshop 16, 255; eds O'Dea, C. & Uson, J.; NRAO GreenBank, WV.

Table 1. Sunyaev-Zel'dovich effect data

Point	Co-ordinates (B1950) RA	dec	Uncorrected $\Delta T_{\rm RJ}/\mu$K	Corrected $\Delta T_{\rm RJ}/\mu$K	Systematic error $\Delta T_{\rm syst}/\mu$K
a	$16^{\rm h}35^{\rm m}37^{\rm s}$	$+66°11'30''$	-125 ± 34	-105 ± 59	± 17
b	$16^{\rm h}35^{\rm m}37^{\rm s}$	$+66°14'30''$	-121 ± 40	-97 ± 34	± 17
c	$16^{\rm h}35^{\rm m}37^{\rm s}$	$+66°16'30''$	-178 ± 28	-176 ± 32	± 19
d	$16^{\rm h}35^{\rm m}37^{\rm s}$	$+66°18'30''$	-427 ± 30	-445 ± 33	± 18
e	$16^{\rm h}35^{\rm m}37^{\rm s}$	$+66°20'30''$	$+279 \pm 32$	-80 ± 77	± 33
f	$16^{\rm h}35^{\rm m}37^{\rm s}$	$+66°22'30''$	-66 ± 59	-98 ± 53	± 18
g	$16^{\rm h}35^{\rm m}37^{\rm s}$	$+66°25'30''$	-106 ± 32	-89 ± 42	± 17

Notes

(1) The uncorrected values of $\Delta T_{\rm RJ}$ are those without source corrections of any kind, but with the data taken under conditions of bad weather removed. Only point e in the scan is affected by radio source contamination at a level greater than the error on the uncorrected $\Delta T_{\rm RJ}$, the dominant source at point e is source 16 of the Moffet & Birkinshaw (1989) survey.

(2) The corrected values of $\Delta T_{\rm RJ}$ have been corrected for radio sources both near the points in the scan and for sources in the reference arcs about these points onto which the 40-m telescope's reference beams switch. Significant corrections for sources in the reference arcs occur for several points in the scan: where sources in the reference arcs contribute more than 100 μK to the signal, the contaminated data have been deleted in calculating the result in the Table. The random errors quoted have been increased by a factor that takes account of the year-to-year discordance in the data (Sec. 2.1).

(3) The systematic errors are those attributable for each point individually (errors 3-5 of Sec. 2.1), and are $\pm 1\sigma$ errors.

(4) In addition to these systematic errors, $\Delta T_{\rm syst}$, the overall zero level of the data shows a systematic error of -43 ± 25 μK (Birkinshaw *et al.* 1992), so that the net $\Delta T_{\rm RJ}$ at point d, for example, is -402 ± 45 μK if all systematic errors are combined with the random error in quadrature.

(5) The overall scale of the brightness temperatures may be in error by a factor of 1.00 ± 0.06.

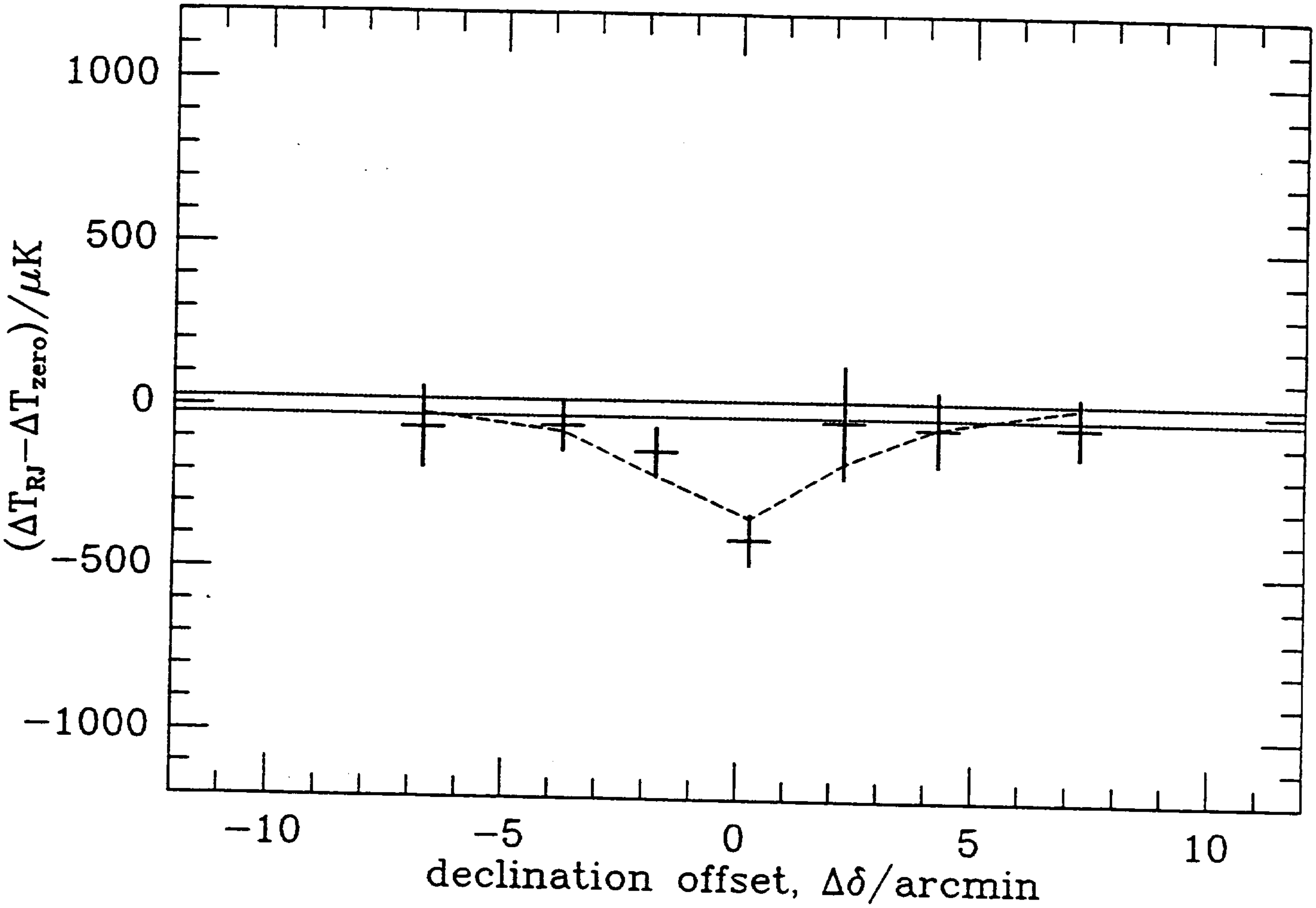

Figure 1. The Sunyaev-Zel'dovich effect data for several points on an NS line through Abell 665. The declination offsets for each point are measured relative to the cluster center deduced from the *Einstein* IPC image, of $16^{h}35^{m}42^{s}\!.8$, $66^{\circ}18'44''\!.5$ (B1950). The crosses at each point represent the microwave background radiation brightness temperature change, as measured with the OVRO 40-m telescope, including an contribution from systematic errors associated with that point (added in quadrature), and corrected for the zero level offset of $-43\ \mu$K. The horizontal dotted lines indicate the $\pm 25\ \mu$K error on this zero level offset. The brightness temperature scale is uncertain by ± 6 per cent. The dashed line represents the isothermal β model that best fits the X-ray data, adjusted to have the best normalization N_{RJ}.

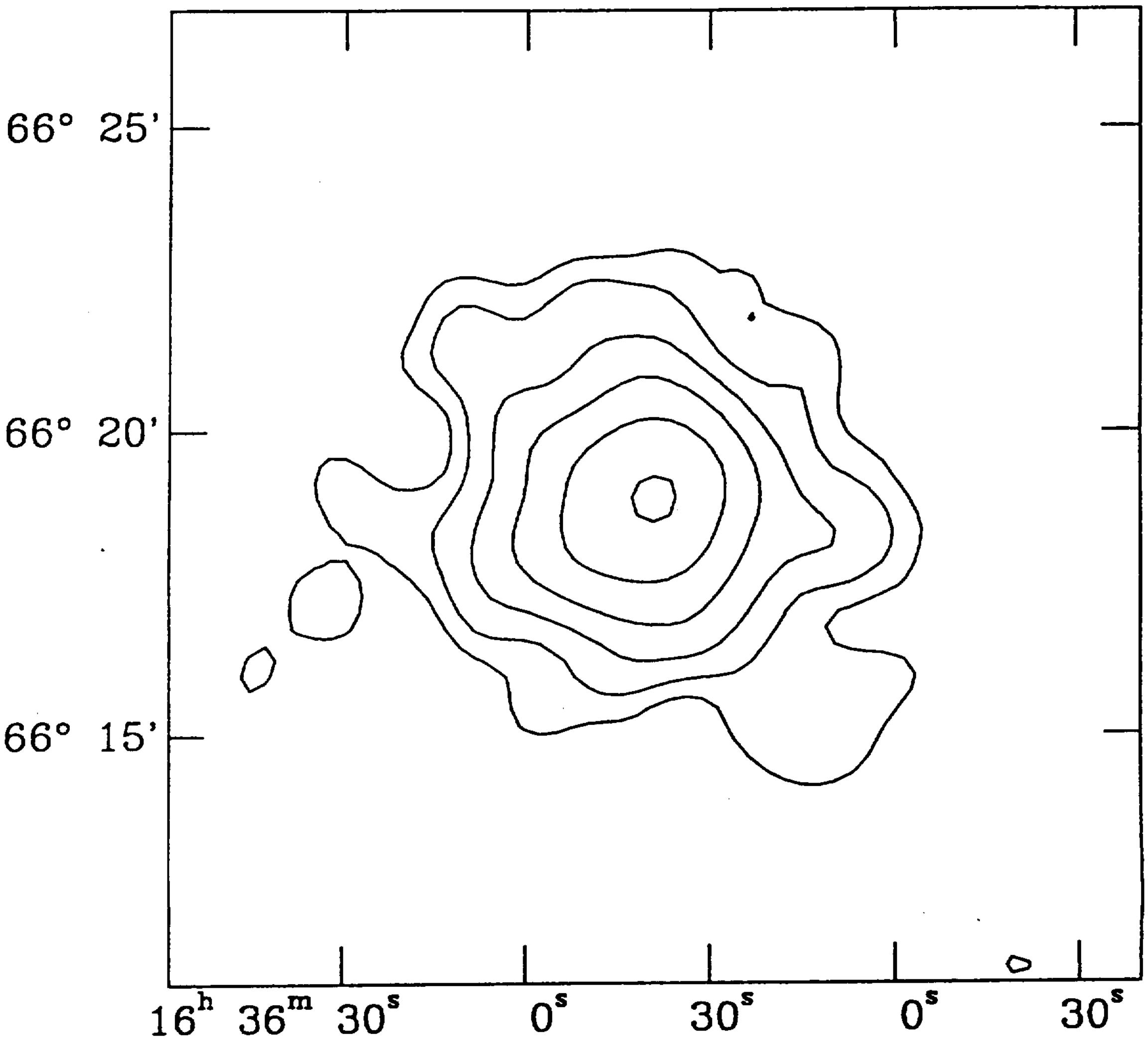

Figure 2. The X-ray images of Abell 2218 from the *Einstein* IPC and HRI. (a) The IPC image, generated from the counts in the energy band 0.8 –3.5 keV by convolution with a gaussian of standard deviation 32 arcsec. The lowest contour corresponds to a value of 5.8×10^{-4} cts s^{-1} arcmin^{-2} which is 3σ above the mean background level in the center of the field. Successively higher contour levels increase in logarithmic steps of 1.85.

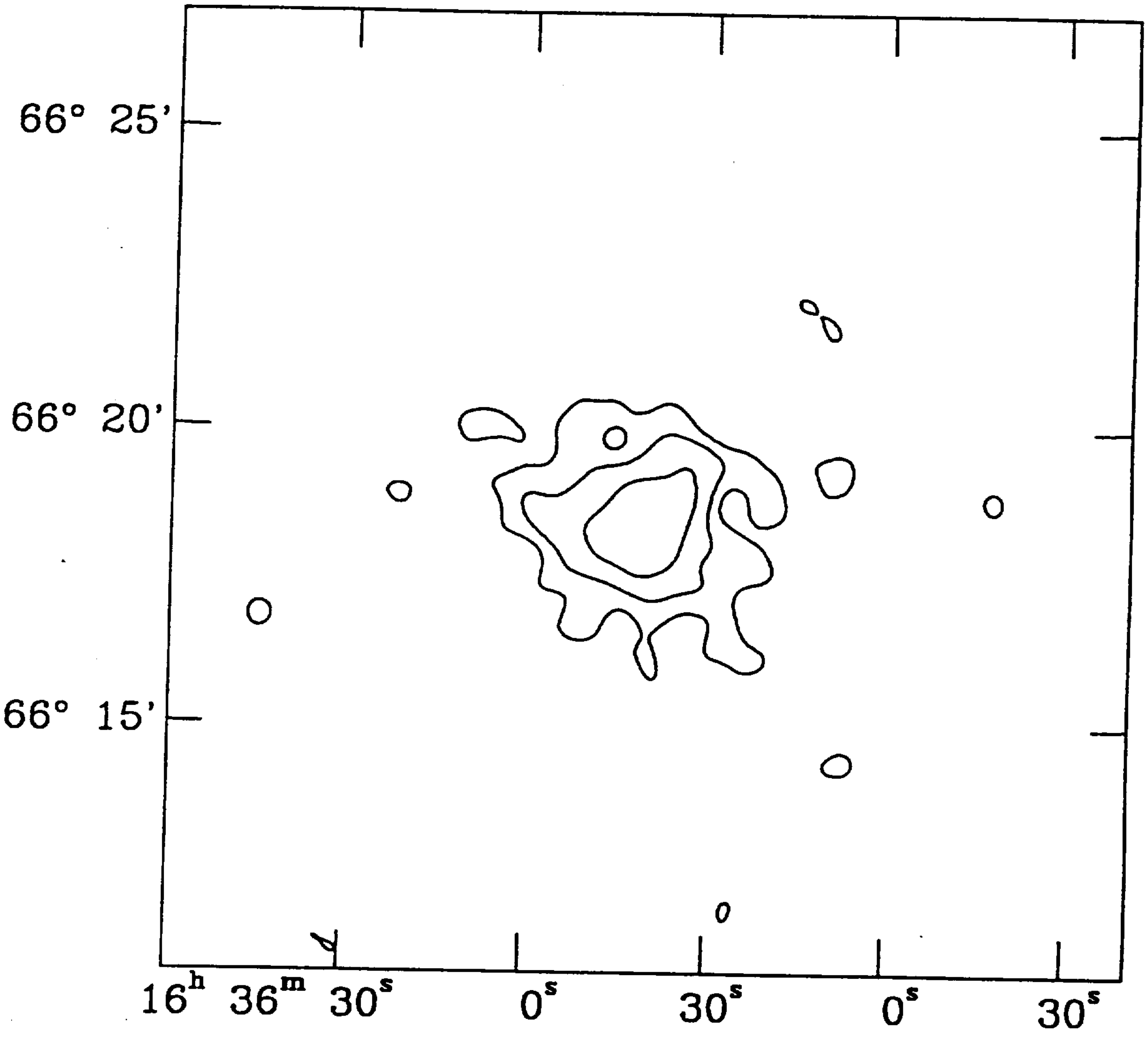

(b) The HRI image, generated from the counts by convolution with a gaussian of standard deviation 16 arcsec. The lowest contour corresponds to a value of 1.2×10^{-3} cts s^{-1} $arcmin^{-2}$ and successively higher contour levels increase in logarithmic steps of 1.85. The inner three contours shown for the HRI were chosen to correspond to the same X-ray brightness as the inner three contours of the IPC image (using the ratio of 3.07 IPC counts per HRI count, based on the best-fit spectral model). Apparent deviations from axisymmetry in this image are not statistically significant.

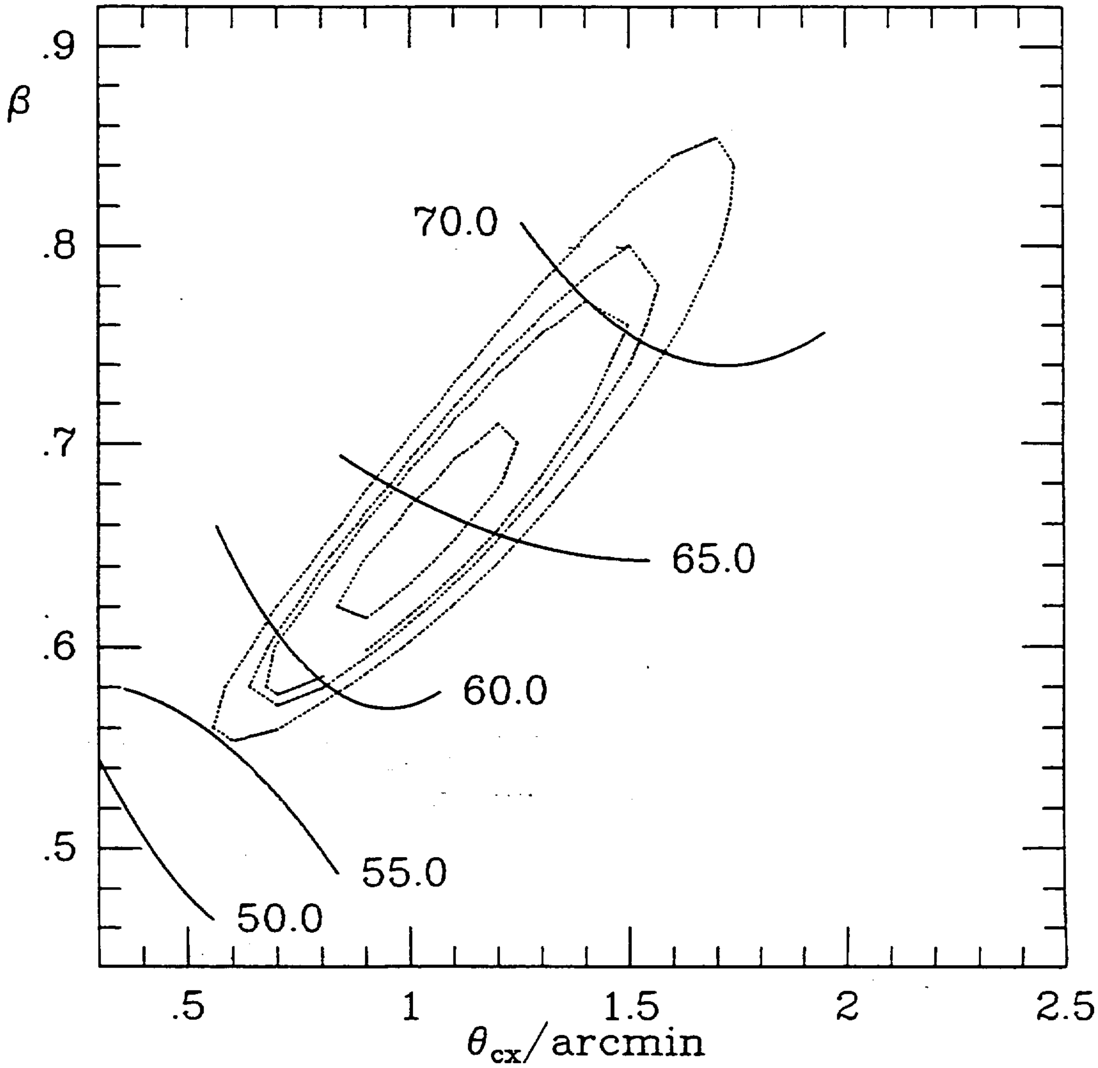

Figure 3. Confidence level contours for fits of isothermal β-models to the IPC image of Abell 2218, with superimposed contours of the value of H_0 (in $\mathrm{km\,s^{-1}\,Mpc^{-1}}$) derived from the X-ray and Sunyaev-Zel'dovich effect data. The best fit lies at $\beta = 0.65$, $\theta_{cx} = 1.0$ arcmin, and corresponds to $H_0 = 65\ \mathrm{km\,s^{-1}\,Mpc^{-1}}$. The random error at this point is $14\ \mathrm{km\,s^{-1}\,Mpc^{-1}}$: when the systematic errors in the X-ray and Sunyaev-Zel'dovich effect data, and an error from the dependence of H_0 on the model values of β and θ_{cx}, are added in quadrature the overall error is increased to $\pm 25\ \mathrm{km\,s^{-1}\,Mpc^{-1}}$.

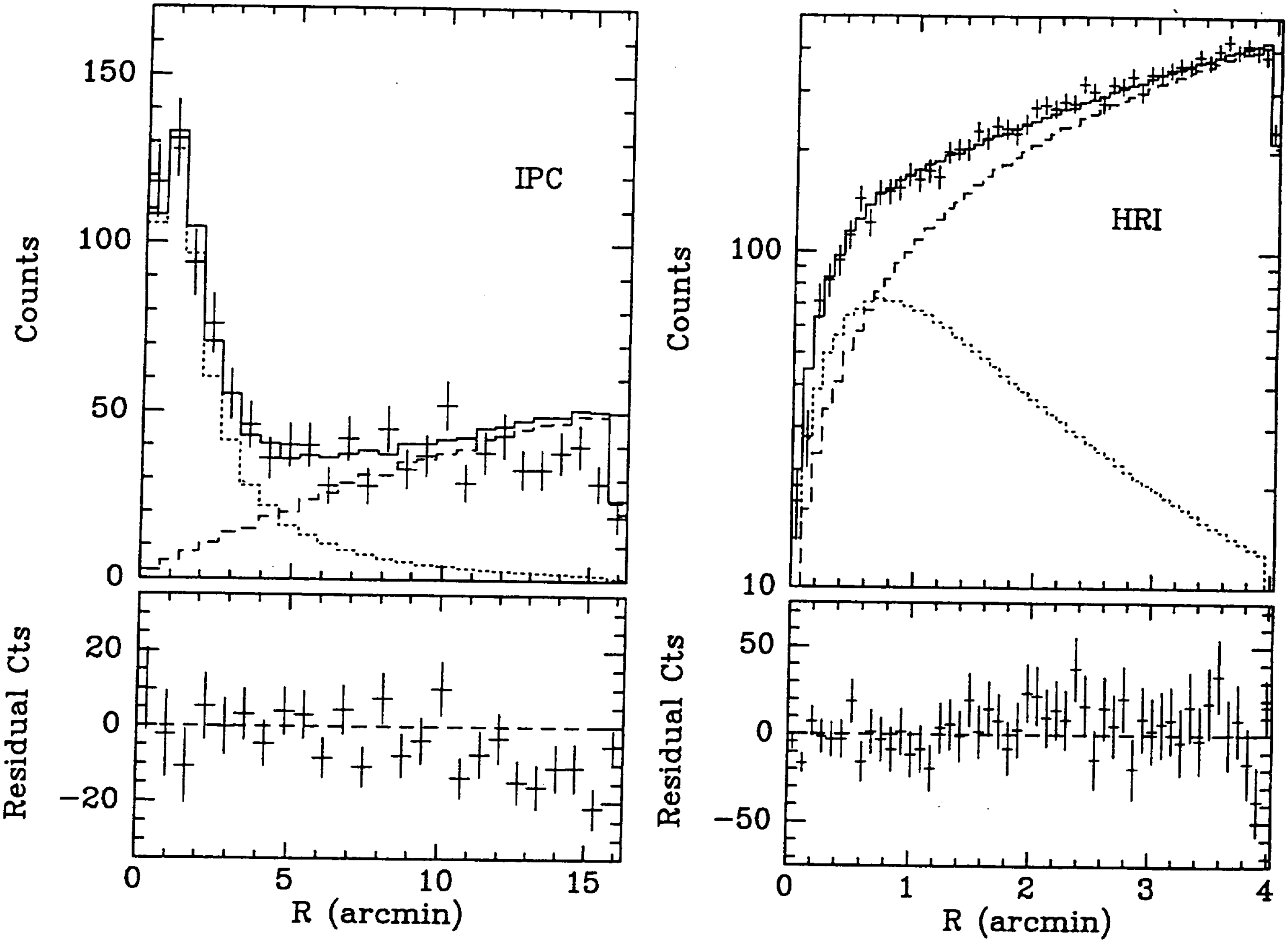

Figure 4. Comparisons of the radial X-ray profiles of the best-fitting isothermal β model (with $\beta = 0.65$, $\theta_{cx} = 1.0$ arcmin) with the IPC and HRI radial profiles. The total numbers of counts in annular rings are shown versus the distance from the center of the cluster. The short dashed curves show the model cluster emission, the long dashed curves show the background, and the solid curves are the sum of these. (Left) Comparison with the IPC. Note that the emission can be traced to about 7 arcmin. (Right) Comparison with the HRI. Note how the background dominates the cluster emission beyond about 0.6 arcmin.

THE ASTROPHYSICAL JOURNAL, 429:545–553, 1994 July 10

NONPOLYTROPIC MODEL FOR THE COMA CLUSTER

R. FUSCO-FEMIANO
Istituto di Astrofisica Spaziale, C.N.R., C.P. 67, 00044 Frascati, Italy
AND
JOHN P. HUGHES
Harvard-Smithsonian Center for Astrophysics, 60 Garden Street, Cambridge, MA 02138
Received 1992 July 27; accepted 1994 January 6

ABSTRACT

In this article we demonstrate, for the first time, how a physically motivated static model for both the gas and galaxies in the Coma Cluster of galaxies can jointly fit all available X-ray and optical imaging and spectroscopic data. The principal assumption of this nonpolytropic model (Cavaliere & Fusco-Femiano 1981, hereafter CFF), is that the intracluster gas temperature is proportional to the square of the galaxy velocity dispersion everywhere throughout the cluster; no other assumption about the gas temperature distribution is required. After demonstrating that the CFF nonpolytropic model is an adequate representation of the gas and galaxy distributions, the radial velocity dispersion profile, and the gas temperature distribution, we derive the following information about the Coma Cluster:

1. The central temperature is about 9 keV and the central density is 2.8×10^{-3} cm^{-3} for the X-ray emitting plasma;
2. The binding mass of the cluster is approximately 2×10^{15} $M_\odot$ within 5 Mpc (for $H_0 = 50$ km s^{-1} Mpc^{-1}), with a mass-to-light ratio of ~ 160 $M_\odot/L_\odot$;
3. The contribution of the gas to the total virial mass increases with distance from the cluster center, and we estimate that this ratio is no greater than ~50% within 5 Mpc.

The ability of the CFF nonpolytropic model to describe the current X-ray and optical data for the Coma Cluster suggests that a significant fraction of the thermal energy contained in the hot gas in this as well as other rich galaxy clusters may have come from the interaction between the galaxies and the ambient cluster medium.

Subject headings: galaxies: clustering — intergalactic medium — X-rays: galaxies

1. INTRODUCTION

Polytropic intracluster gas distributions were introduced by Lea (1975), Gull & Northover (1975), and Cavaliere & Fusco-Femiano (1976). In these models, ignorance about the complex history of the intracluster medium (ICM) is parameterized by a single quantity: the polytropic index γ, which relates the gas density and temperature distributions through $T \sim \rho^{\gamma-1}$. The inequality $\gamma < 5/3$ corresponds to stability against convection, and the value $\gamma = 5/3$ represents the adiabatic distribution. In the limit of an isothermal distribution ($\gamma = 1$) one obtains the hydrostatic isothermal-β model, where the X-ray surface brightness at a projected radius b has an analytical expression given by

$$S(b) = S(0)[1 + (b/R_c)^2]^{-3\beta+1/2} .$$

Here R_c is the core radius, and β is the ratio of the specific energy density of the galaxies and gas (Cavaliere & Fusco-Femiano 1976) expressed as $\beta = \mu m_H \sigma^2/kT$, where σ is the galaxy line-of-sight velocity dispersion and T is the isothermal gas temperature. This relation has been used successfully to fit the X-ray surface brightness emission from numerous clusters of galaxies (Gorenstein et al. 1978; Branduardi-Raymont et al. 1981; Abramopoulos & Ku 1983; Jones & Forman 1984).

In contrast to the X-ray surface brightness distributions of clusters, information on the temperature distribution has been more difficult to obtain due to technical limitations of instrumentation flown on past X-ray astronomy satellites. The Coma Cluster is one of the few clusters for which there is some knowledge of the temperature distribution. Direct X-ray spectral observations (Watt et al. 1992) have shown that the core of the Coma Cluster is very nearly isothermal out to roughly 30′. Other X-ray spectral data, however, obtained from mechanically collimated instruments with fields of view from 45′ to 3°, which examined larger regions of the Coma Cluster than did Watt et al., strongly require a radially decreasing temperature distribution in the cluster atmosphere.

As was first pointed out by Hughes et al. (1988b), self-consistent polytropic models were unable to provide acceptable fits to the X-ray imaging and spectral data on Coma. These authors introduced an ad hoc hybrid model consisting of a central isothermal region surrounded by a polytropic distribution which did yield acceptable fits. This model was motivated by theoretical considerations of the effects of electron heat conduction on the intracluster gas which would occur most rapidly in the central region of a cluster where the electron densities were the highest. Recently David, Hughes, & Tucker (1992) studied the evolution of gas in a cluster of galaxies in the presence of significant electron heat conduction using a hydrodynamical simulation. They found that a large, nearly isothermal central region would develop for values of thermal conductivity between about 0.1 and full Spitzer conductivity. This model was also able to describe eight present-day observed properties of the gas distribution in the Coma Cluster: the central gas density, the slope of the surface brightness profile at large radii, and several observed temperatures.

However, neither of these models was able to make a prediction about the distribution or dynamics of the cluster member galaxies.

In this paper we take a different approach from David et al. (1992). Instead of proposing specific mechanisms for energy input to or transport throughout the intracluster medium, we examine a static model which is really just a generalization of the earlier polytropic models. This new model, originally proposed by Cavaliere & Fusco-Femiano (1981, hereafter CFF), retains the most successful feature of the old polytropic models (that is, the description of the X-ray surface brightness distribution) but allows for the possibility that both the gas temperature and galaxy velocity dispersion distributions are not isothermal. In this new model, which we refer to as the CFF nonpolytropic model, although the temperature and velocity dispersion are functions of radius, they are still related to each other through the parameter β (see equation [1] below).

Unlike previous polytropic models, a solution to the CFF nonpolytropic model requires us to define an explicit form for the gravitational potential of the cluster. In principle, the choice of this function could be arbitrary, although in practice, even for a cluster as well studied as Coma, the current X-ray and optical data are unable to set strong limits on the shape of the underlying gravitational potential (see, for example, Hughes 1989). For simplicity we have assumed that the virial mass follows a King (1966) isothermal sphere model and that the galaxies are distributed like the virial mass. These assumptions allows us to derive self-consistent solutions for the gas and galaxy density distributions, as well as the gas temperature and velocity dispersion profiles, for comparison with observed data.

The slow radial decrease of both the velocity dispersion and gas temperature profiles for the Coma Cluster qualitatively support the model. The purpose of our article is to demonstrate quantitative agreement with the available data on this cluster. Specifically, we examine the X-ray surface brightness data from the *Einstein* imaging proportional counter (IPC) (Hughes et al. 1988b), the spectral data obtained by the X-ray satellites *Tenma* (Hughes et al. 1988b), *EXOSAT* (Hughes, Gorenstein, & Fabricant 1988a), and *Ginga* (Hughes et al. 1993), and the optical velocity dispersion profile and galaxy density distributions (The & White 1986). We determine best-fit values and errors for the various model parameters. The paper is organized as follows. In § 2 we discuss the features of the CFF nonpolytropic model. The fits to the IPC and spectral data are in §§ 3 and 4, respectively. Section 5 reports the fits to the optical data. Discussion of the cluster binding mass implied by the model appears in § 6, and the conclusions are in § 7.

2. THE CFF NONPOLYTROPIC MODEL

The scope of this work is to verify whether the available X-ray and optical data can be described by means of the static model, originally formulated by CFF, in which the heating of the ICM is controlled by local conditions. In particular, we consider the case where the relation

$$kT(R) = \mu m_{\mathrm{H}}\, \sigma^2(R)/\beta \tag{1}$$

holds everywhere throughout the cluster.

This model was originally formulated starting from the constraint that a reasonable fraction of the gas may have come from stars in cluster galaxies, as indicated by the observed metallicity of the intracluster gas (Mitchell et al. 1976; Serlemitsos et al. 1977; Mitchell & Culhane 1977). Early studies (Larson & Dinerstein 1975; De Young 1978) showed that the energy input from a population of supernovae, which yielded the observed iron abundance might be efficiently converted to bulk kinetic energy of the gas and then thermalized to temperatures consistent with the continuum X-ray measurements. The kinetic energy of the ejected gas, initially moving at the galaxy's speed with respect to the cluster center of mass, would be degraded into internal energy by collisions with the ambient intracluster gas. On average, this heating mechanism should give a temperature of the order of $kT \sim \sigma^2$, neglecting any additional energy input to the gas due to the ejection process itself (White 1991).

More recent scenarios for the evolution of the ICM have changed this picture slightly. It is now known that, although some of the intracluster gas must have been injected by the member galaxies to account for the observed metallicities, most of the ICM must be primordial, since the gas mass is much greater than the observed stellar mass of the cluster galaxies (Blumenthal et al. 1984; Davis et al. 1990). During the gravitational collapse of the cluster, this primordial gas would have been compressed and heated by processes different from those which would have heated the galaxies. In addition, simulations of cluster formation indicate that the galaxy velocity anisotropy should vary with radius, which would appear to make it unlikely for equation (1) to be strictly correct throughout the cluster. Nevertheless, the heating of the ICM is a very complex issue, and thus testing the assumptions implicit in the CFF nonpolytropic model against actual cluster data is a valuable excercise.

Inserting equation (1) into the equation that governs the equilibrium condition for the gas and the galaxies in the same potential well,

$$\mu m_{\mathrm{H}}\, n/\rho_G = dp/dp_G\ ,$$

it is possible to obtain the general expression for the gas density,

$$n/n_0 = (\rho_G/\rho_{G_0})^{\beta}(\sigma^2/\sigma_0^2)^{\beta - 1}\ , \tag{2}$$

where n is the gas density, ρ_G is the galaxy density, and $p_G = \rho_G \sigma^2$. Central values of quantities are designed with subscript 0.

An explicit expression is obtained using definite relationships $\sigma = \sigma(W)$ and $\rho_G = \rho_G(W)$, where W is the normalized gravitational potential $[W(R) = G \int_R^{R_t} M(r) r^{-2} \sigma^{-2}\, dr]$. The cluster boundary, R_t, is defined to be the radius where $\rho_G = \sigma = 0$.

The velocity dispersion of the Coma Cluster is observed to decrease with increasing projected distance from the cluster center (Rood et al. 1972; Kent & Gunn 1982; Kent & Sargent 1983; The & White 1986). One of the possible functions consistent with such a monotonic decrease is a King (1966) isothermal sphere, which gives for the velocity dispersion,

$$\frac{\sigma^2}{\sigma_0^2} = \frac{I_{5/2}(W)}{I_{5/2}(W_0)}\,\frac{I_{3/2}(W_0)}{I_{3/2}(W)}\ , \tag{3}$$

and for the galaxy density,

$$\rho_G/\rho_{G_0} = e^{W - W_0} I_{3/2}(W)/I_{3/2}(W_0)\ ,$$

where

$$I_q(W) = \int_0^W e^{-\eta} \eta^q\, d\eta$$

is the incomplete gamma function $\gamma(q + 1, W)$.

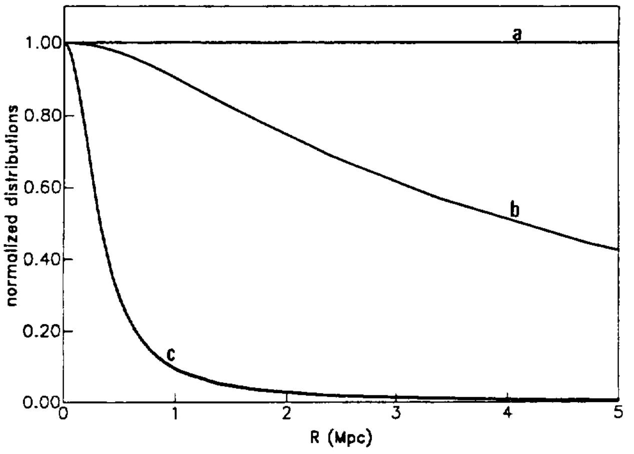

FIG. 1.—Temperature normalized distributions for the isothermal β-model (a) and the CFF nonpolytropic model (b). Density normalized distribution (c) for both the models.

In turn, $W(R)$ is derived from the full Poisson equation that includes the total density $\rho(W) = n(W) + \rho_G(W)$ (we include in ρ_G any "virial mass" distributed like the galaxies) (King 1966; Cavaliere & Fusco-Fermiano 1978). According to relation (1), the temperature distribution is given by equation (3).

In this model the relevant parameters, which are to be determined by fits to the X-ray and optical data, are the following: n_0, the central gas density; T_0, the central gas temperature; R_c, the core radius of the galaxy space distribution; W_0, the central value of the normalized gravitational potential; and β, the ratio of the specific energy between the galaxies and gas. The X-ray imaging and spectral data can be analyzed separately due to the limited energy bandwidth of the IPC (0.5–4 keV) and the very limited spatial resolution of the higher energy spectrometers. The imaging data put constraints on the allowed values for β and R_c, while the spectral data constrain T_0 and W_0. The optical data are most sensitive to W_0. Normalizations to the imaging and spectral data permit us to derive the central gas density n_0.

The expression that allows computation of the cluster binding mass is derived by combining the spherically symmetric condition of hydrostatic equilibrium with the ideal gas law:

$$\frac{kT}{\mu m_{\rm H}}\left(\frac{dn}{n}+\frac{dT}{T}\right) = -\frac{GM(R)}{R^2}\,dR\,,$$

which may be written as

$$M(y) = \frac{kTR_c}{\mu m_{\rm H} G}\left(\frac{dn}{n\,dW}+\frac{dT}{T\,dW}\right)y^2\,\frac{dW}{dy}\,,$$

where $y = R/R_c$. For the CFF nonpolytropic model, the derivatives assume the following forms:

$$\frac{dn}{n\,dW} = \beta + (\beta - 1)\,\frac{e^{-W}W^{5/2}}{I_{5/2}(W)} + \frac{e^{-W}W^{3/2}}{I_{3/2}(W)}\,,$$

$$\frac{dT}{T\,dW} = e^{-W}\,\frac{I_{3/2}(W)W^{5/2} - I_{5/2}(W)W^{3/2}}{I_{3/2}(W)I_{5/2}(W)}\,.$$

The gravitational gradient dW/dy is given by the solution of the full Poisson equation (Cavaliere & Fusco-Femiano 1978).

Figure 1 shows the radial temperature and density distributions (normalized by their central values), which are solutions of the CFF nonpolytropic model. The radial distributions from the isothermal-β model are also shown for comparison.

3. SPATIAL ANALYSIS

The IPC on the *Einstein Observatory* (Giacconi et al. 1979) produced an extensive set of imaging X-ray data on the Coma Cluster. These data were analyzed by Hughes et al. (1988b), and initial reduction procedures are given there. Pointings were made in a number of locations but not in a uniform manner, and since the X-ray image of Coma is distinctly elliptical, it was not possible to obtain a properly averaged radial surface brightness profile from the existing set of images. In this paper, we use the so-called north data set, where the spatial coverage of the cluster was most complete and extended to a radius of roughly 40′ from the cluster center. We have also considered the surface brightness profile composed of data from all the fields (see Hughes 1989), and, although numerical values change somewhat when this data set is used, our conclusions are not modified.

Model surface brightness profiles were determined by calculating the density and temperature as a function of radius from the expressions in § 2 and projecting the quantity $n^2\Lambda(T)$ to the line of sight. To calculate $\Lambda(T)$, the intrinsic emissivity of the gas as seen by the IPC, we needed to assume a value for the distance (140 Mpc), the column density of interstellar absorbing matter in the direction to Coma (3×10^{20} cm^{-2}), and the metal abundance (25%). The convolution of an X-ray spectrum at temperature T generated in conjunction with the preceding parameters with the effective area, and spectral response of the IPC then yielded $\Lambda(T)$. We used the Raymond & Smith (1977; also J. Raymond 1993, private communication) plasma emission model throughout this work. To approximate the spatial response of the IPC, model surface brightness profiles are convolved with a circular Gaussian ($\sigma = 0\farcm6$). The IPC data were most constraining of parameters β, R_c, and n_0, while only a lower bound on the value of W_0 was obtained (see Table 1 and Fig. 8). Because of the limited energy bandwidth of the IPC, the surface brightness data are quite insensitive to the value of T_0, and so we set it to a value of roughly 9 keV and keep it fixed. Varying the central temperature by as much as 20% introduced less than about a 2% change in the best-fit values of β and R_c.

Figure 2 shows the X-ray surface brightness of the Coma Cluster for the data from the northern region, along with the best-fit nonpolytropic model. The best-fit parameter values and the χ^2 value, reported in Table 1 with 90% confidence level errors (single parameter, $\chi^2_{\rm min} + 2.71$), are very similar to those obtained with the isothermal β-model (from Hughes et al. 1988b and reproduced in col. [3] of Table 1). As shown in

TABLE 1

BEST-FIT SPATIAL PARAMETER VALUES FOR COMA CLUSTER

Parameter (1)	Nonpolytropic model (2)	Isothermal β-Model[a] (3)
R_c	$8\farcm1(+0\farcm8;\ -1\farcm0)$	$7\farcm6 \pm 0\farcm7$
β	0.644(+0.032; −0.050)	0.63 ± 0.03
$n_0(\times 10^{-3}\ {\rm cm}^{-3})$[b] ..	2.77(+0.26; −0.20)	2.6 ± 0.3
W_0	9.6(...; −2.4)[c]	...
χ^2(dof)	13.1 (17)	12.8 (18)

[a] Hughes et al. 1988b.

[b] $H = 50$ km s^{-1} Mpc^{-1}.

[c] Indeterminate error bound.

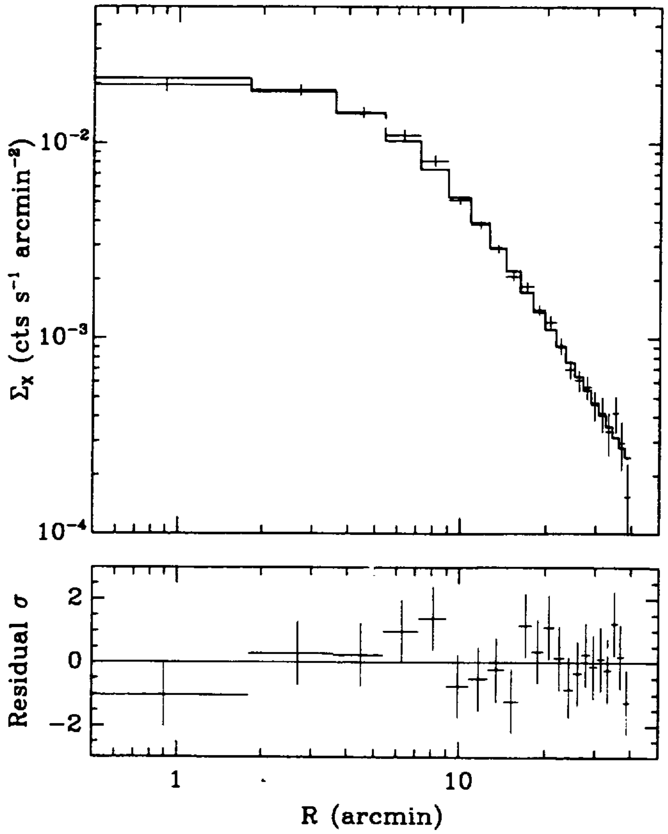

FIG. 2.—Radially averaged IPC X-ray surface brightness of the Coma Cluster with best-fit nonpolytropic model.

Figure 1, the density profile of the CFF nonpolytropic model is virtually indistinguishable from that of the isothermal β-model; $n/n_0 = (\rho_G/\rho_{G_0})^\beta$. This is due to the slow radial decrease of the galaxy velocity dispersion (see eq. [2] and Fig. 6*a*). The slight difference in χ^2 values between the two models is presumably due to the use of the King model approximation, i.e., $n(R)/n_0 = [1 + (R/R_c)^2]^{-3\beta/2}$, in the work of Hughes et al. 1988b.

Figure 3 presents the results of fits for β and R_c in the form of two-dimensional χ^2 contours (68% and 90% confidence levels with $\chi^2_{\rm min} + 2.3$ and $\chi^2_{\rm min} + 4.61$, respectively; see Avni 1976; Lampton, Margon, & Bowyer 1976). Figure 8 shows two-dimensional χ^2 contours for W_0 versus R_c (only the 90% confidence level contour, shown as a dashed line, is given). The imaging data are unable to place an upper bound on the value of W_0.

FIG. 3.—Results of fits to the spatial data. Two-dimensional χ^2 contours (at the 68% and 90% confidence levels) for β vs. R_c using the CFF nonpolytropic model.

4. SPECTRAL ANALYSIS

In order to test further the ability of the CFF nonpolytropic model to describe the X-ray emission from the Coma Cluster, we confront the model with spectral data in the energy range covering 0.7–20 keV obtained by the two Japanese satellites *Tenma* and *Ginga* and by the European satellite *EXOSAT*. In a series of papers over the last several years (Hughes et al. 1988b; Hughes et al. 1988a; Hughes et al. 1993), these data sets were analyzed in a consistent fashion. Since the various instruments viewed larger or smaller regions of the cluster (due to their differently collimated fields of view), it was possible to jointly analyze the data sets to discover the presence of a temperature gradient in the Coma Cluster. Larger field-of-view instruments (or off-center pointings in the case of *EXOSAT* data) consistently yielded lower best-fit temperatures when compared with smaller field-of-view instruments, leaving no doubt that the temperature variation was a global effect and that the inner parts of the cluster were hotter than the outer regions. Although the gradient was weak, it was poorly described by a polytropic model, and a phenomenological model, consisting of an isothermal core surrounded by a polytropic region, was introduced. The three sets of data were all consistent with this model and indicated an isothermal region of temperature about 9 keV extending to a radius of roughly 24′ (~1 Mpc) and decreasing beyond with a polytropic index $\gamma = 1.555$. These are by no means the possible allowed temperature distributions (see Hughes 1989 for a whole host of others), but represented merely a convenient parameterization. Other authors, Watt et al. (1992) in particular, confirm the shallowness of the temperature profile for Coma. These authors find the projected temperature distribution for Coma is nearly constant out to a radius of 30′.

We constructed a two-dimensional grid of nonpolytropic spectral models in the parameters T_0 and W_0, since these are the principal parameters for the spectral analysis. We associated each value of W_0 in the grid with the best-fit values for β, R_c, and n_0 from the imaging analysis (basically running down the middle of the dashed contour in Fig. 8). This procedure guaranteed agreement with the IPC results. Because of the large fields of view of all the spectrometers, the results are not particularly sensitive to these imaging parameters.

For each particular model in the grid of T_0 versus W_0, we employ the following procedure to generate a trial spectrum. The cluster is divided into a large number of constant temperature radial shells which are weighted by the appropriate value of $n(R)^2$, projected to the plane of the sky and convolved with the sky beam pattern of the instrument under consideration. This gives the weighting factor for this temperature value. An isothermal plasma model is calculated at each temperature and multiplied by the weighting factor. The final spectrum is the sum of the individual spectra from the various radial shells. Each instrument has its own unique beam pattern; thus, it was necessary to make a separate grid of models for each data set.

A χ^2 grid was constructed for each data set. To obtain acceptable fits to the spectral models, we need to include (and possibly vary) additional parameters, such as the metal abun-

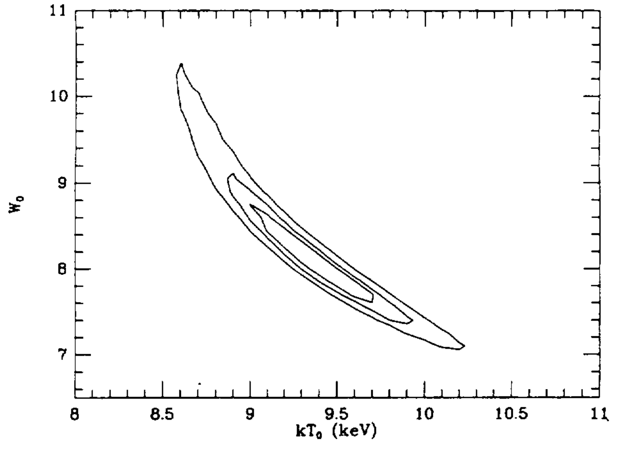

FIG. 4.—Results of the fits to the *Tenma*, *EXOSAT*, and *Ginga* spectra of Coma Cluster. Two-dimensional χ^2 contours (at the 68%, 90%, and 99% confidence levels) for W_0 vs. kT_0 using the CFF nonpolytropic model.

dance, the column density to the source, and the emission measure. We fixed the column density to a value of 3×10^{20} cm^{-2} (as for the IPC imaging analysis), but we let the other spectral parameters be free. The fitted abundance values were in the range 0.2–0.25 of solar, consistent with previous determinations.

In general, each data set by itself was able to constrain the allowed models to lie within a more or less narrow band in T_0, and placed only very weak constraints on W_0. This can be understood qualitatively by realizing that the principal action of variable T_0 in the model is to define the mean temperature for the cluster, while W_0 defines the temperature distribution. The data from these broadband collimated instruments taken individually are quite good at determining a mean cluster temperature, but rather poorer at determining the distribution. However, by adding the χ^2 grids (of T_0 vs. W_0) from the separate data sets, we are able to synthesize the information (albeit limited) on spatial variation of temperature hidden in the different pointing directions and fields of view and obtain a more encouraging result. The summed χ^2 grid is shown in Figure 4 (kT_0 vs. W_0) which gives the 68%, 90%, and 99% confidence intervals for the joint fit to all the spectral data. Table 2 provides actual numerical values for the fitted quantities. The minimum χ^2 is 1550.8 for 1482 degrees of freedom (corresponding to the 90th percentile). This must be considered excellent agreement, since we have not included contributions to χ^2 due to systematic effects such as uncertainties in background subtraction and gain calibration. This is also a considerably better fit than is obtained for a purely isothermal atmosphere, which yields an average temperature of 8.1 keV and a total χ^2 of 1580.0. From the point of view of the X-ray spectra, the CFF nonpolytropic model incorporates one additional free parameter. The F-test indicates that the inclusion of this free parameter is significant at greater than 5 σ confidence level.

TABLE 2

BEST-FIT SPECTRAL PARAMETER VALUES FOR COMA CLUSTER

Parameter	Nonpolytropic Model
T_0(keV)	9.39 (+0.42; −0.47)
W_0	8.05 (+0.83; −0.63)
χ^2(dof)	1550.8 (1482)

In Figure 5 we present the results of the spectral fitting for each data set separately in order to give the reader a sense of their relative importance. The panels show curves of χ^2 versus kT_0 for fixed best-fit values of β, R_c, n_0, and W_0. The curves then are a slice through the contour in Figure 4 at a value of $W_0 = 8.05$. The global best fit for T_0 is marked on each curve as a cross. First, one should note the excellent agreement among the data sets: the individual best-fit T_0 values are all within $\Delta\chi^2 = 2.0$ of the global best-fit T_0 value. Because of the high statistical signal and broad energy coverage, the *Ginga* data are the most constraining of T_0, while the *EXOSAT* off-center observations, which were the lowest statistical signal data of the group, are the least constraining. We stress that all the data sets are of roughly equal importance in constraining the allowed range of W_0.

Recent X-ray spectral observations (Watt et al. 1992) find that the core of the Coma Cluster is very nearly isothermal out to at least 30′. The CFF nonpolytropic model does predict a shallow temperature gradient within the central 30′ of the cluster: the projected temperature decreases from 9 keV at the center to only about 7.5 keV at 30′. We compared the projected temperature values of our best-fit model at 3′, 9′, 15′, 21′, and 27′ with the data from Figure 5 of Watt et al. (1992) and obtained a χ^2 of 9.06 for 5 degrees of freedom (corresponding to the 90% confidence level). We stress that no model parameters were adjusted in this comparison and that most of the contribution to χ^2 came from a difference in the overall temperature scale between the Watt et al. data and our model and not from the form of the temperature gradient. A more detailed analysis is beyond the scope of this work; however, given the simplicity of the comparison, we believe that this is additional supporting evidence in favor of the CFF nonpolytropic model.

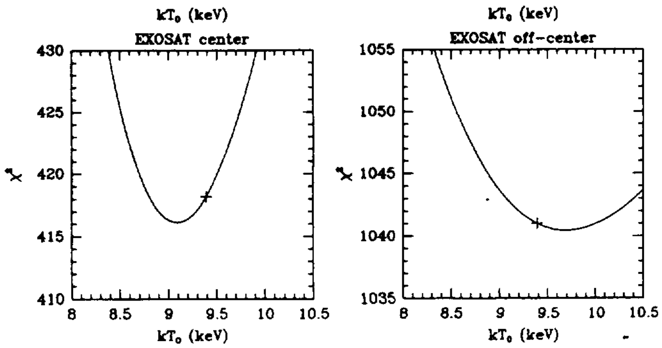

FIG. 5.—Results of the fits to the spectral data. One-dimensional χ^2 contour (90% confidence level) for the central gas temperature (T_0). The other parameter values are set to their best-fit values ($\beta = 0.644$; $R_c = 8'.1$; $W_0 = 8.05$; and $n_0 = 2.77 \times 10^{-3}$ cm^{-3}).

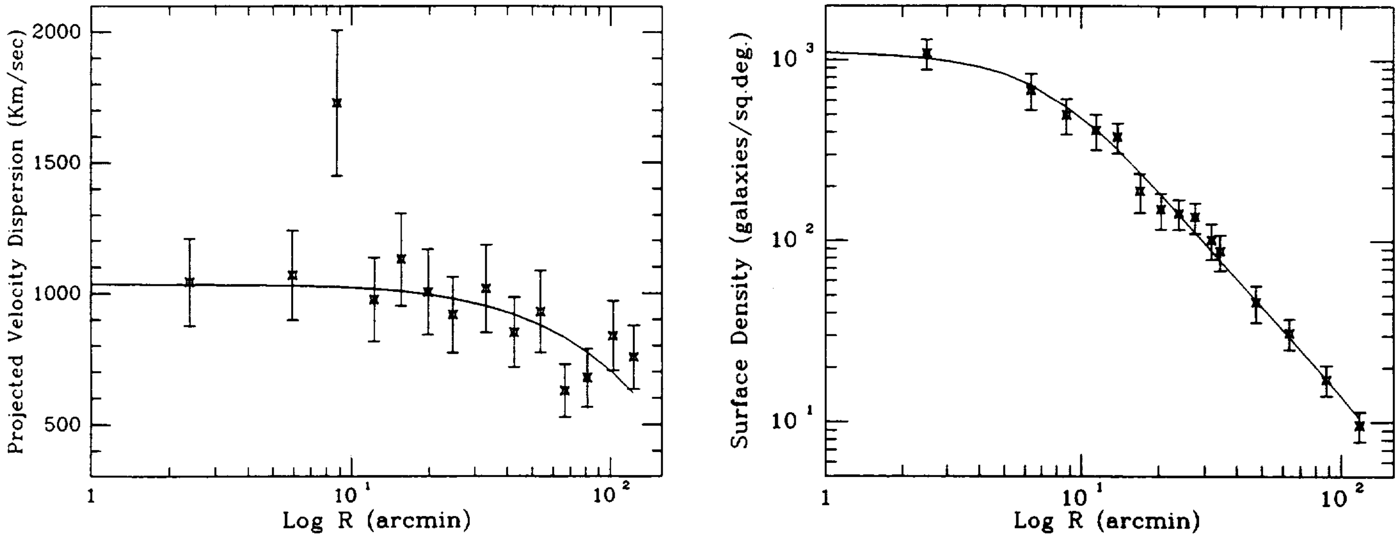

FIG. 6a

FIG. 6b

FIG. 6.—(*a*) Projected velocity dispersion and (*b*) surface galaxy density of the Coma Cluster with best-fit nonpolytropic model

5. ANALYSIS OF THE OPTICAL DATA

In this section, we intend to verify that the parameter values of the CFF nonpolytropic model derived in the preceding sections from fits to the X-ray data are consistent with the galaxy density and velocity dispersion profiles of the Coma Cluster. The & White (1986) studied these profiles starting from the data on galaxy positions and velocities published by Tifft & Gregory (1976) and Kent & Gunn (1982). The data are restricted to radii interior to 133′ because of the very strong possibility that galaxies beyond this radius are contaminated by unvirialized parts of the Coma Supercluster. The projected distributions are shown in Figures 6*a* and 6*b*, along with the best-fit nonpolytropic model; the numerical values of the fitted parameter are reported in Table 3. Note that for the optical analysis we fixed the parameters T_0 and n_0 to the values from the X-ray analysis. The central value of the velocity dispersion is given by the definition of the parameter β:

$$\sigma_0 = (kT_0\,\beta/\mu m_{\rm H})^{1/2} \simeq 1252\beta^{1/2}(kT_0/10\,{\rm keV})^{1/2}\ {\rm km\ s^{-1}}\,.$$

Using the values from Table 3, we derive $\sigma_0 = 1034(+101, -98)$ km s^{-1}.

The error intervals on some of the variable parameters in Table 3 for one or the other optical data set are poorly constrained. For example, fits to the galaxy density profile only set lower limits on the values of W_0 and β. The velocity dispersion data constrain a rather broad region in the $R_c - W_0$ plane but not the ranges of the individual values. Immediately below, we present figures which show the range of parameter space explored and the allowed regions from the fits.

Two-dimensional χ^2 contours (68% and 90% confidence level) for β versus R_c based on the velocity dispersion and surface galaxy density data are shown in Figure 7. The most stringent constraints on β and R_c are imposed by the fit to the X-ray imaging data represented by the dashed contour (this is

TABLE 3

BEST-FIT PARAMETER VALUES FOR COMA CLUSTER FROM OPTICAL DATA

Parameter	Velocity Dispersion	Galaxy Density
R_c	2′59(...; ...)[a]	9′00(+3′22; −2′10)
β	0.76(+0.16, −0.14)	1.56(...; −1.09)[a]
W_0	8.86(...; −2.00)[a]	8.78(...; −0.78)[a]
T_0 (keV)	9.00[b]	9.00[b]
n_0 ($\times 10^{-3}$ cm^{-3})	2.77[b]	2.77[b]
Σ_0 (galaxies deg^{-2})[c]	...	1094.3(+407.4; −410.2)
χ^2 (dof)	14.98 (11)	4.91 (11)

[a] Indeterminate error bound.

[b] Parameter held fixed at value from X-ray analysis.

[c] Central galaxy density.

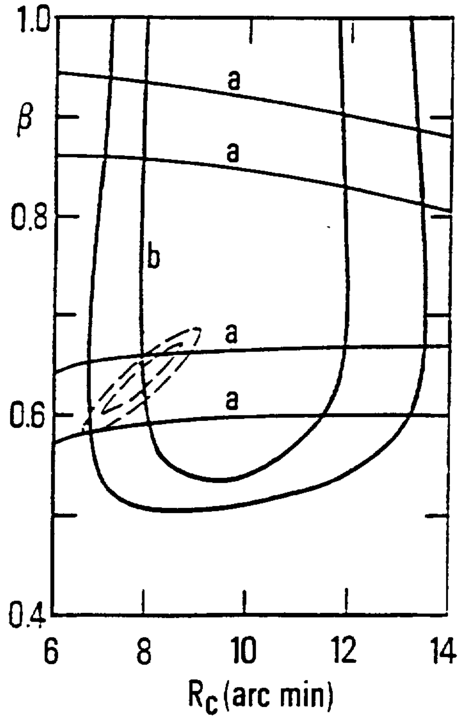

FIG. 7.—Results of fits to the projected velocity dispersion (*a*) and surface galaxy density (*b*). Two-dimensional χ^2 contours (at the 68% and 90% confidence levels) for β vs. R_c. The dashed contours are the results of the fit to the IPC data.

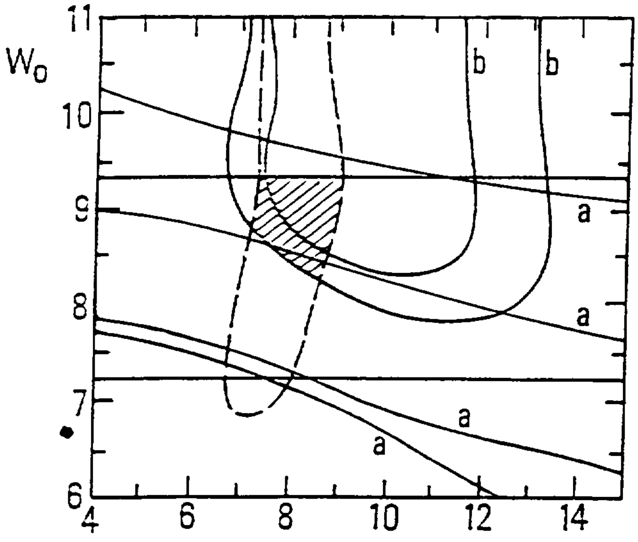

FIG. 8.—Results of the fits to the projected velocity dispersion (*a*) and surface galaxy density (*b*). Two-dimensional χ^2 contours (at the 68% and 90% confidence levels) for W_0 vs. R_c. The dashed contours are the results of the fit to the IPC data (at the 90% confidence level), while the straight lines arise from fits to the spectral data (also at the 90% confidence level). The dashed area indicates the region of overlap between the fits to the X-ray and optical data.

the same set of contours as in Fig. 3). The optical data analysis is fully consistent with this allowed region of parameter space.

The χ^2 contours (68% and 90% confidence levels) for the gravitational potential W_0 versus the core radius R_c are presented in Figure. 8 The figure-shaped dashed contour is from the X-ray imaging data for a fixed central temperature $kT_0 \sim 9$ keV, while the two horizontal lines define the allowed region from the fits to the X-ray spectral data (see Fig. 4). Both of these contours were determined at the 90% confidence level. The results of the fits to the X-ray and optical data show a large region of overlap for parameter ranges of $W_0 = 8.2$–9.3 and $R_c = 7'.3$–$9'.2$. This range is consistent with previously known values of W_0 (8.5) and R_c ($8'.5$) for the Coma Cluster (Merritt 1987). Limits on the central gas temperature are imposed by the fits to the X-ray spectral data (Fig. 4). For the allowed range of W_0 just quoted above, we find that $T_0 =$ 8.8–9.4 keV.

Additional proof that the X-ray and optical data are consistent is given by the acceptable values of χ^2 obtained when the optical data are fitted with the model parameters fixed to the best-fit values from the X-ray analysis (see Tables 1 and 2). The χ^2 values in this case are 17.25 and 12.31 for the velocity dispersion and galaxy density profiles, respectively, both for 14 degrees of freedom.

6. DISCUSSION

From the joint analysis of the X-ray and optical data, we find an acceptable fit to the CFF nonpolytropic model with the following parameter values: $\beta \equiv (0.59$–$0.68)$; $R_c \equiv (7'.3$–$9'.2)$; $W_0 \equiv (8.2$–$9.3)$; $T_0 \equiv (8.8$–$9.4)$ keV; and $n_0 \equiv (2.57$–$3.03) \times 10^{-3}$ cm^{-3}. The central velocity dispersion, σ_0, is a derived parameter based on the definition of β; we find that it lies in the interval (900–1000) km s^{-1}. In Figure 9 we show the temperature and density distributions of the intracluster gas for parameter values taken at the midpoint of the above intervals. The truncation radius of the cluster (where $\rho_G = \sigma = 0$) is ~ 15 Mpc.

The *ROSAT* all sky survey data for Coma obtained values of $\beta = 0.75 \pm 0.03$ and $R_c = 10'.6 \pm 0'.6$ from an azimuthally averaged surface brightness profile (Briel, Henry, & Böhringer 1992). In an analysis which considered the ellipsoidal shape of the X-ray emission from the Coma Cluster, Davis & Mushotzky (1993) obtained values of $\beta = 0.84 \pm 0.10$ and $R_c = 16'.3$ ($+5'.3$, $-3'.2$). These values are indeed different from those we quote above, which were obtained using the so-called north data set from the *Einstein* IPC (see the discussion at the beginning of § 3). However, as Figures 7 and 8 show, these other sets of values are fully consistent with the optical results (as represented by the contours labeled a and b), and thus our conclusions regarding the validity of the CFF nonpolytropic model remain unmodified.

Figures 10*a* and 10*b* show the integral binding and gas mass distributions and the contribution of the gas to the total virial

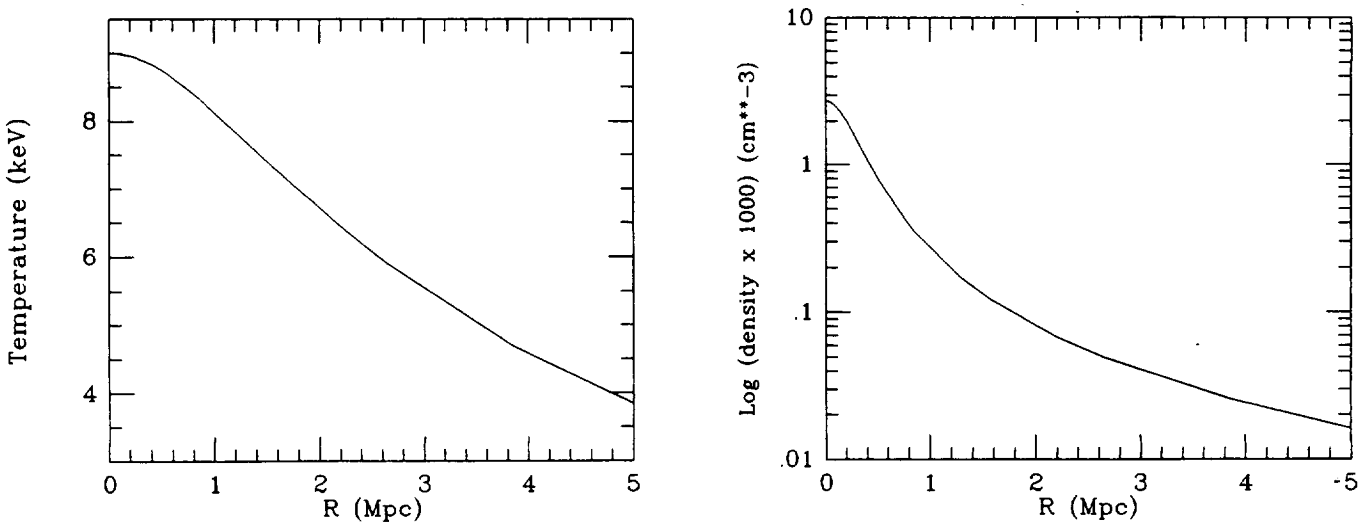

FIG. 9*a*

FIG. 9*b*

FIG. 9.—(*a*) Gas temperature and (*b*) density profiles of the best-fit nonpolytropic model for the combined analysis of the X-ray and optical data of Coma Cluster.

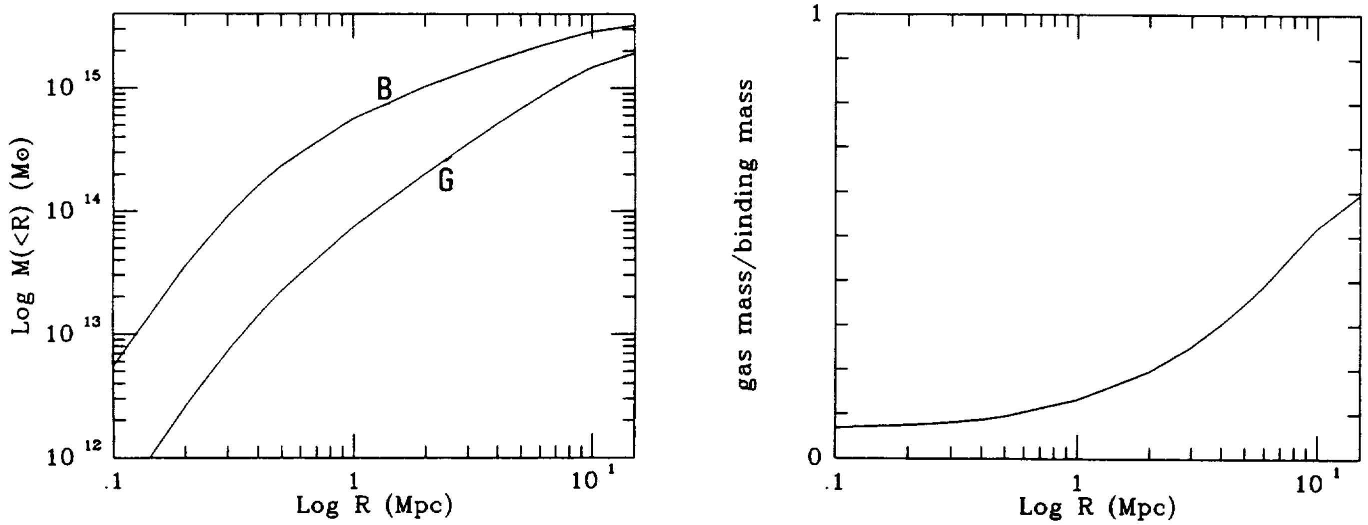

FIG. 10a

FIG. 10b

FIG. 10.—(*a*) Binding (B) and gas (G) mass profiles of the Coma Cluster. (*b*) Contribution of the gas to the total virial mass as a function of radius.

mass of the cluster. The total binding masses within 1 h_{50}^{-1} Mpc ($\sim$24′) and 5 h_{50}^{-1} Mpc ($\sim$122′) are $5.65 \times 10^{14}\ h_{50}^{-1}\ M_\odot$ and $1.96 \times 10^{15}\ h_{50}^{-1}\ M_\odot$, respectively. These values are in agreement with those reported by Hughes (1989) for the mass-follows-light model and more general binding mass distributions. Watt et al. (1992) quote a total cluster mass within 1 Mpc in the range 4.2–$5.2 \times 10^{14}\ h_{50}^{-1}\ M_\odot$ from their X-ray spectral image of the Coma Cluster obtained with a coded mask telescope. The slight difference compared to our reported mass is mainly due to the difference between our temperature profile and the isothermal distribution used to analyze their data.

At a radius of $\sim 2\ h_{50}^{-1}$ Mpc, within which the IPC imaging X-ray data define the gas density relationship, about 20% of the binding mass may be accounted for by the intracluster gas. Beyond this radius we rely on an extrapolation of the gas density distribution based on the model fitting results. At 5 h_{50}^{-1} Mpc for the nominal parameter values, the contribution is $\sim$35%, clearly within the range 16%–53% estimated by Hughes (1989). Varying the values of the parameters R_c, W_0, and T_0 through their allowed ranges introduces a negligible variation of this value. On the other hand, a more significant change arises from variation of the value of β; smaller β values will increase the relative contribution of the gas to the total binding mass. For example, for $\beta = 0.63$ the gas to binding mass ratio (at ratio (at 5 h_{50}^{-1} Mpc) increases to $\sim$44%. To better define this quantity requires imaging data to large radii and spatially resolved X-ray spectra.

The CFF nonpolytropic model gives mass-to-light ratios of 157 $h_{50}\ M_\odot/L_\odot$ and 163 $h_{50}\ M_\odot/L_\odot$ within 1 h_{50}^{-1} Mpc and 5 h_{50}^{-1} Mpc, respectively, where we have assumed total (deprojected) blue luminosities of $0.36 \times 10^{13}\ h_{50}^{-2}\ L_\odot$ (1 h_{50}^{-1} Mpc) and $1.2 \times 10^{13}\ h_{50}^{-2}\ L_\odot$ (5 h_{50}^{-1}) Mpc (from Kent & Gunn 1982; see Hughes 1989).

7. CONCLUSIONS

As we have shown in this paper, the nonpolytropic model originally formulated by CFF is fully consistent with the density and temperature distributions of the gas and galaxies in the Coma Cluster. The principal assumption of this model is that the ratio of the temperatures of the gas and the galaxies is constant throughout the cluster. If gravitational collapse were the only source of energy input to the gas and galaxies, then one would expect the ratio of these temperatures (i.e., β) to be unity. In our fits to the Coma data presented here, we determine a best-fit value of $\beta = 0.64$. Others (Briel et al. 1992; Davis & Mushotzky 1993) have obtained β values in the range 0.75–0.84.

As numerous authors have pointed out (Jones & Forman 1984; White 1991; David, Forman, & Jones 1991), values of β less than unity require an additional source of energy input to the gas (or a mechanism for cooling the galaxies). White (1991) has studied the energetics associated with metal enrichment of the intracluster medium and considered energy input from ram pressure stripping and galactic winds (see also David et al. 1991). He shows that while the energy input from gas stripping processes enters as σ^2 (as we also state in § 2 above), energy input from galactic winds depends on the depth of the potential well of the individual galaxy, as well as the wind speed, and not only on σ^2. However, for rich massive clusters (like Coma) the effects of galactic winds on the energetics of intracluster gas may be marginal ($\sim$10%), merely because the average galaxy velocity through the cluster is so much higher than the average galaxy wind velocity.

The validity of the CFF nonpolytropic model (given the current X-ray and optical data) suggests that a significant fraction of the thermal energy contained in the hot gas in the Coma Cluster may have become from the ram pressure stripping of galaxies by the ambient cluster medium. This should also be the situation for other rich galaxy clusters, while less massive systems should show more evidence for the collective effects of winds from individual galaxies. We look forward to the imminent arrival of greatly improved X-ray data on clusters of galaxies from *ASCA* (*Astro D*), which should allow us to begin discriminating among the various scenarios for the sources of energy input to and transport within the hot intracluster gas of clusters of galaxies.

This work was partially supported by funds from the Smithsonian Institution and the Instituto di Astrofisica Spaziale. J. P. H. also acknowledges support from NASA grants NAG8-699 and NAG 8-181. We appreciate Larry David's careful reading of the manuscript.

REFERENCES

Abramopoulos, F., & Ku, W. H. 1983, ApJ, 271, 446
Avni, Y. 1976, ApJ, 210, 642
Blumenthal, G. R., Faber, S. M., Primack, J. R., & Rees, M. J. 1984, Nature, 311, 517
Branduardi-Raymont, G., Fabricant, D., Feigelson, E., Gorenstein, P., Grindlay, J., Soltan, A., & Zamorani, G. 1981, ApJ, 248, 55
Briel, U. G., Henry, J. P., & Böhringer, H. 1992, A&A, 259, L31
Cavaliere, A., & Fusco-Femiano, R. 1976, A&A, 49, 137
———. 1978, A&A, 70, 677
———. 1981, A&A, 100, 194 (CFF)
David, L. P., Arnaud, K. A., & Forman, W., & Jones, C. 1990, ApJ, 356, 32
David, L. P., Forman, W., & Jones, C. 1991, ApJ, 380, 39
David, L. P., Hughes, J. P., & Tucker, W. H. 1992, ApJ, 394, 452
Davis, D. S., & Mushotzky, R. F. 1993, AJ, 105, 409
De Young, D. S. 1978, ApJ, 223, 47
Giacconi, R., et al. 1979, ApJ, 320, 540
Gorenstein, P., Fabricant, D., Topka, K., Harnden, F. R., Jr., & Tucker, W. H. 1978, ApJ, 224, 718
Gull, S. F., & Northover, K. J. 1975, MNRAS, 173, 585
Hughes, J. P. 1989, ApJ, 337, 21
Hughes, J. P., Butcher, J. A., Stewart, G. C., & Tanaka, Y. 1993, ApJ, 404, 611
Hughes, J. P., Gorenstein, P., & Fabricant, D. 1988a, ApJ, 329, 82
Hughes, J. P., Yamashita, K., Okumura, Y., Tsunemi, H., & Matsuoka, M. 1988b, ApJ, 327, 615
Jones, C., & Forman, W. 1984, ApJ, 276, 38
Kent, S. M., & Gunn, J. E. 1982, AJ, 87, 945
Kent, S. M., & Sargent, W. L. 1983, AJ, 88, 697
King, I. R. 1966, AJ, 71, 64
Lampton, M., Margon, B., & Bowyer, S. 1976, ApJ, 208, 177
Larson, R. B., & Dinerstein, H. L. 1975, PASP, 87, 911
Lea, S. M. 1975, ApJ, 16, L141
Merritt, D. 1987, ApJ, 313, 121
Mitchell, R. J., & Culhane, J. L. 1977, MNRAS, 178, 75p
Mitchell, R. J., Culhane, J. L., Davison, P. J., & Ives, J. C. 1976, MNRAS, 176, 29p
Raymond, J. C., & Smith, B. W. 1977, ApJS, 35, 419
Rood, H. J., Page, T. L., Kintner, E. C., & King, I. R. 1972, ApJ, 175, 627
Serlemitsos, P. J., Smith, P. W., Boldt, E. A., Holt, S. S., & Swank, J. H. 1977, ApJ, 211, L63
The, L. S., & White, S. D. M. 1986, AJ, 92, 1248
Tifft, W. G., & Gregory, S. A. 1976, ApJ, 205, 696
Watt, M. P., Ponman, T. J., Bertram, D., Eyles, C. J., Skinner, G. K., & Willmore, A. P. 1992, 258, 738
White, R. E., III. 1991, ApJ, 367, 69

The University of Alabama
Preprint Series in Astronomy

ABUNDANCE GRADIENTS IN COOLING FLOW CLUSTERS: *GINGA* LAC & *EINSTEIN* SSS SPECTRA OF A496, A1795, A2142 & A2199

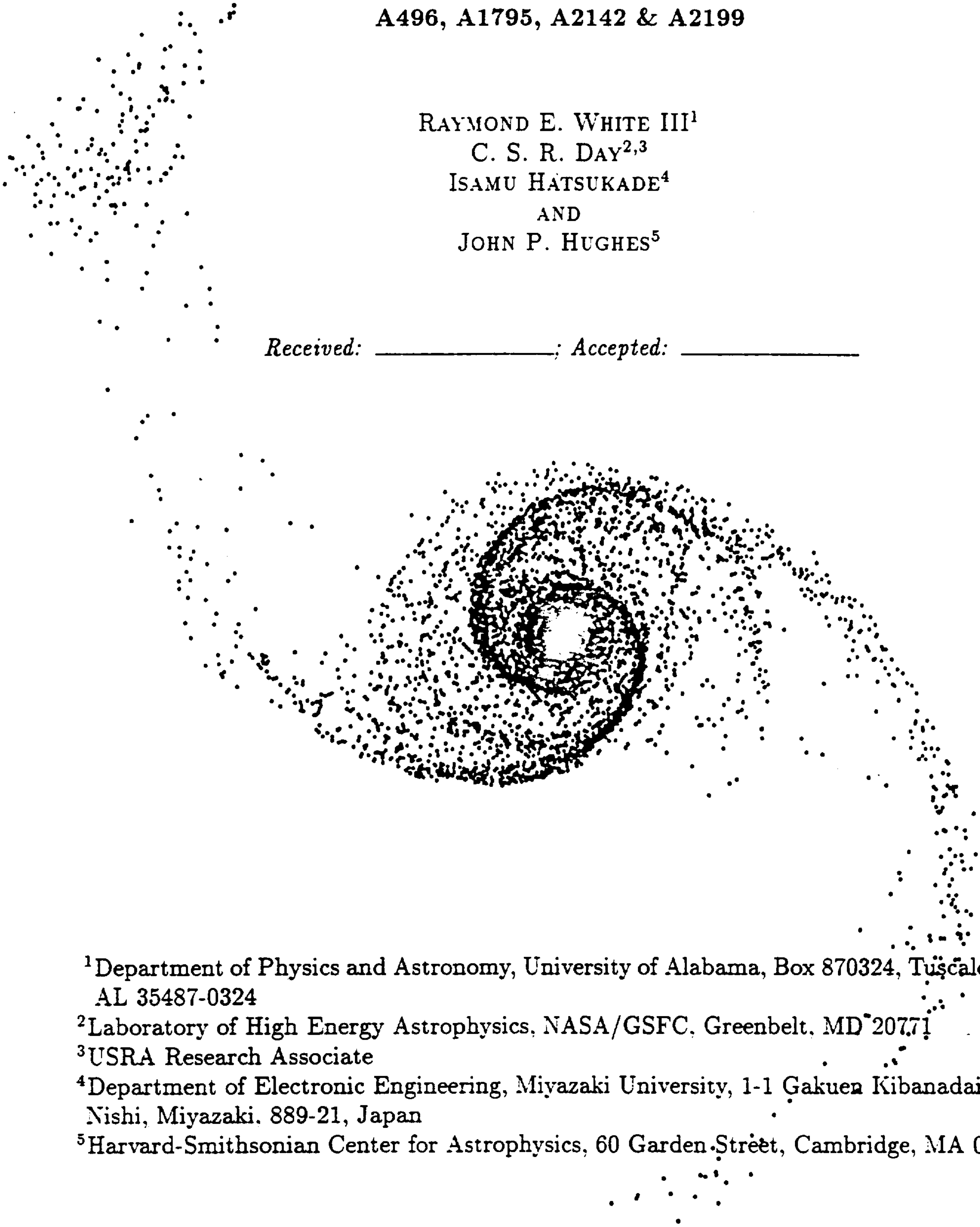

RAYMOND E. WHITE III[1]
C. S. R. DAY[2,3]
ISAMU HATSUKADE[4]
AND
JOHN P. HUGHES[5]

Received: _______________; *Accepted:* _______________

[1] Department of Physics and Astronomy, University of Alabama, Box 870324, Tuscaloosa, AL 35487-0324
[2] Laboratory of High Energy Astrophysics, NASA/GSFC, Greenbelt, MD 20771
[3] USRA Research Associate
[4] Department of Electronic Engineering, Miyazaki University, 1-1 Gakuen Kibanadai, Nishi, Miyazaki, 889-21, Japan
[5] Harvard-Smithsonian Center for Astrophysics, 60 Garden Street, Cambridge, MA 02138

Department of Physics and Astronomy, The University of Alabama
Box 870324, Tuscaloosa, Alabama 35487-0324 (205)348-5050

ABSTRACT

We analyze the *Ginga* LAC and *Einstein* SSS spectra of four cooling flow clusters. A496. A1795, A2142 and A2199, each of which shows firm evidence of a relatively cool component. The inclusion of such cool spectral components in joint fits of SSS and LAC data leads to somewhat higher global temperatures than are derived from the high energy LAC data alone. We find little evidence of cool emission outside the SSS field of view. Metal abundances appear to be centrally enhanced in all four cluster, with varying degrees of model dependence and statistical significance: the evidence is statistically strongest for A496 and A2142, somewhat weaker for A2199 and weakest for A1795. We also explore the model-dependence in the amount of cold, X-ray absorbing matter discovered in these clusters by White *et al.* (1991).

Subject headings: galaxies: abundances — galaxies: clustering — galaxies: intergalactic medium — galaxies: X-rays — X-rays: general

1. INTRODUCTION

Some of the most accurate temperatures and iron abundances available for the hot gas in many galaxy clusters have been obtained from X-ray spectra taken with the Large Area Counters (LAC) on the *Ginga* satellite (Takano *et al.* 1989; Hatsukade 1989; McHardy *et al.* 1990; Koyama *et al.* 1991; Day *et al.* 1991; Arnaud *et al.* 1991; Birkinshaw *et al.* 1991; Ikebe *et al.* 1992; Allen *et al.* 1992; Arnaud *et al.* 1992; Johnstone *et al.* 1992; Hughes and Tanaka 1992; Hughes *et al.* 1993). However, with an effective lower energy limit of ~ 1 keV, the LAC was not very sensitive to the spectral signatures of cooling flows which occur in the centers of many clusters. In contrast, the lower-energy *Einstein Observatory* Solid State Spectrometer (SSS) and Focal Plane Crystal Spectrometer (FPCS) were particularly sensitive to emission from cooling flows passing through temperatures $kT \lesssim 1$ keV (Mushotzky and Szymkowiak 1988; Canizares, Markert and Donahue 1988). Recent re-analysis of cluster SSS spectra has also revealed large quantities of relatively cold, X-ray-absorbing gas in many cooling flow clusters, quantities well in excess of the Galactic column of cold material in their lines of sight (White *et al.* 1991, hereafter WFJMA). This intrinsic absorption is attributed to the accumulation of cooling flow condensates and may account for much of the total material likely to have been accreted during the lives of the cooling flows (WFJMA). Wang & Stocke (1993) also found evidence of absorption in *Einstein* IPC spectra of distant clusters. Furthermore, spatially resolved *ROSAT* PSPC spectra of the copious cooling flow cluster A478 confirm the SSS evidence for an absorption component and also show that it is indeed confined to the cooling flow (Allen *et al.* 1993).

While many clusters have had analyses of their SSS or LAC spectra published, only one cluster, A478, has had its LAC and SSS data analyzed together, although the spectral models were not fit simultaneously (Johnstone *et al.* 1992). Joint analyses of SSS and LAC spectra are particularly informative because their different passbands provide complementary constraints on spectral models, particularly when their differing fields of view are taken into account: the SSS had a circular field of view with a $6'$ diameter (flat top), while the LAC had a much larger, elliptical field of view, $1° \times 2°$ (FWHM). The complementary nature of these data is illustrated by considering a cluster which is largely isothermal except for a central cooling flow which is cooling from the same temperature as the exterior cluster gas. If such a cluster were nearby, a centered SSS spectrum would be dominated by the cooling flow emission, while the LAC spectrum would include emission from the entire cluster. The cooling flow spectrum would be determined in part by its initial temperature, but this temperature would tend to be underestimated by an analysis of the soft SSS spectrum alone. The LAC spectrum, in turn, would provide an accurate global temperature and abundance, but would not be able to constrain the properties of the cooling flow (accretion rate, abundances, internal absorption) very well because much of the cooling flow emission and the effects of internal absorption would be most evident at energies lower than the LAC passband.

The power of joint spectral analysis is best realized by fitting the complementary spectra simultaneously. Hughes and Tanaka (1992) simultaneously analyzed the *Einstein* IPC and *Ginga* LAC spectra of A665 and were able to constrain its temperature distribution. These authors found this could not have been achieved by analyzing the data sets separately. Moreover, simultaneous fitting allows more accurate assessment of the parameter uncertainties, since all the relevant model fitting parameters can co-vary in the course of error analysis.

Inspection of the isothermal fits to LAC spectra in Hatsukade (1989) reveals persistent positive residuals below ~ 2 keV in several clusters known to have cooling flows. Whether these positive soft residuals are due to central cooling flows or, say, to cool emission in the outer parts of clusters may be distinguished by a joint analysis of the SSS and LAC spectra. If the cool emission is fully accounted for within the smaller SSS field-of-view, the cool emission seen in the LAC spectra is not likely to come from cluster exteriors. The differing fields of view can also be exploited to determine whether there are gradients in abundances or cool X-ray absorbing material.

In this paper, we investigate these possibilities with a joint analysis of the LAC and SSS X-ray spectra for four clusters, A496, A1795, A2142 and A2199. In §2 we describe how the cluster X-ray spectral data were reduced. We analyze the four individual clusters in §3, in order of Abell number (which are in right ascension order). A2199 and A496 have the highest quality data, followed by A1795, while A2142, the most distant cluster of the four, has the poorest statistics. We summarize and further discuss our results in §4. Imaging data will be incorporated in later studies of individual clusters.

2. DATA REDUCTION

2.1 *Ginga LAC spectra*

The *Ginga* observations presented here of A496, A1795 and A2142 have been analyzed before by Hatsukade (1989), who primarily investigated isothermal models. For these clusters, we use a similar set of reduced *Ginga* data as Hatsukade (1989). Analysis of the *Ginga* observations of A2199 has not been previously published.

The eight Large Area Counters (LAC) on *Ginga* covered the energy range 1–37 keV with 48 channels and an energy resolution of 18% at 6 keV. The (unimaged) field of view was 1° × 2° FWHM and the combined geometric collecting area was 4,000 cm^2. Descriptions of *Ginga* and the LAC can be found in Makino *et al.* (1987) and Turner *et al.* (1989), respectively. The data for A496, A1795 and A2142 are collected from the top and middle of the three LAC layers, while the data for A2199 are from the top layer alone. A log of the *Ginga* observations is given in Table 1. The *Ginga* observations of these four clusters yielded spectra integrated over the entire cluster and their immediate surroundings with high signal-to-noise but modest spectral resolution.

Of primary concern when reducing *Ginga* data from moderate to faint sources is the proper subtraction of the background, both X-ray and non-X-ray. We adopt the most straightforward way of removing the background: subtracting an observation of a nearby blank field taken on an adjacent day. By observing a nearby field, the dependence of the diffuse X-ray background on sky position is accounted for, while observing on an adjacent day ensures that the geomagnetic conditions of the background closely match those of the cluster. In addition, we discard data collected from the five (of fifteen) satellite orbits per day which passed through the South Atlantic Anomaly, thereby incurring a high background.

Each spectrum was associated with a response matrix tailored to the gain state of the LAC at the time of the observation. To guard against misinterpreting subtle spectral features caused by residual uncertainties in the response matrix, we followed the standard practice of adding systematic errors of 1% to the spectral (PHA) data. We ignored PHA channels 1–2, which do not contain valid data, and high energy channels where the sensitivity falls off, leaving an energy range of 1.2–17.4 keV. A few channels in some of the cluster spectra were rebinned to improve statistics.

2.2 Einstein SSS spectra

We extracted the SSS spectra of the four clusters from the HEASARC data base (see Table 1 for the observation log). Ice accumulated on the spectrometer entrance window in a time variable manner (through a series of frost and de-frost cycles), causing variable absorption of soft X-rays, so each spectral data file requires its own response matrix. The latest models of ice buildup were incorporated into the response matrix generation and are advertised to work best for spectra in which the ice parameter changes by less than 10% during the integration. The new ice models obviate the inclusion of the previously recommended 2% systematic errors (Christian *et al.* 1992). The statistical errors are far larger than any residual systematic errors. PHA channels 1 and 86–94 were ignored, leaving an approximate energy range of 0.5–4.5 keV, which overlaps the low energy *Ginga* LAC spectral coverage. Some channels were rebinned to improve statistics. To analyze the SSS spectra, we followed the detailed prescription given by Drake, Arnaud and White (1992), which describes how to subtract the two SSS background components (see Szymkowiak 1986 and WFJMA).

3. DATA ANALYSIS

The *Ginga* LAC spectra of three of these clusters are among the eleven analyzed previously by Hatsukade (1989), who fit a variety of spectral models: thermal bremsstrahlung, bremsstrahlung plus one and two emission lines (due to iron Kα and Kβ), and collisional ionization equilibrium (CIE) models based on the emissivity calculations of Masai (1984). An additional power-law component was considered for two clusters which are not in the current subset.

The *Einstein* SSS spectra of these clusters were previously analyzed by Mushotzky (1984), Mushotzky and Szymkowiak (1988) and WFJMA. In re-analyzing nearly all the clusters in the SSS database, WFJMA discovered the need for considerable amounts of intrinsic absorption in most of the clusters with cooling flows. As mentioned above, this intrinsic absorption component tends to be well in excess of the Galactic column, and was attributed to the accumulation of cooling flow condensates over the lives of the cooling flows.

We used the XSPEC (version 8.33) software package to individually and simultaneously analyze the SSS and LAC spectra for each cluster. We fitted a variety of spectral models, including single- and dual-temperature thermal models, and thermal plus cooling flow models, among others. In models with two emission components, we also allowed the abundances of the two components to vary independently. The results of the model fits are listed in Tables 2-5, the entries of which are described in the notes to Table 2: for brevity we will refer to specific model results by table and line number: *e.g.* T2.1 refers to line 1 of Table 2. The results of these fits are now described for each cluster in turn.

3.1 Abell 496

Abell 496 is a Bautz-Morgan type I cluster with a central cD. At a redshift $z = 0.0320$, the luminosity distance to A496 is 193 h_{50}^{-1} Mpc and $1' = 53$ h_{50}^{-1} kpc (where h_{50} is the Hubble constant in units of 50 km s^{-1} Mpc^{-1} and we take $q_0 = \frac{1}{2}$, so the angular diameter distance is 182 h_{50}^{-1} Mpc). The LAC field of view (FWHM) encompasses $3.2 \times 6.4 h_{50}^{-1}$ Mpc at this distance, while the SSS field of view has a $318 h_{50}^{-1}$ kpc diameter. The cluster appears dynamically relaxed, since it does not have much velocity or spatial substructure (Zabludoff, Huchra & Geller 1990, hereafter ZHG) and its IPC X-ray images have smooth isophotes in the central regions. The IPC images show no serendipitous sources with sufficient flux to be significant compared to that of the cluster. The nominal center of the SSS field of view is 0.24′ from the IPC X-ray peak, while the nominal center of the larger LAC field of view is 4.6′ away from the IPC X-ray peak.

The presence of a cooling flow in A496 was first posited by Heckman (1981) on the basis of its central Hα emission, thought to be due to cooling flow condensates cooling through 10^4 K. More recent optical observations show extended emission (Cowie *et al.* 1983, hereafter CHJY). Nulsen *et al.* (1982) found a soft X-ray component in the *Einstein* SSS spectra for this cluster and estimated a cooling accretion rate of ~ 200 $M_\odot$ yr^{-1}. Subsequent analysis of SSS spectra by Mushotzky (1984) and Mushotzky and Szymkowiak (1988) indicated an accretion rate of 200–400 $M_\odot$ yr^{-1}, while Canizares *et al.* (1988) derived upper limits of 200 and 310 $M_\odot$ yr^{-1} from individual X-ray lines in FPCS spectra. Further imaging analyses of IPC data by Arnaud and Fabian (1987) and Thomas *et al.* (1987) derived a total accretion rate of ~100–120 $M_\odot$ yr^{-1} and a cooling radius of $\sim$ 3.0′–3.4′. The larger of these cooling radius estimates extends 0.4′ beyond the SSS field of view. However, in both of these imaging analyses, the age of the cooling flow was assumed to be 2×10^{10} yr. Depending upon the cooling time criterion adopted, this may lead to an overestimate of the cooling radius by as much as a factor of $\gtrsim 2$ if the true age is $\lesssim 10^{10}$ yr, given the observed density profile. Thus, the bulk of the cooling flow emission may be within the SSS field of view, but we test this below.

3.1.1 Separate LAC and SSS Spectral Fits

We fitted a Raymond-Smith (hereafter denoted RS) isothermal model for the X-ray emission from an optically-thin hot plasma in collisional ionization equilibrium (Raymond & Smith 1977) to the LAC data for comparison with the results of Hatsukade (1989). In XSPEC, the cosmic abundance of iron (by number) relative to hydrogen is −4.5 dex, while Hatsukade (1989) adopted a value of −4.4 dex (Allen 1976). Our abundance determinations (which are driven mostly by iron) will then be ~1.26 times larger than Hatsukade's for the same iron fraction. For this comparison we adopted the same Galactic line-of-sight hydrogen column density as Hatsukade (1989): $N_H = 5 \times 10^{20}$ cm^{-2} (N_H is used to parameterize the soft X-ray absorption due to cool intervening Galactic material — see Morrison and McCammon 1983). Although the best fit is not good (the reduced χ^2 per degree of freedom $\chi^2_\nu = 2.21$ for $\nu = 19$ degrees of freedom: see line 1 of Table 2, denoted T2.1), we found the temperature and abundance to be well-determined, with $kT = 3.97$ (3.91–4.04) keV and $A = 0.48$ (0.43–0.53), where A is the heavy element abundance relative to the cosmic value (A is assumed to be the same for all elements) and the values in parentheses are 90% confidence intervals (see Table 2, where the 90% confidence limits vertically bracket the best-fit values). Using Masai emissivities, Hatsukade (1989) found a slightly smaller temperature, $kT = 3.91$ (3.84–3.97) keV, and a slightly larger iron abundance, $A = 0.53$ (0.48–0.58) (adjusting upward a factor of 1.26), which are nonetheless within the 90% confidence intervals of the present values. If the column density of hydrogen is allowed to vary freely, it is not well-determined. Zero column provides the smallest χ^2, reducing χ^2 by 10.6 while reducing the number of degrees of freedom ν by one. That the previous model (see T2.1) has larger χ^2 is due to the fact that there is excess emission compared to the model at the lowest energies, which becomes even more obvious when the minimum expected absorption (due to the Galaxy) is taken into account in the model. This excess emission is likely due to a relatively cool component analyzed further below.

We also analyzed the two SSS spectra (of three total) for which the ice varied by less than 10% in the course of the integration (see Table 1). We first fitted isothermal models and found an excellent fit ($\chi^2_\nu = 0.80$ for $\nu = 148$: see T2.2) with a somewhat lower temperature, $kT = 3.68$ (3.08–4.34) keV, than the LAC data indicated, although the LAC temperature is within the 90% confidence upper limit. The derived fractional abundance $A = 1.50$ (0.94–2.28) is supersolar, substantially higher than that of the LAC spectrum. Fixing the abundance of the SSS spectra to match the half-solar value found in the LAC spectrum produced a significantly worse fit, with $\Delta\chi^2 = +15$ while $\Delta\nu = +1$; an F-test shows that the previous variable abundance fit is preferred with > 99.9% confidence. This is a strong indication of enhanced abundances in the SSS spectra relative to the more global LAC spectrum. WFJMA also noted a roughly cosmic abundance for the cooling flow component in the SSS data of this cluster, although no errors were given. They fitted a two-component emission model to the data, with one component being an isothermal model at the *EXOSAT*-derived temperature of 4.8 keV (Edge *et al.* 1990) and the other an isobaric cooling flow model. We also found the large column density of X-ray absorbing material previously found in the SSS spectra by WFJMA. The best-fit value for this model is $N_H = 1.2(1.0\text{–}1.5)\times10^{21}$ cm^{-2}, which is twice the Galactic value interpolated from Stark *et al.* (1992), but we will show that the inferred amount is rather model dependent.

We also considered whether the high abundance seen in the SSS spectra may be an artifact of systematic errors in the ice model adopted for the SSS spectra. The generation of SSS response matrices depends on only one variable, the ice parameter appropriate for a given observation (see Table 1). The ice parameter has a maximum uncertainty of ±0.4 during the time these data were taken (Christian *et al.* 1992). We re-analyzed the SSS spectra using a response matrix characterized by an ice parameter 0.4 larger than the best-estimate value used above. This increases the amount of ice assumed to be on the SSS entrance window, so the inferred internal absorption will be reduced: in refitting our isothermal model, the best-fit absorption was brought down to $N_H = 6.9(4.7\text{–}9.4)\times10^{20}$ cm^{-2}, which is within $\sim 50\%$ of the Galactic value. The best-fit value of the fractional abundance was reduced to $A = 0.99$ (0.67–1.39), the 90% confidence range of which is still outside that of the more global LAC spectrum. Although systematic errors may make the absolute value of the central abundance somewhat insecure, the *existence* of a central enhancement seems more robust.

3.1.2 Joint Spectral Fits

3.1.2.1 Raymond-Smith Models

We next analyzed the LAC and SSS spectra jointly. The simplest plausible model is isothermal and assumes the SSS and LAC spectra are characterized by the same abundances and column density of cool absorbing matter. The normalizations were allowed to vary independently for the two instruments, to allow for their different fields of view. This model fit poorly, with $\chi^2 = 203.3$ for $\nu = 169$ ($\chi^2_\nu = 1.20$: see T2.3). Allowing an additional spectral component with the same temperature and abundance but with an intrinsic absorbing column (at the redshift of the cluster) in addition to a fixed Galactic column provided only a marginally improved fit. (Note that for this and subsequent analysis of the other clusters, when we are not directly comparing to the work of Hatsukade 1989, we use Galactic values of N_H derived from Stark *et al.* 1992, using K. Arnaud's GETNH program.) A much better fit was provided by a two-temperature model in which the cooler component was allowed an intrinsic absorbing column in addition to a fixed Galactic column: $\chi^2 = 163.3$ for $\nu = 167$ (so $\chi^2_\nu = 0.98$ and $\Delta\chi^2 = -40$ for $\Delta\nu = -2$; see T2.4). In this model the cool component is attributed to the cooling flow and its normalization was constrained to be the same in the SSS and LAC fields of view, which assumes that the cooling flow emission is fully contained in each.

Finally, we allowed the abundance to vary independently in each of the two temperature components, which provided a significantly better fit, with $\chi^2 = 153.6$ for $\nu = 166$ ($\chi^2_\nu = 0.93$; see T2.5). The improvement over the single-abundance model of T2.4 ($\Delta\chi^2 = -9.7$ for $\Delta\nu = -1$) is significant with $> 99.8\%$ confidence by the F-test. The best-fitting such two-temperature model is shown with the data in Figure 1, along with the residuals of the fit. This model has a hot component with $kT = 4.30$ (4.19–4.41) keV and a cooler component with $kT = 1.64$ (1.39–2.01) keV. The temperature χ^2 distributions are shown in Figure 2a where the dashed horizontal lines represent the single-parameter 90% and 99% confidence levels (corresponding to $\Delta\chi^2 = +2.71$ and $+6.63$, respectively). The temperature of the hotter component is $\sim 8\%$ greater than that derived from the LAC spectrum alone. The fractional abundance associated with the hotter component is $A_{hot} = 0.47$ (0.42–0.53), while that of the cool component exceeds the cosmic value: $A_{cool} = 2.63$ (1.01–>5). The χ^2 distributions for the abundances of the two temperature components are shown in Figure 3a, which shows that the abundance of the cool component, while having large errors, is nonetheless substantially greater than that of the hot component, at a confidence level of >99%. The ratio of model fluxes in the SSS and LAC fields of view is consistent with the ratio derived from IPC imaging data; the model fluxes were calculated in the 0.16–3.5 keV energy band appropriate to the background-subtracted, vignetting-corrected IPC images on the SAO CD-ROMs. The cooler spectral component of this model has an excess absorbing column density of $4.0(2.5\text{–}5.6)\times10^{21}$ cm^{-2}, nine times higher than the Galactic column. The N_H χ^2 distribution is illustrated in Figure 4a, where the Galactic value in the line of sight to A496 is also indicated. If the "intrinsic" absorption is distributed uniformly over the size of the cooling flow (with radius $R_{cool} \approx 100$ kpc), there would be $\sim 9 \times 10^{11} M_\odot$ of cool material. We considered a model which allowed the covering fraction of absorbing material to vary and the subsequent best-fit value was unity (so the fit was not improved), with a 90% confidence lower limit of $> 83\%$ coverage. However. since the intrinsic absorption is associated with the cool component in this spectral model. its total angular covering fraction may be substantially less than this if the cool emission component itself is clumped and the absorption is spatially correlated with the cool emission.

The column density associated with the cooler component of the two-temperature fit is three times larger than that inferred from the previous analysis of SSS spectra alone. This is because the best-fit temperature in the previous isothermal SSS analysis is larger than the temperature of the cooler component in the two-temperature fit and N_H is anticorrelated with the temperature: for a fixed spectral shape at low energies, the effect of reducing the temperature can be offset by increasing the absorbing column. This anticorrelation is illustrated in Figure 5, which shows the 1σ, 90% and 99% confidence contours for N_H *vs.* T in the previous isothermal fit to SSS data alone.

To test whether the intrinsic absorption is largely confined to the cooling flow (that is, within the SSS field of view), we considered a two-temperature, two-abundance model which allowed only one global value of absorbing column to be fit. The best-fitting such model is only marginally worse than the best model illustrated above, having $\Delta\chi^2 = +3.9$ for $\Delta\nu = 0$ (see T2.6), but the best-fit value of N_H is more than twice the Galactic value. This value is very close to that found in the previously described fit to the SSS data alone. which illustrates the insensitivity of the LAC data to N_H. Thus, we cannot demonstrate that the extra absorption is confined to the SSS field of view. However. it is unreasonable for the extra absorption to be due to an error in the estimate of the Galactic component. since typical errors in interpolating Galactic values on small angular scales from broad-beam surveys such as that of Stark *et al.* (1992) are only of order 10^{20} cm^{-2} (Elvis *et al.* 1986).

Although the model illustrated in Figures 1 and 2a–4a provide an excellent fit to the LAC and SSS data, inspection of the χ^2 residuals for the best-fitting two-temperature model above shows structure in the lowest-energy LAC channels which may suggest that the LAC sees somewhat more cool emission than the SSS. To test whether the bulk of the cool component is confined within the SSS field of view. we allowed the LAC and SSS normalizations for the cool component to vary independently. The resulting respective normalizations were the same within their errors and the fit was not significantly improved. In an additional test, we added a third temperature component to the model which could contribute only to the LAC spectrum. This LAC-only component ended up being very cool ($kT \approx 1$ keV) and significantly improved the fit, reducing χ^2 by ~ 12. However, this cool component contributed only 1–2% of the flux in the LAC passband. which is at the level expected from calibration uncertainties and unresolved background sources; thus there is little evidence of cool emission outside the SSS field of view. *ROSAT* imaging data will be incorporated in a subsequent paper.

3.1.2.2 Cooling Flow Models

In the previous two-temperature analysis we attributed the cooler of two temperature components to the cooling flow at the center of A496. However. a cooling flow spectrum is only roughly approximated by a single-temperature RS thermal model. We therefore investigated models incorporating a more realistic cooling flow spectral component in order to constrain the accretion rate and to assess the model-dependence of the high metal abundances and absorption columns we deduce for the cool component. We adopted the cooling flow spectral model of Mushotzky and Szymkowiak (1988), in its most recent implementation in XSPEC (v.8.33). There are six variables in the cooling flow model: the temperature from which gas cools T_{high}, the temperature to which gas cools T_{low}, the accretion rate $\dot{M}$ (which is the normalization), the fractional metal abundance A, the redshift z, and a slope parameter s for a temperature-dependent weighting of the isobaric emission measure *vs.* temperature relation (the slope is zero for an isobaric cooling flow). The bulk of the cooling flow emission will be radiated under roughly isobaric conditions in the outer half of the cooling flow. We find from XSPEC simulations that pure cooling flow spectra (with T_{low} below X-ray-emitting temperatures) are fit reasonably well by isothermal RS models with temperatures $\sim$ 2–3 times smaller than T_{high} (also see White and Sarazin 1987). The cooler component in the previously discussed two-temperature model thus has roughly the temperature one expects from a cooling flow starting at the higher of the two temperatures.

In our fits incorporating a cooling flow spectrum, we couple the cooling flow model to a RS isothermal model for the cluster emission exterior to the cooling flow. As with the previous two-temperature fits, we included a (fixed) Galactic absorption component and we associated an additional (variable) "intrinsic" absorption component with the cooling flow. In the cooling flow model we set T_{high} equal to the temperature of the exterior isothermal component, we fixed T_{low} at 0.1 keV (below the bulk of X-ray emitting energies), fixed the redshift, and set the cooling flow slope parameter to zero (for isobaric flow). The accretion rate, the abundances of the cooling flow and the exterior RS components, and the intrinsic absorption freely varied, while T_{high} was tied to and varied with the temperature of the exterior RS component.

We found an excellent fit for a model in which the cooling flow normalizations were the same for the SSS and LAC: $\chi^2_\nu = 0.91$ for $\nu = 167$ (see T2.7), which has $\Delta\chi^2 = -1.9$ (for $\Delta\nu = +1$) compared to the best two-temperature RS model with tied cool component normalizations. The accretion rate was found to be 154 (127-188) $M_\odot$ yr^{-1}, consistent with previous determinations, but with smaller errors. The abundance of the cooling flow, $A_{cf} = 3.79$ (1.58->9), was found to be significantly greater than that of the exterior gas, $A_{hot} = 0.25$ (0.16-0.37). The χ^2 distributions for the abundances of the two spectral components are shown in Figure 6a. Despite its large error, the cooling flow abundance is greater than that of exterior gas at $> 99\%$ confidence, which is consistent with the results of the previous two-temperature analysis. The ratio of model fluxes in the SSS and LAC fields of view are again consistent with that derived from IPC imaging data. The best-fitting value of intrinsic N_H is very close to that of the previous analysis: $N_H = 3.8(3.2–4.6)\times 10^{21}$ cm^{-2}. Using a similar RS plus cooling flow spectral model (but with the cluster temperature fixed), WFJMA found a lower value for the intrinsic column density: $N_H = 2 \times 10^{21}$ cm^{-2}. This disparity is largely due to WFJMA adopting the *EXOSAT*-derived temperature of 4.8 kev (Edge *et al.* 1990), which is ~15–20% higher than that derived by the higher quality *Ginga* spectrum. We further assessed the significance of the relatively enhanced cooling flow abundance by considering a model with only a single variable abundance for both the cooling flow and RS components. This model (see T2.8) produced a significantly larger χ^2 ($\Delta\chi^2 = +17$ for $\Delta\nu = +1$) than the dual-abundance model of T2.7, which is preferred with 99.99% confidence with the *F*-test. To test whether the extra absorption component is confined to the SSS field of view, we considered a model with one variable global value of N_H (see T2.9), rather than a variable absorption component intrinsic to the cooling flow; this provided a much worse fit ($\Delta\chi^2 = +40$ for $\Delta\nu = 0$) than the model of T2.7. This suggests that the extra absorption is mostly confined to the SSS field of view (but recall that a similar global-N_H model employed in a previous dual-RS fit [T2.6] did *not* show such a pronounced degradation in the quality of the fit). A model allowing a partial covering fraction for the intrinsic absorption produced a best-fit value of unity and a 90% confidence lower limit of > 85% coverage. To assess whether the cooling flow emission extends outside the SSS field of view, we allowed the LAC and SSS cooling flow normalizations to vary independently. The fit was not significantly improved.

We conclude that A496 has a cool spectral component attributable to a central cooling flow. This cool component is associated with a large column density of X-ray absorbing material, but these data do not unambiguously show that it is confined to the SSS field of view. There appears to be an abundance gradient in A496, with abundances substantially larger at the center and declining outward. The amount of metals in the cooling flow is far larger than what could be produced by present levels of stellar mass loss, however, the metals could have been produced during the integrated history of mass loss in the central dominant galaxy and other galaxies in the core. There does not appear to be much cool emission outside the SSS field of view.

3.2 Abell 1795

Abell 1795 is a Bautz-Morgan type I cluster with a central cD. At a redshift $z = 0.0620$, the cluster has a luminosity distance of 377 h_{50}^{-1} Mpc, and $1' = 96\ h_{50}^{-1}$ kpc (for an angular diameter distance of 335 h_{50}^{-1} Mpc). The central cD has a significant peculiar velocity, 370 km s^{-1}, given its cluster velocity dispersion of $\sigma = 773$ km s^{-1} (ZHG, Gebhardt and Beers 1991); more general velocity substructure is not apparent in its velocity histogram (ZHG). In the inner parts of the central cD, McNamara & O'Connell (1992) found a pronounced optical color gradient relative to that expected from a normal giant elliptical and attributed this to ongoing star formation in the surrounding cooling flow.

Einstein IPC X-ray imaging analyses find accretion rates ranging from ~340–400 $M_\odot$ yr^{-1} (Stewart *et al.* 1984, Arnaud and Fabian 1987). This range is similar to that deduced from SSS spectra by Mushotzky (1984) and Mushotzky and Szymkowiak (1988): 425–560 $M_\odot$ yr^{-1}. Arnaud and Fabian (1987) find a cooling radius of $\sim 2.2'$, well within the SSS field of view. The long optical filament discovered by CHJY (extending to $\sim 45''$ from near the center), which may be a cooling flow condensate, is also well within the SSS field of view.

IPC images of A1795 show that there are several compact sources in the LAC field of view (but outside the SSS field of view). The brightest of these sources is a Seyfert 1 galaxy (EXO 1346.2+2645). The flux from these sources is $\lesssim 3\%$ of the total in the *Einstein* passband, so their presence does not effect these spectral fits significantly. The nominal center of the SSS pointing is within $0.6'$ of the IPC X-ray peak, while the nominal center of the LAC pointing is within $8'$ of the X-ray peak.

3.2.1 Separate LAC and SSS Spectral Fits

The previous LAC analysis of Hatsukade (1989) found a collisional ionization equilibrium model temperature of $kT = 5.34$ (5.23–5.45) keV and an (adjusted) fractional iron abundance $A = 0.46$ (0.41–0.51), for an assumed Galactic hydrogen column of $N_H = 1.7 \times 10^{20}$ cm^{-2}. We fitted a RS isothermal model to the LAC spectrum alone with the same value of N_H and found a slightly higher temperature and lower abundance: $kT = 5.57$ (5.45–5.69) keV and $A = 0.43$ (0.38–0.48), with 90% confidence intervals which overlap those of Hatsukade (see T3.1). If the hydrogen column density is allowed to vary freely, it is not well-determined; the smallest χ^2 is associated with zero column, but χ^2 is reduced by only 2.4 for $\Delta\nu = -1$.

Of the six SSS spectra available for A1795, we analyzed three. Two of the omitted SSS spectra had ice variations of $\sim 50\%$ in the course of their integrations and the third omitted spectrum had twice as much ice as the remaining three (see Table 1). Our isothermal model fits to the SSS spectra have significantly lower temperatures than found in the LAC spectrum. With the abundance free to vary, the best-fitting temperature of an adequate fit ($\chi^2_\nu = 1.07$ for $\nu = 225$) is 3.67 (3.26–4.14) keV. The abundance is very low and poorly constrained, with a 90% confidence upper bound of 0.24 cosmic and no lower bound (see T3.2). However, fixing the abundance to that indicated in the LAC spectrum significantly worsened the fit ($\Delta\chi^2 = +9$ for $\Delta\nu = +1$; $\chi^2_\nu = 1.11$); an F-test shows that the previous fit with variable abundance is significantly better at the 99.5% confidence level.

3.2.2 Joint Spectral Fits

3.2.2.1 Raymond-Smith Models

Having the SSS spectra characterized by a temperature lower than that of the LAC spectrum motivated a two-temperature model jointly fit to the SSS and LAC data. This provided an improvement in χ^2_ν. The model is nearly the same type as used in A496, incorporating a fixed Galactic absorption column and an additional variable absorption component associated with the cooler of the two temperature components. As before, the additional "intrinsic" absorption was assumed to be at the redshift of the cluster. In this cluster, however, the abundance of the cool component was tied to that of the hot component since the SSS data provided such a poor constraint on the abundance. In modeling a cool component associated with the central cooling flow, we can safely assume that the SSS field of view encompasses all of the cooling flow emission, given the distance to A1795. (There is still the possibility of cool emission in the outer parts of the cluster where it could be detected by the LAC, but only a small projected portion of which would be detected by the SSS.) The best-fitting model is quite good ($\chi^2_\nu = 0.99$, $\nu = 244$) and is illustrated with the data in Figure 7. The temperatures of the two components are $kT = 5.73$ (5.59–5.87) keV and $kT = 0.74$ (0.58–0.90) keV (see T3.4); their χ^2 distributions are shown in Figure 2b. The overall fractional abundance is $A = 0.43$ (0.38–0.48) and its χ^2 distribution is illustrated in Figure 3b. When we allowed the abundance of the cool component to vary independently of that of the hot component, we found that the fit was not improved and the cool abundance was poorly constrained. Thus, these RS models provided no evidence of centrally enhanced abundances. The ratio of model fluxes in the SSS and LAC fields of view is consistent with that derived from IPC imaging data.

A substantial absorbing column is associated with the cool component, $N_H = 5.1(2.4\text{-}7.6)\times10^{21}$ cm^{-2}, which is $\sim$ 45 times larger than the line-of-sight Galactic column; Figure 4b shows the N_H χ^2 distribution. As we show below, this high value of N_H is very model-dependent, with much lower values provided by models incorporating cooling flow spectra.

This model provided a significantly better fit than simpler alternatives, the simplest being characterized by a single temperature, abundance and absorbing column. The best-fitting such model (see T3.3) had $\Delta\chi^2 = +42$ (for $\Delta\nu = +2$) relative to the previous two-temperature model. We further tested the significance of the cooler component by forcing the temperatures of the two components to be the same, but allowing one of the isothermal components to have intrinsic absorption at the cluster redshift (in addition to an overall absorption fixed at the Galactic value). The best-fitting such model had $\Delta\chi^2 = +46$ (for $\Delta\nu = +1$) compared to the previous two-temperature model with intrinsic absorption. The need for a cooler component is evidently extremely significant: the F-test shows that the improvement provided by the second temperature component is significant with > 99.99% confidence. We tested whether the "intrinsic" absorbing column is confined to the SSS field of view by forcing the two-temperature model to have only one global value of N_H. The best-fitting such model had $N_H = 3\times10^{20}$ cm^{-2}, three times the Galactic value, but provided a somewhat poorer fit, with $\Delta\chi^2 = +6.2$ for $\Delta\nu = 0$. The poorer fit is weak evidence for the extra absorption being confined to the SSS field of view, but the value of N_H is consistent with that indicated in the isothermal analysis of the SSS data alone (see T3.2), so the LAC data again provide a poor constraint on N_H and its coverage. We also considered a partial coverage model for the intrinsic absorption component (in a spectral model otherwise like that of T3.4) and found the best-fit value of the covering fraction to be unity (so the fit was not improved), with a 90% confidence lower limit of > 80% coverage.

As for A496, we tested whether the LAC saw significantly more cool emission than was in the SSS field of view by adding a third RS component to the LAC spectral model. The resulting best-fit χ^2 was not significantly improved and the contribution of the (cool) third component to the LAC passband was only $\sim$ 1%. As we saw before in A496, this is at the level expected from calibration uncertainties and unresolved background sources.

3.2.2.2 Cooling Flow Models

Since a central cool component was strongly indicated above, we also considered a spectral model incorporating a cooling flow component in order to constrain its accretion rate and assess the model dependence of the intrinsic N_H. Given the lack of evidence of enhanced abundances in the SSS spectra relative to the LAC spectrum, we initially tied the abundances of the two spectral components together. The cooling flow normalization $\dot{M}$ was taken to be the same in the LAC and SSS spectra. The best-fitting model is quite good, although not quite as good as the best-fitting two-temperature model described above: in this case, $\chi^2/\nu = 252.6/245$ ($\chi^2_\nu = 1.03$, see T3.5), so compared to the better fitting two-temperature model (T3.4), $\Delta\chi^2 = +10$ for $\Delta\nu = +1$. The exterior temperature, $kT = 6.07$ (5.85–6.33) keV, is $\sim$ 9% larger than in the previous two-temperature RS model. The fractional abundance $A = 0.45$ (0.40–0.50) is the same as derived previously. The intrinsic absorption, $N_H = 8.9(5.8\text{–}11.5)\times10^{20}$ cm^{-2} is $\sim$ 6 times smaller than that associated with the cool component of the previous model; this is still $\sim$ 8 times larger than the Galactic column in this line of sight and $\sim 10\%$ larger than the value found by WFJMA. The accretion rate is consistent with previous estimates: $\dot{M} = 411$ (290–533) $M_\odot$ yr^{-1}.

When we allowed the abundances of the cooling flow and RS components to vary independently, a slightly better fit was achieved, with $\Delta\chi^2 = -3.9$ for $\Delta\nu = -1$ (see T3.6); this improvement is significant at the 95% level by the F-test. The cooling flow abundance $A_{cf} = 0.58$ (0.46–0.71) ended up significantly larger than that of the hot component $A_{hot} = 0.14$ (0.04–0.37), with non-overlapping 90% limits, but A_{hot} is poorly determined. The χ^2 distributions for the abundances of the two spectral components are shown in Figure 6b. The ratio of model fluxes in the SSS and LAC fields of view is consistent with that derived from IPC imaging. We also tested whether this model allows the extra absorbing column to be confined to the SSS field of view: allowing only a global value of N_H led to a slightly worse fit, with $\Delta\chi^2 = +1.6$ for $\Delta\nu = 0$. The best-fit global value of N_H is ~ 4 times higher than the Galactic value (see T3.7) and several times higher than the plausible uncertainty in the Galactic value. However, given the comparable quality of the fit, we cannot prove that the extra absorption is confined to the SSS field of view. We also considered a partial covering model for the intrinsic absorption (in a model otherwise like that of T3.6) and found the best-fit value to be unity (so the fit was not improved), and the 90% confidence lower-limit was $> 45\%$ coverage.

We conclude that there is a cool spectral component attributable to a cooling flow in A1795. In contrast to A496, the evidence is mixed on there being a significant central abundance enhancement: the dual-temperature RS models show no evidence of a significant enhancement, while the poorer-fitting cooling flow models do show evidence of an enhancement. We found the amount of cool, X-ray absorbing material first found by WFJMA to be rather model-dependent, but still very substantial. We found no evidence in this data of the LAC seeing significantly more cool emission than the SSS.

3.3 Abell 2142

Abell 2142 is a Bautz-Morgan type II cluster, with a dominant pair of giant ellipticals at its center (Rood-Sastry type B), one of which has multiple nuclei (Hoessel 1980). With a redshift $z = 0.0899$, the cluster is the most distant in our sample: it has a luminosity distance of 551 h_{50}^{-1} Mpc, so $1' = 132$ h_{50}^{-1} kpc (for an angular diameter distance of 464 h_{50}^{-1} Mpc).

X-ray imaging analysis indicated the presence of a cooling flow with an accretion rate of ~ 55 $M_\odot$ yr^{-1} (Arnaud and Fabian 1987) and a cooling radius of $\sim 0.7'$. Previous analysis of SSS spectra provided an upper limit to the cooling flow accretion rate of $\dot{M} <$ 540 $M_\odot$ yr^{-1} (Mushotzky and Szymkowiak 1988). Since the cooling flow is contained in only $\sim 5\%$ of the SSS field of view, its emission is heavily diluted by hotter exterior gas.

The IPC image has three other sources in the *Ginga* field of view which are outside the SSS field of view: a K5 star (SAO 84114) and a Seyfert 1 galaxy (1556+259) very close together on the sky (Reichert *et al.* 1982) and a QSO (1557+272). They contribute only $\sim 2\%$ of the flux in the IPC field, so their contribution is negligible compared to that of the cooling flow. The nominal center of the SSS pointing is $0.53'$ from the IPC X-ray peak, while that of the LAC is $3.6'$ away.

3.3.1 Separate LAC and SSS Spectral Fits

Hatsukade (1989) previously found a temperature of kT = 8.68 (8.48–8.88) keV and an abundance of 0.35 (0.30–0.40) cosmic in the LAC spectrum. Our best-fitting RS isothermal model using the same value of N_H has a slightly larger temperature kT = 8.99 (8.78–9.18) and virtually identical fractional abundance A = 0.34 (0.29–0.39) (see T4.1). This isothermal model provides a formally excellent fit, with $\chi^2_\nu = 0.85$ for $\nu = 21$ (see T4.1). When N_H is allowed to vary freely, it is poorly determined and χ^2 is not significantly improved.

We also analyzed the three SSS spectra available for this cluster. We first fitted isothermal models and found an excellent fit ($\chi^2_\nu = 0.94$, $\nu = 248$; see T4.2) with a temperature of kT = 7.81 (6.74–9.01) keV; the 90% confidence upper limit encompasses the LAC-derived temperature. However, the derived fractional abundance A = 1.97 (1.08–3.26) is much higher than that indicated in the LAC spectrum and the hydrogen column of 8.4(7.2–9.5)$\times10^{20}$ cm^{-2} is about twice the Galactic value. A χ^2 contour of kT–A shows that the abundance enhancement is not the result of temperature uncertainties, since there is a firm 99% confidence lower limit of $A \gtrsim 0.5$. Fixing the model abundance to match the smaller value found in the LAC spectrum produced a significantly worse fit ($\Delta\chi^2$=+11.6, for $\Delta\nu = +1$), which is rejected relative to the former model (in T4.2) at the 99.95% confidence level by the F-test.

As for A496, we assessed whether the super-solar abundance may be due to systematic errors in the SSS ice model. The maximum uncertainty in the ice parameter for these data is again ±0.4, so we again employed response matrices which were characterized by ice parameters 0.4 larger than the best-estimate value used above. The subsequent best-fitting isothermal RS model had a smaller abundance, A = 0.71 (0.44–1.04), however its 90% confidence range is still outside that of the more global LAC spectrum. This is a strong indication that abundances are enhanced in the SSS field of view relative to exterior gas. The absorbing column was reduced to N_H = 2.8(1.5–4.1)$\times10^{20}$ cm^{-2}, which is consistent with the Galactic value.

3.3.2 Joint Spectral Fits

3.3.2.1 Raymond-Smith Models

In a joint analysis of the SSS and LAC spectra, we found a formally good fit for the simplest plausible RS model, characterized by a single temperature, abundance and column density ($\chi^2_\nu = 0.98$, $\nu = 271$: see T4.3), although the best-fit "global" N_H is twice the Galactic column. Since the SSS data alone seem to require roughly cosmic abundances, while the LAC data require abundances which are one third as much, we also considered a dual RS model with the same temperature but with independently varying abundances. We found a somewhat improved fit ($\Delta\chi^2 = -6.6$ for $\Delta\nu = -2$; see T4.4), but the abundance of the dominant RS component (with normalization dictated by the LAC) vanished. This means that virtually all of the line emission seen by the LAC could conceivably come from within a region defined by the SSS field of view, leaving few metals to the exterior. The fractional abundance of the (cooler) component within the SSS field of view is A_{cool} = 2.35 (0.99–>4), while the 90% upper limit to the hot component fractional abundance is $A_{hot} \lesssim 0.20$.

A two-temperature model with separately variable abundances (see T4.5) provided an additional improvement on this already acceptable fit, giving $\chi^2_\nu = 0.95$ or $\Delta\chi^2 = -5.4$ for $\Delta\nu = -1$ relative to the previous model in T4.4; this improvement is significant at the 98% level by the F-test. Once again, however, the dominant component (now hotter) has a vanishing abundance (with a 90% confidence upper limit of $A_{hot} \lesssim 0.22$ solar). This model and the data are shown in Figure 8. The χ^2 distributions for the temperatures of the two RS components are shown in Figure 2c. The temperature of the hot component is $\sim$ 10% greater than that derived from the LAC data alone. The χ^2 distributions for the hot and cool abundances are shown in Figure 3c, where it is clear that the abundances differ with > 99% confidence. This model also required an intrinsic absorbing column of $\sim$ 5 times the line-of-sight Galactic value: $N_H = 2.0(1.3\text{–}3.9)\times10^{21}$ cm^{-2}; the N_H χ^2 distribution is shown in Figure 4c. The ratio of model fluxes in the SSS and LAC fields of view is consistent with that derived from IPC imaging.

Fixing the abundance of the hot component to be equal to that derived from the LAC data alone provided an acceptable fit ($\chi^2_\nu = 0.97$ for $\nu = 269$: see T4.6) although with some degradation compared to the previous model with vanishing abundances: $\Delta\chi^2 = +6.3$ for $\Delta\nu = +1$. The fractional abundance of the cool component remained relatively high, with a 90% confidence interval which just touched that of LAC data analyzed alone: $A_{cool} = 0.97$ (0.39–2.35). Finally, the need for two abundances was further tested by forcing the cool and hot components to have the same abundances. The best fit (see T4.7) had $\Delta\chi^2 = +8.9$ for $\Delta\nu = +1$ relative to the dual-abundance model in T4.5; the need for the additional abundance component is significant at the 99.7% confidence level by the F-test.

We tested whether the substantial intrinsic absorbing column required above is confined to the SSS field of view by fitting a two-temperature, two-abundance model with only one (variable) global column density. The resulting best fit is nearly as good as that detailed in T4.5 ($\Delta\chi = +1.3$ for $\Delta\nu = 0$), so we cannot demonstrate that the absorption is confined to the SSS field of view. However, the best-fitting N_H is twice as high as the Galactic value, eight times larger than its likely uncertainty. We also explored a partial covering fraction model for the intrinsic absorption: the best fit value of the covering fraction was unity (so the fit was not improved), with a 90% confidence lower limit of $\sim$ 60%.

3.3.2.2 Cooling Flow Models

We also investigated spectral models incorporating a cooling flow component in order to constrain its accretion rate. A RS model plus the standard cooling model employed for the previous clusters provided about as good a fit as the best-fitting dual RS models, with $\chi^2_\nu = 0.95$ for $\nu = 269$ (see T4.8). The abundance of the RS model exterior to the cooling flow was again very low, with $A_{hot} = 0.12$ (0–0.32), while the cooling flow component has a super-solar abundance with large errors: $A_{cf} = 3.6$ (0.93–>5.6): the χ^2 distributions for the abundances of these two spectral components are shown in Figure 6c. The accretion rate is $\dot{M} = 439$ (345–545) $M_\odot$ yr^{-1}, substantially higher than that derived from the imaging analysis of Arnaud and Fabian (1987). Substantial intrinsic absorption is again indicated, with a higher column than in the previous dual RS fits: $N_H = 3.5(3.4\text{–}5.5)\times10^{21}$ cm^{-2}. This is several times higher than the intrinsic column found by WFJMA. The SSS/LAC model flux ratio for this model is consistent with that derived from IPC imaging.

Forcing the abundances of the cooling flow and exterior RS components to be equal degraded the quality of the fit somewhat ($\Delta\chi^2 = +6.4$ for $\Delta\nu = +1$; see T4.9); the former dual-abundance model (T4.8) is preferable at the 99% confidence level by the F-test. As we did for the dual RS models, we also tested whether the intrinsic absorbing column is confined to the SSS field of view: still keeping the abundances of the two spectral components tied, we allowed only one globally varying absorbing column and found little additional degradation in the best fit (see T4.10), so we cannot prove that the absorption is confined to the SSS field of view. Nonetheless, the best-fitting global absorbing column was about twice the nominal Galactic value, just as we found in the dual RS test, so the excess absorption is several times larger than the likely error in the Galactic column. The best-fitting accretion rate, $\dot{M} = 177\ M_{\odot}\ \mathrm{yr}^{-1}$, is less than half that derived in models which allowed for an intrinsic absorption component. We also considered a partial covering fraction model for the intrinsic absorption; in a model similar to that of T4.8, we found a best-fit value of unity for the covering fraction (so the fit was not improved), with a 90% confidence lower limit of $> 80\%$.

We conclude from these various spectral model fits that there is strong spectral evidence for a relatively cool central component in A2142 and that its abundance is likely to be enhanced relative to that of exterior gas, although its absolute level is somewhat uncertain due to SSS ice parameter uncertainties. We found that the amount of intrinsic absorption previously found by WFJMA, although large, is rather model-dependent. The spectrally-derived cooling accretion rate depends sensitively upon how the intrinsic absorption is distributed.

3.4 Abell 2199

A2199 is a cD cluster of Bautz-Morgan type I. The central cD, NGC 6166, has a triple nucleus (Hoessel 1980), one of which contains unresolved Hα emission (CHJY). At a redshift $z = 0.0309$, the luminosity distance is 187 h_{50}^{-1} Mpc, the closest in our sample, and $1' = 51\ h_{50}^{-1}$ kpc (for an angular diameter distance of 176 h_{50}^{-1} Mpc). There is pronounced asymmetry in the cluster's histogram of galaxy velocities (ZHG) and NGC 6166 has a peculiar velocity of ~ 380 km s^{-1} relative to the cluster mean. ZHG found this peculiar velocity to be significant compared to the cluster velocity dispersion of 794 km s^{-1}, but Gebhardt and Beers (1991), using a more robust statistical test, suggest otherwise. McNamara and O'Connell (1992) found photometric evidence of ongoing star formation in the central cD: a modest optical color gradient relative to the color profiles of "normal", non-star-forming template ellipticals.

X-ray imaging studies indicate the presence of a central cooling flow with an accretion rate of ~ 100–$220\ M_{\odot}\ \mathrm{yr}^{-1}$ (Stewart *et al.* 1984; Arnaud and Fabian 1987; Thomas *et al.* 1987). Cooling radius estimates range from 3.2′–6.7′ (Arnaud and Fabian 1987; Thomas *et al.* 1987), extending beyond the 3′ radius of the SSS field of view. However, as noted for A496, if the system age were $\lesssim 10^{10}$ yr, rather than the 2×10^{10} yr adopted in these studies, the cooling radius may be within the SSS field of view. Mushotzky (1984) and Mushotzky and Szymkowiak (1988) deduce an accretion rate of ~ 45–$60\ M_{\odot}\ \mathrm{yr}^{-1}$ from SSS spectra. No serendipitous sources significant enough to affect this study appear in the IPC image of this cluster. The nominal center of the SSS field is 0.10′ from the IPC X-ray peak, while that of the LAC is 10.7′ away.

3.4.1 Separate LAC and SSS Spectral Fits

A RS isothermal spectral model fit to the LAC data alone provides an adequate fit (χ^2_ν = 1.10 for ν = 22) with a temperature kT = 4.48 (4.41–4.54) keV and a fractional abundance A = 0.43 (0.39–0.46) (see T5.1). Fixing the absorbing column to the very low Galactic value ($\sim 9 \times 10^{19}$ cm^{-2}), rather than allowing it to be fit freely, increased χ^2 by 1.4 (while $\Delta\nu = +1$), so there was little significant effect.

There are three SSS spectra and all have good ice parameters. The best-fitting isothermal model provided a mediocre fit, with χ^2_ν = 1.15 for ν = 248 (see T5.2). The temperature kT = 3.34 (3.05–3.70) keV is 25% lower than that derived from the LAC spectrum and the respective 90% confidence χ^2 limits do not overlap. The fractional abundance, A = 0.61 (0.44–0.82) may be somewhat higher than that indicated in the LAC spectrum, but the 90% confidence intervals overlap slightly. Intrinsic absorption is strongly indicated in the SSS spectra, with $N_H = 7.9(6.8\text{–}9.1) \times 10^{20}$ cm^{-2}, which is $\sim$ 9 times larger than the Galactic column in this line of sight.

3.4.2 Joint Spectral Fits

3.4.2.1 Raymond-Smith Models

In joint spectral fits, the simplest reasonable model employing RS components is characterized by a single temperature, abundance and absorbing column for both spectral data sets. This model did not provide a good fit, having χ^2_ν = 1.31 (see T5.3).

Having the SSS spectra characterized by a cooler temperature than the LAC spectrum motivated a joint, two-temperature fit to both data sets. As before, the cooler component was assumed to be completely contained within the SSS field of view, so it had the same normalization for both the SSS and LAC spectra. With the abundances of the two temperature components tied together, the resulting best fit is shown in Figure 9 and has χ^2_ν = 1.15 for ν = 271 (see T5.4). The higher temperature component, with kT = 5.28 (4.86–5.46) keV, is $\sim$ 20% hotter than indicated by the LAC spectrum alone. The temperature of the cooler component, kT = 3.15 (1.82–3.36) keV, is consistent with the temperature found in the isothermal analysis of the SSS spectra alone (see T5.2). The χ^2 distributions for the two temperature components are shown in Figure 2d, while that of the (tied) abundance is in Figure 3d. The intrinsic absorption has the same large column that was found in the previous SSS analysis, $N_H = 8.1(7.1\text{–}24.7) \times 10^{20}$ cm^{-2}, and its χ^2 distribution is shown in Figure 4d. The ratio of model fluxes in the SSS and LAC fields of view is consistent with that derived from IPC imaging data. When we allowed the fractional abundances of the two temperature components to vary independently, the fit was not significantly improved and the best-fit abundance of the cool component was only $\sim$ 25% higher than that of the hot component — their 90% confidence limits also overlapped substantially. Isothermal models with either one or two abundances provided much worse fits. A variable covering fraction model for the intrinsic absorption had a best-fit value of unity for the covering fraction, with a 90% confidence lower limit of 73%.

A better fit was provided by a two-temperature model with a single global absorption component (see T5.5), rather than the combination of fixed Galactic N_H plus variable intrinsic absorption described above. However, the SSS/LAC flux ratio in this model *exceeds* that derived from IPC imaging data (by 5%), so this model is not preferred: since the LAC field of view exceeds that of the IPC, the SSS/LAC model flux ratio should be less than or equal to that derived from the IPC.

To assess whether the central component spreads significantly outside the SSS field of view, we allowed the cool component normalization to vary independently in the SSS and LAC spectral groups: the best-fit values did not differ significantly. We also added a third RS component which was allowed to be seen by the LAC alone, and this also failed to significantly improve χ^2. The amount of flux this third (cool) component ended up contributing to the LAC passband was $\sim$ 1%. This is at the level expected from uncertainties in calibration and unresolved background sources.

3.4.2.2 Cooling Flow Models

As previously, we assessed the model-dependence of the abundance and intrinsic N_H estimates by considering a spectral model incorporating a cooling flow component. The cooling flow was again assumed to be isobaric, with an initial temperature equal to that of the exterior isothermal atmosphere, and the cooling flow normalization (accretion rate) was the same for the SSS and LAC spectra. This cooling flow model provided a better fit than any of the previous two-temperature models, having $\chi^2_\nu = 1.05$ for $\nu = 271$ (see T5.6). The best-fitting exterior temperature, $kT = 4.74$ (4.65–4.83) keV, is $\sim$ 6% larger than that derived from the LAC spectrum alone. The abundances of the two spectral components were allowed to vary independently and the best-fitting cooling flow abundance was near cosmic, with $A_{cf} = 1.15$ (0.65–2.11) while the exterior gas had $A_{hot} = 0.37$ (0.30–0.43), somewhat smaller than that derived from the two-temperature fits (see Figure 6d for its χ^2 distribution). The best-fitting intrinsic absorption column, $N_H = 3.0(2.7\text{–}3.4)\times10^{21}$ cm^{-2}, is $\sim$ 4 times larger than that associated with the previous two-temperature model. This is also twice as high as the value found by WFJMA. The accretion rate associated with the cooling flow is $\dot{M} = 150$ (129–173) $M_\odot$ yr^{-1}. The ratio of model fluxes in the SSS and LAC fields of view is consistent with that derived from IPC imaging data. The quality of this fit suggests that the bulk of the cooling flow emission is indeed within the SSS field of view. When the cooling flow normalizations were allowed to vary independently in the LAC and SSS data sets (to test whether there is significant cooling flow emission outside the SSS field of view) we found the normalizations did not differ significantly and the χ^2 was not significantly improved. To test the reality of the enhanced cooling flow abundances, we tied the abundances of the two spectral components together. The resulting best fit was significantly worse, having $\Delta\chi^2 = +7$ for $\Delta\nu = +1$ (for $\nu = 272$; see T5.7). The F-test shows that the need for the additional abundance component in the previous model (T5.6) is significant at the 99% level. A model allowing a partial covering fraction for the intrinsic absorption (but like the model in T5.6 in other respects) produced a best-fit value of unity for the covering fraction, with a 90% lower limit of > 85% coverage.

To test whether the intrinsic absorption component is truly intrinsic, we fitted a model with a single, variable, global absorption component. The resulting best-fit model (see T5.8) had $\Delta\chi^2 = +10$ compared to the previous best-fitting model and the absorption was still $\sim$ 9 times larger than the Galactic value, which is unlikely to be wrong by such a large factor. This poorer fit suggests that the intrinsic absorption is not globally distributed, but mostly confined within the SSS field of view.

We conclude that there is strong evidence for a cool emission component with intrinsic absorption in A2199. Evidence for an abundance gradient is model-dependent: the dual RS models did not have compelling evidence for an abundance gradient, but the better-fitting models with cooling flow spectra did have cooling flow abundances significantly enhanced compared to exterior gas.

4. SUMMARY AND DISCUSSION

We jointly analyzed *Ginga* LAC and *Einstein* SSS spectra for four galaxy clusters thought to contain cooling flows. Each cluster's spectra showed strong evidence for a relatively cool spectral component associated with the central cooling flow. The inclusion of these cool components caused the temperatures derived for the more dominant hotter components to be as much as $\sim 20\%$ larger than those derived from isothermal analyses, with $\sim 10\%$ increases being more typical. We found no compelling evidence for significant amounts of cool emission outside the central regions encompassed by the SSS field of view (*i.e.* within a $3'$ radius of the center). We also explored the model-dependence in the amount of cool X-ray absorbing matter in each of the clusters: this cool absorbing material was first discovered by WFJMA to be ubiquitous in cooling flow clusters.

All four clusters show evidence of centrally enhanced metal abundances, with varying degrees of model dependence and statistical significance: the evidence is statistically strongest for A496 and A2142, weaker for A2199 and weakest for A1795. In A496, both dual-temperature RS spectral models and models incorporating cooling flow spectra provide the best fits when abundances are enhanced within the SSS field of view (at F-test confidence levels of $\geq 99.85\%$ when compared to a single-abundance model). Central abundance enhancement is also seen in both kinds of spectral models for A2142 (at F-test confidence levels of $\geq 99\%$ when compared to a single abundance model). In A2199, dual-temperature RS models see no significant central abundance enhancement, while the better-fitting cooling flow models do produce central abundance enhancements (the latter at an F-test significance level of 99% compared to a single-abundance model). Dual-temperature RS models for A1795 also showed no compelling evidence for a significant abundance gradient, but these models provided better overall fits than did models incorporating cooling flows, which did show evidence of a central abundance gradient (at an F-test confidence level of 95% relative to a single abundance model).

Previous observations of abundance distributions in clusters have also produced rather heterogeneous results. In M87/Virgo, Lea *et al.* (1982) used two pointings of the *Einstein* SSS to determine that abundances were about solar at the center and stayed so out to $7'$ from the center. However, Koyama *et al.* (1991) found the abundance to drop from ~ 0.5 solar at the center to only 0.1–0.2 solar beyond 1° from the center in a scanning observation with the *Ginga* LAC.

Ulmer *et al.* (1987) found in a *Spartan 1* observation of the Perseus cluster (A426) that the iron abundance dropped from 0.8 solar within $5'$ to 0.4 solar between $6'$ and $20'$ from the center. A recent reanalysis of the *Spartan 1* data finds a somewhat steeper abundance gradient (Kowalski *et al.* 1993). Ponman *et al.* (1990) claim an even steeper abundance gradient in *Spacelab 2* spectra of Perseus, with iron practically vanishing beyond $\sim 20'$. Meanwhile, Edge (1990) found no abundance gradient within $\sim 20'$ in *EXOSAT* data. Recent *BBXRT* results by Arnaud *et al.* (1993) show no abundance gradient out to 13′, but the measured abundances are greater than those indicated by the previously noted spectra from broad-beam instruments.

For the Coma cluster (A1656), Hughes *et al.* (1988) and Edge (1990) used several *EXOSAT* pointings to deduce that the iron abundance is roughly constant out to 45′. More recently, Hughes *et al.* (1993) used a combination of *Tenma*, *EXOSAT*, and *Ginga* data to limit the allowed spatial distribution of iron in the Coma cluster. These authors found that any gradient in the iron distribution must be shallow and that, in fact, the total mass of iron in the cluster out to 2 Mpc can be no less than ~75% of the amount estimated assuming a uniform iron distribution.

In *BBXRT* observations of NGC 1399, the central galaxy in the Fornax cluster, Serlemitsos *et al.* (1993) found roughly half-solar abundances out to $\sim 8'$, with weak evidence for an outward decline. A spatially unresolved *Ginga* LAC spectrum of this object indicates somewhat higher, nearly solar, abundances (Ikebe *et al.* 1992).

In a continuation of this heterogeneous theme, recent metallicity determinations from *ROSAT* PSPC observations of gas in groups of galaxies have also produced varying results with regard to overall abundances: Ponman & Bertram (1993) found a very low metal abundance ($\sim$ 15% solar) in the compact group HCG 62. Mulchaey *et al.* (1993) also found abundances to be small ($\lesssim$ 20% solar) in the NGC 2300 group. However, David *et al.* (1994) found abundances of $\sim$ 80% solar in the NGC 5044 group, with no discernible gradient. The low metallicities in the HCG 62 and NGC 2300 groups are in conflict with the metallicity—temperature trend found in rich clusters, where cool clusters have higher abundances than hot clusters do (Hatsukade 1989; Edge and Stewart 1991).

Summarizing these disparate observations, some clusters seem to have fairly flat abundance distributions in their inner regions, while others have centrally enhanced abundances, and some may have declining abundances in their outskirts. Early results on abundances in groups show a large scatter, and represent a significant departure from the metallicity—temperature anti-correlation observed in rich clusters.

These observations raise the question: why are abundances centrally enhanced in some clusters, but not in others? In addressing this issue we need to consider the dominant mechanism(s) by which intracluster metals are injected into intracluster gas in the first place. The two mechanisms proposed most often for metal contamination in intracluster gas are supernovae-driven proto-galactic winds (Larson & Dinerstein 1975, Vigroux 1977, De Young 1978) and ram-pressure stripping of gas from galaxies (Gunn & Gott 1972, Norman and Silk 1979, Sarazin 1979, Nepveu 1981). Whereas proto-galactic winds would inject both metals and energy into intracluster gas, ram-pressure stripping would inject only metals (White 1991). Current observations of X-ray surface brightness profiles and spectra of intracluster gas indicate that the gas seems to have a greater specific energy than cluster galaxies, with the disparity being largest for cool clusters (White 1991). This suggests the gas has experienced energy deposition in excess of that associated with cluster collapse, which is indicative of proto-galactic winds (David *et al.* 1990, White 1991). Spatially resolved spectra for many clusters are required to confirm whether intracluster gas, particularly in cool clusters, has significantly more specific energy than cluster galaxies.

Observations of the metallicity of distant clusters may also constrain the source of metals. The detection of metals in very distant clusters would suggest a protogalactic wind origin. If the metals are primarily due to gas ram-pressure stripped from galaxies, the metallicity may build more slowly and secularly, as the central gas density of the cluster increases over time and supplements galaxy-galaxy stripping encounters.

If galactic winds are necessary to account for some of the energy content of intracluster gas, one may expect that the metals borne by the winds would be well-mixed in the cluster. This may account for the bulk of the metals in the intracluster gas, but makes the central abundance enhancement in some clusters problematic.

There are several possible causes of the centrally enhanced abundances in some clusters, including: 1) in the context of the galactic wind origin for metals, a population gradient of wind-blowing galaxies in the cluster may imprint an abundance gradient; that is, if only early-type galaxies had winds, the fact that the fraction of early-type galaxies declines outward in a cluster may lead to a declining metallicity gradient; 2) metal-rich gas may be preferentially stripped from galaxies passing through the dense gas at cluster centers (Nepveu 1981); 3) metal-rich stellar mass loss in a central dominant galaxy may accumulate within the galaxy if some fraction of the stellar ejecta does not participate in its cooling flow; 4) given that the central dominant galaxy in a cluster has the deepest potential well of any galaxy in the cluster, the metals ejected by its proto-galactic wind (if it had one) may not escape or be well-mixed, remaining confined mostly near the cluster center; 5) given the anti-correlation of metallicity and temperature in intracluster gas, perhaps clusters with central abundance enhancements have ingested a relatively cool, metal-rich subcluster; 6) heavy ions may have gravitationally settled from exterior parts of the cluster (Fabian & Pringle 1977); however, it is now thought that the timescale for ionic settling to occur is too long for it to be important (Raphaeli 1978).

The first possibility above, that abundance gradients may be imprinted by population gradients in wind-blowing galaxies, can be tested by comparing observed population gradients with the many intracluster abundance profiles that will be derived in the near future from *ASCA* satellite data. Clusters without metallicity gradients in the inner regions may have particularly low spiral fractions, so any population gradient would be weak in the inner regions. The Coma and Perseus clusters are consistent with this. A2142 provides a possible counterexample, since it is a very hot cluster, so it is likely to have a small spiral fraction, but the analysis of this paper suggests it has a substantial central abundance enhancement. Another problem with this hypothesis is that the observed temperature—metallicity anti-correlation for clusters may provide counterevidence, since cool clusters tend to have smaller fractions of early-type galaxies, but have the highest metal abundances.

The second possibility, that galaxies are preferentially ram-pressure stripped in cluster centers, also has some difficulties: the metallicity of the gas stripped from galaxies must be at least equal to that of the central regions, which may be near solar. However, if spiral galaxies are the primary source of stripped gas, the gas will come largely from the outer parts, where the average metallicity in extended HI disks is likely to be less than solar. Furthermore, if the metal-rich gas is largely stripped from early-type galaxies, their abundances are turning out to be very sub-solar: for example, *BBXRT* observations of NGC 4472 in the Virgo cluster reveal an iron abundance of ~ 0.2 solar (Serlemitsos *et al.* 1993). This process is unlikely to produce strong gradients in the cores of rich clusters like Coma, since the stripping saturates (Hughes *et al.* 1993).

The third and fourth possibilities listed above attribute central abundance enhancements to the stellar mass loss of the central dominant galaxies. Even if the central abundances were not 2–3 times greater than the exterior or average abundances, the total amount of metals is about two orders of magnitude too large to be generated by current stellar mass loss rates in the central dominant galaxies: however, it is possible that the metals had accumulated in the vicinity for a long time, due to protogalactic winds from or atmospheric stripping of the central dominant galaxy and neighboring galaxies in the core regions. The current cooling flows, which extend 100—200 kpc from the cluster centers, will then consist of this particularly metal-rich gas. The historical contribution of the central dominant galaxies' mass loss may be assessed by determining the physical extent of the abundance-enhanced region.

The fifth possibility mentioned above is that a cool, high-metallicity subcluster may merge with and settle to the center of a hotter, lower-metallicity cluster to create a central abundance enhancement. One may then expect some correlation between the existence of central abundance enhancements and signs of a merger. A496 and A1795 provide counterexamples to this expectation: A496 appears to have centrally enhanced abundances but has no signs of a significant recent merger: A1795 has only weak evidence of centrally enhanced abundances, but the high peculiar velocity of its central cD is suggestive of a recent merger. Alternatively, cluster mergers may act in the opposite sense, by washing out pre-existing metallicity gradients, particularly if the sub-clumps are of comparable mass, so the gravitational potential is maximally perturbed. A recent numerical simulation by Roettiger *et al.* (1993) suggests that subclump material will be thoroughly mixed during the merger. However, recent *BBXRT* observations of the merging cluster A2256 suggest that a pre-existing cooling flow in one of the two major subclumps has been disrupted, but a region of relatively cool, X-ray absorbing gas still persists (Miyaji *et al.* 1993); the merging system is not yet relaxed, so it is not clear whether this possible cooling flow remnant will retain its coherence post-relaxation. If mergers homogenize at least the central abundance distributions, then one expects an anti-correlation between the existence of central abundance enhancements and signs of significant mergers. At present, this seems more consistent with the observations: A496 and Virgo are examples of clusters with central abundance enhancements but no evidence of a recent disruptive merger, while Perseus and Coma are clusters with centrally homogeneous metal distributions and evidence of significant mergers (if the binary central dominant galaxies in Coma can be interpreted as relics of two former subclusters). A1795 may be added to the latter list if the weakness of its evidence for a central abundance enhancement is emphasized. Counterexamples to this trend may be provided by A2142 and A2199, which seem to have centrally enhanced abundances but also have signs of significant mergers (if binary central dominant galaxies are again taken to be such a sign in the case of A2142).

Spatially resolved spectra from the *ASCA* satellite will be able to provide more accurate assessments of abundance gradients in intracluster gas. As *ASCA* spectra accumulate for many clusters, the energetics of the gas can be compared to those of the galaxies and the dark matter to determine whether protogalactic winds are indicated. The overall metallicity and the nature of any metallicity gradients will be more readily correlated with other cluster properties, such as spiral fraction, in order to determine whether the primary metal injection mechanism is galactic winds or ram-pressure stripping. Finally, correlating the presence or absence of central abundance enhancements with such cluster properties as the local spiral fraction or merger signatures will help determine whether a separate metal injection mechanism is required to create them.

REW, CSRD, and JPH thank F. Makino and the Institute of Space and Astronautical Science for their hospitality and scientific support during our stays in Japan. We also thank K. Arnaud, A. Tennant and O. Day for invaluable help with XSPEC, and R. Mushotzky for stimulating discussions. We especially appreciate the effort by K. Arnaud, R. Johnstone and D. White in developing the cooling flow model within XSPEC. JPH thanks M. Arnaud and K. Yamashita for advice and assistance during the preliminary reduction of the A2199 *Ginga* LAC data. REW and CSRD were supported in part by NASA grant NAG 8-228. Additional support for REW was provided by the NSF and the State of Alabama via EPSCoR II. JPH was supported in part by NASA grant NAG 8-181. This research has made use of data obtained through the High Energy Astrophysics Science Archive Research Center On-line Service, provided by the NASA-Goddard Space Flight Center. This research has also made use of the NASA/IPAC Extragalactic Database (NED), which is operated by the Jet Propulsion Laboratory, Caltech, under contract with NASA.

TABLE 1

SPECTRAL DATA LOG

cluster	det	seq #	time (yr.day)	expos (sec)	count rate	ice	Δ ice	RA (1950)	Dec (1950)	comment
A496	SSS	1433	79.221	6144	0.64	0.75	0.11	4 31 18	-13 22 05	hi Δice
	"	"	79.222	5652	0.63	1.00	0.02	4 31 18	-13 22 05	
	"	"	79.223	7372	0.65	1.02	0.03	4 31 18	-13 22 05	
	LAC		88.288	12618	32.9	...	...	4 31	-13 21	
A1795	SSS	1442	79.018	5816	0.59	2.61	0.01	13 46 34	+26 50 24	hi ice
	"	"	79.195	1228	0.77	0.44	0.26	13 46 33	+26 50 36	hi Δice
	"	"	79.196	4587	0.68	0.79	0.38	13 46 33	+26 50 36	hi Δice
	"	"	79.197	7864	0.72	1.27	0.02	13 46 33	+26 50 36	
	"	"	79.198	5242	0.62	1.35	0.01	13 46 33	+26 50 36	
	"	"	79.199	6062	0.61	1.39	0.03	13 46 33	+26 50 36	
	LAC		88.174	10493	47.1	...	...	13 46	+26 51	
A2142	SSS	1431	79.232	5898	0.74	0.81	0.03	15 56 15	+27 22 10	
	"	"	79.233	15155	0.73	0.86	0.08	15 56 15	+27 22 10	
	"	"	79.234	5160	0.70	0.94	0.02	15 56 15	+27 22 10	
	LAC		88.222	8827	40.0	...	...	15 56	+27 22	
A2199	SSS	1440	79.209	8929	0.77	1.02	0.02	16 26 55	+39 39 36	
	"	"	79.231	5652	0.91	0.67	0.02	16 26 55	+39 39 36	
	"	"	79.232	10240	0.96	0.70	0.03	16 26 55	+39 39 36	
	LAC		90.068	22024	38.4	...	...	16 26	+39 39	

det = detector
seq # = sequence number of observation
time = year and day of observation
expos = exposure time
count rate in counts/sec
ice = ice parameter
Δice = change in ice parameter during observation
RA & Dec = pointing position
comment = reason spectrum rejected from consideration:
Δice/ice > 10% or ice relatively high compared to others

TABLE 2

A496 Model Fit Parameters

	model - inst	kT	A	N_H	LAC norm	SSS norm	cool kT	cool A	cool N_H	cool norm	χ^2	ν	PHA	χ_ν^2	prob	comment
(1)	a rs - LAC	4.04 3.97 3.91	0.53 0.48 0.43	5.0*	10.16 10.01 9.85						42.0	19	22	2.21	1.8-3	1T,1A
(2)	a rs - SSS	4.34 3.68 3.08	2.28 1.50 0.94	14.6 12.0 9.9		3.32 2.89 2.51					118.8	148	152	0.80	0.97	1T,1A,1H
(3)	a rs	3.90	0.51	10.6	10.16	3.53					203.3	169	174	1.20	0.037	1T,1A,1H
(4)	a(z(rs)+rs)	4.34	0.53	4.5*	8.47	1.83	1.60	0.53=	35.4	2.15	163.3	167	174	0.98	0.50	2T,1A,1.5H
(5)	a(z(rs)+rs)	4.41 4.30 4.19	0.53 0.47 0.42	4.5*	9.12 8.79 8.29	2.38 2.13 1.70	2.01 1.64 1.39	>5.00 2.63 1.01	55.8 40.1 24.9	1.57 0.76 0.26	153.6	166	174	0.93	0.75	2T,2A,1.5H
(6)	a(rs+rs)	4.06	0.47	11.9	9.70	2.87	1.51	9.97		0.10	157.5	166	174	0.95	0.67	2T,2A,1H
(7)	a(z(cf)+rs)	4.29 4.20 4.12	0.37 0.25 0.16	4.5*	8.91 8.57 8.03	2.04 1.71 1.27	4.20=	>9.00 3.79 1.58	45.6 38.5 32.3	188 154 127	151.7	167	174	0.91	0.80	1T,2A,1.5H
(8)	a(z(cf)+rs)	4.20	0.51	4.5*	7.68	1.16	4.20=	0.51=	31.3	194	168.6	168	174	1.00	0.47	1T,1A,1.5H
(9)	a(cf+rs)	4.13	0.29	16.8	9.45	2.46	4.13	4.53		91	192.3	167	174	1.15	0.087	1T,2A,1H

models are fit jointly to LAC & SSS unless otherwise noted under "inst"

model components:
a = Wisconsin absorption model (Morrison and McCammon 1983)
z = redshifted intrinsic absorption
rs = Raymond-Smith thermal model
cf = cooling flow model of Mushotzky and Szymkowiak (1988), with slope fixed at 0

kT = temperature in keV
A = abundance relative to solar
N_H = line-of-sight column density of neutral hydrogen $\times 10^{20}$ cm^{-2}
norm = normalization: Raymond-Smith normalization in 10^{12} cm^{-5}; cooling flow normalization in $M_\odot$/yr; cool norm is normalization of component taken to be common to LAC and SSS fields of view.
ν = degrees of freedom in spectral fit
PHA = number of data channels fit
χ_ν^2 = χ^2 per degree of freedom
prob = probability that model can produce χ^2 greater than it does
comment = code for number of independent temperatures T, abundances A and column densities H; (1.5H => one free (intrinsic) column plus one fixed Galactic column)

* => fixed parameter
= => tied parameter

TABLE 3

A1795 Model Fit Parameters

	model - inst	kT	A	N_H	LAC norm	SSS norm	cool kT	cool A	cool N_H	cool norm	χ^2	ν	PHA	χ_ν^2	prob	comment
(1)	a rs - LAC	5.69 5.57 5.45	0.48 0.43 0.38	1.7*	8.24 8.12 8.00						21.8	19	22	1.15	0.29	1T,1A
(2)	a rs - SSS	4.14 3.67 3.26	0.24 0.06 0.00	5.2 3.7 2.2		5.52 5.16 4.80					241.5	225	229	1.07	0.22	1T,1A,1H
(3)	a rs	5.67 5.57 5.45	0.48 0.43 0.38	0.8 0.0 0.0	8.22 8.10 7.99	4.45 4.36 4.29					283.9	246	251	1.15	0.049	1T,1A,1H
(4)	a(z(rs)+rs)	5.87 5.73 5.59	0.48 0.43 0.38	1.1*	8.05 7.91 7.76	4.12 3.97 3.82	0.90 0.74 0.58	0.43=	75.5 51.5 24.0	2.40 1.24 0.65	242.4	244	251	0.99	0.52	2T,1A,1.5H
(5)	a(z(cf)+rs)	6.33 6.07 5.85	0.50 0.45 0.40	1.1*	6.84 6.31 5.79	2.99 2.43 1.88	6.07=	0.45=	11.5 8.9 5.8	533 411 290	252.6	245	251	1.03	0.36	1T,1A,1.5H
(6)	a(z(cf)+rs)	6.26	0.37 0.14 0.04	1.1*	5.58	1.73	6.26=	0.71 0.58 0.46	8.4	558	248.7	244	251	1.02	0.42	1T,2A,1.5H
(7)	a(cf+rs)	6.04	0.44	4.7	6.42	2.51	6.04=	0.44=		395	254.2	245	251	1.04	0.33	1T,1A,1H

see notes for Table 2

TABLE 4

A2142 Model Fit Parameters

	model - inst	kT	A	N_H	LAC norm	SSS norm	cool kT	cool A	cool N_H	cool norm	χ^2	ν	PHA	χ_ν^2	prob	comment
(1)	a rs - LAC	9.18 8.99 8.78	0.39 0.34 0.29	5.0*	9.02 8.89 8.78						17.8	21	24	0.85	0.66	1T,1A
(2)	a rs - SSS	9.01 7.81 6.74	3.26 1.97 1.08	9.5 8.4 7.2		3.72 3.35 2.96					234.0	248	252	0.94	0.73	1T,1A,1H
(3)	a rs	8.90	0.34	7.8	8.95	4.07					266.0	271	276	0.98	0.57	1T,1A,1H
(4)	a(z(rs)+rs)	8.94	0.20 0.00 0.00	3.8*	5.07	0.01	8.94=	0.89 0.81 0.53	4.6	3.83	259.4	269	276	0.96	0.65	1T,2A,1.5H
(5)	a(z(rs)+rs)	10.36 9.91 9.46	0.22 0.00 0.00	3.8*	8.25 7.81 6.08	3.27 2.75 1.86	6.51 5.23 4.01	>4.00 2.97 0.99	38.7 19.6 13.3	2.05 1.02 0.37	254.0	268	276	0.95	0.72	2T,2A,1.5H
(6)	a(z(rs)+rs)	9.94	0.34*	3.8*	7.69	2.79	3.94	2.35 0.97 0.39	26.7	1.25	260.3	269	276	0.97	0.64	2T,1.5A,1.5H
(7)	a(z(rs)+rs)	10.07	0.38	3.8*	7.17	2.31	5.02	0.38=	16.8	1.82	262.9	269	276	0.98	0.59	2T,1A,1.5H
(8)	a(z(cf)+rs)	9.87 9.60 9.34	0.32 0.12 0.00	3.8*	8.41 8.04 7.64	3.31 3.00 2.50	9.60=	>5.60 3.60 0.93	54.5 44.9 34.2	545 439 345	256.4	269	276	0.95	0.70	1T,2A,1.5H
(9)	a(z(cf)+rs)	9.58	0.39	3.8*	7.62	2.74	9.58=	0.39=	35.6	475	262.8	270	276	0.97	0.61	1T,1A,1.5H
(10)	a(cf+rs)	9.10	0.35	9.4	8.50	3.56	9.10=	0.35=		177	264.0	270	276	0.98	0.59	1T,1A,1H

see notes for Table 2

TABLE 5

A2199 Model Fit Parameters

	model - inst	kT	A	N_H	LAC norm	SSS norm	cool kT	cool A	cool N_H	cool norm	χ^2	ν	PHA	χ_ν^2	prob	comment
(1)	a rs - LAC	4.54	0.46	1.6	11.09						24.3	22	26	1.10	0.33	1T,1A,1H
		4.48	0.43	0.0	10.96											
		4.41	0.39	0.0	10.83											
(2)	a rs - SSS	3.70	0.82	9.1		4.70					286.0	248	252	1.15	0.049	1T,1A,1H
		3.34	0.61	7.9		4.41										
		3.05	0.44	6.8		4.12										
(3)	a rs	4.37	0.45	5.8	11.18	4.40					357.2	273	278	1.31	4.6-4	1T,1A,1H
(4)	a(z(rs)+rs)	5.46	0.50	0.9*	9.42	2.56	3.36	0.46=	24.7	4.74	311.1	271	278	1.15	0.047	2T,1A,1.5H
		5.28	0.46		6.71	0.04	3.15		8.1	4.59						
		4.86	0.42		6.53	0.00	1.82		7.1	2.16						
(5)	a(rs+rs)	4.50	0.44	8.3	10.59	3.80	1.18	0.44=		0.84	290.2	271	278	1.07	0.20	2T,1A,1H
(6)	a(z(cf)+rs)	4.83	0.43	0.9*	9.56	2.63	4.74=	2.11	34.2	173	285.3	271	278	1.05	0.26	1T,2A,1.5H
		4.74	0.37		9.20	2.33		1.15	30.0	150						
		4.65	0.30		8.82	2.01		0.65	26.6	129						
(7)	a(z(cf)+rs)	4.75	0.46	0.9*	8.78	2.02	4.75=	0.46=	26.7	172	292.3	272	278	1.08	0.19	1T,1A,1.5H
(8)	a(cf+rs)	4.50	0.33	8.1	10.75	3.68	4.50=	7.79		51	295.2	271	278	1.09	0.15	1T,2A,1H

see notes for Table 2

REFERENCES

Allen. C. W. 1976, *Astrophysical Quantities*. (Athlone: London), p. 31

Allen. S. W., Fabian, A. C., Johnstone, R. M., Nulsen. P. E. J., & Edge, A. C. 1992, MNRAS. 254, 51

Allen. S. W.. Fabian. A. C., Johnstone. R. M.. White, D. A.. Daines, S. J., Edge. A. C. & Stewart. G. C. 1993, MNRAS. 262, 901

Arnaud. K. A. & Fabian. A. C. 1987. preprint

Arnaud. K. A. *et al.* 1993. preprint

Arnaud M., Lachieze-Rey, M., Rothenflug, R.. Yamashita. K. & Hatsukade. I. 1991. A&A, 243, 67

Arnaud. M., Hughes, J. P.. Forman. W., Jones. C.. Lachieze-Rey, M.. Yamashita. K., & Hatsukade. I. 1992. ApJ, 390. 345

Birkinshaw. M., Hughes, J. P., & Arnaud, K. A. 1991, ApJ. 379. 466

Canizares. C. R.. Markert. T. H. & Donahue. M. E. 1988, in *Cooling Flows in Clusters and Galaxies*, ed. A. C. Fabian. Kluwer Academic Publishers. Dordrecht. p. 63

Christian. D. J.. Swank, J. H., Szymkowiak. A. E.. & White. N. E. 1992. *Legacy*, 1, 38

Cowie. L.. Hu, E. M., Jenkins, E. B. & York. D. G. 1983. ApJ. 272, 29 (CHJY)

David. L. P.. Arnaud. K. A., Forman. W. & Jones. C. 1990. ApJ, 356. 32

David. L. P. Forman. W. & Jones 1994. preprint.

Day, C. S. R.. Fabian, A. C., Edge, A. C., Raychaudhury. S. 1991. MNRAS. 252. 394

De Young, D. 1978. ApJ. 223, 47

Drake, S., Arnaud, K. & White. N. 1992. *Legacy*, 1, 43

Edge, A. C. 1990, PhD thesis, University of Leicester

Edge. A. C. & Stewart, G. C. 1991. MNRAS. 252. 414

Edge. A. C., Stewart, G. C., Fabian. A. C. & Arnaud. K. A. 1990. MNRAS, 245. 559

Elvis. M., Green. R. F., Bechtold. J.. Schmidt. M.. Neugebauer. G.. Soifer. B. T.. Matthews, K.. & Fabbiano, G. 1986. ApJ. 310. 291

Fabian. A. C. & Pringle, J. E. 1977. MNRAS. 181, 5p

Gebhardt. K. and Beers, T. C. 1991. ApJ, 383. 72

Gunn. J. E. & Gott, J. R. III 1972. ApJ. 176. 1

Hatsukade, I. 1989. Ph.D. thesis. Osaka University

Heckman. T. M. 1981, ApJ, 250. L59

Hoessel, J. G. 1980. ApJ, 241, 493

Hughes. J. P.. Butcher, J. A., Stewart. G. C.. & Tanaka. Y. 1993 ApJ. 404. 611

Hughes. J. P., Gorenstein. P., & Fabricant, D. 1988. ApJ. 329. 82

Hughes. J. P. & Tanaka 1992, ApJ. 398. 62

Ikebe. Y., Ohashi. T., Makishima. K.. Tsuru. T.. Fabbiano. G., Kim. D.-W.. Trinchieri, G., Hatsukade, I., Yamashita. K.. & Kondo. H. 1992. ApJ. 384. L5

Johnstone. R. M.. Fabian. A. C.. Edge. A. C. & Thomas. P. A. 1992. MNRAS. 255. 431

Kowalski. M. P.. Cruddace, R. G.. Snyder, W. A. & Fritz G. G. 1993. ApJ. 412. 489

Koyama. K.. Takano, S.. & Tawara. Y. 1991. Nature. 350. 135

Larson. R. B. & Dinerstein. H. L. 1975. PASP. 87. 911

Lea. S. M.. Mushotzky, R. F. & Holt. S. S. 1982. ApJ, 262. 24

Makino. F., & Astro-C Team 1987. ApLettComm. 25. 223

Masai. K. 1984. ApSpSci. 98, 367

McHardy, I. M., Stewart, G. C., Edge, A. C., Cook, B., Yamashita, K. & Hatsukade, I. 1990. MNRAS, 242, 215

McNamara, B. R. & O'Connell, R. W. 1992, ApJ, 393, 579

Miyaji, T., Mushotzky, R. F., Loewenstein, M., Serlemitsos, P. J. Marshall, F. E., Petre, R., Jahoda, K. M., Boldt, E. A., Holt, S. S., Swank, J., Szymkowiak, A., & Kelley, R. 1993, ApJ, 419, 66

Morrison, R., & McCammon, D. 1983, ApJ, 270, 119

Mulchaey, J. S., Davis, D. S., Mushotzky, R. F., & Burnstein, D. 1993, ApJ, 404, L9

Mushotzky, R. F. 1984, Physica Scripta, T7, 157

Mushotzky, R. F. and Szymkowiak, A. E. 1988, in *Cooling Flows in Clusters and Galaxies*, ed. A. C. Fabian, Kluwer Academic Publishers, Dordrecht, p. 53

Nepveu, M. 1981, A&A, 101, 362

Norman, C. & Silk, J. 1979, ApJ, 233, L1

Nulsen, P. E. J., Stewart, G. C., Fabian, A. C., Mushotzky, R. F., Holt, S. S., Ku, W., H.-M., Malin, D. F. 1982, MNRAS, 199, 1089

Ponman T. J. & Bertram, D. 1993, Nature, 363, 51

Ponman, T. J. *et al.* 1990, Nature, 347, 450

Raphaeli, Y. 1978, ApJ, 225, 335

Raymond J. C., and Smith, B. W. 1977, ApJS, 35, 419

Reichert, G. A., Mason, K. O., Thorstensen, J. R. & Bowyer, S. 1982, ApJ, 260, 437

Roettiger, K., Burns, J., & Loken, C. 1993, ApJ, 407, L53

Sarazin, C. L. 1979, ApLet, 20, 93

Serlemitsos, P. J., M. Loewenstein, Mushotzky, R. F., Marshall, F. E. & Petre, R. (1993), ApJ, 413, 518

Stark, A. A., Gammie, C. F., Wilson, R. W., Bally, J., Linke, R. A., Heiles, C., & Hurwitz, M. 1992, ApJS, 79, 77

Stewart, G. C., Fabian, A. C., Jones, C. & Forman, W. 1984, ApJ, 285, 1

Szymkowiak, A. E. 1986, Ph.D. thesis, University of Maryland (NASA Technical Memorandum 86169)

Takano, S., Awaki, H., Koyama, K., Kunieda, H., Tawara, Y., Yamauchi, S., Makishima, K., & Ohashi, T. 1989, Nature, 340, 289

Thomas, P. A., Fabian, A. C., & Nulsen, P. E. J. 1987, MNRAS, 228, 973

Turner, M. J. L. *et al.* 1989, PASJ, 41, 373

Ulmer, M. P. *et al.* 1987, ApJ, 319, 118

Vigroux, L. 1977, A&A, 56, 473

Wang, Q. & Stocke, J. T. 1993, ApJ, 408, 71

White, D. A., Fabian, A. C., Johnstone, R. M., Mushotzky, R. F., and Arnaud, K. A. 1991, MNRAS, 252, 72 (WFJMA)

White, R. E. III 1991, ApJ, 367, 69

White, R. E. III & Sarazin, C. L. 1987, ApJ, 318, 621

Zabludoff, A. I., Huchra, J. P., & Geller, M. J. 1990, ApJS, 74, 1 (ZHG)

FIGURE CAPTIONS

FIG. 1 – Two-temperature RS spectral models jointly fit to *Einstein* SSS and *Ginga* LAC data for A496; see line 5 of Table 2 for best-fit parameters.

FIG. 2 – Temperature (kT, in keV) χ^2 distributions for two-temperature RS models: a) A496; b) A1795; c) A2142; d) A2199. The lower and upper dashed lines are the 90% and 99% confidence levels, corresponding to $\Delta\chi^2 = 2.71$ and 6.63, respectively.

FIG. 3 – χ^2 distributions for the abundance(s) of the hot and cool components in the fits of Fig. 1: a) A496; b) A1795 (abundances of the two temperature components were set equal); c) A2142; d) A2199 (abundances of the two temperature components were set equal).

FIG. 4 – χ^2 distributions for the "intrinsic" hydrogen column density associated with the cooler spectral component of the a) A496; b) A1795; c) A2142; d) A2199. Galactic values are also indicated by vertical lines.

FIG. 5 – N_H–T contours for isothermal fit to SSS data of A496.

FIG. 6 – χ^2 distributions for abundances of cooling flow (cf) and RS (hot) components of joint fits to LAC and SSS spectra. a) A496; b) A1795; c) A2142; d) A2199.

FIG. 7 – Two-temperature RS spectral models jointly fit to *Einstein* SSS and *Ginga* LAC data for A1795; see line 4 of Table 3 for best-fit parameters.

FIG. 8 – Two-temperature RS spectral models jointly fit to *Einstein* SSS and *Ginga* LAC data for A2142; see line 4 of Table 4 for best-fit parameters.

FIG. 9 – Two-temperature RS spectral models jointly fit to *Einstein* SSS and *Ginga* LAC data for A2199; see line 4 of Table 5 for best-fit parameters.

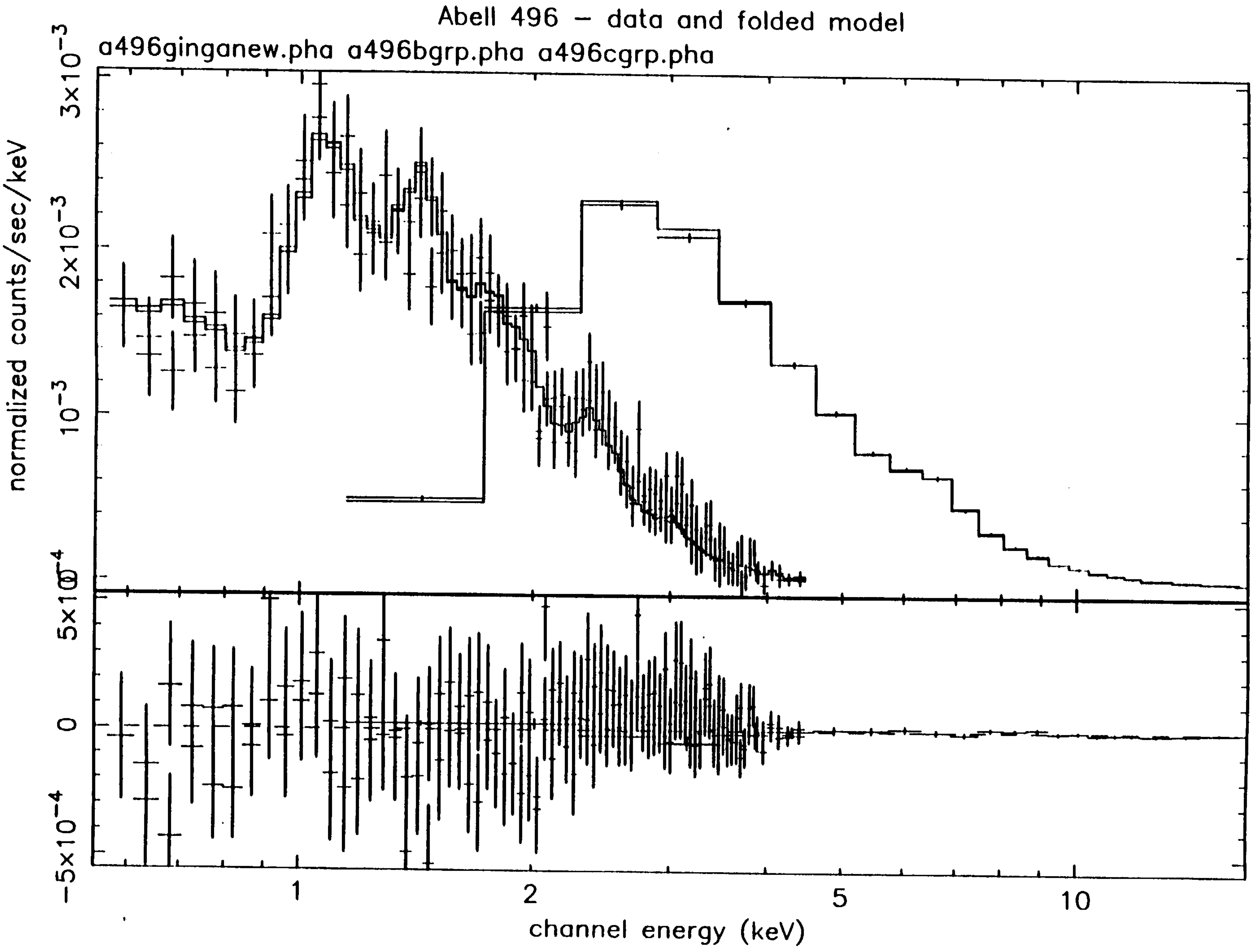
Abell 496 – data and folded model
a496ginganew.pha a496bgrp.pha a496cgrp.pha
normalized counts/sec/keV
3×10^{-3}
2×10^{-3}
10^{-3}
0
5×10^{-4}
0
−5×10^{-4}
1
2
5
10
channel energy (keV)

FIGURE 1

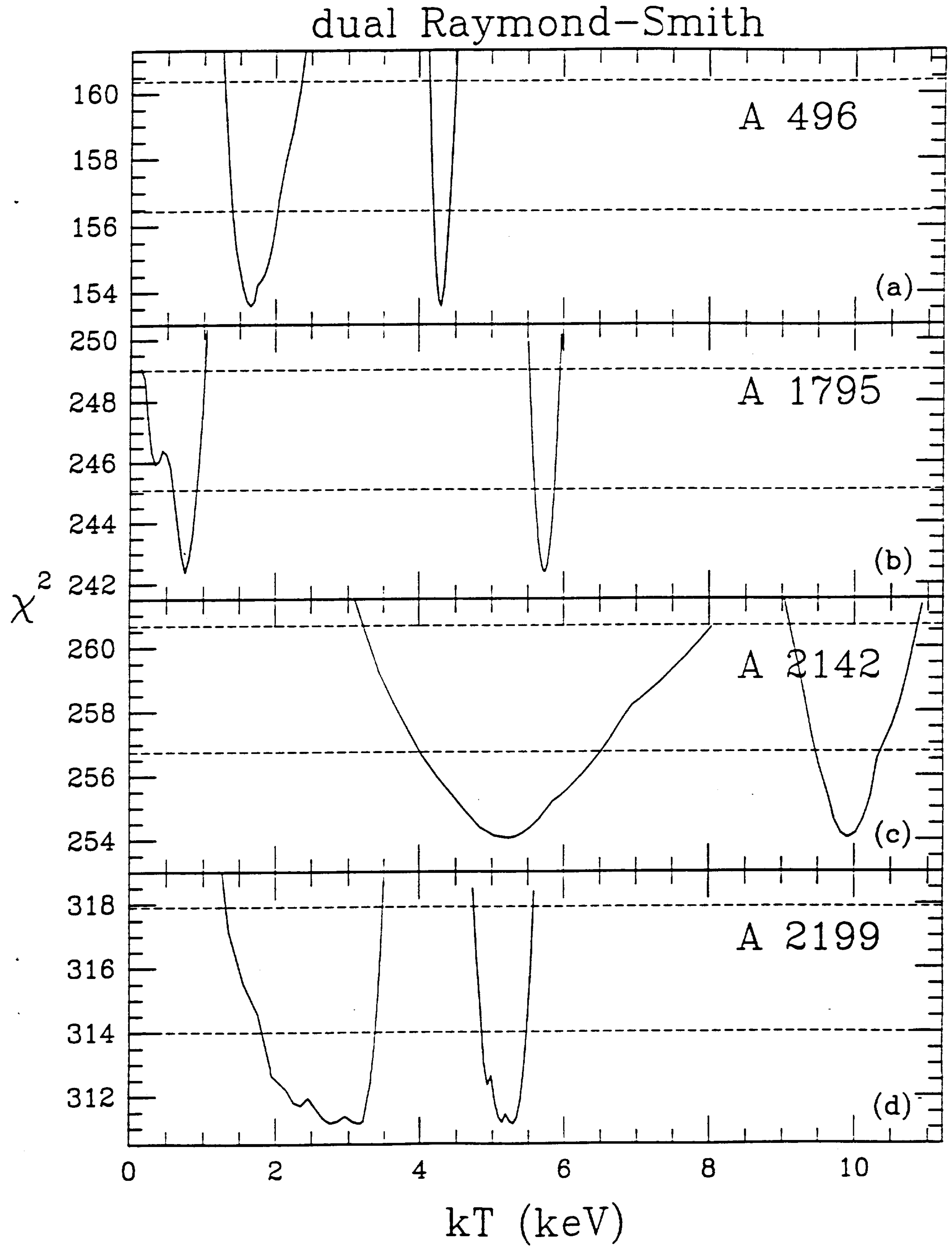
dual Raymond-Smith
A 496
A 1795
A 2142
A 2199
(a)
(b)
(c)
(d)
χ^2
160
158
156
154
250
248
246
244
242
260
258
256
254
318
316
314
312
0
2
4
6
8
10
kT (keV)

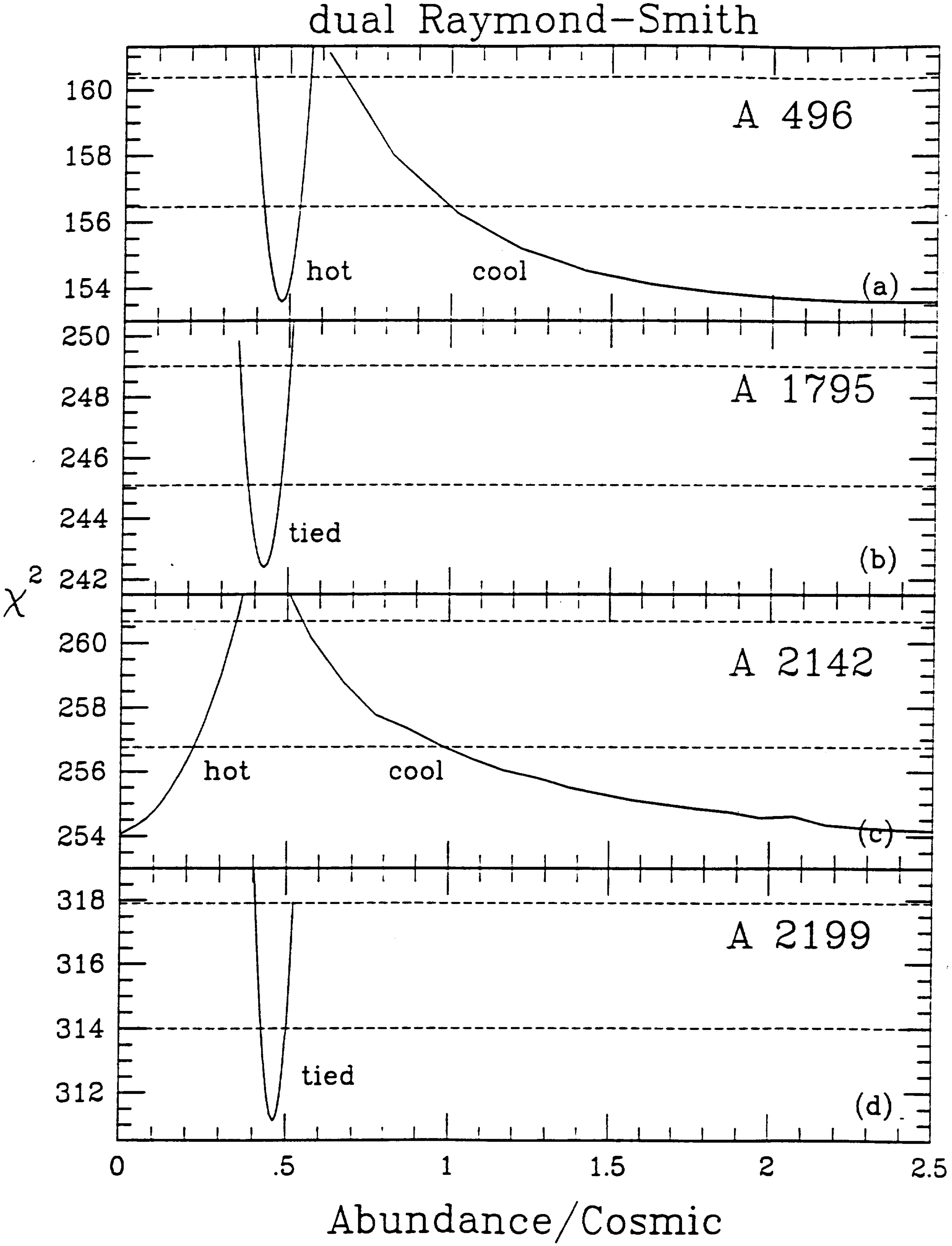
dual Raymond-Smith
A 496
hot
cool
(a)
A 1795
tied
(b)
A 2142
hot
cool
(c)
A 2199
tied
(d)
χ^2
160
158
156
154
250
248
246
244
242
260
258
256
254
318
316
314
312
0
.5
1
1.5
2
2.5
Abundance/Cosmic

FIGURE 3

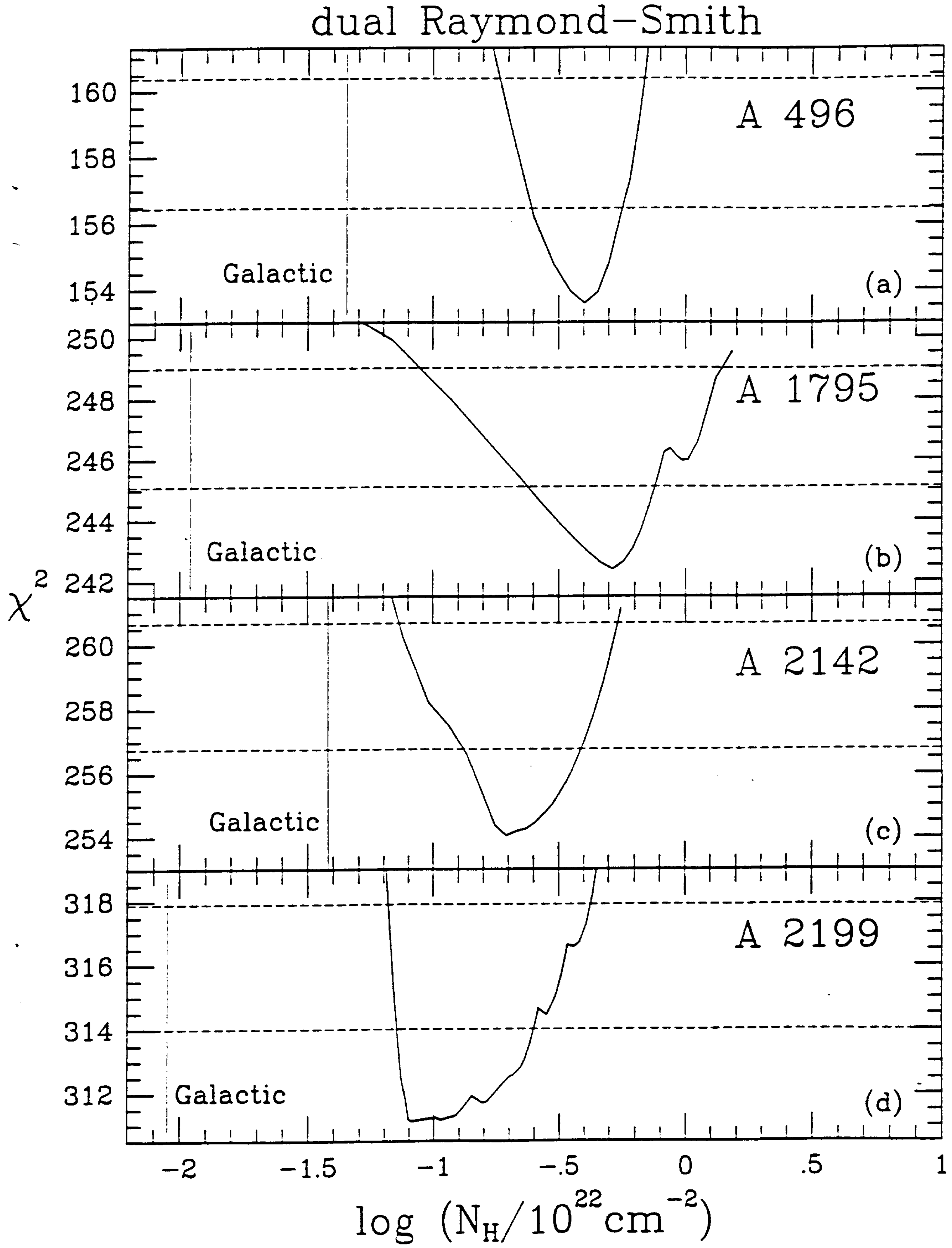
dual Raymond−Smith
A 496
A 1795
A 2142
A 2199
Galactic
Galactic
Galactic
Galactic
(a)
(b)
(c)
(d)
160
158
156
154
250
248
246
244
242
260
258
256
254
318
316
314
312
χ^2
−2
−1.5
−1
−.5
0
.5
1
$\log\,(N_H/10^{22}\,cm^{-2})$

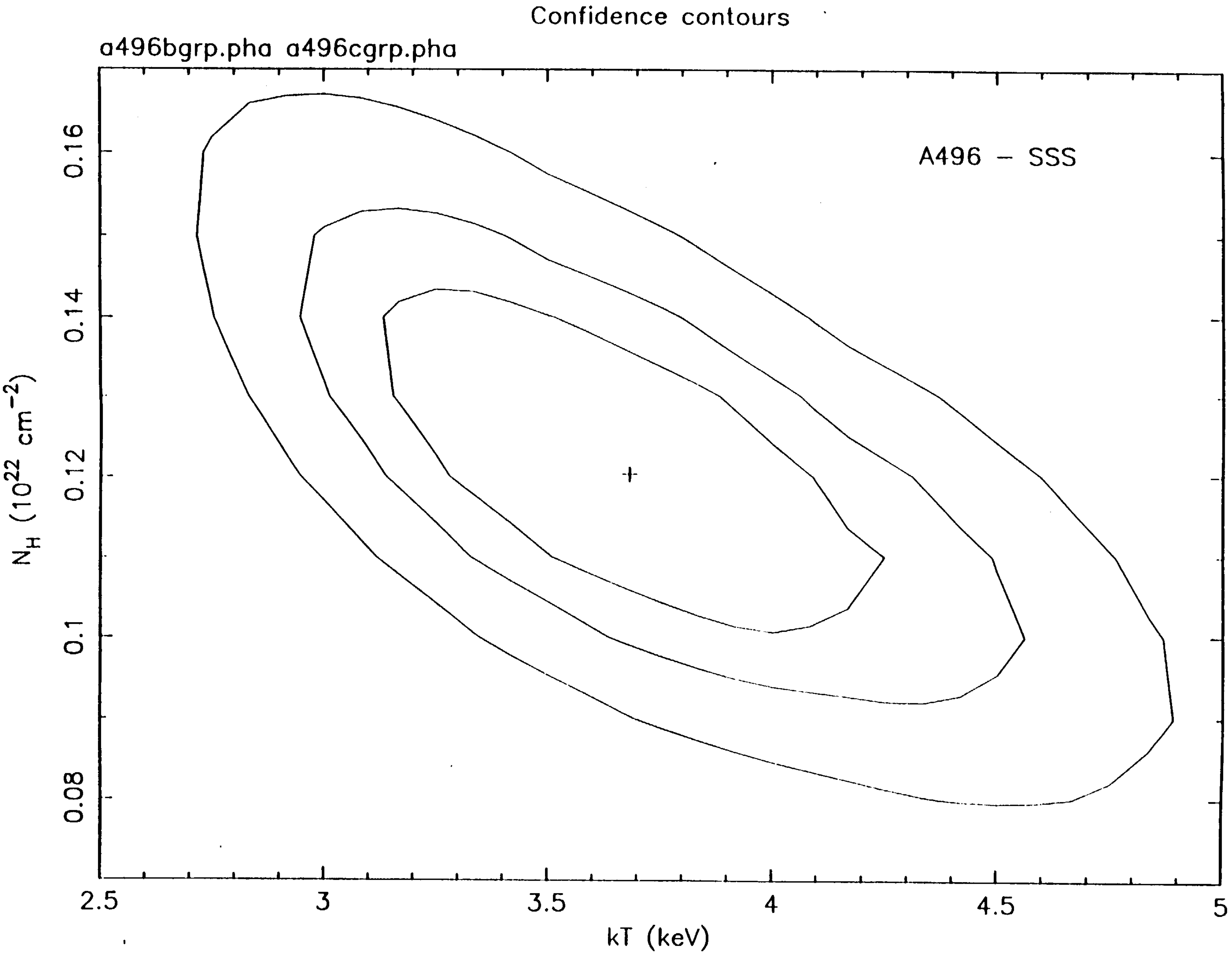
Confidence contours
a496bgrp.pha a496cgrp.pha
A496 – SSS
0.16
0.14
0.12
0.1
0.08
N_H (10^{22} cm^{-2})
2.5
3
3.5
4
4.5
5
kT (keV)

FIGURE 5

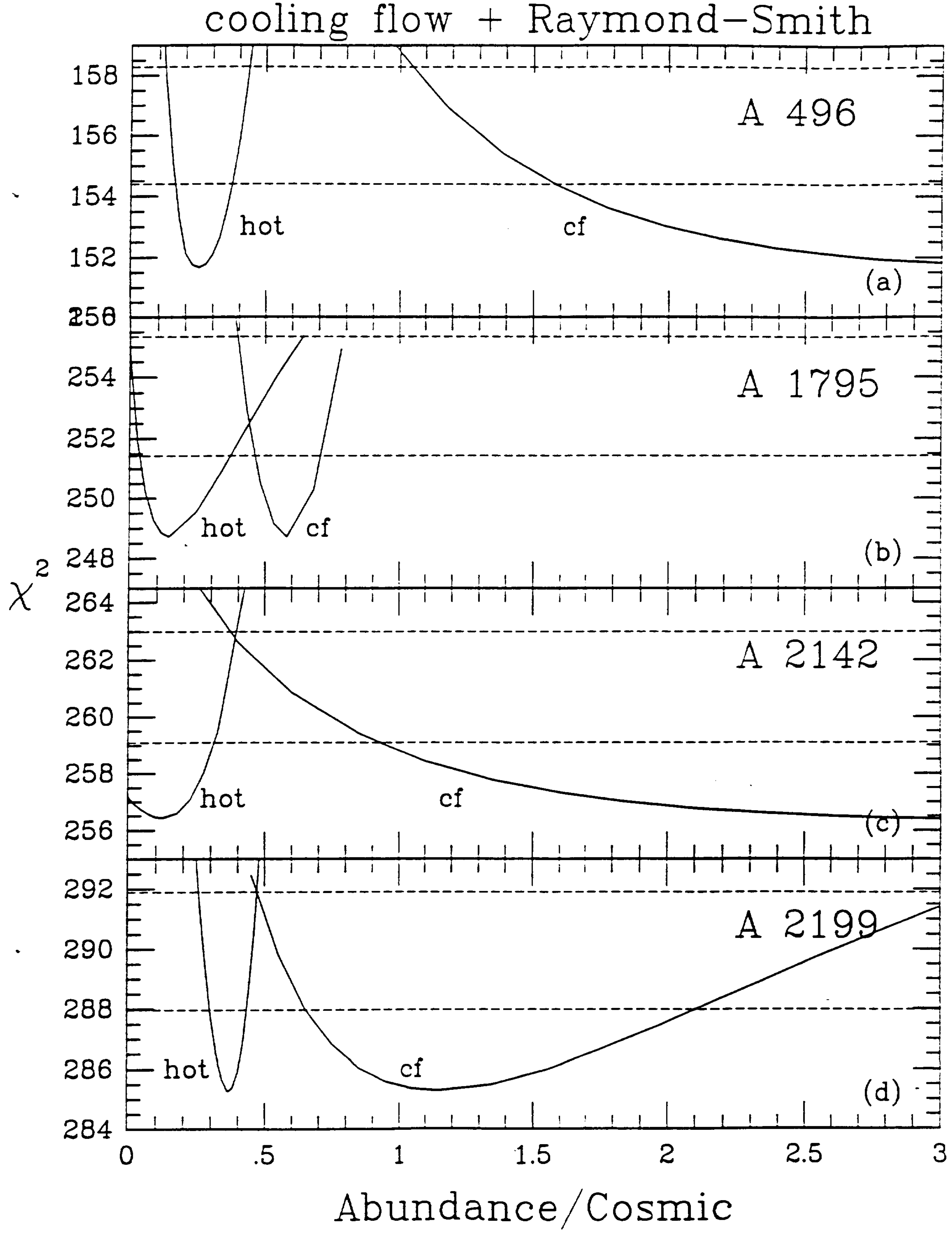
cooling flow + Raymond–Smith
A 496
hot
cf
(a)
A 1795
hot
cf
(b)
A 2142
hot
cf
(c)
A 2199
hot
cf
(d)
χ²
158
156
154
152
256
254
252
250
248
264
262
260
258
256
292
290
288
286
284
0
.5
1
1.5
2
2.5
3
Abundance/Cosmic

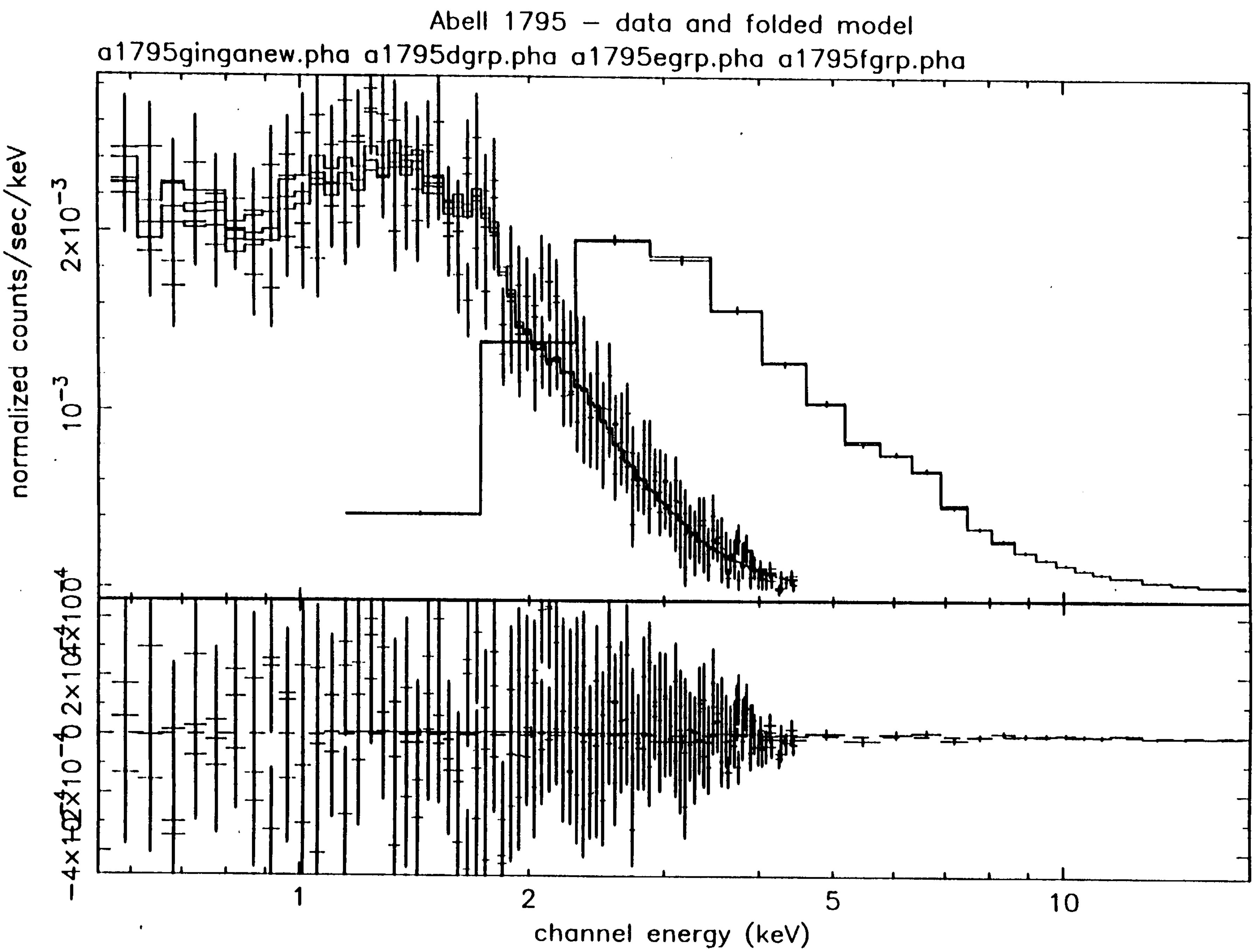
Abell 1795 – data and folded model
a1795ginganew.pha a1795dgrp.pha a1795egrp.pha a1795fgrp.pha
normalized counts/sec/keV
2×10^-3
10^-3
10^-4
4×10^-4
2×10^-4
0
-2×10^-4
-4×10^-4
1
2
5
10
channel energy (keV)

FIGURE 7

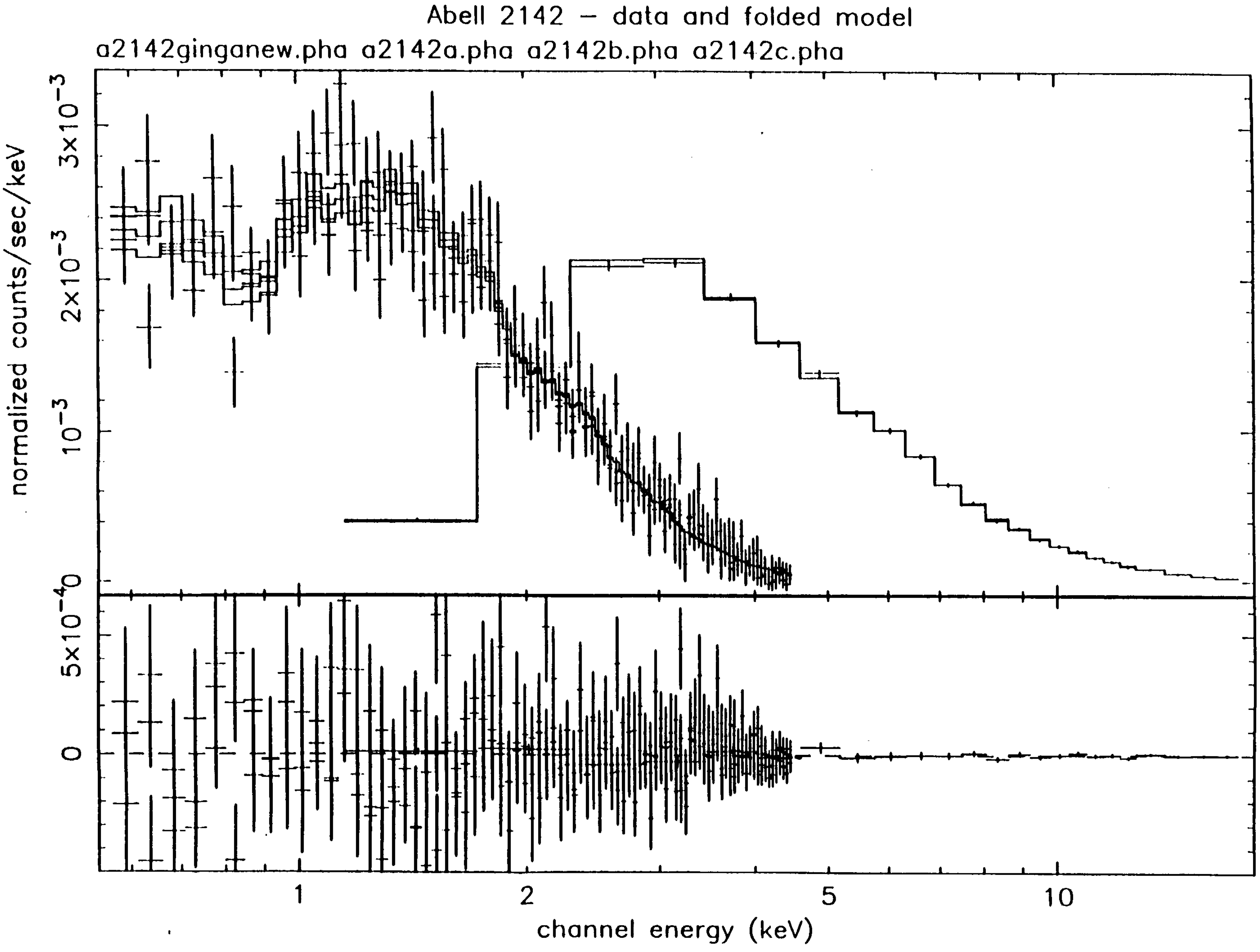
Abell 2142 – data and folded model
a2142ginganew.pha a2142a.pha a2142b.pha a2142c.pha
normalized counts/sec/keV
3×10^{-3}
2×10^{-3}
10^{-3}
0
5×10^{-4}
0
1
2
5
10
channel energy (keV)

FIGURE 8

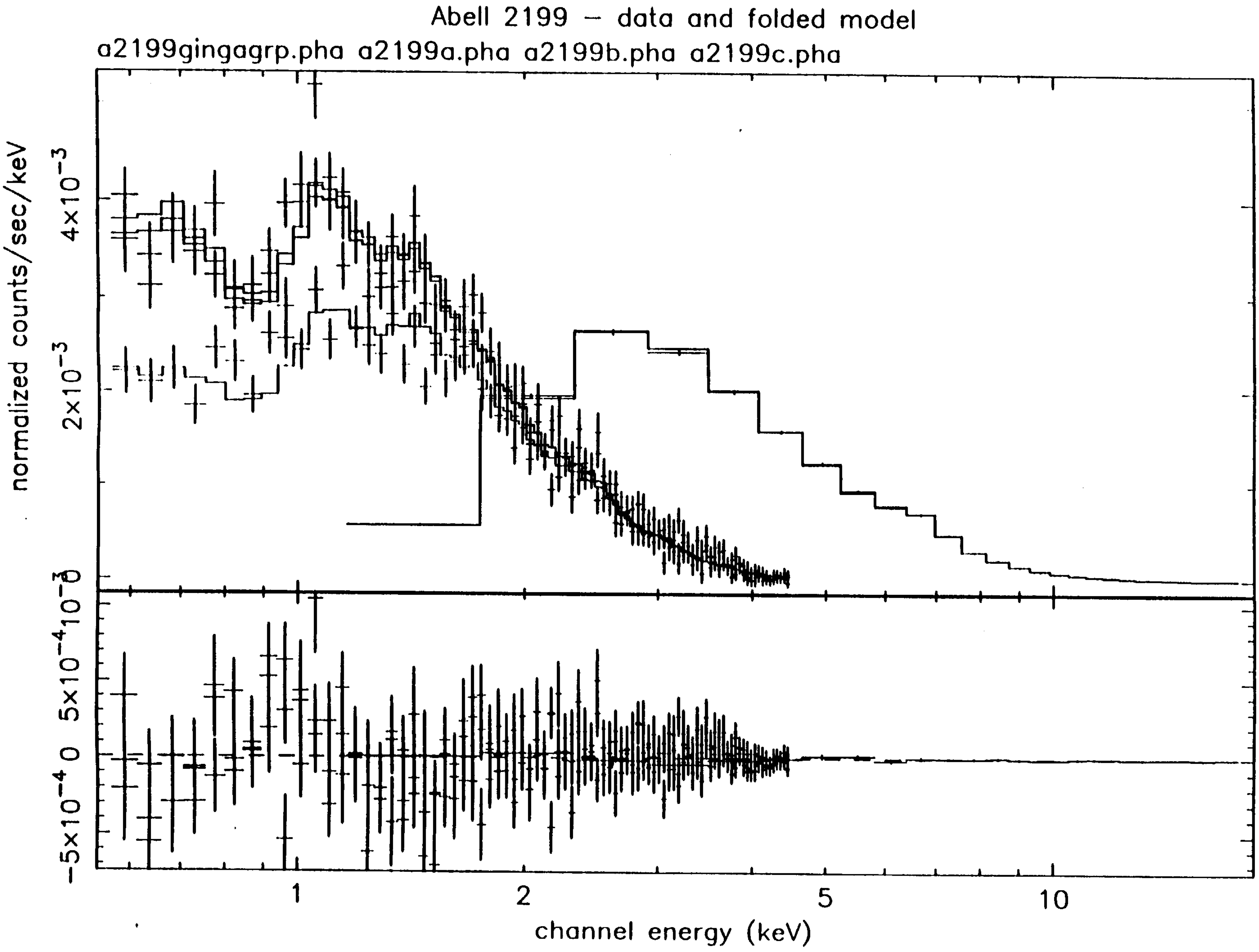
Abell 2199 – data and folded model
a2199gingagrp.pha a2199a.pha a2199b.pha a2199c.pha
normalized counts/sec/keV
4×10^{-3}
2×10^{-3}
0
10^{-3}
5×10^{-4}
0
-5×10^{-4}
1
2
5
10
channel energy (keV)

FIGURE 9